

Particle Production in p+p and d+Au Collisions at $\sqrt{s_{NN}} = 200$ GeV

Hongyan Yang



Thesis for the degree of Philosophiae Doctor (PhD)
at the University of Bergen

October 2007

Acknowledgments

Without the help and love from many people I am going to thank here, this thesis would not be here for you. First of all, my most sincere grateful thanks go to my supervisor Prof. Dieter Rörhich - for giving me the opportunity to study in this beautiful city of Bergen, and also the chance to work in the BRAHMS experiment at RHIC/BNL, for being a great and kind supervisor during the past three years, and helping me go through those difficulties I have had in my study in a unique and kind way. Meanwhile, he has also provided me a lot of opportunities to travel for conferences, and working with other colleagues. I have benefited from those travels for the work I have done for this thesis. I feel in debt of gratitude to Prof. Daicui Zhou and Prof. Xu Cai, without their guidance at the very beginning since 1999, I would not have entered the field of heavy ion physics, and continued with pursuing high level of study after university period in Wuhan. I have learned a lot about the field in many interesting discussions and seminars in the group before I came to Norway. The enthusiasm and their unremitting attempts towards physics they had shown to all students during that four years, I will always bear in my mind. Thank you - these two words are simply not enough to all of you.

In the several collaboration meetings and travels to Brookhaven at Long Island, where BRAHMS/RHIC experiment is located, I got to know more colleagues from BRAHMS. Many thanks go to Flemming Videbaek for being patient in explaining me everything I have ever asked him as a newcomer, and the informal and friendly atmosphere in the collaboration helped me a lot to overcome the unnecessary shyness. As a very late joined member in BRAHMS Collaboration three years ago, being not familiar with the experiment at Brookhaven, earlier BRAHMS members from Norway, Jens Ivar Jødre, Zhongbao Yin in Bergen, Bjørn Samset in Oslo have given me the first hand introduction to the analysis work in BRAHMS. And later, several trips to the Niels Bohr Institute, Claus Jørgensen and Djamel Ouerdane just before they were leaving the institute, together with Catalin Ristea, Truls Larsen and Christian Holm Christensen kindly helped me get started with the work. I feel grateful for the encouraging spirit in the HEHI group that Prof. Jens-Jorgen Gaardhøje and Ian Bearden created at NBI during several of my stays there. For the analysis work on the d+Au and p+p data for this thesis, the help from Ramiro Debbe and the discussions with him have been the most thankworthy part. I thank Pawel Staszal, J H Lee, Trine Tveter, Stephen Sanders, Kris Hagel, Micheal Murray, Natalia Katrynska and Eun-Joo Kim for the effective collaboration, for those hours spent in the counting house. I feel lucky to have worked with people as nice as you. It was nice to work with friends like Radoslaw Karabowicz (Radek) and Ionut Arsene in the collaboration, thank you

for being there.

I thank Prof. Lianshou Liu, Prof. Jiarong Li, Prof. Enke Wang and Prof. Yuanfang Wu *et al* for their wonderful teaching on those essential subjects for nuclear and particle physics in those years I spent in the Institute of Particle Physics at Hua-zhong Normal University in Wuhan. I thank Prof. Laszlo Cernai, Prof. Johann Rafelski, and Prof. Dieter Rörhich for giving interesting lectures on heavy ion physics during the period I was in the Physics Department at the University of Bergen. I feel lucky I have made close friend like Ágnes Nyíri, who cares about me and has been very supportive in the past few years we have spent in Bergen, who has made my time in Bergen even more unforgettable. What's more, I thank her for reading part of the thesis. I thank all members of the *tungione* (heavy ion physics) group, Sebastian Bablok, Matthias Richter, Håvard Helstrup, Dag Toppe Larsen, Gaute Øvrebekk, Kenneth Aadmodt and Dominik Fehlker *et al*, who have made the group a warm place. And I enjoyed the nice discussion and conversation with Eteer Molnar and Sven Zschocke from the theoretical group, whom I would like to thank. I thank my officemate Kalliopi Kanaki, whom I share quite a few interests with, for being very supportive and having many nice conversations on a lot of interesting topics since she moved in four months ago, also for spending time helping me on \LaTeX and improving the wording in this thesis. There are far too many people I would like to thank during the time I spent in Wuhan and Bergen, who have helped me in all kinds of ways. Sorry for not listing them all.

I thank the financial support from Lånekassen (Norwegian State Educational Loan Fund) since January 2004.

There is a special thank I would like to give to a special friend of mine Bianca Ross. She has been always caring about my life since the dark evening I arrived at Bergen. I deeply appreciate the trust, the support, the help and the love she has offered me whenever I needed. The last thank goes to my family, especially my parents, without the freedom you have given me, I would not have gone so far away from home and have this work done. As the youngest child in the family, being far away from home, I deeply owe you a lot of concern I should have given to you. I thank my elder brother and sister, being always at my side, even without much understanding about what I have been doing though.



Preface

In ultra-relativistic heavy ion physics, heavy nuclei such as lead, gold and copper have been accelerated to ultra-relativistic velocity and brought to collide with each other in order to study the properties of the extreme hot and dense matter created in such violent interactions in the laboratory. Although the main aim is the study of the deconfined phase of the strongly interacting matter created in central Au+Au collisions, measurements of p+p and d+Au reactions are essential for the understanding of the properties of the new state of matter. The data from the small (binary) systems is not only needed as a reference for the nucleus-nucleus system, e.g. for the nuclear modification factor, and to disentangle initial state effects (already visible in d+Au) from final state effects due to the deconfined phase, but also allows to verify models like pQCD and provides a testbed for the study of new phenomena like the Colour Glass Condensate.

The **B**road **R**ange **H**adron **M**agnetic **S**pectrometer (BRAHMS) experiment at the **R**elativistic **H**avy **I**on **C**ollider (RHIC) at **B**rookhaven **N**ational **L**aboratory (BNL) collected data from d+Au and p+p collisions in 2003 and 2005. The calibration of the raw detector data and the event reconstruction turned out to be complicated due to the incomplete installation in 2003 and to unstable performance of both the trigger and spectrometer detectors, e.g. the inelasticity and beam-beam counters and time-of-flight (TOF) detectors (H1 and H2) in the forward spectrometer. The reconstruction process had to be iterated several times, and the selection of good runs was time consuming.

Most of the work went into the quality analysis of runs in order to select valid runs/sets, into the development and improvement of (fault-tolerant) particle identification methods and into the development of correction and normalization schemes (Chapter 4). The result, spectra of identified charged hadrons (π^\pm, K^\pm and $\bar{p}(p)$) at different rapidities, is shown in Chapter 5 for minimum bias p+p, d+Au and centrality selected d+Au collisions. Particle ratios are presented in Chapter 5. A systematic study was performed on the extrapolation of the spectra outside the transverse momentum acceptance (Chapter 4). The extrapolation procedure yields rapidity densities and mean transverse momenta (Chapter 5). A special emphasis is on the net-proton yields in Chapter 7. The nuclear modification factors R_{dAu} are discussed in Chapter 6. Since the p+p and d+Au data are a reference for theoretical models and nucleus-nucleus collisions, they are compared to data from other experiments when available and checked for consistency in Chapter 8.

Contents

Acknowledgments	iii
Preface	v
1 Nuclear Collisions at Ultra-relativistic Energies	1
1.1 Collision phenomenology	1
1.1.1 Collision evolution	2
1.1.2 Experimental observables	2
1.2 Recent results from RHIC	6
1.2.1 Stopping	7
1.2.2 Jet quenching	7
1.2.3 Elliptic flow v_2 at partonic level	9
1.3 Objective of the thesis	10
2 Theoretical Concepts for Describing Nuclear Collisions	13
2.1 Perturbative QCD (pQCD)	14
2.2 Color Glass Condensate (CGC)	18
2.2.1 Properties of a CGC	19
2.2.2 Applications of CGC to RHIC	20
2.3 pQCD <i>vs</i> CGC	22
2.4 Other theoretical models	23
2.4.1 HIJING	23
2.4.2 AMPT	24
2.4.3 Parton recombination model	25
3 RHIC and the BRAHMS Experiment	29
3.1 The Relativistic Heavy Ion Collider	29
3.2 The BRAHMS experimental Setup	30
3.2.1 Mid-rapidity spectrometer (MRS)	31
3.2.2 Forward Spectrometer (FS)	31
3.3 Detectors	32
3.3.1 Global detectors and trigger system	32
3.3.2 Tracking detectors	36
3.3.3 Particle identification (PID) detectors	38

4	Spectra Analysis	43
4.1	Data selection	43
4.1.1	Event and track selection	44
4.2	Particle Identification	47
4.2.1	Particle identification by Time-of-Flight	47
4.2.2	Particle identification by Čerenkov detectors	48
4.2.3	Treatment of RICH inefficiency	51
4.3	Corrections	52
4.3.1	Geometrical acceptance correction	52
4.3.2	Tracking efficiency correction	53
4.3.3	PID efficiency correction	55
4.3.4	Physics corrections by BRAG/GEANT	56
4.4	Normalization and spectra construction	57
4.4.1	Corrections and normalization	57
4.4.2	Settings combination and final spectra	58
4.4.3	Errors from setting combinations	59
4.5	GEANT simulation study	59
4.6	p_T extrapolation	61
4.6.1	Particle yields	61
4.6.2	Mean transverse momentum $\langle p_T \rangle$	64
4.6.3	Yields for net-proton	65
4.6.4	Systematic errors	66
5	Spectra and yields	69
5.1	p_T spectra	69
5.2	Particle ratios	69
5.2.1	Like-particle ratios	70
5.2.2	Unlike-particle ratios	76
5.3	Rapidity densities	81
5.4	Mean transverse momentum $\langle p_T \rangle$	83
6	Nuclear Modification Factors	91
7	Stopping	99
8	Comparisons and Discussion	103
8.1	Minimum bias d+Au collisions at $\sqrt{s_{NN}} = 200$ GeV	103
8.2	p+p collisions at $\sqrt{s} = 200$ GeV	103
8.3	Nuclear modification factors at mid-rapidity	106
8.4	Pseudo-rapidity density	108
8.5	Net-proton dN/dy	109
9	Summary and Conclusion	113
A	BRAHMS Collaboration	115
B	Kinematics	117

C Some Characteristics of RHIC	119
D Fit functions	121
E Spectra and fit study	123
F Publications	135

List of Figures

1.1	Transparency scenario	2
1.2	Stopping scenario	2
1.3	Collision space time evolution	2
1.4	Constant cross section $d\sigma/dx$ for the reaction $p+p \rightarrow p+X$ after integration over the transverse momentum	3
1.5	Probability distribution for protons to lose rapidity $-\Delta y$ in collisions with protons	4
1.6	Net-proton density in p+p and p+Pb collisions at SPS energy (NA49)	5
1.7	Rapidity distribution of protons from p+A collisions as a function of rapidity loss	5
1.8	Net-proton rapidity distribution and rapidity loss in central Au+Au collisions measured by the BRAHMS experiment at RHIC, compared to results at AGS, SPS energies	7
1.9	A schematic view of the inelastic scattering between two partons	8
1.10	Disappearance of back-to-back jets in central Au+Au collisions at RHIC	8
1.11	Nuclear modification factor measured by the BRAHMS experiment in minimum bias collisions of d+Au and central Au+Au collisions	9
1.12	Elliptic flow v_2 for mesons and hadrons at partonic level in Au+Au collisions measured by PHEINX and STAR experiments	10
2.1	Phase diagram (critical temperature <i>vs</i> baryon density) and LQCD prediction	13
2.2	Comparison of PHENIX measurement of invariant differential cross section for inclusive π^0 production at mid-rapidity to NLO pQCD calculations for p+p collisions at $\sqrt{s} = 200$ GeV	15
2.3	Comparison of BRAHMS measurement in p+p collisions at $\sqrt{s} = 62.4$ GeV to NLO pQCD calculations	16
2.4	Scale evolution of the $R_g^A(x, Q^2)$ as a function of x for nucleus Pb ($A=208$) at a fixed Q^2	16
2.5	R_{dAu} by pQCD (LO) calculation comparing to BRAHMS experimental data	17
2.6	R_{CP} by pQCD (LO) calculation for homogeneous shadowing with the FGS1 parametrization	18
2.7	The HERA data for the gluon distribution function as a function of x for various values of Q^2	19

2.8	A physical picture of the low x gluon density inside a hadron as a function of energy	20
2.9	Comparison of a CGC prediction to hadron multiplicity measurements in Au+Au and d+Au collisions at RHIC	21
2.10	Nuclear modification factor R_{dAu} of charged hadrons at different rapidities. CGC calculation and BRAHMS experimental data	21
2.11	CGC calculation of nuclear modification factor R_{CP} of charged particles $(h^+ + h^-)/2$ at mid-rapidity and R_{CP} of negatively charged particles h^- at forward rapidity, compared to BRAHMS experimental data	22
2.12	Cronin effect on pion production at Fermilab and RHIC	23
2.13	Pseudo-rapidity distributions of charged particles in d+Au collisions at $\sqrt{s_{NN}} = 200$ GeV with centralities determined from N_{part}	24
2.14	Transverse momentum spectra of π^+ , K^+ and protons from AMPT for minimum-bias d+Au collisions, and ratios of the transverse momentum spectra from AMPT for d+Au collisions over those for p+p collisions	25
2.15	Comparison between positive pion spectrum from STAR measurement and parton recombination model	26
2.16	Comparison between proton spectrum from STAR measurement and parton recombination model	26
3.1	Schematic overview of the RHIC accelerator complex	29
3.2	Schematic picture of the BRAHMS experiment	31
3.3	Top view of the BRAHMS experiment	32
3.4	Beam-Beam counters	33
3.5	The inelasticity counter setup	34
3.6	Schematic view of the interaction region, and locations of left and right ZDCs	34
3.7	Centrality cut and the evaluation of average number of collisions	35
3.8	Tracks in TPM2	37
3.9	Basic TOF principles	38
3.10	Side view of C1	39
3.11	Side view of the RICH	40
3.12	An example of a typical ring image on RICH	40
3.13	BRAHMS acceptance map for pions, kaons and protons	41
4.1	An example of track selection at FS: cuts on χ^2	45
4.2	$3\text{-}\sigma$ cut on matching hits on TOFW and tracks at MRS	46
4.3	An example of primary track selection at both MRS and FS	47
4.4	m^2 vs p distribution. Resolution curves are obtained by a simultaneous fit, a $2\text{-}\sigma$ cut on m^2 width was used	48
4.5	An example of m^2 measurement by H1 and H2	49
4.6	An example of the direct PID method by the RICH	50
4.7	PID by H1 and H2, augmenting the RICH	51
4.8	Correction on geometrical acceptance for setting 90B1050	53
4.9	T1 efficiency study in d+Au collisions	54
4.10	Tracking efficiency (FS), setting 4B3450	55

4.11	GEANT corrections for physics processes	56
4.12	Combination of several settings in the rapidity interval $2.90 < y < 3.10$, and the construction of spectrum for π^-	57
4.13	An example of the final p_T spectra for pions at $2.90 < y < 3.10$ after all the corrections	58
4.14	Study on ratios between spectrum from different settings and the aver- age spectrum for positive pions at $2.90 < y < 3.10$ in p+p collisions . .	59
4.15	GEANT simulation study at $2.95 < y < 3.05$ in p+p collisions	60
4.16	GEANT simulation study, consistency study between the input and spectrum after correction	60
4.17	An example of the extraction of dN/dy from the final p_T spectra for charged pions in p+p collisions at $-0.10 < y < 0.10$, using a power law function and exponential function in p_T	62
4.18	An example of the extraction of dN/dy from the final p_T spectra for charged kaons in d+Au collisions at $-0.10 < y < 0.10$, using various fit functions	63
4.19	An example of the extraction of dN/dy from the final p_T spectra for charged protons in p+p collisions at $-0.10 < y < 0.10$, using an expo- nential function in m_T and a Boltzmann function	64
4.20	An example of the extraction of net-proton yield dN/dy from the p_T spectra for net-proton in p+p collisions at $-0.10 < y < 0.10$	65
4.21	An example of the extraction of net-proton yield dN/dy from the p_T spectra for net-proton in p+p collisions at $2.90 < y < 3.10$	66
5.1	Spectra for positive hadrons in minimum bias d+Au collisions at $\sqrt{s_{NN}} =$ 200 GeV	70
5.2	Spectra for negative hadrons in minimum bias d+Au collisions at $\sqrt{s_{NN}} =$ 200 GeV	70
5.3	Spectra at rapidity $y = 0, 1$ and 3 in minimum bias d+Au collisions . .	71
5.4	Spectra at rapidity $y = 0$ in d+Au collisions for different centralities . .	72
5.5	Spectra at rapidity $y = 1$ in d+Au collisions for different centralities . .	73
5.6	Spectra at rapidity $y = 3$ in d+Au collisions for different centralities . .	74
5.7	Spectra for positive hadrons in p+p collisions at $\sqrt{s} = 200$ GeV	75
5.8	Spectra for negative hadrons in p+p collisions at $\sqrt{s} = 200$ GeV	75
5.9	Spectra at mid-rapidity in p+p collisions at $\sqrt{s} = 200$ GeV	76
5.10	Spectra at forward rapidity in p+p collisions at $\sqrt{s} = 200$ GeV	77
5.11	Like-particle ratios at rapidities $y = 0, 1$ and 3 in minmum bias d+Au collisions	78
5.12	Like-particle ratios at rapidity $y = 0, 1$ and 3 in d+Au collisions with different centralities	79
5.13	Like-particle ratios at/near mid-rapidity and at forward rapidities in p+p collisions.	80
5.14	K/ π ratios at rapidity $y = 0$ and $y = 3$ in minimum bias d+Au collisions compared to those in p+p collisions at the same rapidities.	81
5.15	K/ π ratios at rapidity $y = 0$ and $y = 3$ in d+Au collisions witin different centrality classes	82

5.16	K/ π ratios at mid-rapidities and forward rapidities in p+p collisions . . .	83
5.17	p/ π ratios at rapidity $y = 0$ and $y = 3$ in minimum bias d+Au collisions, compared to those in p+p collisions at the same rapidities	84
5.18	p/ π ratios at rapidity $y = 0$ and $y = 3$ in d+Au collisions for different centralities	85
5.19	p/ π ratios at mid-rapidities and forward rapidities in p+p collisions. . .	86
5.20	Rapidity densities and p_T integrated particle ratios versus rapidity in p+p collisions at $\sqrt{s} = 200$ GeV	87
5.21	Rapidity densities and particle p_T integrated ratios versus rapidity in d+Au collisions at $\sqrt{s_{NN}} = 200$ GeV	88
5.22	$\langle p_T \rangle$ in d+Au collisions at $\sqrt{s_{NN}} = 200$ GeV	89
5.23	$\langle p_T \rangle$ for charged hadrons in p+p collisions at $\sqrt{s} = 200$ GeV	90
6.1	Rapidity dependence of R_{dAu} for charged pions, kaons and protons in minimum bias d+Au collisions	92
6.2	Centrality dependence of R_{dAu} for charged pions, kaons and protons in d+Au collisions	93
6.3	R_{dAu} for positive and negative pions, kaons, and protons (anti-protons) in minimum bias d+Au collisions at rapidity $y = 0, 1$ and 3	94
6.4	R_{dAu} for positive and negative pions, kaons, and protons (anti-protons) in the most central (0-30%) d+Au collisions at rapidity $y = 0, 1$ and 3	95
6.5	R_{CP} as a function of p_T for charged hadrons of different species at $y = 0, 1$ and 3	97
6.6	R_{CP} as a function of p_T for charged hadrons of different specie at $y = 0$ and $y = 3$	98
7.1	Net-proton rapidity density in p+p collisions and model comparison at $\sqrt{s} = 200$ GeV	99
7.2	Net-proton rapidity desity in minimum bias d+Au collisions, compared to results by HIJING/B estimation	100
7.3	Centrality dependence of net-proton rapidity density in d+Au collisions at $\sqrt{s_{NN}} = 200$ GeV	100
8.1	Spectra for charged hadrons at rapidity $y = 0$ in minimum bias d+Au collisions compared to results from other RHIC experiments at mid-rapidity	104
8.2	Spectra of charged hadrons at rapidity $y = 0$ in p+p collisions, compared to the results from other RHIC experiments at mid-rapidity	105
8.3	Spectra of charged hadons at rapidity $y = 3$ in p+p collisions compared to the recent published BRAHMS results ($y = 2.95$)	106
8.4	Comparison of BRAHMS measurement to NLO calculations for p+p collisions at $\sqrt{s} = 200$ GeV	107
8.5	Comparison of R_{dAu} for charged pions, kaons and protons (including \bar{p}) from BRAHMS to other RHIC experiments at mid-rapidity for minimum bias d+Au collisions	107

8.6	Comparison of BRAHMS measurements of the identified hadrons to the charged hadron pseudo-rapidity density distribution in d+Au collisions [1] at $\sqrt{s_{NN}} = 200$ GeV.	108
8.7	Comparison of $dN/d\eta$ of the identified hadrons to PHOBOS and UA5 measurements of charged hadron pseudo-rapidity distribution in p+p and p+ \bar{p} inelastic collisions at $\sqrt{s} = 200$ GeV.	108
8.8	Net-proton rapidity density comparison: d+Au <i>vs</i> Au+Au	109
8.9	Net-proton rapidity density comparison: p+p <i>vs</i> Au+Au	110
8.10	Net-proton rapidity density in d+Au collisions at $\sqrt{s_{NN}} = 200$ GeV, compared to net-proton, net- Λ and net-baryon rapidity densities measured by STAR experiment at RHIC	110

List of Tables

3.1	The running periods at RHIC until now	30
3.2	Trigger overview for Run IIIa and Run V.	35
3.3	Summary of the main characteristics of the TPCs	36
3.4	Summary of the main characteristics of magnets	37
3.5	Performance of the TOF PID devices in BRAHMS (with a $3\text{-}\sigma$ cut)	38
4.1	All data settings in d+Au and p+p collisions at $\sqrt{s_{NN}} = 200$ GeV for this thesis	44
4.2	Event selection	45
4.3	Track selection	47
4.4	Parameters used in the particle identification by TOFW (MRS) in d+Au collisions	48
4.5	Parameters used in the particle identification by TOFW (MRS) in p+p collisions	49
4.6	Refractive index <i>vs</i> run number	50
4.7	Tracking efficiency for charged hadrons at MRS	53
4.8	Fit function and fit range dependence of proton yield dN/dy at $2.90 < y < 3.10$ in p+p collisions	67
4.9	Fit function and fit range dependence of anti-proton yield dN/dy at $2.90 < y < 3.10$ in p+p collisions	67

Chapter 1

Nuclear Collisions at Ultra-relativistic Energies

We can learn from nuclear collisions at ultra-relativistic energies about the properties of strongly interacting matter at high energy density. In a central collision, a large fraction of the energy of the two beams, consisting of two bunches of nuclei which have been accelerated to relativistic energy, is deposited in a small region of space. This fact results in the formation of a very high energy density in the collision region. After the collisions, this high energy density is eventually converted into particle production (mostly pions), and probably also a blast of thermal waves accompanied with the particle production. The aim of nuclear collisions at ultra-relativistic energies is to study the matter at high energy density and the evolution of the collision system from two slats of Lorentz contracted nuclei at the initial stage till the the final freeze-out of the produced particles.

The RHIC at Brookhaven National Laboratory makes nuclei collide with each other and produces this matter with high energy density in the laboratory. The collider is designed to accelerate nuclei to an energy of 100 GeV per nucleon in the center-of-mass (CM) system, which accounts for about a CM energy of 40 TeV in the collision when the nucleus is gold (Au).

1.1 Collision phenomenology

After being accelerated to relativistic energy, two colliding nuclei become two fast moving slats. There are two different collision scenarios, transparency and stopping by Bjorken [2] and Landau [3] respectively. If the two nuclei are transparent to each other, as shown in figure 1.1, the colliding nuclei lose only a small fraction of their energy and move forward with their original speed which would result in a net-baryon free central region. A fully stopping picture is shown in figure 1.2. In this picture, all the nucleons in the colliding nuclei are fully stopped. All the initial energy carried by nucleons are deposited in the vicinity of the center of mass of the collision.

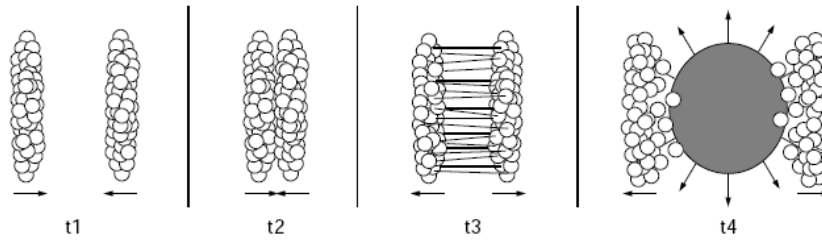


Figure 1.1: Transparency scenario [2].

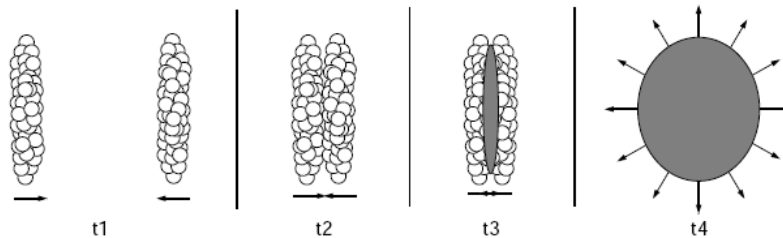


Figure 1.2: Stopping scenario [3].

1.1.1 Collision evolution

The evolution of the collision system is phenomenologically described as the following four stages: initial parton scattering, fireball formation, hadronization and freeze-out of hadrons. Figure 1.3 shows the evolution of the collision system in light-cone coordinate system. When two nuclei are approaching each other, partons from nucleons inside nuclei scatter at partonic level, which is regarded as the initial condition of the collisions, and a partonic fireball is created. When the energy density in the central rapidity region is high enough, the system gets thermalized, and a quark gluon plasma (QGP) may be created. As the system expands, it cools down and starts to hadronize. Finally, hadrons will freeze-out when the temperature of the system drops.

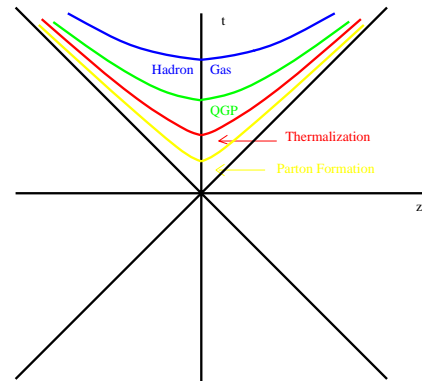


Figure 1.3: *Collision space time evolution [4] in light-cone coordinate system.*

1.1.2 Experimental observables

In the experiment, what characterize the particle production are the particles' momenta. From those information, one can study the degree of stopping in the collisions, construct invariant differential cross sections, from which particle yields and ratios

can be extracted for the study of the chemistry of the system. Further more, nuclear modification factors can be constructed to study medium effects. Angular correlations of particles are the result of di-jets, and the **H**anbury-**B**rown **T**wiss (HBT) effect leads to momentum correlations of identical particles. Last but not least, flow is an important observable, from which one can study the collective effects and the degree of the thermalization in the system. In the following, the observables related to the discussion in this thesis will be introduced.

Nuclear stopping power

Nuclear stopping power was introduced in high energy nuclear collisions by Busza and Goldhaber [5] in 1983 to discuss the degree of stopping power which an incident nucleon suffers when it collides with nuclear matter. The kinetic energy loss of the incident nuclear matter which is correlated to the rapidity loss of the incident protons, is converted into the production of a large number of particles (mostly pions). The distribution of protons with momentum fraction x_F ¹ is approximately uniform over the whole range of x_F in p+p collisions at $p_{\text{lab}} = 100$ and 175 GeV/c [6], as shown in figure 1.4. A constant x_F distribution corresponds to an exponential distribution in rapidity with the maximum near beam rapidity (see figure 1.5). A quantitative analysis shows that only approximately 50% of the beam energy is available for particle production in minimum bias p+p collisions; 50% of the beam energy is carried away by the projectile and target fragments.

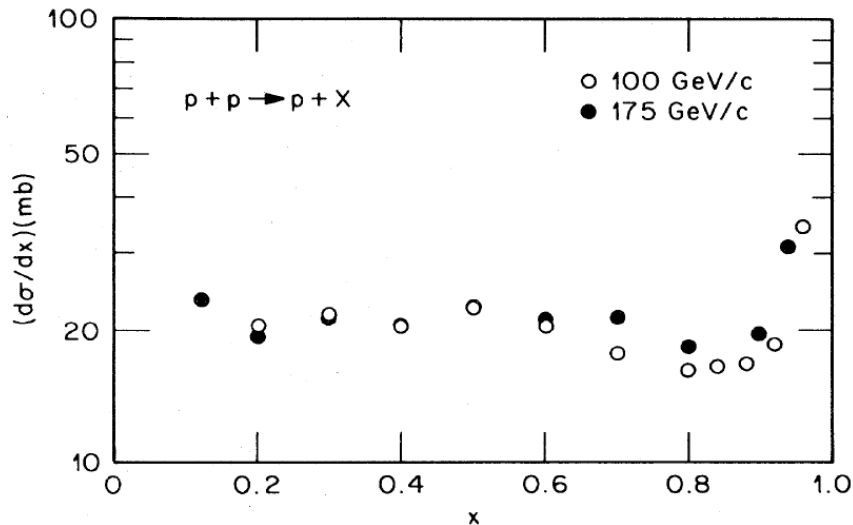


Figure 1.4: Cross section $d\sigma/dx$ for the reaction $p+p \rightarrow p+X$ after integration over the transverse momentum [6]. Here, x is the Feynman variable x_F .

Figure 1.6 shows the total net-proton density as function of x_F (left panel) and projectile component of net-proton density (right panel) in p+p and p+Pb collisions

¹Feynman variable is defined as $x_F = (E+p_L)/(E_0+p_0)$. The relation between x_F and $\Delta y = y-y_0$ is $\ln x_F = \Delta y + \ln m_T/m$. It was labeled as x in figure 1.4

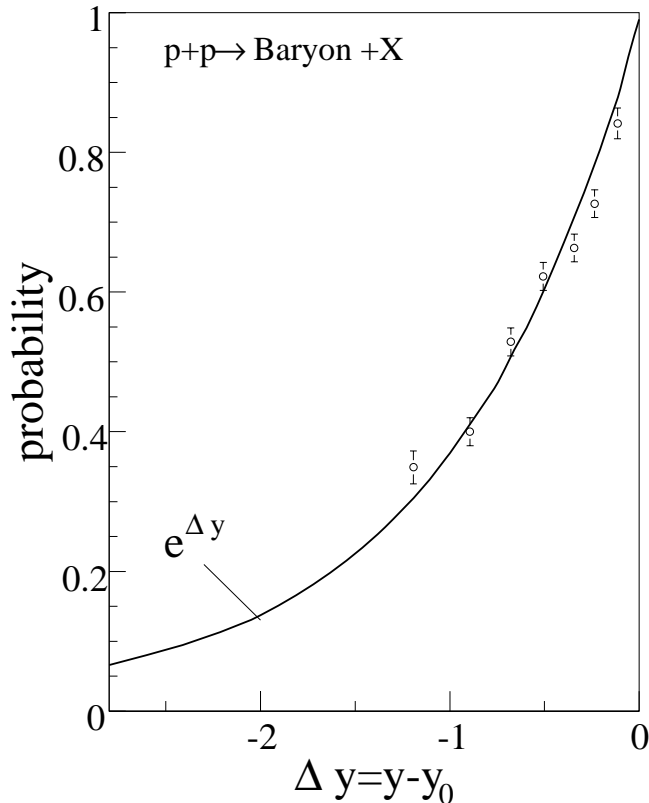


Figure 1.5: Probability distribution for protons to lose rapidity $-\Delta y$ in collisions with protons. The solid line $e^{\Delta y}$ corresponds to a uniform probability in x (x_F). This figure is taken from [5].

with different centralities at SPS energy $\sqrt{s_{NN}} = 17.2$ GeV using the NA49 detector. p+Pb collisions show an approximately exponential decrease of the net-proton yield with increasing x_F . The decrease is stronger for central p+Pb collisions. For $x_F < 0.1$ (corresponding about 2.3 units of rapidity away from the beam), the yield in central p+Pb collisions is larger than the yield in semi-central collisions; for $x_F > 0.1$ the semi-central collisions dominate. Plotted *vs* rapidity, the distribution of the leading proton from p+A fixed-target collisions has been characterized by a flat distribution for approximately 2 \sim 3 units of rapidity, without obvious energy dependence (figure 1.7 [8]).

In high energy central nucleus nucleus collisions, a large fraction of the longitudinal energy is converted into the energy of the matter which was produced in the vicinity of the center of mass of the colliding system [9]. The degree of stopping will reveal whether the energy density deposited in the vicinity of the center of mass is high enough to allow a phase transition, leading to the formation of QGP. From the measurements on the remaining baryon rapidity density from the beams, one can study the degree of stopping power.

The net-proton rapidity density can be obtained by subtracting the \bar{p} yields from proton yields, which can be extracted by fitting their spectra with certain functions at different rapidities. The method will be discussed later in detail in Chapter 4. In Chapter 7, results from d+Au and p+p collisions at $\sqrt{s_{NN}} = 200$ GeV will be

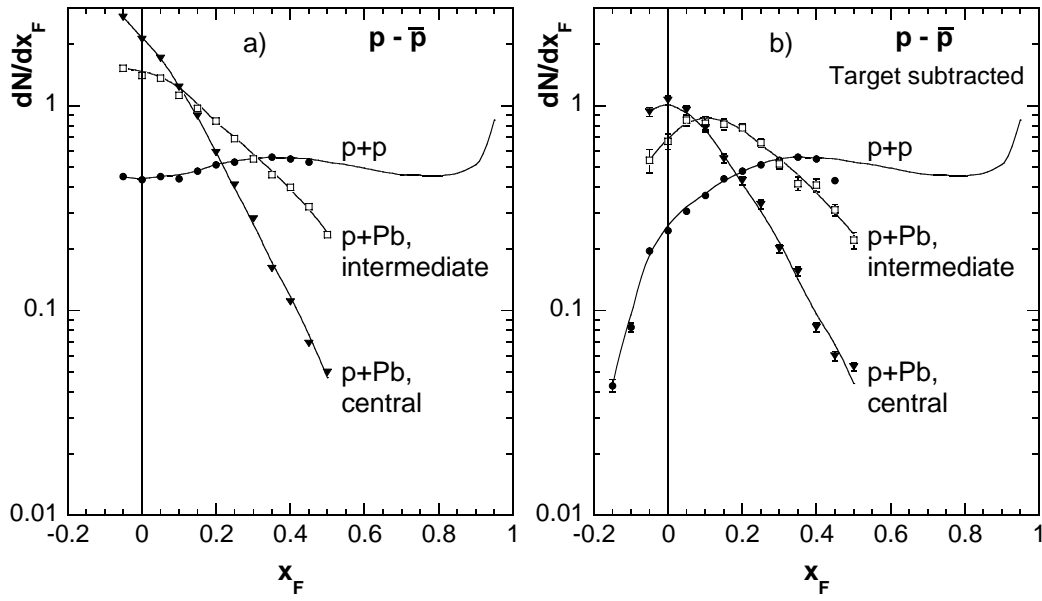


Figure 1.6: a) total net-proton density as function of x_F ; b) projectile component of net-proton density. This figure is taken from [7].

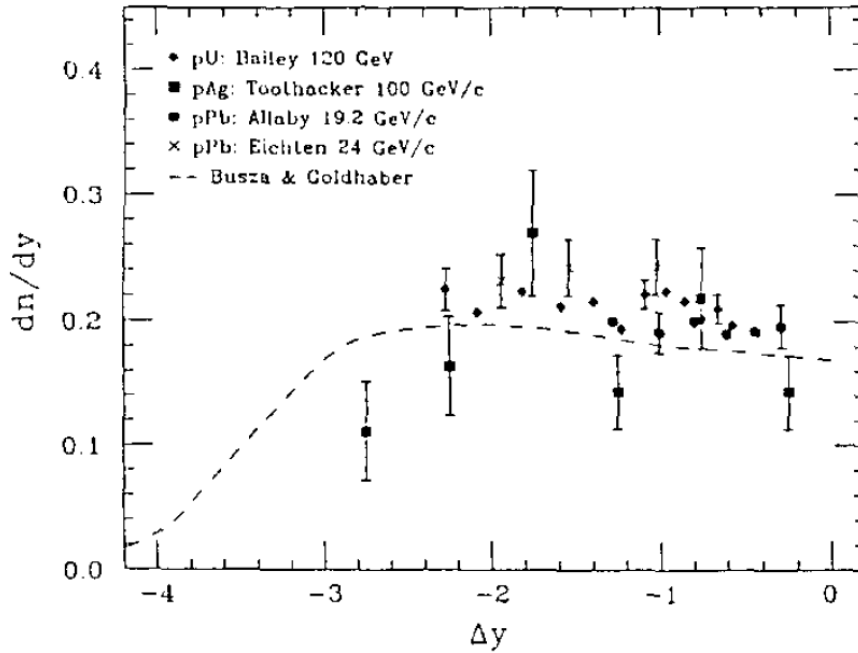


Figure 1.7: Rapidity distribution of protons from $p+A$ collisions as a function of rapidity loss, $\Delta y \equiv y - y_{\text{beam}}$. The dashed curve is from Busza and Goldhaber [5] for $p+Pb$ collisions. This figure is taken from [8]

presented.

Transverse momentum spectrum

The invariant differential cross section of produced particles, measured by counting the number of particles in a two dimensional y - p_T phase space bin then scaled by a factor of 2π and p_T , is defined as

$$E \frac{d^3\sigma}{d^3p} = \frac{1}{2\pi p_T} \frac{d^2N}{dp_T dy}. \quad (1.1)$$

It is the basic measurement which can be used to compare with theory calculations. From the spectra, we can construct the nuclear modification factor to study nuclear effects in nucleus nucleus collisions. The spectra of identified particles will be presented in Chapter 5.

Particle rapidity density and particle ratios

Based on the particle spectra and particle identification ability one can obtain the particle rapidity density dN/dy as a function of rapidity. Besides the rapidity density, particle ratios are thought to be a tool to study the chemistry of the system. In Chapter 5, the rapidity density and particle ratios are presented.

Nuclear modification factors

The nuclear modification factor for A+B collisions is defined as the following

$$R_{AB} = \frac{1}{\langle N_{\text{coll}} \rangle} \cdot \frac{d^2 N^{AB}/dp_T dy}{\times d^2 N^{\text{NN}}/dp_T dy}. \quad (1.2)$$

It is used to quantitatively study the nuclear medium effects, which modify the expected scaling e.g. the suppression of the high p_T hadron spectra in central Au+Au collisions at $\sqrt{s_{NN}} = 200$ GeV. In equation 1.2, $\langle N_{\text{coll}} \rangle$ is the average number of binary collisions in A+B collisions, and $N^{AB}(N^{\text{NN}})$ is the yield per event in A+B (N+N) collisions. If there are no initial or final state effects, $R_{AB} = 1$. The central to peripheral ratio, R_{CP} is used as an alternative to R_{AB} , for the centrality study of the nuclear modification factor. R_{CP} is defined as:

$$R_{CP} = \frac{\langle N_{\text{coll}}^{\text{peripheral}} \rangle}{\langle N_{\text{coll}}^{\text{central}} \rangle} \cdot \frac{d^2 N^{\text{central}}/dp_T dy}{dN^{\text{peripheral}}/dp_T dy}, \quad (1.3)$$

where $N^{\text{central}}(N^{\text{peripheral}})$ is the yield per event in the central (peripheral) collision, and $\langle N_{\text{coll}}^{\text{central}} \rangle (\langle N_{\text{coll}}^{\text{peripheral}} \rangle)$ is the average binary collisions in central (peripheral) collisions. If the yield of the process scales with the number of binary collisions, $R_{CP} = 1$. In Chapter 6, the centrality and rapidity dependence of R_{dAu} of identified hadrons will be presented.

1.2 Recent results from RHIC

A very high energy density has been reached in the laboratory at RHIC [10]. The hot and dense matter is produced by colliding heavy nuclei (gold) at ultra-relativistic energies. To investigate the nuclear matter under extreme condition of high temperature

and pressure and advance the understanding of the QCD vacuum, quark confinement, chiral symmetry breaking, and new unexpected phenomena in this outer limit of the QCD phase diagram, the produced particles, for instance, mesons and baryons are detected and identified in various experiments.

Results from RHIC are presented in the following for stopping, elliptic flow at partonic level, hadron suppression at high p_T , and the disappearance of back-to-back jets in the central Au+Au collisions.

1.2.1 Stopping

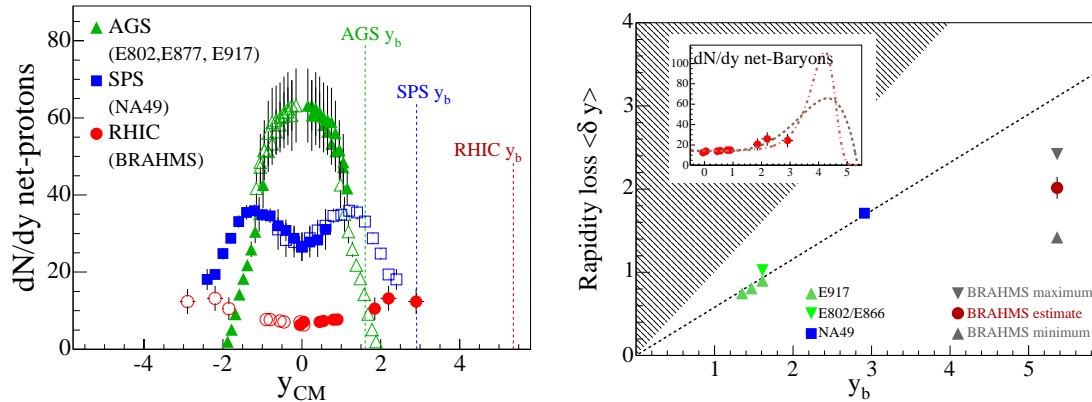


Figure 1.8: *Net-proton rapidity distribution and rapidity loss in central Au+Au collisions measured by the BRAHMS experiment at RHIC. Left panel, the comparison of the net-proton rapidity density at RHIC with that at AGS and SPS energies; right panel, the rapidity loss at different energies. [11]*

The left panel in figure 1.8 shows the recent results on rapidity density of net protons measured at AGS (5 A GeV), SPS (17 A GeV) and BRAHMS/RHIC (200 A GeV) for top 5% most central Au+Au (Pb+Pb) collisions [11]. The right panel shows the rapidity loss estimation by an extrapolation to the full net-baryon distribution as a function of projectile rapidity (in the CM system). The hatched area indicates the unphysical region, and the dashed line shows a phenomenological scaling $\langle \delta y \rangle \sim 0.58 y_p$.

As shown in figure 1.8, at RHIC a broad minimum has developed spanning several units of rapidity, indicating that at RHIC energies collisions are quite transparent. The rapidity loss at RHIC is clearly less than the phenomenological linear rapidity scaling would predict; about 73% of the initial energy is deposited in the collisions region [11].

1.2.2 Jet quenching

Particles with high momenta are informative for probing the conditions of the produced medium in relativistic energy nuclear collisions. They are thought to be associated with the jet production in the initial hard parton scattering, as illustrated by figure 1.9. After they are produced, they are expected to suffer energy loss when they traverse

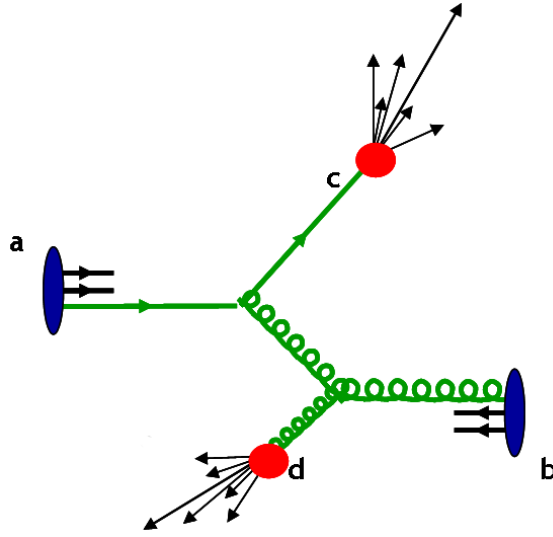


Figure 1.9: A schematic view of the inelastic scattering between two partons, a and b , and the production of two back to back-to-back jets.

a medium with high density of color charges because of the induced gluon radiation on their way. This would result in a depletion of high p_T particles. The energy loss effect for the high p_T particles in the medium is called jet quenching. As a fact, high p_T suppression in nuclear collisions at RHIC has been observed comparing to the particle production in $p+p$ collisions at the same energy, and also the disappearance of back-to-back di-jets has been seen in central Au+Au collisions.

Disappearance of the back-to-back jets

Figure 1.10 is the measurement done by the STAR experiment at RHIC [12]. The back-to-back dihadron correlation is absent in central Au+Au collisions, but in peripheral Au+Au collisions the correlation appears quite similar to that seen in $p+p$ and d+Au collisions. This suppression in Au+Au central collisions can be explained by the dense medium effect on the hard-scattered partons.

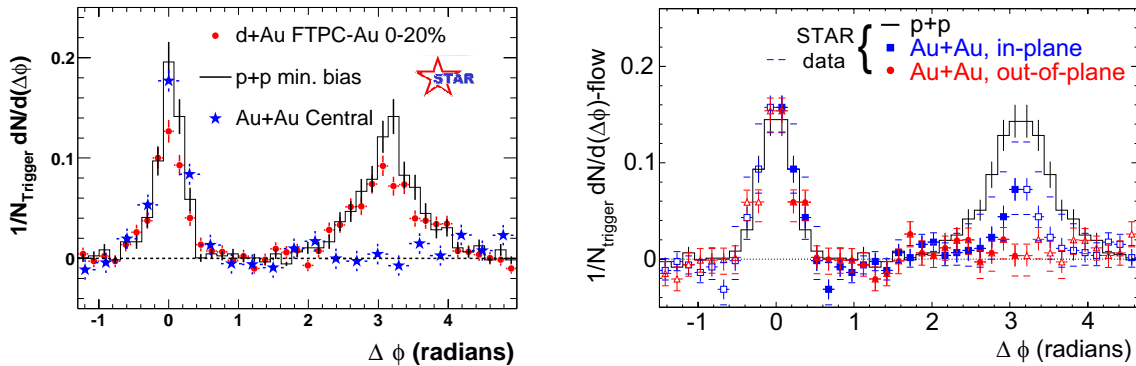


Figure 1.10: Disappearance of back-to-back jets in central Au+Au collisions at RHIC [12].

High p_T suppression

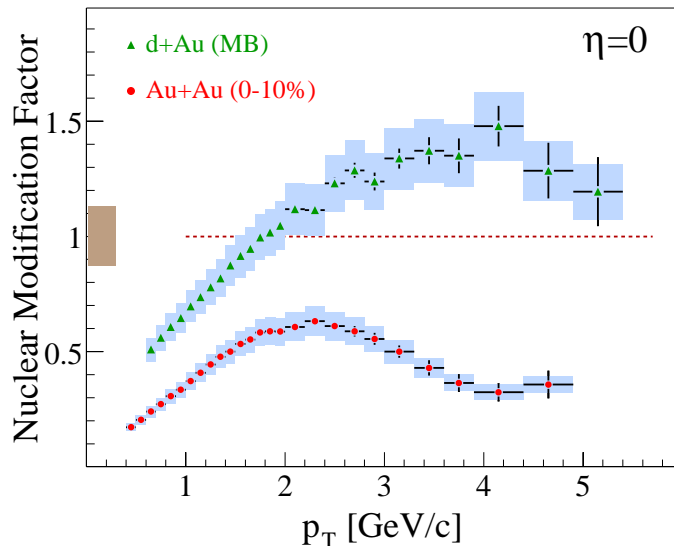


Figure 1.11: Nuclear modification factor measured by the BRAHMS experiment in minimum bias collisions of d+Au and central Au+Au collisions. [13].

BRAHMS has measured the nuclear modification factor for charged hadrons in minimum bias d+Au collisions and in central Au+Au collisions (0-10%), shown in figure 1.11. R_{dAu} shows no suppression at intermediate p_T , but an enhancement instead, while R_{AuAu} in the most central collisions exhibits a significant suppression at high p_T . The completely different result at high p_T in minimum bias d+Au collisions and the most central Au+Au collisions reveals the fact that the medium suppresses the jets before they finally fragment. Other experiments at RHIC have reported similar results [14, 15, 12].

1.2.3 Elliptic flow v_2 at partonic level

Elliptic flow v_2 is considered as an effect of the pressure in the interaction region, and is defined as the second Fourier expansion coefficient of the azimuthal momentum distribution distribution,

$$E \frac{d^3N}{d^3p} = \frac{1}{2\pi} \frac{d^2N}{p_T dp_T dy} \left\{ 1 + \sum_{n=1}^{\infty} 2v_n \cos [n(\phi - \Psi_r)] \right\}, \quad (1.4)$$

where ϕ is the azimuthal angle of the produced particle, and Ψ_r stands for the real reaction plane angle which is defined as the angle between the x -axis and the reaction plane. Therefore, v_2 can be evaluated by

$$v_2(p_T, y) = \left\langle \cos [2\phi(p_T, y)] \right\rangle \quad (1.5)$$

where $\langle \dots \rangle$ represents an averaging over many particles and events in the y - p_T space. Elliptic flow v_2 is sensitive to the equation of state of nuclear matter and also to the degree of thermalization reached in the system.

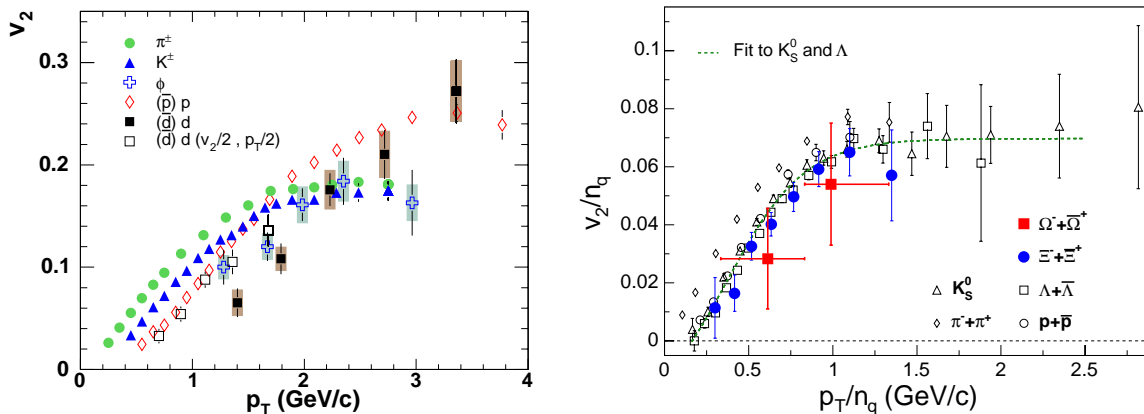


Figure 1.12: *Elliptic flow v_2 for mesons and hadrons at partonic level in Au+Au collisions at $\sqrt{s_{NN}} = 200$ GeV measured by PHENIX [16] (left) and STAR experiment [17] (right).*

Flow for heavier particles is particularly interesting because it is less sensitive to the final stage of the evolution, e.g. the freeze-out temperature. For example, ϕ -mesons are not created via kaon coalescence, and do not participate strongly in hadronic interactions. Figure 1.12 shows the elliptic flow v_2 for mesons and baryons in Au+Au collisions at $\sqrt{s_{NN}} = 200$ GeV measured by PHENIX [16] and STAR experiments [17]. These results show e.g. the heavier s quarks flow as strongly as the lighter u and d quarks, which demonstrate the partonic collectivity in central Au+Au collisions at RHIC.

1.3 Objective of the thesis

This thesis will focus on the p_T (m_T) spectra of π^\pm , K^\pm , and $p(\bar{p})$ in both p+p and d+Au collisions at $\sqrt{s_{NN}} = 200$ GeV over a wide rapidity range ($-0.2 < y < 3.6$). Various data sets, minimum bias p+p and d+Au collisions, and three different centrality classes (i.e. 0-30%, 30-60% and 60-80%) in d+Au collisions are analyzed for this purpose. Nuclear stopping will be discussed, as well as the nuclear modification factor for the smaller system, R_{dAu} (R_{CP}).

The following results will be presented:

- Identified particle p_T spectra, for different centrality ranges, and at different rapidities;
- Centrality, rapidity dependence of particle ratios: negative/positive, K/π , p/π ;
- Centrality, rapidity dependence of nuclear modification factors R_{dAu} (R_{CP});
- Centrality, rapidity dependence of charged hadron and net-proton rapidity density dN/dy .

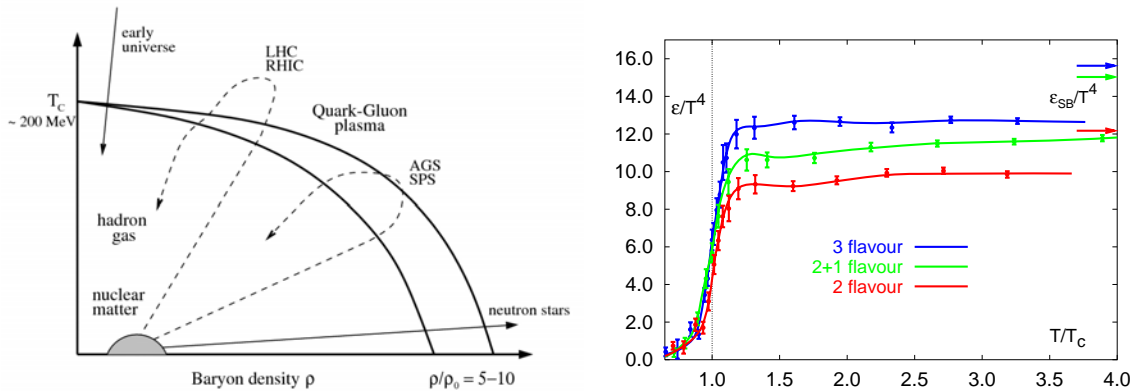
The aim of this thesis is twofolded:

- Systems like p+p and d+Au collisions are needed as a reference for Au+Au collisions to disentangle the modification of the parton distributions in nuclei (e.g. shadowing) and the change of p_T spectra of produced particles caused by initial and final state multiple scattering in cold nuclear matter (e.g. Cronin effect [18]).
- On the other hand, p+p data is needed to check the validity of pQCD calculations, at mid-rapidity and at forward rapidities to shed light on the (soft) baryon transfer processes during stopping and to test new small- x phenomena like gluon saturation at very forward rapidities in d+Au.

Chapter 2

Theoretical Concepts for Describing Nuclear Collisions

Apart from the phenomenological descriptions in Chapter 1, various models have been developed to study nuclear collisions at high energies. The **Q**uark **G**luon **P**lasma (QGP) created in relativistic heavy ion collisions with high enough temperature and energy density, is an unavoidable consequence of the fundamental strong interactions, and is quantitatively calculable by the SU(3) theory, **Q**uantum **C**hromo-**D**ynamics (QCD) [19]. QCD is a theory of strong interaction (strong force) and a representation of the interactions between partons (quarks and gluons), mediated by color charged gluons. There are 6 flavors of quarks in 3 generations, (**u**, **c**, **t**) with positive charge $+\frac{2}{3}$ and their corresponding counterparts (**d**, **s**, **b**) with negative charge $-\frac{1}{3}$ in the unit of the electron charge. They carry the colors, *red*, *green* and *blue*, which are thought to be the source of the strong force [20]. Interactions between partons of specific flavors are propagated via a number of possible color exchanges.



(a) Critical temperature vs baryon density [9]. (b) Lattice QCD prediction, a rapid increase in energy density around a certain temperature T_c [21]

Figure 2.1: Phase diagram (a) and LQCD prediction (b).

In reality, not a single free quark has been seen. Quarks are assumed to be confined inside hadrons. In relativistic heavy ion collisions quarks may be deconfined from nucleons when the energy density in the system is high enough. A new form of matter

which consists of deconfined quarks and gluons, the so-called QGP, was first proposed by Shuryak [22]. Figure 2.1 (a) shows a phase diagram of nuclear matter i.e. the critical temperature as a function of baryon density. The phase change from a hadronic phase to a partonic one is predicted by Lattice QCD (LQCD) [21]. Figure 2.1 (b) shows that the energy density strongly increases at the vicinity of the transition temperature T_c . The drastic change in the behaviour of the energy density which indicates that the QCD (phase) transition to the plasma phase indeed is deconfining [21].

The details about the SU(3) gauge theory of QCD and the calculation of LQCD are beyond the range of this thesis, but a brief introduction to the *perturbative QCD* (pQCD) will be given. A number of other models, such as a recent gluon saturation model of the *Color Glass Condensate* (CGC) [4] which is more concerned about the gluon saturation effect at the initial stage of the nuclear collisions, and the LUND string model of *PYTHIA* [23] which is based on a string breaking mechanism for particle production will also be briefly introduced.

2.1 Perturbative QCD (pQCD)

Without medium effects, nuclear collisions might be described as the superposition of many binary nucleon nucleon collisions. The standard pQCD calculation of hard scattering process in the basic nucleon nucleon collisions is based on the following factorization [24]

$$\frac{d\sigma_{pp}^h}{dydp_T^2} = K \sum_{a,b,c,d} \int dx_a dx_b f_a(x_a, Q^2) f_b(x_b, Q^2) \frac{d\sigma}{d\hat{t}}(ab \rightarrow cd) \frac{D_{h/c}^0}{\pi z_c}, \quad (2.1)$$

in which $f_a(x_a, Q^2)$ and $f_b(x_b, Q^2)$ are the parton distribution functions (PDF) for parton a and b , x_a and x_b are the initial momentum fraction carried by the parton a and b , $\frac{d\sigma}{d\hat{t}}(ab \rightarrow cd)$ is the differential cross section for $ab \rightarrow cd$ scattering, and $\frac{D_{h/c}^0}{\pi z_c}$ is the fragmentation function for the parton of flavor c . The factor K in the formula is phenomenologically introduced to describe the difference between the leading and higher order cross sections, which has no precise definition [25]. The differential cross section $\frac{d\sigma}{d\hat{t}}(ab \rightarrow cd)$ can be calculated by pQCD at leading order (LO) or the next-to-leading order (NLO) of the coupling constant α_s .

The comparison between NLO pQCD calculations with the measurement of π^0 by the PHENIX experiment in p+p collisions at $\sqrt{s} = 200$ GeV [28] and the BRAHMS experiment at 62.4 GeV [27] are shown in figure 2.2 and figure 2.3 respectively. The invariant differential cross section for inclusive π^0 production (points) and the results from NLO pQCD calculations using different fragmentation functions are shown in figure 2.2. A good agreement between experiment and the “**K**niehl-**K**ramer-**P**ötter” (KKP) pQCD calculation is observed. Figure 2.3 shows the differential cross sections for π^- at rapidity $y = 2.7$ and $y = 3.3$ at $\sqrt{s_{NN}} = 62.4$ GeV, compared to the NLO pQCD calculation using the KPP fragmentation function evaluated at $\mu = p_T$ scale [27]. As concluded in [27], the NLO pQCD gives a satisfactory description of the charged pion data at high rapidity though at rapidity $y = 3.3$ there is a tendency for the pQCD calculation to underestimate the π^- cross section at higher p_T .

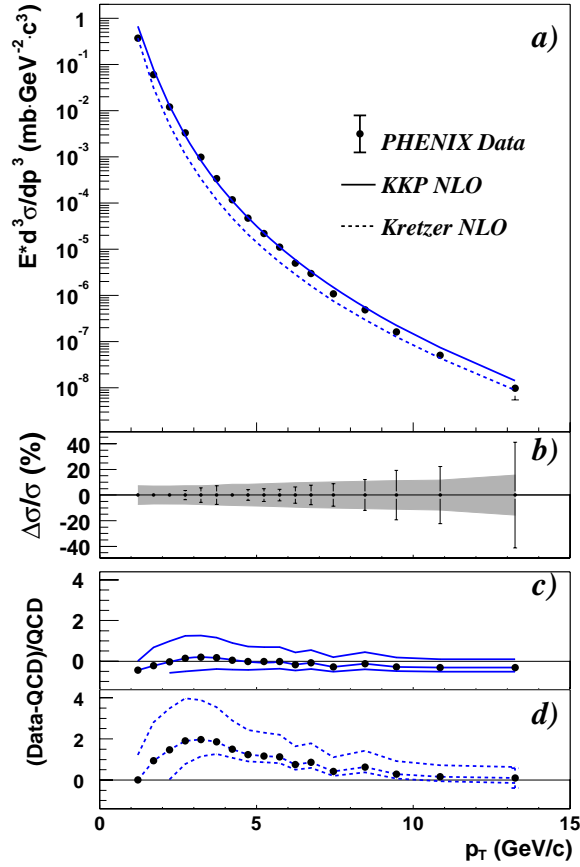


Figure 2.2: Comparison of PHENIX measurement of invariant differential cross section for inclusive π^0 production at mid-rapidity to NLO pQCD calculations for $p+p$ collisions at $\sqrt{s} = 200$ GeV. Panel a) shows the PHENIX data (points) and the results from NLO pQCD calculation with equal renormalization and factorization scales of p_T using the KKP (solid line) and “Kretzer” (dashed line) sets of fragmentation functions. b) The relative statistical (points) and point-to-point systematic (band) errors. c,d) The relative difference between the data and the theory using KKP (c) and Kretzer (d) fragmentation functions with scales of $p_T/2$ (lower curve), p_T , and $2p_T$ (upper curve). This figure is taken from [26].

The nuclear structure functions in nuclei are different from the superposition of the constituent nucleons [29, 30]. The ratio $R_{F_2}^A(x, Q^2)$ is defined as the nuclear structure function per nucleon divided by the nucleon structure function

$$R_{F_2}^A(x, Q^2) = \frac{F_2^A(x, Q^2)}{A F_2^{\text{nucleon}}(x, Q^2)}, \quad (2.2)$$

where F_2^A is the nuclear structure function, and F_2^p the nucleon structure function. The nuclear effects observed in this ratio are usually discussed according to different regions of Bjorken- x variables. The ratio $R_{F_2}^A < 1$ corresponds to small x region $x \leq 0.1$ with shadowing effect; anti-shadowing, $R_{F_2}^A > 1$, at $0.1 \leq x \leq 0.3$; EMC effect, $R_{F_2}^A < 1$ at $0.3 \leq x \leq 0.7$; Fermi motion, $R_{F_2}^A > 1$ at $x \rightarrow 1$ and beyond.

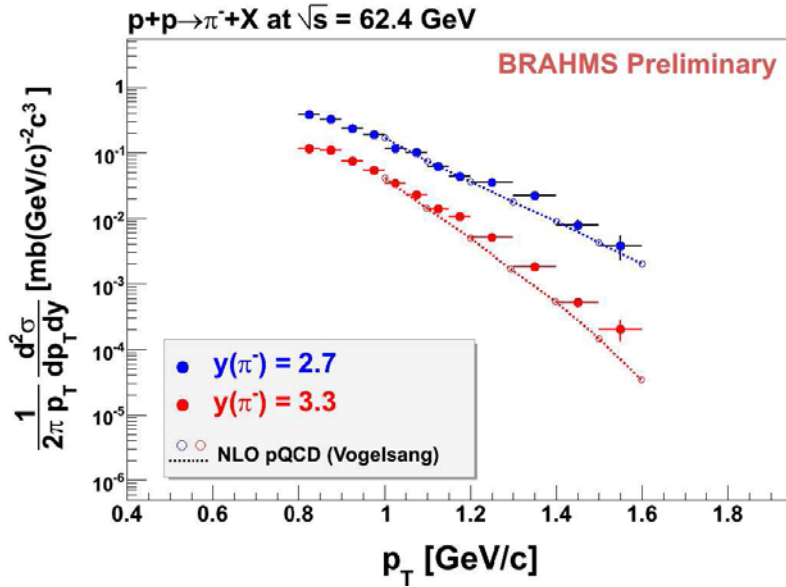


Figure 2.3: Comparison of invariant cross sections for π^- at $y = 2.7$ and $y = 3.3$ to NLO pQCD calculations with factorization and renormalization scales set equal to p_T [27].

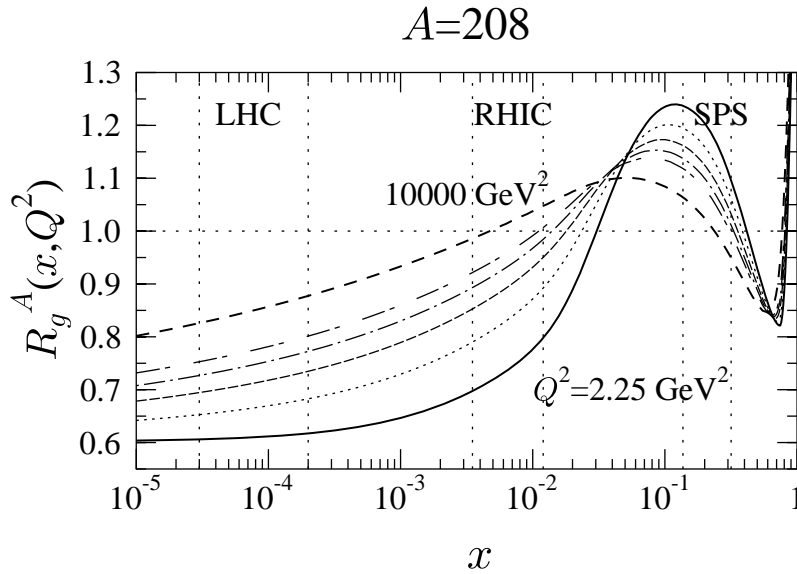
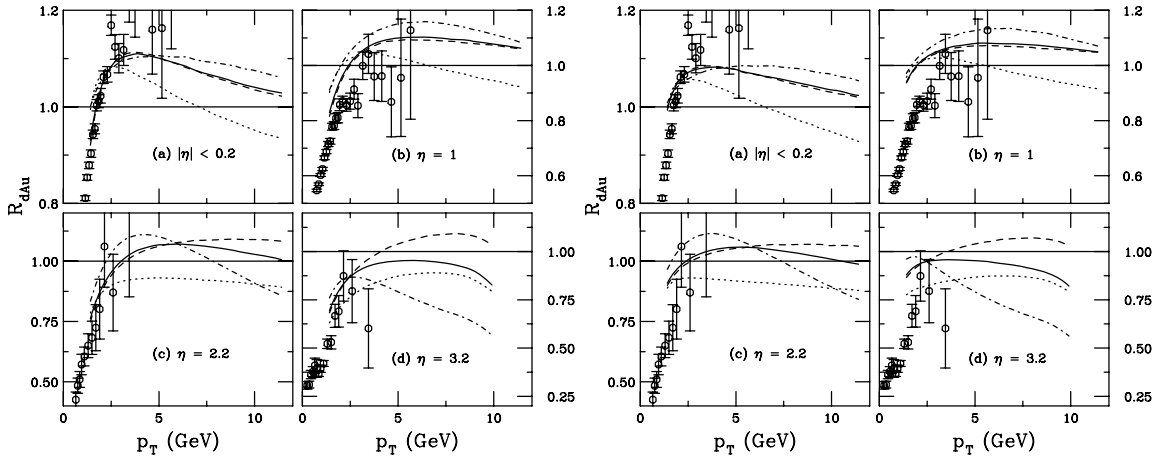


Figure 2.4: Scale evolution of the $R_g^A(x, Q^2)$ as a function of x for nucleus Pb ($A=208$) at a fixed Q^2 . This figure is taken from [31].

Similarly, the ratio $R_i^A(x, Q^2)$ for parton i is defined as

$$R_i^A(x, Q^2) = \frac{f_i^A(x, Q^2)}{f_i^P(x, Q^2)}, \quad (2.3)$$

where f_i^P and f_i^A are the distributions of parton i in a free proton and a nucleus with



(a) *pQCD* calculation for homogeneous shadowing with the FGS1 parametrization

(b) *pQCD* calculation for homogeneous shadowing with the EKS98 parametrization

Figure 2.5: R_{dAu} by *pQCD* (LO) calculation [32] comparing to the minimum bias BRAHMS data (data points) [33] at various pseudo-rapidities. The dashed curves are for the charged pions, the dot-dashed ones are for the kaons and the dotted ones are for the protons and anti-protons. The sum over all charged hadrons shown as the solid curves.

mass number A respectively. Figure 2.4 shows the gluon modification $R_g^A(x, Q^2)$ for heavy nucleus (Pb) obtained from a DGLAP analysis. The ratio R_g^A turns below 1 at small x , indicating shadowing effects.

In d+Au collision this additional shadowing effects have to be considered. By replacing one projectile by a heavy nucleus, its PDF has to be modified by taking into account the depletion of small- x partons in the nucleus (nuclear shadowing). Secondly, multiple scattering of a projectile parton on partons in the nucleus before a hard collision gives the scattering parton an additional p_T -kick which leads to the Cronin effect. Both effects are initial state effects and can be taken into account by adding appropriate factors to equation 2.1. Final state effects like the scattering of produced particles in cold nuclear matter might also contribute e.g. to the nuclear modification factor.

pQCD (LO) calculations for d+Au collisions are shown in figure 2.5 and figure 2.6 [32]. Figure 2.5 shows the *pQCD* calculations using two different parameterizations, FGS1 and EKS98 parameterizations of nuclear shadowing, compared to the nuclear modification factor R_{dAu} at different pseudo-rapidities measured by BRAHMS experiment at RHIC [33]. Figure 2.6 shows the *pQCD* calculation for R_{CP} using the FGS1 parameterization, compared to the BRAHMS results. The results for minimum bias d+Au collisions at $\sqrt{s_{NN}} = 200$ GeV in the aforementioned figures agree reasonably well with the BRAHMS data, while the calculated centrality dependence underestimates the data [32]. Other efforts made recently by Armesto, based on *pQCD* calculation and including multiple scattering approaches [34] suggest a large amount of shadowing and tend to indicate that shadowing for gluons is stronger than that for quarks, but DGLAP evolution disfavors such situation in view of the existing data on Q^2 -evolution of nuclear modification factors.

On the other hand, at lower energies, $\sqrt{s_{NN}} = 19.4, 23.8, 27.4$ GeV, Cronin

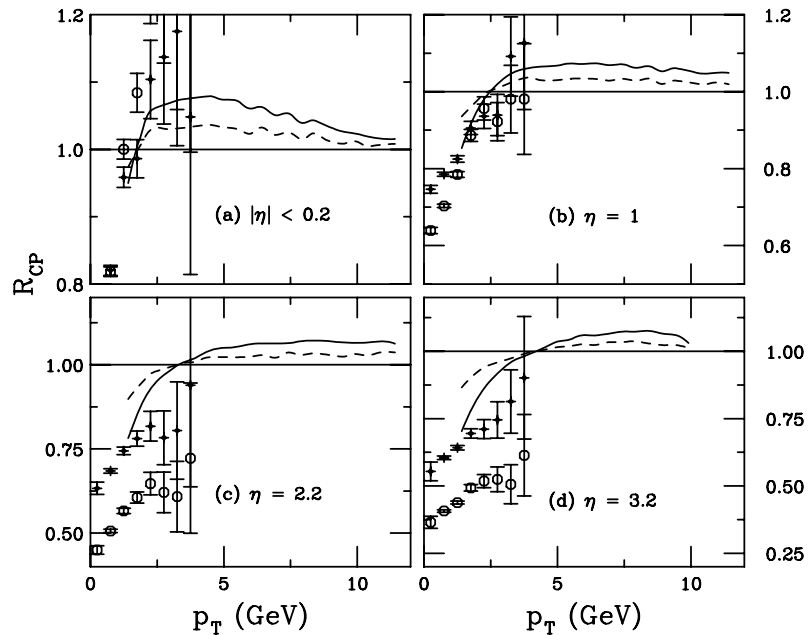


Figure 2.6: R_{CP} by pQCD (LO) calculation for homogeneous shadowing with the FGS1 parametrization [32] comparing to the minimum bias BRAHMS data (data points) [33] at various pseudo-rapidities. The calculated ratios of the most central to peripheral and semi-central to peripheral collisions are shown in the solid and dashed curves, respectively. The BRAHMS data are given by the open circles (most central) and diamonds (semi-central).

et al have measured the effect of the propagation and scattering of projectile particles through the color field of a nucleus [35]. The enhancement of particle production in p+A collisions leading to $R_{pA} > 1$ was observed in [18] and is usually referred to as Cronin effect. Cronin effect is interpreted as the result of multiple scattering of partons inside the nucleus though it is not enough to explain the species dependence of this effect, namely the enhancement of baryons in p+A collisions being significantly larger than that of mesons. Phenomenologically, various models have been established in the last decade, which are to be discussed in the next sections.

2.2 Color Glass Condensate (CGC)

CGC is an effective gluon saturation theory of QCD at high energy, providing initial condition for the high energy nuclear collisions. The study of gluon saturation was initiated from the small x problem in deep inelastic scattering (DIS) experiment at HERA, as shown in Figure 2.7. The gluon density $xG(x, Q^2)$ is rising rapidly as a function of decreasing x . At high energy (or small x), gluons are the most abundant partons in nucleons, see figure 2.8 [4].

Using pQCD one can calculate the evolution of the PDFs, but not the PDFs themselves. Various calculations were made for the purpose. The evolution of gluon distribution function has been formulized by Dokshitzer-Gribov-Lipatov-Altarelli-Parisi

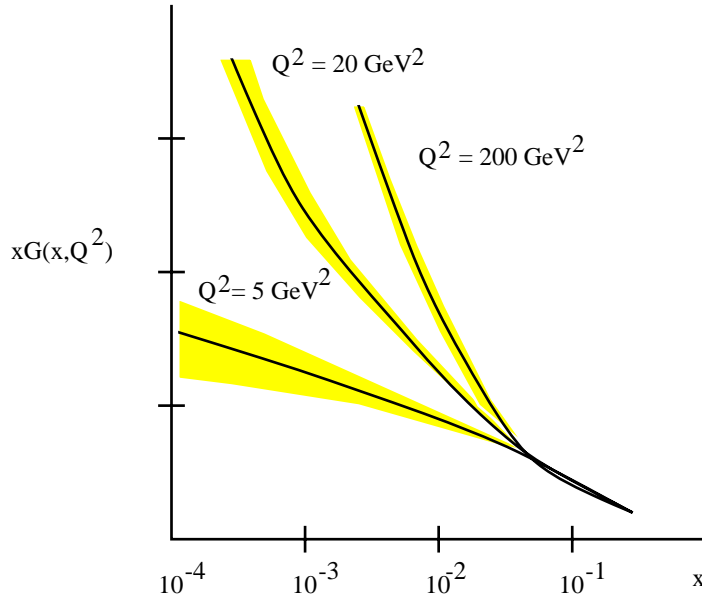


Figure 2.7: The HERA data for the gluon distribution function as a function of x for various values of Q^2 [4].

(DGLAP) evolution equation [36, 37, 38], which is known as the renormalization group equation for the parton number operator. According to the DGLAP formalism, the gluon distribution function $xG(x, Q^2)$ grows fast with both x and Q^2 for a fixed coupling constant α_s ,

$$xG(x, Q^2) \sim e^{\sqrt{\alpha_s \log(1/x \log Q^2)}}. \quad (2.4)$$

While when Q^2 is limited, the approximation made by Balitsky-Fadin-Kuraev-Lipatov (BFKL) [39, 40] approach yields

$$xG(x, Q^2) \sim e^{\lambda \log 1/x}, \quad (2.5)$$

with $\lambda \equiv 4 \log 2 \cdot N_c \alpha_s / \pi$ for a fixed coupling constant. This means that pQCD radiation leads to a fast growth of the gluon distribution function with increasing energy or decreasing x , which makes a hadron a dense system of gluons at high energy.

According to the BFKL and DGLAP approaches, which only include radiation of gluons, the gluon density increases linearly with energy, i.e. a fast growth of gluon distribution with increasing energy or decreasing x . But this growth can not go on forever since this would lead to the violation of unitarity for physical cross section. As being pointed out firstly by Gribov, Levin and Ryskin [41] and later by Muller and Qiu [42] (GLR-MQ), some recombination processes of gluons with smaller x into gluons with larger x may slow down the growth of the gluon distribution function.

2.2.1 Properties of a CGC

CGC is an effective theory of QCD at high energy (small x) which extends the applicability of pQCD to a dense system of gluons [4, 43, 44, 45, 46, 47, 48]. In this system,

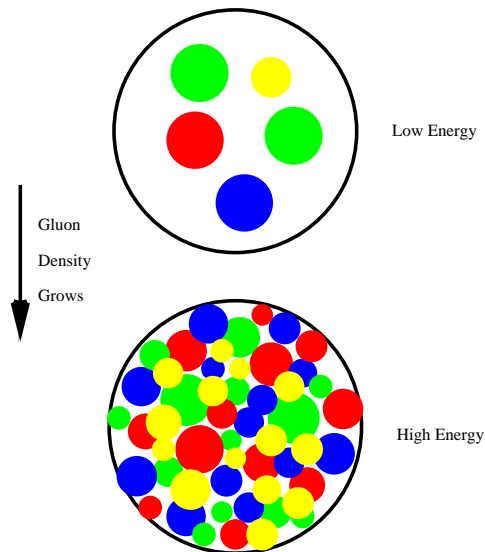


Figure 2.8: *A physical picture of the low x gluon density inside a hadron as a function of energy [4].*

the density of gluons is high but limited, and small x gluons are closely packed together. Strong interactions between partons become weak, i.e. $\alpha_s \ll 1$. This weakly coupled system is called a CGC [46, 47, 48] because of the reasons below:

Color: the gluons carry color charge.

Glass: gluons at smaller x are generated from gluons at larger x , whose time scales are Lorentz time dilated for their large velocity in the infinite momentum frame, which corresponds to a slow evolution.

Condensate: gluons are very dense in hadrons, the high density limit of which is expected to be a Bose condensate because gluons are massless.

2.2.2 Applications of CGC to RHIC

The CGC model [4, 43, 44, 45, 46, 47, 48] has provided a valuable tool to study the interaction of hadrons and nuclei at relativistic energies. The idea that the rapid growth of the gluon distribution at high energy is tamed by gluon recombination leads to a saturated gluon density described by a saturation scale Q_s . Due to the high occupation numbers of the gluons, the system can be treated approximately by a classical field. In high energy nuclear collisions the gluon density in each nucleus is enhanced by a factor $\sim A^{1/3}$ due to the Lorentz contraction of the longitudinal size of the nucleus and it has been argued that the CGC can provide the initial conditions for the formation of the QGP [49].

CGC predicts a strong suppression of pion production at large rapidities, where small- x value of about 10^{-3} can be reached. A comparison between the CGC calculation to the hadron multiplicity production at RHIC was made. One can see good agreements with data in figure 2.9. Another success of the model is the agreement with nuclear modification factors for hadrons in d+Au collision from the BRAHMS experiment. Figure 2.10 shows the comparison to R_{dAu} from BRAHMS experiment [33],

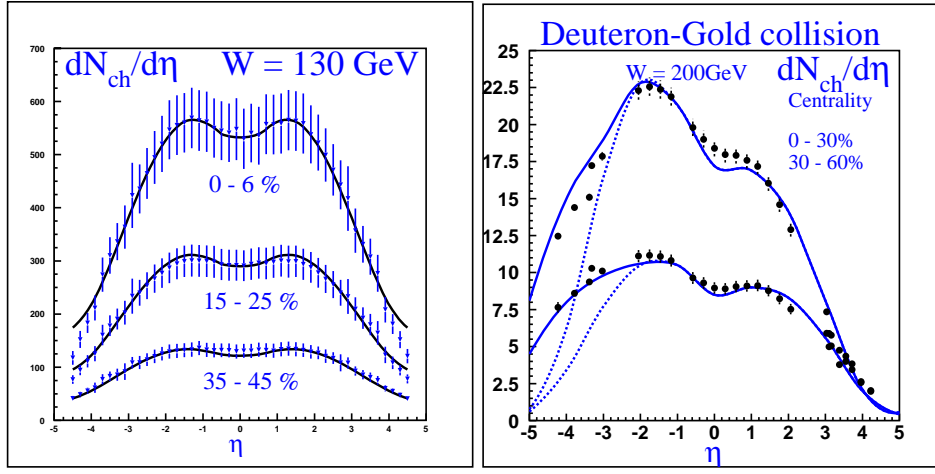


Figure 2.9: Comparison of a CGC prediction to hadron multiplicity measurements in Au+Au (left) and d+Au (right) collisions at RHIC [44].

and figure 2.11 shows the comparison to R_{CP} .

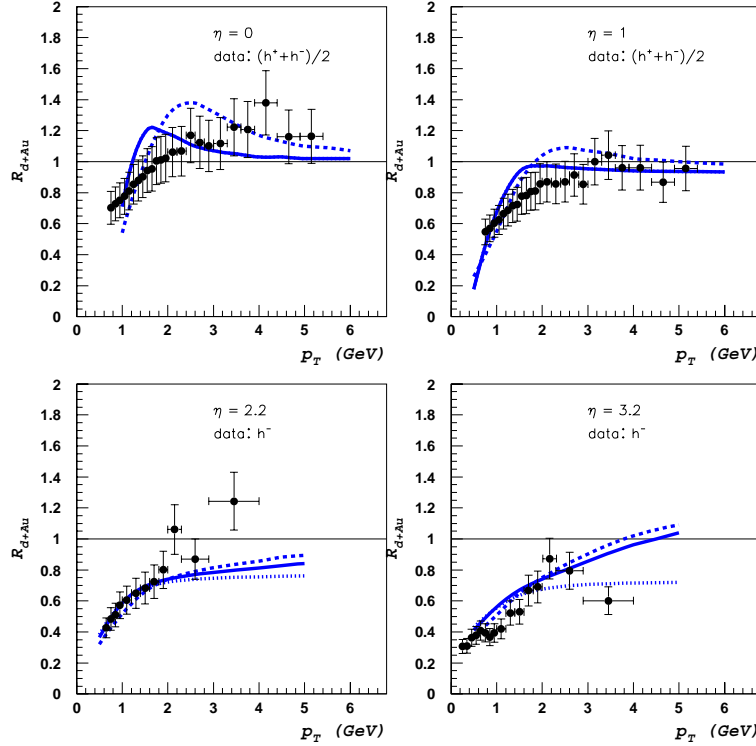


Figure 2.10: Nuclear modification factor R_{dAu} of charged hadrons at different rapidities. CGC calculation (curves) [45] and BRAHMS experimental data (points) [33].

The top two plots in figure 2.10 correspond to $\eta = 0$ and 1, in which the solid line represents the $(h^- + h^+)/2$ contribution calculated with $\kappa = 0$ in the isospin-

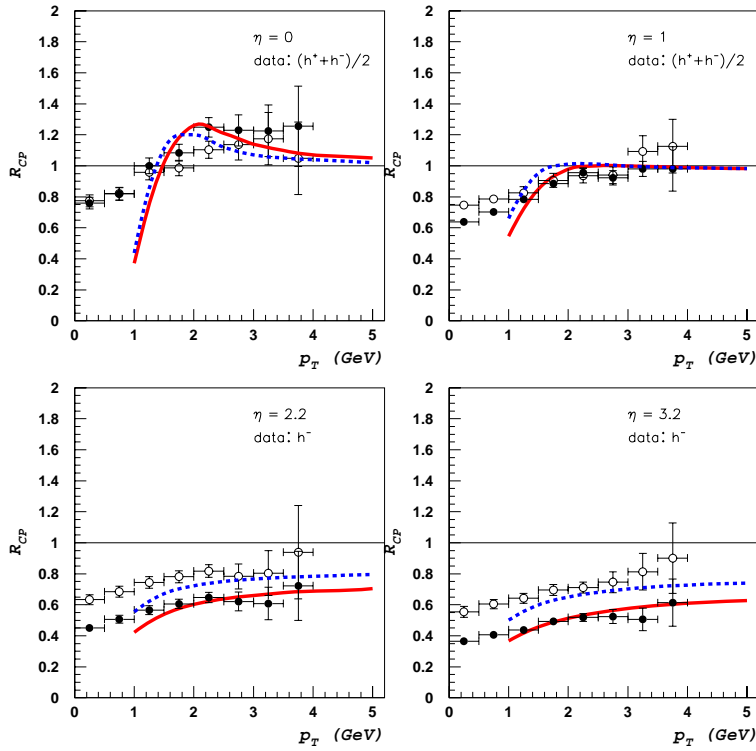


Figure 2.11: CGC calculation of nuclear modification factor R_{CP} of charged particles $(h^+ + h^-)/2$ at mid-rapidity and R_{CP} of negatively charged particles h^- at forward rapidity (curves) [45], compared to BRAHMS experimental data (symbols) [33]. The solid symbols and lines stand for the R_{CP} from central-to-pheripheral ratios, and open symbols and dashed lines are for R_{CP} from semi-central-to-pheripheral ratios.

independent approximation¹, the dashed lines give the same $(h^- + h^+)/2$ contribution but with $\kappa = 1$ GeV. The bottom two plots correspond to $\eta = 2.2, 3.2$, in which the solid lines give the h^- contribution calculated in the constituent quark model with $\kappa = 0$, the dashed line gives the same h^- contribution for $\kappa = 1$ GeV, while the dotted lines at $\eta = 2.2$ and 3.2 give the $(h^+ + h^-)/2$ contribution with $\kappa = 0$.

The top two plots in figure 2.11 correspond to pseudo-rapidity $\eta = 0$ and 1 , and the bottom two correspond to $\eta = 2.2$ and 3.2 . The solid curves and solid symbols stands for R_{CP} from central-to-pheripheral ratios (0-20%/60-80%), and the dashed curves and open symbols gives that from semi-central-to-pheripheral ratios (30-50%/60-80%). Good agreement with the data is seen.

2.3 pQCD vs CGC

The unitarity can be naturally preserved by implementing the Glauber-Eikonal (GE) [53, 54, 55] approach [52], in which sequential multiple partonic collisions are computed in the framework of pQCD. As a result, the low p_T spectra in p+A collisions are

¹ κ is the typical non-perturbative scale [45]

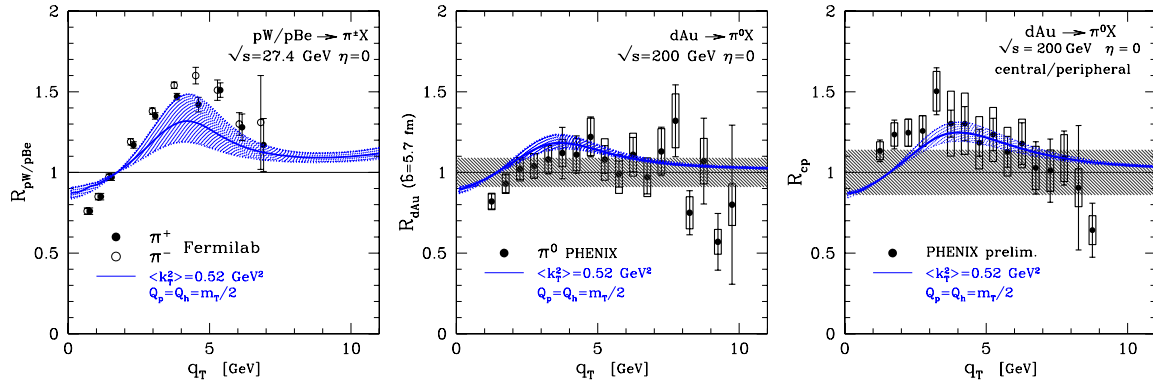


Figure 2.12: Cronin effect on pion production at Fermilab [18, 35, 50] and RHIC [51] at $\eta = 0$. The solid curve is the GE computation. Theoretical errors due to the fit of p_0 are shown as a shaded band around the solid curve. The rightmost panel shows the 0-20%/60-88% centrality classes ratio. The figure is taken from [52]

suppressed by unitarity, but enhanced at moderate p_T by the accumulation of transverse momentum. And on the other hand, high p_T spectra in p+p collisions are to be recovered, which suggests that no high p_T shadowing would occur in this approach. Figure 2.12 shows the Cronin effect on pion production at Fermilab (left panel) and PHENIX experiment (middle panel for R_{dAu} and right one for R_{CP}), compared to the GE computation (solid curves). pQCD explains the nuclear effects without the violation of unitarity.

2.4 Other theoretical models

Three main type of theoretical models have been developed in the past decades. They are hydrodynamical models, statistical models and microscopic models.

Hydrodynamical models treat nuclear matter under extreme conditions as an expanding relativistic fluid. Statistical models assume that thermal dynamical laws govern the hadron gas. Some results from several microscopic models will be presented, such as the **Heavy Ion Jet Interaction Generator** (HIJING) and **A Multi-Phase Transport** model (AMPT).

2.4.1 HIJING

HIJING [56], proposed by Gyulassy and Wang, is a QCD inspired model for multiple jets production. It is a Monte Carlo program designed to study jet and the associated particle production in high energy p+p, p+A and A+A collisions. The physics behind the program includes multiple mini-jet production, soft excitation, nuclear shadowing of parton distribution functions and jet interactions in dense matter. In this model, multiple mini-jet production is combined together with a Lund type string model for soft interactions ($p_T < 2$ GeV/c). The number of binary collisions at a given impact parameter can be determined from a Glauber calculation [57, 9]. Dashed curves in figure 2.13 shows HIJING estimation to the pseudo-rapidity distributions of charged

particles in d+Au collisions at $\sqrt{s_{NN}} = 200$ GeV with centralities determined from N_{part} (solid curves are from AMPT model calculation).

2.4.2 AMPT

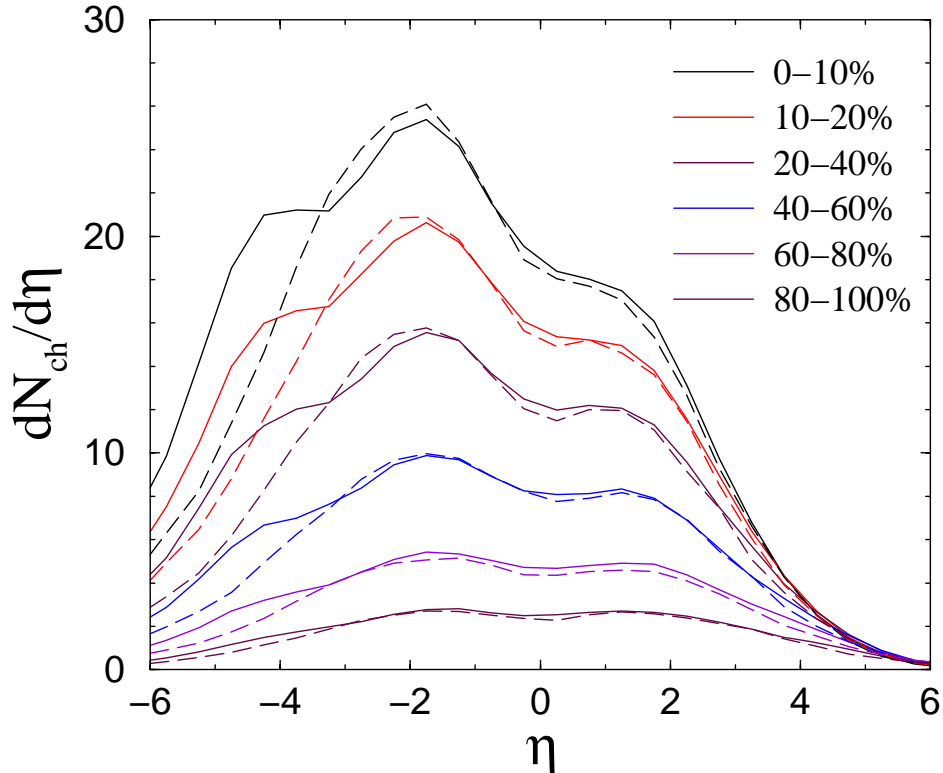


Figure 2.13: *Pseudo-rapidity distributions of charged particles in d+Au collisions at $\sqrt{s_{NN}} = 200$ GeV with centralities determined from N_{part} . Solid and dashed curves represent results from the AMPT model and the HIJING model (without quenching), respectively [58].*

AMPT, developed by Ko *et al*, includes both final state partonic and hadronic interactions [59, 60, 61]. It consist of four components: the initial conditions, the parton cascade, the conversion from partonic to hadronic matter and the hadron cascade. The AMPT model uses the number of initial mini-jet partons from HIJING calculation as input, and Zhang's parton cascade model (ZPC) [62] to describe interactions among mini-jet partons. After the partons stop interacting, they are recombined with their parents strings, which are produced from initial soft nucleon nucleon interactions, and fragment into hadrons according to the Lund string fragmentation model [63, 23]. The dynamics of resulting hadronic matter is described by a hadronic cascade based on the relativistic transport model [64]. Final hadronic observables including contributions from the strong decay of resonances are determined when the hadronic matter freezes out.

This model has been very useful for understanding various observables in Au+Au collisions at RHIC, such as the rapidity distribution and transverse momentum dis-

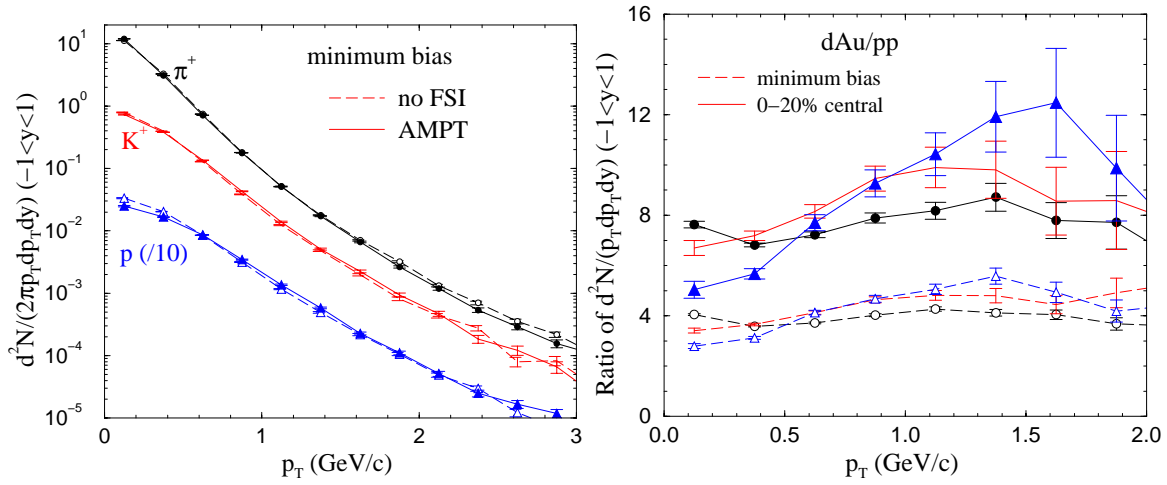


Figure 2.14: *Left: transverse momentum spectra of π^+ , K^+ and protons from AMPT with (solid) or without (dashed) final-state interactions for minimum-bias d+Au collisions. The proton spectra are scaled down by a factor of 10. Right: ratios of the transverse momentum spectra from AMPT for d+Au collisions over those for p+p collisions. Solid and dashed curves correspond to 0-20% central and minimum bias d+Au collisions, respectively [58].*

tribution of various particles. It allows one to study both thermal and chemical equilibration in the partonic and hadronic matter formed in these collisions. The AMPT model has also been extended to include the string melting mechanism, in which soft strings produced from initial nucleon-nucleon interactions are converted directly into partons.

Using AMPT model, pseudo-rapidity distribution and particle productions in d+Au collisions are studied [58]. As claimed in the review, final state partonic and hadronic interactions affect the p_T spectra of protons more than those of kaon and pions. Relative to p+p collisions, at the same center-of-mass energy per nucleon pair, the effect of final state interactions on the charged particle transverse momentum spectra in d+Au collisions is much smaller than data from RHIC, indicating that initial-state effects such as the Cronin effect are important. Pseudo-rapidity density distributions with different centralities from AMPT calculation in d+Au collisions are shown in figure 2.13 (comparing to results from HIJING). Figure 2.14 shows AMPT calculations of the spectra for positive hadrons (left panel), with and without final state interactions, and ratios (right panel) of the transverse momentum spectra from AMPT for minimum-bias (dashed curves) and central (solid curves) d+Au collisions over those for p+p collisions [58].

2.4.3 Parton recombination model

The parton recombination model is a final-state effect model. Recombination mechanism assumes a fast hadron can be created by the recombination of a hard parton with a slow anti-quark, which may come from the sea quarks in a hadron, or be generated from the excitation of a gluon. In the quark deconfined QGP (if it is formed), coales-

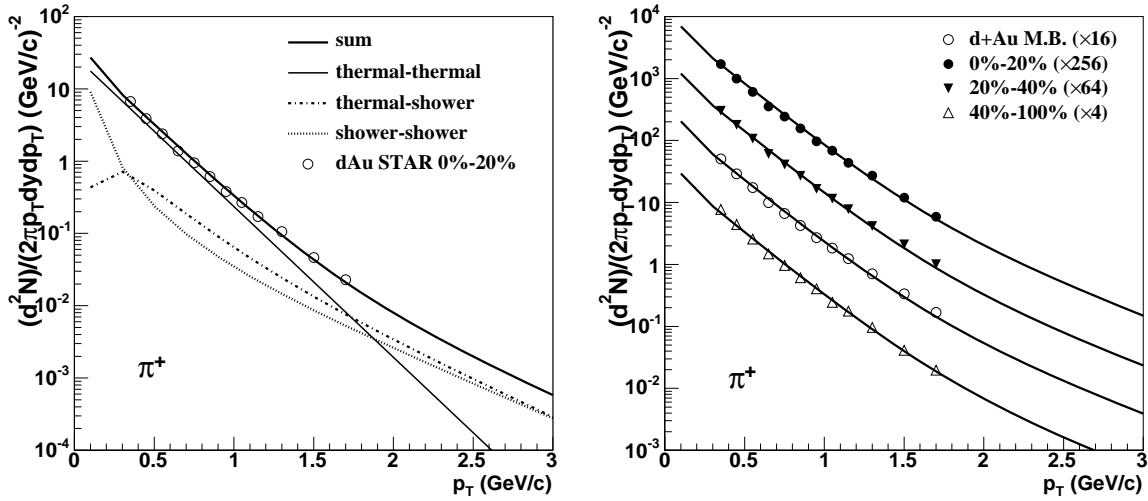


Figure 2.15: (left) The invariant yield for π^+ in 0%-20% d+Au collisions as a function of p_T . The open circles are data points. (right) The invariant yields for π^+ in minimum bias and centrality selected d+Au collisions as a function of p_T . The symbols represent STAR data points. The curves on the top of the symbols are the corresponding calculation results from recombination model. The figure is taken from [67].

cence of the abundant thermal partons in the QGP might provide another important hadron production mechanism. At RHIC energies, the parton recombination model assumes that coalescence proceeds via constituent quarks in hadrons [65, 66].

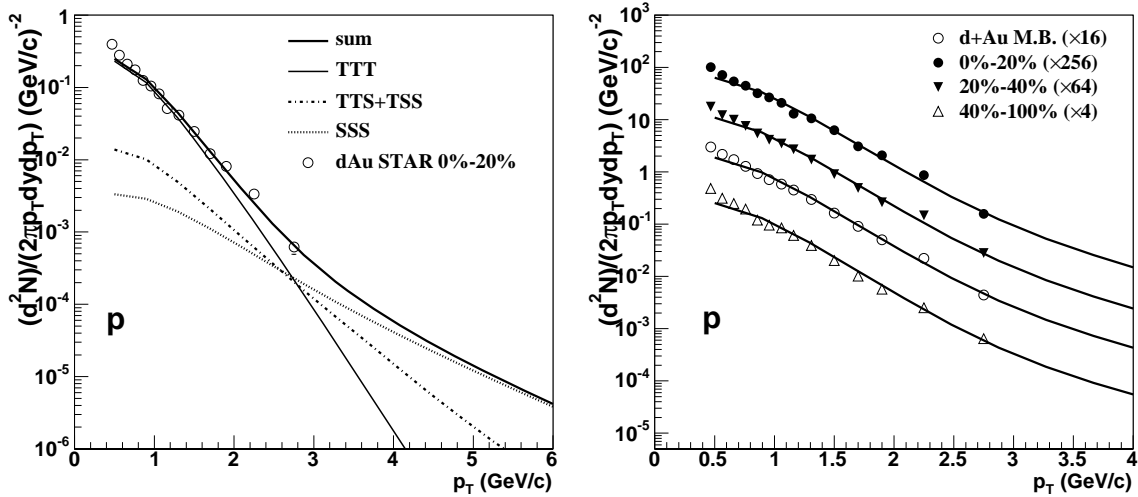


Figure 2.16: (left) The invariant yield for p at 0%-20% d+Au collisions as a function of p_T . (right) The invariant yields for p in minimum-bias and centrality selected d+Au collisions as a function of p_T . The symbols represent STAR data points. The curves on the top of the symbols are the corresponding calculation results from recombination model. The figure is taken from [67].

In [67], a comparison between results for d+Au collisions measured by the STAR experiment and the parton recombination model [65, 66] was made. Figure 2.15 shows

the invariant yield for π^+ in d+Au collisions from STAR (symbols), compared to a parton recombination model calculation. Different centrality cases are shown in the right panel. Figure 2.16 shows the similar comparison for proton production.

These two figures show that the parton recombination model reproduces the spectra of pion and proton in minimum bias and centrality selected d+Au collisions at mid-rapidity in STAR. This agreement suggests that the Cronin enhancement may be not only an initial state effect (multiple scattering or gluon saturation), but that the final state effect (parton recombination) plays an important role too [67].

Chapter 3

RHIC and the BRAHMS Experiment

The data analyzed for this thesis were collected by the BRAHMS, one of the four experiments at RHIC during the physics run of d+Au collisions at full energy ($\sqrt{s_{NN}} = 200$ GeV) in 2003 and p+p collisions in 2005. A brief introduction to the accelerator and a more specific introduction to the BRAHMS experiment will be given in this chapter.

3.1 The Relativistic Heavy Ion Collider

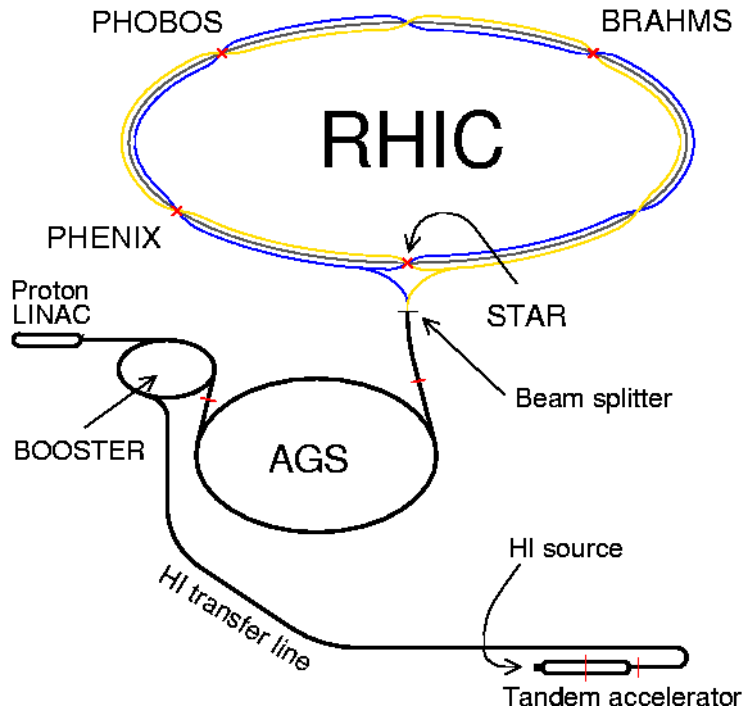


Figure 3.1: Schematic overview of the RHIC accelerator complex [68].

RHIC at the Brookhaven National Laboratory has a top beam energy of $\sqrt{s} = 100$ GeV per nucleon for nuclei of mass $A \sim 200$. Figure 3.1 shows a schematic overview of the complete accelerator complex, consisting of the Tandem Van de Graaff, the Booster Accelerator, the **A**lternating **G**radient **S**ynchrotron (AGS) and RHIC. The Tandem accelerator is used as an ion source. Beams from the Tandem are injected into the Booster for extraction and get stripped fully by colliding with one more stripping target on their way to the synchrotron (AGS). For the protons runs, 200 MeV protons from a LINAC are transferred to the Booster. Each bunch of ions from the Booster is accelerated to top AGS energy (28 GeV for protons; 11 GeV/nucleon for gold) and then transferred to the collider by a magnet system installed in the existing transfer line tunnels. 57 separate bunches of ions are injected into two RHIC rings (3833 m in total circumference for each ring) with opposite directions, which are identified as the blue and yellow beams. Thus, the RHIC machine could provide C.M. collision energies for gold beams ranging from 1.5+1.5 GeV/nucleon to 100+100 GeV/nucleon. For more detailed information see [69, 70].

At four of the six beam crossing points (see figure 3.1), the blue and yellow beams are brought to collision, where the four RHIC detectors (STAR [71], PHENIX [72], PHOBOS [73] and BRAHMS [74]) study the relativistic heavy ion collisions. In table 3.1 a full list of RHIC runs from 2000 up to the summer of 2006 is shown.

Run Period	System	\sqrt{s} [A GeV]	Time
Run I	Au+Au	130	Summer 00
Run IIa	Au+Au	200	Autumn 01
Run IIb	p+p	200	Autumn 01
Run IIIa	d+Au	200	Winter 02/03
Run IIIb	p+p	200	Spring 03
Run IVa	Au+Au	200	Winter 03/04
Run IVb	Au+Au	62.4	Spring 04
Run IVb	p+p	200	Spring 04
Run Va	Cu+Cu	200	Winter 04/05
Run Vb	Cu+Cu	62.4	Spring 05
Run Va	p+p	200	Spring 05
Run VIa	p+p	200	Spring 06
Run VIb	p+p	62.4	Spring/Summer 06

Table 3.1: *The running periods at RHIC until now.*

3.2 The BRAHMS experimental Setup

BRAHMS is designed to measure charged hadron (π^\pm , K^\pm , p (\bar{p})) production over a wide pseudo-rapidity range $0 \leq \eta \leq 4.0$ ($2^\circ \leq \theta_{lab} \leq 90^\circ$) in relativistic nuclear collisions and to provide a very good particle identification [74]. The experiment consists of two moveable spectrometers, namely the mid-rapidity spectrometer (MRS) and the forward spectrometer (FS), and a set of global detectors, like **Z**ero **D**egree **C**alorimeters (ZDC), inelasticity counters (INEL), **B**eam-**B**eam counters (BB) and **M**ultiplicity **A**rrays (MA). It is located at the 2 o'clock intersection of the RHIC ring.

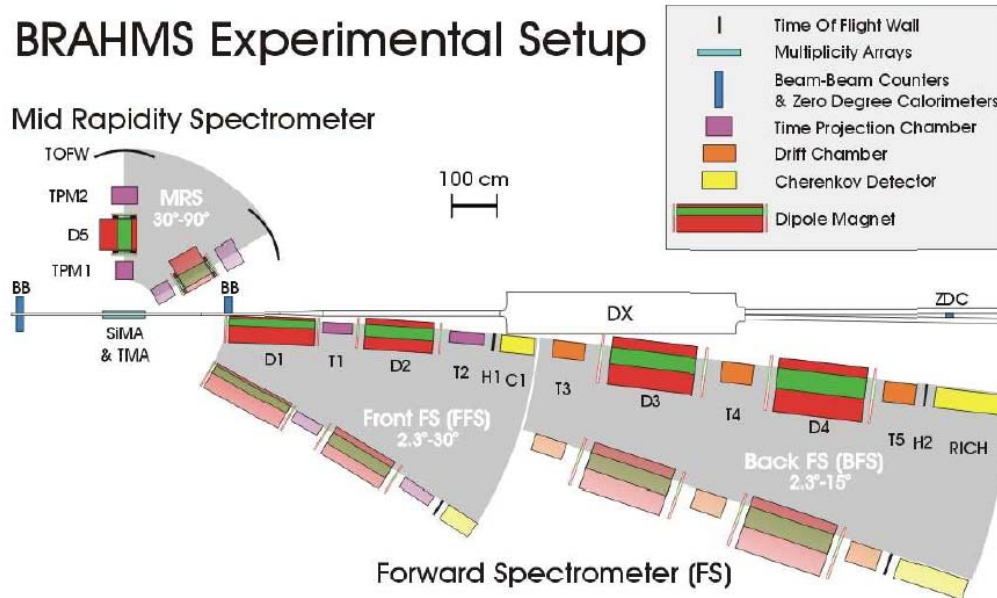


Figure 3.2: Schematic view of the BRAHMS experiment (top view). The mid-rapidity spectrometer (MRS) and forward spectrometer (FS) are rotatable.

Figure 3.2 shows the schematic layout of the BRAHMS experimental detector system. In the following, the detectors in the BRAHMS experimental apparatus shown in the figure will be briefly described.

3.2.1 Mid-rapidity spectrometer (MRS)

The mid-rapidity arm is a single dipole magnetic spectrometer of 8 mrs solid angle designed to cover the angular region 30-90°. It is designed to measure and identify particles with momenta in the range of $p \sim 0.2 - 5 \text{ GeV}/c$. TPM1 and TPM2 are two **T**ime **P**rojection **C**hambers (TPCs) sitting on each side of the dipole magnet D5. TPCs determine the trajectories of charged particles within the TPC active volume and together with the magnet, their momenta and the interaction vertex. The time-of-flight is measured by the **T**ime-**O**f-**F**light **W**all (TOFW), an array of 225 plastic scintillators placed 4 m away from the **I**nteraction **P**oint (IP). Each element is 22 cm high with a cross section of $0.6 \times 0.6 \text{ cm}^2$, and it is instrumented with two fast photomultiplier tubes resulting in a time resolution of $\sigma \leq 75 \text{ ps}$. This gives a π/K separation up to 2 GeV/c and a K/p separation to about 3.5 GeV/c .

3.2.2 Forward Spectrometer (FS)

The forward spectrometer arm contains four magnets, D1-D4, for sweeping and analyzing primary particles created in the collisions. There are two TPCs, T1 and T2 in the front forward spectrometer (FFS), and three drift chambers (DCs), T3, T4 and T5 in the back forward spectrometer (BFS), to measure the positions and thus the momenta of tracks.

Particle identification of particles with lower momentum is based on two time-of-flight hodoscopes, H1 and H2, with a time resolution $\sigma \leq 75$ ps. The H1 array, located 9 m away from the IP, can provide a 4σ separation of π and K up to 3.3 GeV/c and up to 5.7 GeV/c for K/p. The H2 array is 20 m away from the IP, behind magnet D4, and can separate π and K up to 5.0 GeV/c and K and p to 8.5 GeV/c. For higher momentum particles, Čerenkov detectors are used. C1, at the end of the FFS, behind H1, is a conventional segmented Čerenkov tank. A ring imaging Čerenkov detector (RICH) with C_4F_{10} as radiator gas, sitting behind H2 at the end of the BFS, is used to separate K and π up to 25 GeV/c, and K and protons at even higher momenta.

3.3 Detectors

In this section, global detectors and tracking and PID detectors will be described in more detail.

3.3.1 Global detectors and trigger system

In the BRAHMS experiment Beam-Beam counters, inelasticity counters, zero degree calorimeters and multiplicity arrays are used to provide global characteristics of collisions from which trigger decisions are derived (see figure 3.3).

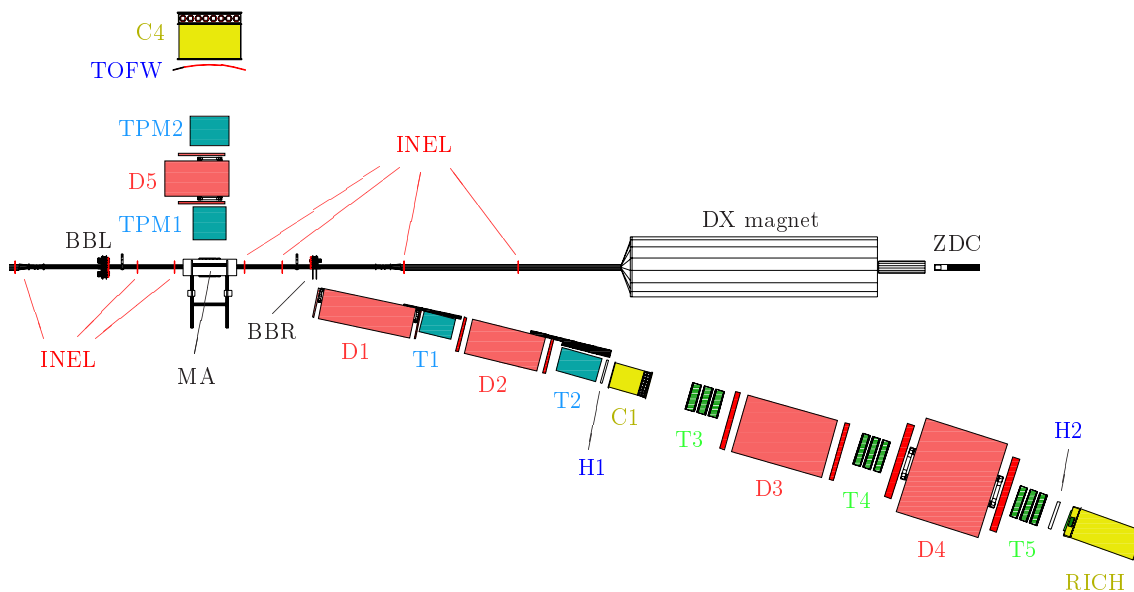


Figure 3.3: *Top view of the BRAHMS experiment.*

Beam-Beam counters (BB)

Beam-beam counters [76] are designed to measure the primary vertex location along the z -axis. They consist of two arrays of fast Čerenkov radiators coupled to photo-multipliers. The arrays are placed at 2.19 m on each side of the IP. Each array (left and right) is composed of two types of tubes for a finely segmented detection. Half

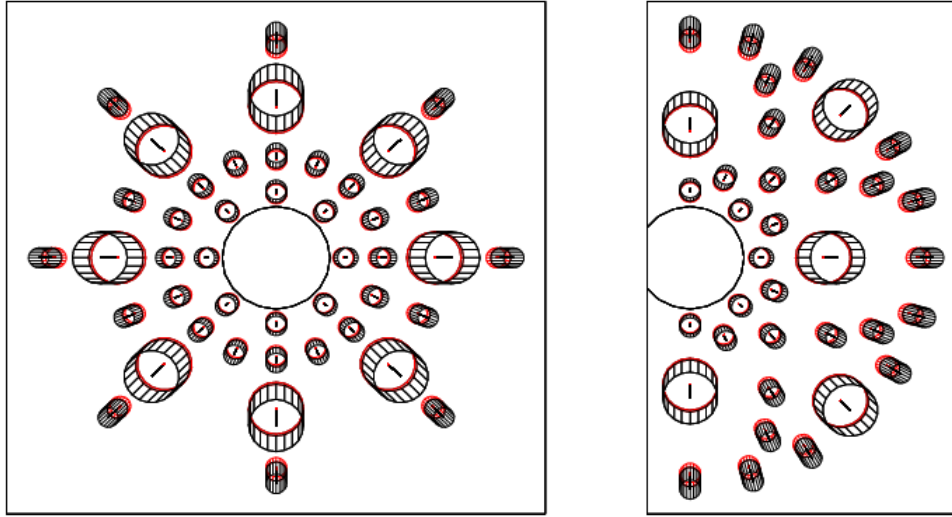


Figure 3.4: *Beam-Beamer counters. The figure is taken from [75].*

of the right array is missing to allow particles to fly undisturbed into the FS. The pseudo-rapidity covered by BB counters is $2.2 < |\eta| < 4.6$. When charged particles hit the Čerenkov radiators, they produce Čerenkov photons if their velocity β is above the threshold c/n ($n \approx 1.5$, $\beta \approx 0.67$). The intrinsic time resolution is 50 ps; for further characteristics of the BB counters cf. [74]. This detector is installed in almost all BRAHMS measurements, but in d+Au and p+p collisions its efficiency drops due to the small event multiplicity. Therefore, in d+Au and p+p collisions the vertex position is determined mainly by the INEL counters and the CC counters.

Inelasticity counters (INEL)

The inelasticity (INEL) counter system from the pp2pp experiment [77] was designed to have a high efficiency for detecting minimum bias double diffractive p+p events (95% of the total inelastic cross section), and it has been implemented in the BRAHMS d+Au and p+p runs. It is used as a minimum bias trigger, when signals from BB counters and ZDCs can not detect low multiplicity events. The INEL counter system consists of 8 rings of plastic scintillators, 4 on each side of the IP, positioned at $z = \pm 75, \pm 155, \pm 416$ and ± 660 cm. Each ring has 4 scintillation plates surrounding the beam pipe and connected to a photomultiplier. By the difference of timing signals from a pair of rings from each side of the IP, collision vertices are determined with a resolution of ~ 5 cm.

CC counters

In p+p collisions at $\sqrt{s} = 200$ GeV (RUN V), the vertex is measured by a set of Čerenkov radiators (CC counters), which are placed symmetrically with respect to the interaction point. The Monte Carlo study using GEANT with PYTHIA generator shows that the CC counters measure $70 \pm 5\%$ of the total inelastic proton-proton cross

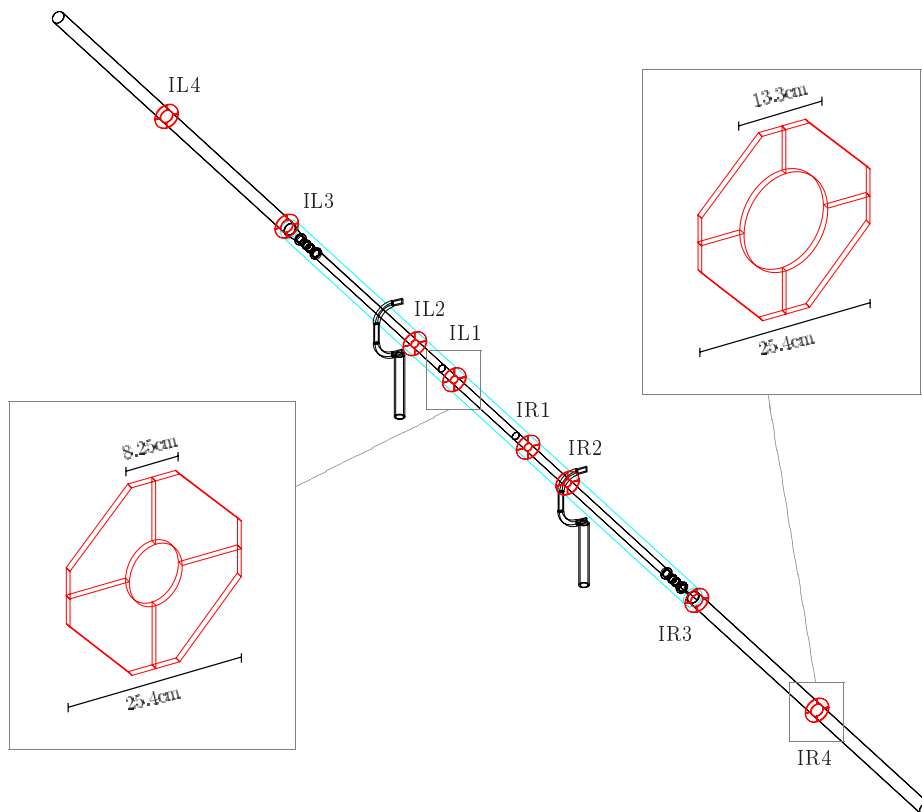


Figure 3.5: *The inelasticity counter setup. The eight rings are placed such that they cover angles from 0.58° to 9.75° on each side of the nominal interaction point. The figure is taken from [68].*

section of 42 mb at 200 GeV, but only 80% of the total number of tracks reach the CC counters, which requires a correction of 87.5% on spectra in total due to this inefficiency from CC counters.

Zero degree calorimeters (ZDC)

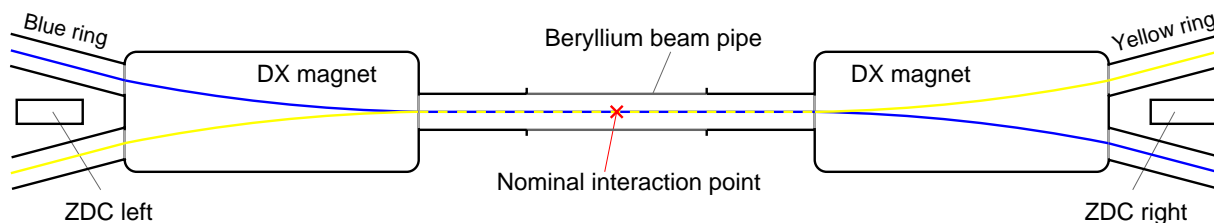


Figure 3.6: *Schematic view of the interaction region and the locations of the left and right ZDCs [68].*

Zero degree calorimeters are the common detector for all RHIC experiments. RHIC operators also use them for beam intensity measurements [70]. The ZDCs are lead-tungsten calorimeters sitting at 18 m on each side of the IP, behind the focusing

DX magnets, which sweep away charged nuclear fragments coming along with the neutrons. The ZDCs are designed to measure the spectator neutrons which continue at very small angles after the collisions. The measurement of neutrons are used for centrality determination, the arrival time can be used to determine the vertex of the collisions [74].

Multiplicity array (MA)

The multiplicity arrays measure the energy deposited by charged particles when they traverse the detector elements, from which the particle multiplicity and collision centrality can be calculated. The MAs consist of two hexagonal detector barrels that surround the interaction region and cover a pseudo-rapidity range $|\eta| < 2.2$. The inner part of the MA is a silicon detector and the outer part consists of plastic scintillator tiles. Details about the MAs and how the MAs can be used to determine the centrality is given in [79].

Figure 3.7 shows an example of the centrality cut by a GEANT simulation, which allows the calculation of the number of collisions for the centrality bin 30-60%. There is a 5% uncertainty for the total multiplicity inside the MA acceptance.

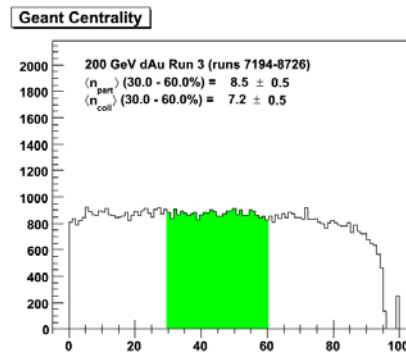


Figure 3.7: An example of centrality cut (30-60%) and the evaluation of $\langle N_{\text{coll}} \rangle$ [78].

Spectrometer trigger detectors

Spectrometer trigger detectors are used to enhance the fraction of events which have at least one track in the spectrometers. The T0 detector in the MRS (MRST0) was used during the d+Au and p+p runs in 2003. It consists of 6 scintillator slats placed in front of TPM1. They cover the complete azimuthal ϕ acceptance of the spectrometer and ± 15 cm in the x direction (in front of TPM1). The MRST0 has two purposes: the signals from the 6 slats are used as an MRS trigger (trigger 3) in the d+Au and

Trigger	Run IIIa (d+Au)	Run V (p+p)
1	BB	BB
2	FS	FS
3	MRS	MRS
4	ZDC	ZDC
5	INEL (MB)	CC
6	FFS	FFS
7	Pulser	Pulser
8	Sync.	Sync.

Table 3.2: Trigger overview for Run IIIa and Run V. Detailed information on the setup can be found in ref. [80].

p+p runs; the time signals were used as a start time for the TOFW and TFW2 time-of-flight measurements. The trigger counters used for the data which are analyzed for this thesis are listed in table 3.2.

Signals from single subdetectors or combinations of them are used to trigger the DAQ system to record data from all the detectors. Triggers are scaled down by different factors during data taking, which means only a certain fraction of the data is recorded. For instance, if we want to collect as many as possible FS events, we set the scale down factor for trigger 2 to 1; on the other hand, we have to consider the limited bandwidth of the DAQ system and the limited storage capacity of the system. INEL counters and CC counters are used to derive a minimum bias (MB) trigger. They are also used to determine the collision vertex in d+Au collisions in Run III and p+p collisions in Run V respectively.

3.3.2 Tracking detectors

The purpose of tracking detectors is to measure the trajectories of the produced particles by recording the energy deposited in the medium they traverse. In the BRAHMS experiment, the hits and the interactions between produced particles with the medium, are recorded by time projection chambers (TPCs) and drift chambers (DCs).

Time projection chambers (TPC)

BRAHMS has four TPCs, two in the FS spectrometer, namely T1 and T2, located behind magnets D1 and D2, and two in the MRS spectrometer, TPM1 and TPM2, sitting at the front and the back of the magnet D5. The TPCs are designed to provide high position resolution measurements of charged particle trajectories in 3 dimensions. Figure 3.8 shows an example of tracks found in TPM2. Characteristics of the four TPCs are listed in table 3.3

TPCs	Width [cm]	Height [cm]	Length [cm]	Gas-mixture	N_{row}	N_{pads}/row
T1	33.60	19.80	56.00	Ar-CO ₂	14	96
T2	39.60	19.80	75.50	Ar-CO ₂	16	112
TPM1	38.40	20.00	36.60	Ar-CO ₂	12	96
TPM2	67.68	19.80	50.00	Ar-CO ₂	20	144

Table 3.3: *Summary of the main characteristics of TPCs. The gas-mixture is 90% Ar and 10% CO₂. For more information about the TPCs see [74, 80, 81, 82].*

Drift chambers (DC)

Three DCs (T3, T4 and T5) are located in the back arm of the FS spectrometer. They are multi-wire proportional chambers, and each of them is composed of three modules with 8-10 planes. With the spatial information coming from 3 modules combined, tracks can be reconstructed by the intersection of wires which were hit (see [74, 83, 84] for more details about drift chambers in BRAHMS). The tracking detectors thus provide information on positions and directions of local tracks.

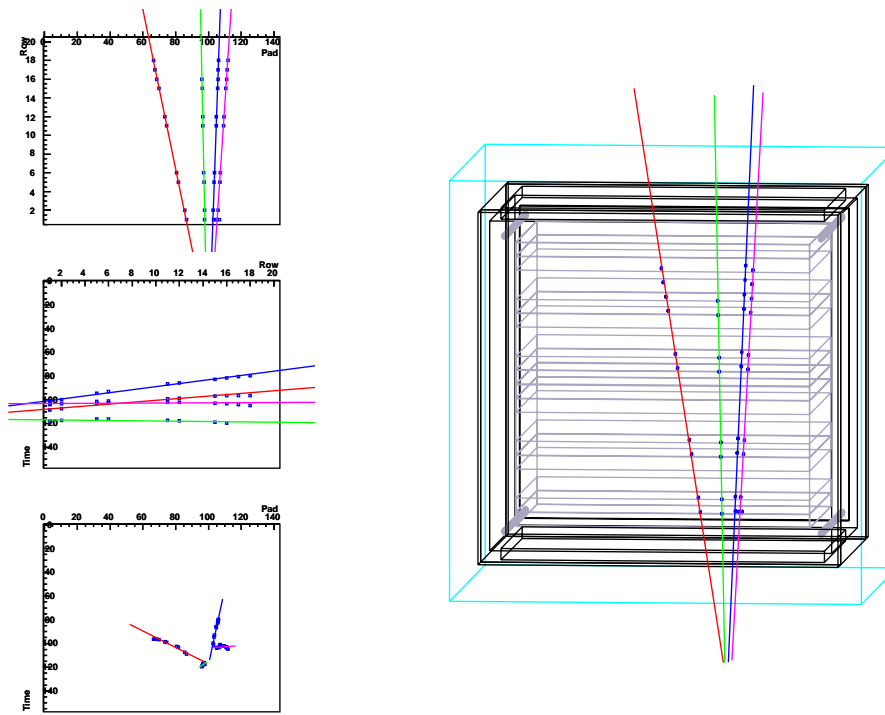


Figure 3.8: *Tracks in TPM2 (online monitoring).*

Dipole magnets

BRAHMS has five magnets. D1 to D4 are in the FS spectrometer, and D5 is in the MRS. All are conventional dipole magnets, sitting between tracking chambers. Inside the magnets the field is approximately constant and has only a vertical component, i.e. particles are deflected only in the x direction. The acceptance of the BRAHMS experiment is determined by the magnetic field strength and the magnet gap dimension. The field strength determines that only particles within a certain momenta range can be deflected into the subsequent magnets or detectors. In table 3.4 the average momentum $\langle p \rangle$ are determined under various magnetic fields. For D1-D4, numbers like 1/8 and 1/5 etc. stand for the magnetic field as the fraction of the full field for each magnet, but for D5, corresponding numbers represent the fields in Gauss unit. In the

magnet	gap dimension [cm]			I_{max} [A]	B_{max} [T]	aver. mom. $\langle p \rangle$ /setting [GeV/c]				
	Width	Height	Length			1/8	1/5	1/4	1/3	1/2
D1	8.0	20.0	200.0	3400	1.26	p not determined				
D2	30.0	13.5	160.0	3000	1.68	2.0	3.0	3.5	5.0	6.5
D3	40.0	25.4	200.0	3000	1.22	3.0	4.5	5.5	7.2	10.0
D4	44.6	32.1	183.0	2750	1.19	3.0	4.5	5.5	7.2	10.0
						164	350	500	700	1000
D5	35.0	10.0	76.2	2500	1.45	0.30	0.35	0.40	0.45	0.55

Table 3.4: *Summary of the main characteristics of magnets used in the BRAHMS experiment. For more information about the magnets see [74, 80, 85].*

FS, the A polarity is for detecting negative particles, and the B polarity for positive ones. In the MRS, due to large acceptance behind D5, a single polarity setting can detect particles with both positive and negative charges. Table 3.4 gives a list of the characteristics of the five magnets.

3.3.3 Particle identification (PID) detectors

Time-of-flight detectors

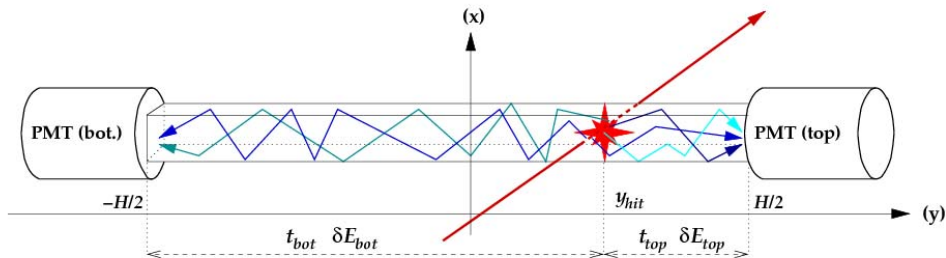


Figure 3.9: *Basic TOF principle. The figure is taken from [86]*

Particle identification is accomplished by a combination of two main techniques, namely Time-of-Flight hodoscopes and Čerenkov detectors. In the MRS spectrometer, we used a time-of-flight wall (TOFW) and a Čerenkov radiator (C1), and in the FS spectrometer we used two TOF hodoscopes (H1 and H2) and a Čerenkov ring imaging detector (RICH) for PID. In the following, a brief overview over these two techniques is given.

TOF name	distanc from IP	species separation	maximum p (GeV/c) within 3-sigma cut
H1	8.7 m	π/K	3.8
		K/p	6.5
H2	18.6 m	π/K	5.8
		K/p	9.7
TOFW	4.3 m	π/K	2.5
		K/p	4.3

Table 3.5: *Performance of the TOF PID devices in BRAHMS (with a 3- σ cut); parameters are taken from [85].*

Table 3.5 shows the basic characteristics of the TOF systems used in the BRAHMS experiment, H1 and H2 in the FS and TOFW in the MRS. Each TOF consists of a row of rectangular scintillator slats wrapped in aluminum foil for guiding the light, and dark tape for light insulation. When a charged particle traverses through a plastic scintillator, molecules along its path are excited. The de-excitation produces photons, which are collected by the PMTs at the ends of the slat. See figure 3.9 for the basic principle of TOF.

From the measurement of the time-of-flight and the path length of the track one can calculate the velocity by $\beta = L_{path}/ct_{tof}$. The identification is done by evaluating the m^2 of the particle when the velocity and the momentum of the particle are known,

$$m^2 = p^2 \left(\frac{1}{\beta^2} - 1 \right). \quad (3.1)$$

Čerenkov detectors

All Čerenkov detector designs are based on the fact that a charged particle with a velocity β larger than the speed of light in the medium c/n emits electromagnetic radiation when traversing the medium whose refractive index is $n > 1$. BRAHMS has three Čerenkov detectors, C1 and C4 are threshold Čerenkov detectors in the FFS and MRS, and RICH is a ring imaging Čerenkov detector (BFS). They all use the same radiator gas C_4H_{10} .

C1 and C4, are similarly designed as a single volume of radiator gas. At the back of the volume, two mirrors reflect the emitted Čerenkov light up or down to arrays of photomultiplier (PM) tubes. There are 32 PM tubes in C1, and 16 in C4. A side view of C1 is shown in figure 3.10. When a charged particle traversing the radiator gas volume has a velocity above the light speed in the gas $v_{threshold}$ it will give a signal.

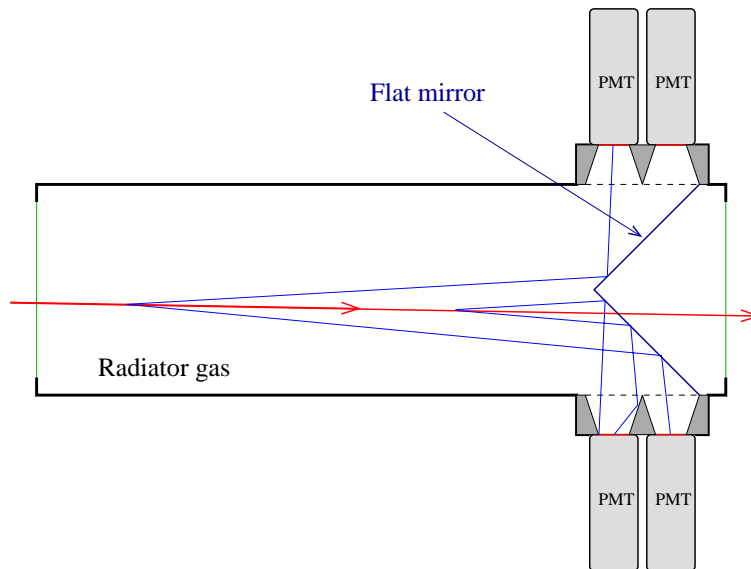


Figure 3.10: *Side view of C1. The emitted Čerenkov photons are reflected on the two 45° mirrors and measured by arrays of PM tubes. The central line (red) with arrow shows a particle track through the detector and all the other lines (blue) indicate the photon reflection on the mirrors.*

The RICH consists of a radiator gas volume, a spherical mirror which reflects and focuses the emitted Čerenkov photons and a segmented photons detection plane. From the radius of the ring on the image plane, the velocity of the particle can be calculated from the Čerenkov angle θ_C ,

$$\tan \theta_C = \frac{r}{L_f}, \cos \theta_C = \frac{1}{\beta n}, \quad (3.2)$$

where $L_f = 150$ cm is the focal length of the mirror, β is the velocity of the particle and n is the refractive index of the gas in the volume. Then finally the mass square of the particle can be reconstructed according to equation 3.1, by which particles can be identified. Figure 3.11 shows a side view of the RICH, and figure 3.12 shows a typical ring image found by the ring finding algorithm [74].

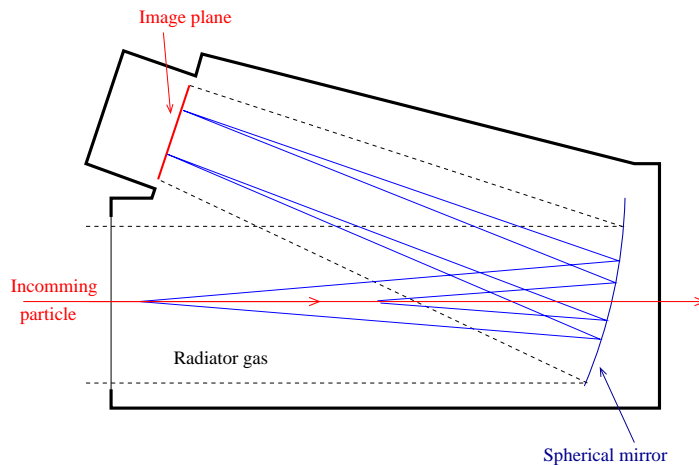


Figure 3.11: Side view of the RICH. The emitted Čerenkov photons are reflected on the mirror and form a ring image on the sensitive image plane. The line with arrows in the horizontal direction (red) represent a particle track through the detector and all the other lines indicate the photon reflection on the mirror.

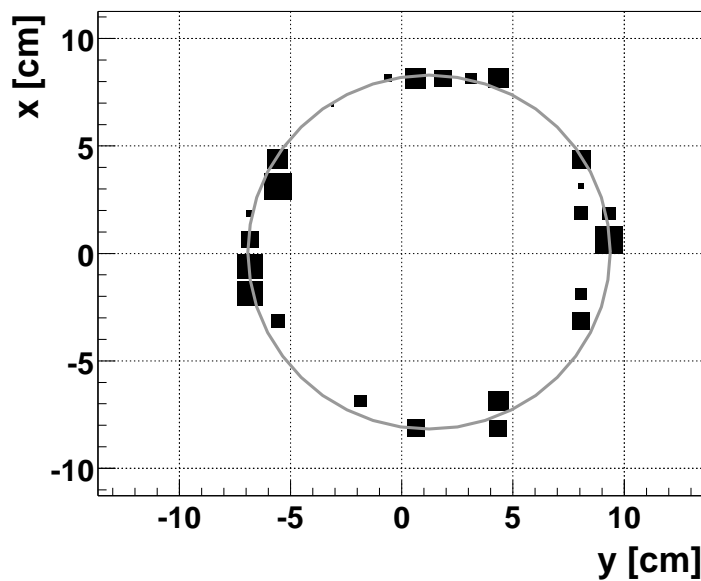


Figure 3.12: An example of a ring image on RICH. For details see [68, 74].

Acceptance

The spectrometers described above determine the rapidity and momentum coverage of the BRAHMS experiment. The following figure shows the acceptance in y - p_T for identified hadrons after combining different angle and magnetic field settings. Analysis details will be discussed Chapter 4.

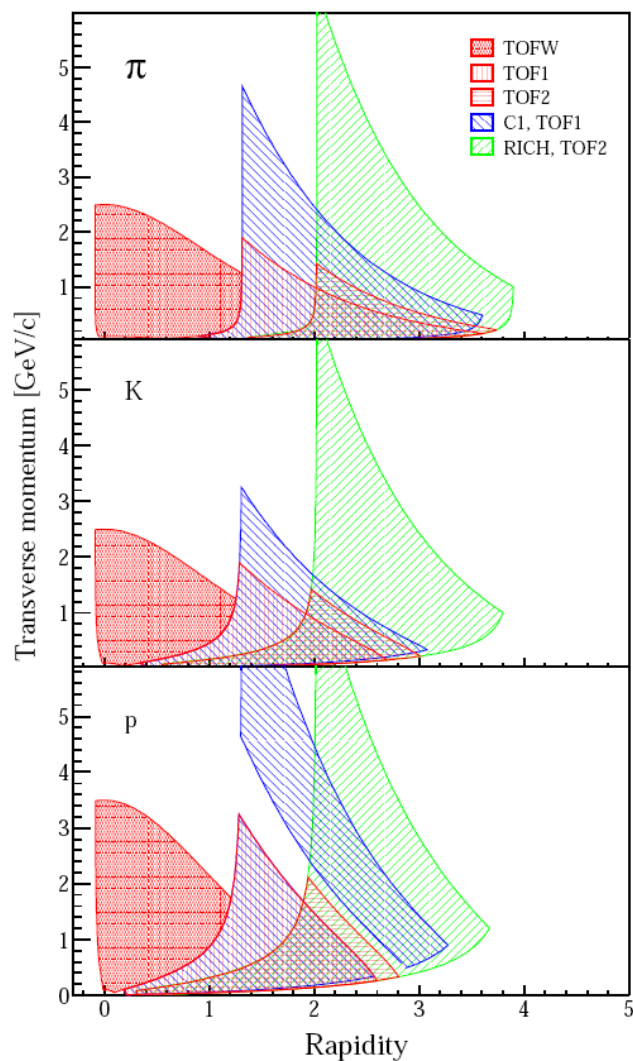


Figure 3.13: *BRAHMS* acceptance maps for pions (upper panel), kaons (middle panel) and protons (lower panel). The regions with different patterns represent the y - p_T coverage for different spectrometer settings, and PID methods as indicated in the legend on the top right corner in the upper panel. The figure is taken from [85].

Chapter 4

Spectra Analysis

Raw data, mainly the analog to digital convertor (ADC) and the time to digital convertor (TDC) signals, have to be transformed into physics data, from which a physics analysis can be carried out. The process of transforming raw data to physics data is called event reconstruction. The basic procedure of the reconstruction consists of detector calibration, tracking, the reconstruction of the primary vertex (interaction point), the momentum determination of tracks and the particle identification (PID).

Detailed descriptions of the detector calibrations are given in [86, 87], and in [86, 68] one can find the basic ideas of the event reconstruction processes, which are therefore not repeated here. This chapter will focus on the physics analysis, namely the analysis method starting from the reconstructed data summary tree (DST) to obtain normalized identified particles spectra in d+Au and p+p collisions at $\sqrt{s_{NN}} = 200$ GeV in run IIIa (2003) and run V (2005).

The spectrum is defined as the invariant cross section in a narrow rapidity y interval as a function of transverse momentum

$$f(p_T) = \frac{1}{N_{evt}} \frac{d^2N}{2\pi p_T dy dp_T}, \quad (4.1)$$

where N_{evt} is the total number of events. All necessary steps to obtain the identified particles spectra, such as event and track selections, corrections (including tracking efficiency, multiple scattering and decay correction, geometrical acceptance corrections and particle identification efficiency), as well as particle identification methods are discussed in this chapter.

4.1 Data selection

Table 4.1 gives a list of all the data sets collected by the BRAHMS experiment in d+Au and p+p collisions at $\sqrt{s_{NN}} = 200$ GeV which are used in this analysis, for both MRS and FS. A (B) is the polarity of the magnets, as mentioned earlier in Chapter 3. In the MRS settings, 90° , 60° , 45° , 40° and 34° are the angles of the MRS arm relative to the beam pipe. Numbers after the polarity, 2255, 2000, 1050, 700, 500 and 350, are the fields strength in Gauss unit. In the FS settings we have data with the FS arm at angles 4° and 2.3° , and with field strengths of 3450, 2442, 1723, 1692, 861 (843)

	d+Au $\sqrt{s_{NN}} = 200$ GeV	p+p $\sqrt{s} = 200$ GeV
MRS	90A/B1050, 90A/B350 40A/B1050, 40A/B500 40B2000	90A/B2255, 90A/B1050 60A/B700, 34A/B700, 34B2255 45A/B1050, 45A/B700, 40A700
FS	4A/B3450, 4A/B1692 4A/B843	4A/B3450, 4A/B2442, 4A/B1723, 4A/B1692 4A/B861, 4A/B430, 2.3A/B3450 2.3A/B1723, 2.3A/B861

Table 4.1: All data settings in d+Au and p+p collisions at $\sqrt{s_{NN}} = 200$ GeV used in the analysis for this thesis.

and 430 Gauss. In the following, selections of data, more specifically, cuts on global variables and local tracks are explained in detail.

4.1.1 Event and track selection

For the event selection, a number of cuts are implemented in order to obtain clean data for physics analysis.

Global selection

Events are selected by different triggers. MRS events are defined by the MRS spectrometer trigger, i.e. trigger 3, while FS events are determined by trigger 2, which is an FS spectrometer trigger, in both d+Au and p+p data, as listed already in table 3.2. The spectrometer trigger conditions are given by an energy deposition above a threshold in the MA corresponding to 20% central events and a BB vertex restriction consisting of a narrow time difference between left and right arrays and a track in the spectrometer. As explained earlier in Chapter 3, spectrometer triggers are usually not scaled down during the data taking, which means that all events satisfying the trigger conditions have been recorded.

Minimum bias triggers are used to count the total number of events, which is essential for the normalization of the spectra. For d+Au collisions in Run III the INEL counters determine trigger 5. For p+p collisions in Run V, the reaction rate from the CC counters was used for the normalization purpose. Cuts are applied to the MRS/FS events in order to select good events. A cut on the vertex determined by global detectors (INEL counters or CC counters) selects events within the certain range around the interaction point. For MRS/FS events a cut on the vertex range [-30 cm, 30 cm] is used in d+Au collisions, and [-40 cm, 40 cm] in p+p collisions.

A centrality cut has been implemented in the d+Au analysis for the centrality dependence study. The centrality was determined from the MA charged particle multiplicity. The uncertainty on the centrality determination comes from the uncertainty in the minimum bias trigger efficiency and from the finite statistics and binning of the distribution from which the centrality is determined. Spectra of particles for three centrality bins 0-30%, 30-60%, 60-80% and in minimum bias events have been constructed; see table 4.2 for a summary of the cuts at event selection level.

Cuts	d+Au $\sqrt{s_{NN}} = 200$ GeV	p+p $\sqrt{s} = 200$ GeV
Vertex	$-30cm \leq V_Z(INEL) \leq 30cm$	$-40cm \leq V_Z(CC) \leq 40cm$
MB trigger	trigger 5 (INEL)	-
MRS trigger	trigger 3	trigger 3
FS trigger	trigger 2	trigger 2
FFS trigger	trigger 6	trigger 6
Centrality	MB, 0-30%, 30-60%, 60-80%	MB

Table 4.2: *Event selection at global level, cuts on vertex position in beam direction, selection of spectrometer trigger, and centrality cuts.*

Track selection

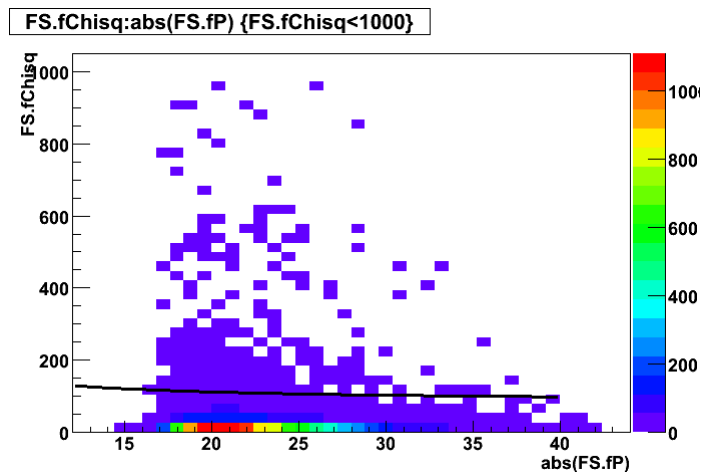


Figure 4.1: *Selected tracks by cutting on the χ^2 of tracks (the curve represents the χ^2 function) at FS. A factor of 4 is used for the FS settings (this setting is 4A3450). The solid curve is the empirical function.*

The electrostatic field and thus the drift velocity close to the walls of the TPC field cage are not perfectly uniform, which results in distorted local track segments. By implementing fiducial cuts on the magnet gaps one can remove those tracks. Usually a volume with a width of 1 cm is removed in both x and y direction. Alternatively, as done in this analysis, a cut on the χ^2 removes those tracks. The χ^2 has been calculated by matching local tracks from different tracking detectors. A track with a certain momentum p which has a χ^2 value larger than a value determined by an empirical function

$$f(p) = \text{factor} \times (28.5 + 180.0/p) , \quad (4.2)$$

is removed from the track sample (p is the momentum in units of GeV/ c). Factors of 4 and 10 are chosen for the FS and MRS respectively. An example of the effects of such cuts on χ^2 is shown in figure 4.1 for the FS. Only very few percent of the tracks are removed by the cut on χ^2 .

A fiducial cut was applied to the RICH. In p+p collisions, a narrow fiducial cut on TPM2 at MRS is implemented because the TOFW behind it was inefficient for

a range of certain slats. The dead slats range is excluded by defining the good slats both in the acceptance map generation and in the cuts on tracks.

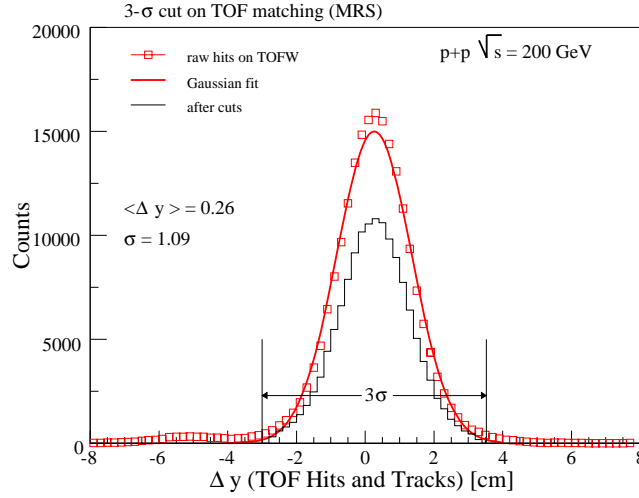


Figure 4.2: An example of a $3\text{-}\sigma$ cut on the matching between hits on TOFW and tracks.

Tracks which do not have a matching hit in the TOF detector are removed by a $3\text{-}\sigma$ cut on the difference in y :

$$\frac{\Delta y - \Delta y_{offset}}{\sigma_{\Delta y}} \leq N_{\sigma} , \quad (4.3)$$

where $\Delta y = y_{track} - y_{hit}$ is the difference between the y -coordinates of the reconstructed track and that of the hits on TOFW, Δy_{offset} is the offset of the Δy distribution, and $\sigma_{\Delta y}$ is the width. Figure 4.2 is an example of a $3\text{-}\sigma$ cut on the matching between hits on TOFW and tracks.

The last criterion is the selection of primary tracks. Not all the particles detected by the spectrometers come from the primary collisions. One has to compare the track vertex, which is defined as the projection of the front part of the global track to the z - y plane (the beam pipe defines the z direction) with the primary vertex in order to reject most of the secondary particles. The intersection with the plane gives the track vertex in y - z plane, i.e. V_y and V_z . In d+Au and p+p collisions the following condition is used for the primary track selection (for both MRS and FS)

$$\left(\frac{\Delta V_z - \Delta V_z^{offset}}{\sigma_{\Delta V_z}} \right)^2 + \left(\frac{V_y - V_y^{offset}}{\sigma_{V_y}} \right)^2 \leq N_{\sigma}^2 , \quad (4.4)$$

where $\Delta V_z = V_z^{global} - V_z^{track}$. In d+Au collisions $V_z^{global} = V_z^{INEL}$, in p+p collisions $V_z^{global} = V_z^{CC}$. Figure 4.3 shows an example of primary track selection for both MRS (left) and FS (right). Typically, few percent of the total tracks are removed. Table 4.3 gives a summary of all the parameters used in this analysis.

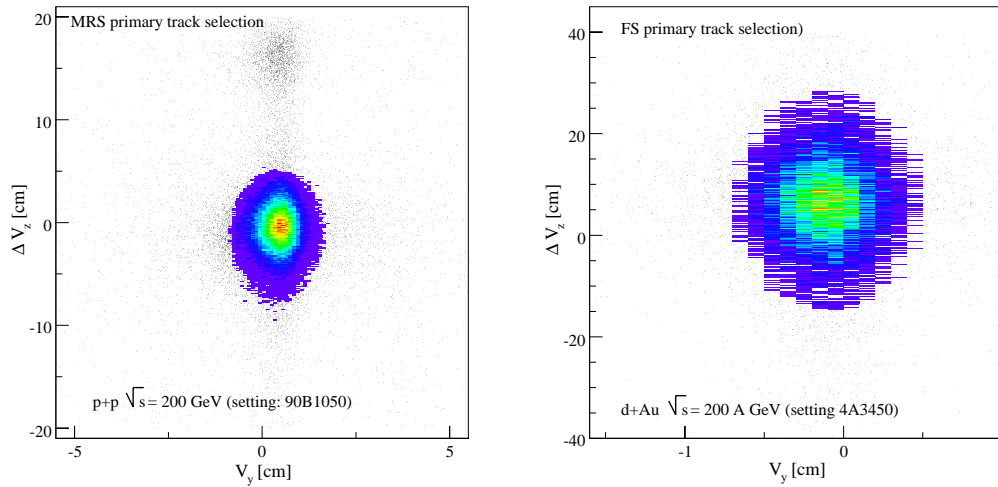


Figure 4.3: An example of primary track selection at both MRS (left) and FS (right). Scattered points are the data before track selection, and the contours (colored) represent the selected tracks.

Cuts for track selection	d+Au $\sqrt{s_{NN}} = 200$ GeV	p+p $\sqrt{s} = 200$ GeV
Fiducial cuts at FS	D1 X: 0 cm, Y:0 cm RICH X: 20 cm, Y:15 cm	D1 X: 0 cm, Y:0 cm RICH X: 20 cm, Y:15 cm
Fiducial cuts at MRS	D5 X: 0 cm, Y:0 cm -	D5 X: 0 cm, Y:0 cm TPM2 X: (-20 cm,8 cm)
TOFW slats range	33-110	33-110
χ^2 cut at FS	factor = 4	factor = 4
χ^2 cut at MRS	factor = 10	factor = 10
Matching TOF hits and tracks	3- σ	3- σ
Primary track selection	3- σ	3- σ

Table 4.3: Track selections including fiducial cuts on magnets, and PID detectors, and cuts on tracks in beam direction, selection of spectrometer trigger.

4.2 Particle Identification

4.2.1 Particle identification by Time-of-Flight

As described earlier in Chapter 3, particle identification can be done by calculating m^2 of the particles by the relation between p and β

$$m^2 = p^2 \left(\frac{1}{\beta^2} - 1 \right), \quad (4.5)$$

from which the TOF m^2 resolution can be derived according to the error propagation [86]

$$\left(\frac{\sigma_{m^2}}{m^2} \right)^2 = 4 \frac{\sigma_p^2}{p^2} + 4 \frac{\sigma_\beta^2}{\beta^2(1-\beta^2)^2}, \quad (4.6)$$

where σ_p and σ_β are the resolution of momentum p and velocity β . σ_p^2/p^2 can be parametrized by $\sigma_p^2/p^2 = p^2 \sigma_{angular} + (1 + m^2/p^2) \sigma_{ms}^2$ [86], where $\sigma_{angular}$ is the track

angular resolution and depends on the field setting, σ_{ms} takes multiple scattering into account, and the velocity resolution β can be parametrized by $\sigma_\beta^2 \equiv \sigma_t = c\sigma_{tTOF}/L$ [86]. Thus, the m^2 resolution becomes

$$\sigma_{m^2}^2 = 4 \left[(m^2 + p^2)^2 p^2 \sigma_t^2 + m^4 p^2 \sigma_{angular}^2 + m^4 (1 + m^2/p^2) \sigma_{ms}^2 \right]. \quad (4.7)$$

Figure 4.4 shows an example of the measured m^2 distribution as a function of the momentum by TOFW (MRS), in which the curves indicate $\pm 2\sigma_{m^2}$ around the m^2 for pions, kaons and protons. Three parameters in this function, namely σ_t , $\sigma_{angular}$, and σ_{ms} , are obtained by fitting simultaneously the width of m^2 in narrow momentum intervals in a range of m^2 of $[-0.1, 0.1]$, $[0.15, 0.35]$ and $[0.6, 1.2]$ for pions, kaons and protons respectively. The parameters for different settings (MRS) in d+Au and p+p collisions which are used in this thesis are given in table 4.4 and table 4.5.

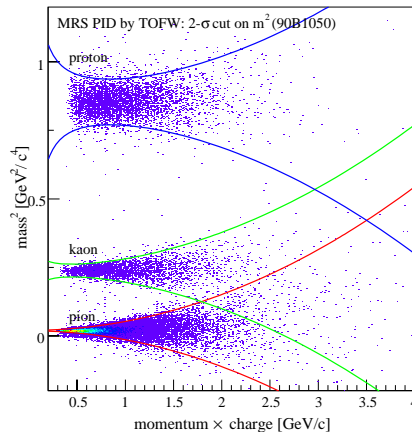


Figure 4.4: Particle identification by TOFW by a simultaneous fit using equation 4.7, A 2- σ cut on m^2 width was used.

settings	σ_t	$\sigma_{angular}$	σ_{ms}
90A1050	0.014	0.009	0.010
90B1050	0.018	0.025	0.008
90A350	0.013	0.014	0.027
90B350	0.018	0.0001	0.043
40A1050	0.014	0.0001	0.012
40B1050	0.015	0.0001	0.010
40A500	0.014	0.0001	0.027
40B500	0.012	0.0001	0.026
40B2000	0.010	0.0001	0.006

Table 4.4: Particle identification by TOFW (MRS): resolution parameters for different settings in d+Au collisions at $\sqrt{s_{NN}} = 200$ GeV.

The performance of the two time-of-flight hodoscopes H1 and H2 in the FS is not as good as expected. Figure 4.5 shows the m^2 distribution measured by H1 and H2 at forward rapidity. Setting 4A3450 in the d+Au collisions is used as an example. No reliable particle identification can be done for most of the runs. Therefore, one has to rely on the RICH detector for PID in the FS.

4.2.2 Particle identification by Čerenkov detectors

As mentioned earlier in Chapter 3 two types of Čerenkov detectors were used. One is a threshold detector (C1 and C4) and the another one is a RICH. In the d+Au and p+p runs the threshold detectors were not efficient, thus in the analysis for the thesis RICH

settings	σ_t	$\sigma_{angular}$	σ_{ms}
90A2255	0.008	0.0001	0.008
90B2255	0.009	0.008	0.007
90A1050	0.008	0.0001	0.013
90B1050	0.008	0.0001	0.013
60A700	0.008	0.0001	0.024
60B700	0.008	0.0001	0.025
45A1050	0.008	0.009	0.012
45B1050	0.009	0.009	0.013
45A700	0.007	0.0001	0.034
45B700	0.008	0.0001	0.021
40A700	0.007	0.0001	0.034
34B2255	0.008	0.006	0.005
34A700	0.009	0.0003	0.021
34B700	0.008	0.016	0.020

Table 4.5: *Particle identification by TOFW (MRS): resolution parameters for different settings in $p+p$ collisions at $\sqrt{s} = 200$ GeV.*

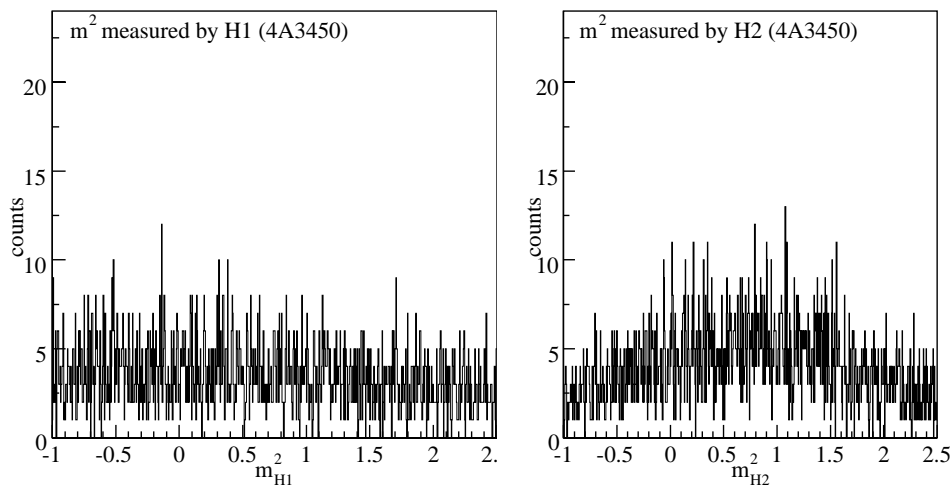


Figure 4.5: m^2 measurement by H1 and H2. Setting 4A3450 (FS) in $d+Au$ collisions is used as an example. There are no peaks.

was the only Čerenkov detector used for particle identification at FS. The ring finding algorithm reconstructs the radius of the ring image on the RICH surface and one can identify particles by calculating their mass from their ring radius by equation 3.2 and get

$$m^2 = p^2 \left(\frac{1}{(n \cos \theta_c)^2} - 1 \right) = p^2 \left(\frac{n^2 L_f^2}{L_f^2 + r^2} - 1 \right), \quad (4.8)$$

where $L_f = 150$ cm is the focal length and n is the refractive index of the gas in the RICH. n is constant for a certain range of runs. Table 4.6 shows the change of the index with run number.

The relation between ring radius r and particle momentum p is derived from equa-

run range	8173-8306	8307-8459	8524-8543	for all p+p data
refractive index	1.00193	1.00188	1.00173	1.00172

Table 4.6: *Refractive index vs run number.*

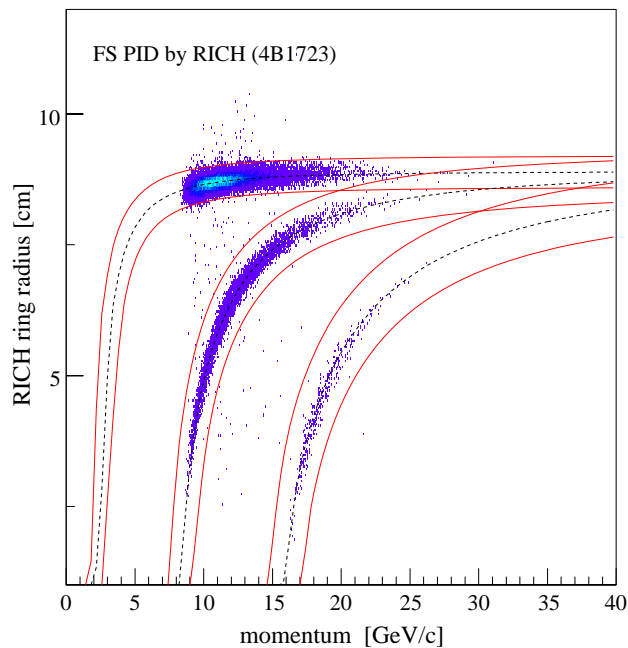


Figure 4.6: *An example of the direct PID method by the RICH: the ring radius as a function of momentum. The solid curves are defined by equations 4.10 and 4.11, the dashed line is determined by equation 4.9, where $\delta r = n_\sigma \cdot \sigma_r$ and a $n_\sigma = 3$ cut are used.*

tion 3.2

$$r = L_f \tan \left[\cos^{-1} \frac{1}{n} \sqrt{1 + \frac{m^2}{p^2}} \right]. \quad (4.9)$$

The calculation of the particle selection envelope is defined by the following equations:

$$r_{upper} = L_f \tan \left[\cos^{-1} \frac{1}{n} \sqrt{1 + \frac{m^2}{(p + \Delta p)^2}} \right] + \Delta r ; \quad (4.10)$$

$$r_{lower} = L_f \tan \left[\cos^{-1} \frac{1}{n} \sqrt{1 + \frac{m^2}{(p - \Delta p)^2}} \right] - \Delta r . \quad (4.11)$$

The ring radius is assumed to have an uncertainty of $\Delta r = 0.45$ cm, and the uncertainty of the momentum for each species is 0.4, 0.6 and 0.8 GeV/c for pions, kaons and protons respectively; m is the rest mass. Figure 4.6 shows the particle identification by the envelopes as defined above.

4.2.3 Treatment of RICH inefficiency

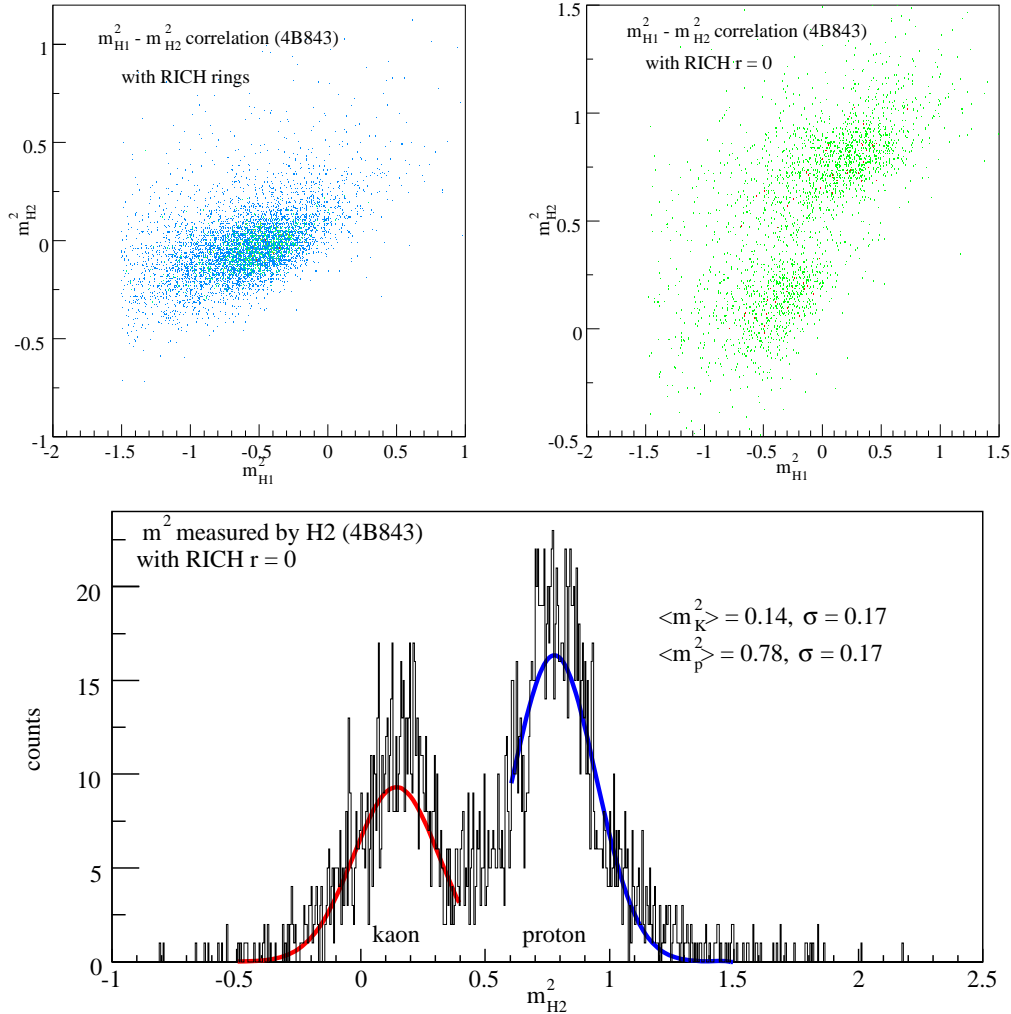


Figure 4.7: $H1$ and $H2$ are used to identify particles without ring image on the RICH mirror. The two top panels show the correlation between m^2 from $H1$ and $H2$ with (left) and without (right) RICH rings for setting 4B843. The bottom panel is the projection the correlation to the m_{H2}^2 . Solid curves are Gaussian fits to the two peaks in the distribution, corresponding to kaon and proton.

In the data analysed for this thesis, the RICH detector has not always been 100% efficient to give ring images for all particles above their momentum threshold, or the ring finding algorithm did not reconstruct all the rings on the mirror. Particles which did not give rings in the RICH were recorded as having $r = 0$. We can try to identify those particles by the time-of-flight hodoscopes in the FS spectrometer ($H1$ and $H2$). The information from hodoscopes $H1$ and $H2$ can only be used for certain runs/settings.

Figure 4.7 gives an example of the reconstructed m^2 correlation from $H1$ and $H2$. From the projection onto each axis, a $2\text{-}\sigma$ cut was made on two Gaussian fits centered at the kaon and proton m^2 to separate kaons and protons (\bar{p}) in cases where the

particles did not give reconstructable ring images on the RICH.

When H1 and H2 are not available for PID and the ring radius is zero, an indirect method is used to identify protons. For particles without a ring image on RICH, if their momenta are above the kaon threshold and below that of the proton, namely $10 \text{ GeV}/c < p < 17 \text{ GeV}/c$, the particle is regarded as a proton with a certain contamination of pions and kaons. The contamination introduced by this indirect method will be estimated later in the PID efficiency correction discussion.

4.3 Corrections

BRAHMS can only measure the produced particles from hadronic collisions in a very small solid angle due to the small geometrical acceptance of the magnetic spectrometers. Spectra measured in a small solid angle have to be corrected by the geometrical acceptance to obtain the yield in 2π . The geometrical correction is done by multiplying the number of detected particles by a factor of $2\pi/\Delta\phi$ where $\Delta\phi$ is the azimuthal coverage of the spectrometer. Additional factors $1/\Delta y$ (or $\Delta\eta$) and $1/\Delta p_T$ normalize the yield per unit rapidity and p_T . Furthermore, the spectra have to be corrected for the trigger counter inefficiency. This correction has to be considered in the analysis of the p+p data of Run V.

The efficiency of the detector has to be taken into account to restore the produced particles' real spectra, i.e. trigger efficiencies (both minimum bias trigger and spectrometer trigger efficiencies), tracking efficiencies of the Drift Chambers (DCs) and the Time Projection Chambers (TPCs). In addition, other effects such as the decay and absorption of the produced particles in the materials, multiple scattering, secondary interactions in the beam pipe and detector materials have to be estimated.

4.3.1 Geometrical acceptance correction

The geometrical acceptance is defined as the fraction of the particles we can detect by our spectrometers in a narrow y - p_T bin

$$\text{Acceptance}(p_T, y) = \frac{\text{detected number of particles}}{\text{total number of produced particles}}. \quad (4.12)$$

A Monte Carlo simulation is used to estimate the acceptance. Exactly the same geometry and magnetic fields as those in the real data-taking are used in the BRAHMS GEANT (BRAG) simulation to generate the acceptance maps for different settings, namely different polar angle and magnetic field combinations. By tracing a very large number of charged particles with certain momentum from the same vertex through the spectrometer and counting the accepted particles which fall inside the fiducial volumes, the fraction of the accepted particles comparing to the total number of thrown particles can be calculated as

$$\epsilon_{geom}(p_T, y) = \frac{\text{accepted number of particles}}{\text{total number of thrown particles}} \times \frac{\Delta\phi}{2\pi}. \quad (4.13)$$

The fractions in each two dimensional Δp_T - Δy bin for all vertex bins are the acceptance maps. The content of the acceptance map in each Δp_T - Δy bin for a certain

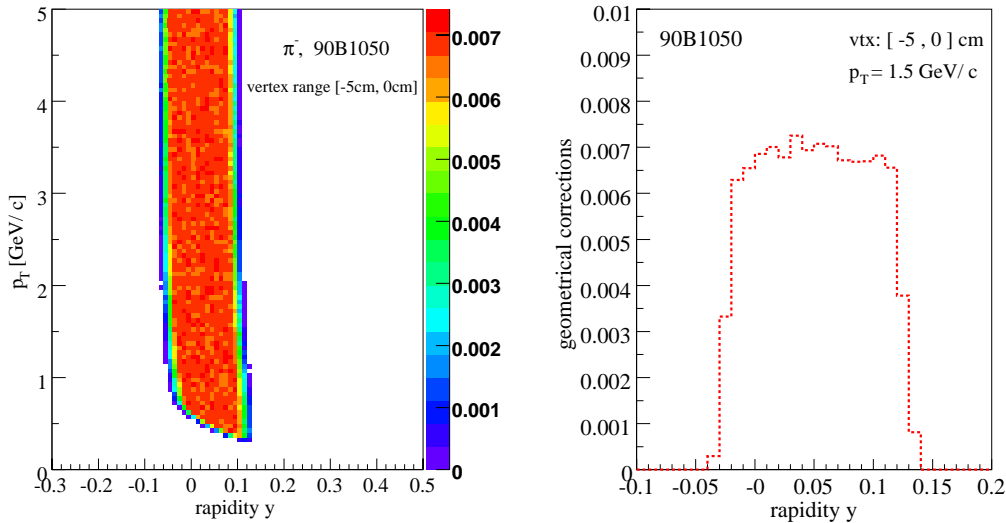


Figure 4.8: An example of a y - p_T acceptance map for the vertex range $[-5 \text{ cm}, 0 \text{ cm}]$ (left), and the geometrical corrections at $p_T = 1 \text{ GeV}/c$ (right). This figure is for setting 90B1050 (MRS).

vertex range shows the azimuthal (ϕ) acceptance of that Δp_T - Δy bin. Figure 4.8 shows a typical geometrical acceptance map.

4.3.2 Tracking efficiency correction

The tracking efficiency in the MRS is studied using a track embedding method [82]. Tracks are generated by a Monte Carlo simulation, within the acceptance of the MRS and merged with raw data. They are then reconstructed according to the same processing procedures as the raw data. Tracking efficiencies are determined by

$$\epsilon_{trk}^{embedding} = \frac{\text{number of reconstructed tracks}}{\text{number of embedded tracks}} . \quad (4.14)$$

The results from [82] are used in the MRS analysis for this thesis

$$\varepsilon(H) = p_0 + p_1 \cdot H , \quad (4.15)$$

where p_0 and p_1 are fit parameters, and H is the total number of hits (occupancy) in the MRS. Typical values of H are below 10 in both d+Au and p+p collisions at $\sqrt{s_{NN}} = 200 \text{ GeV}$. Table 4.7 gives the tracking efficiency functions at MRS, which are used in this analysis.

particle species	pion	kaon	proton
eff. function	$0.948 - 9.6 \cdot 10^{-5} \cdot H$	$0.955 - 9.0 \cdot 10^{-5} \cdot H$	$0.959 - 7.2 \cdot 10^{-5} \cdot H$

Table 4.7: Tracking efficiency function for pions, kaons and protons as a function of the total number of hits (MRS). Functions and parameters are the results from [82].

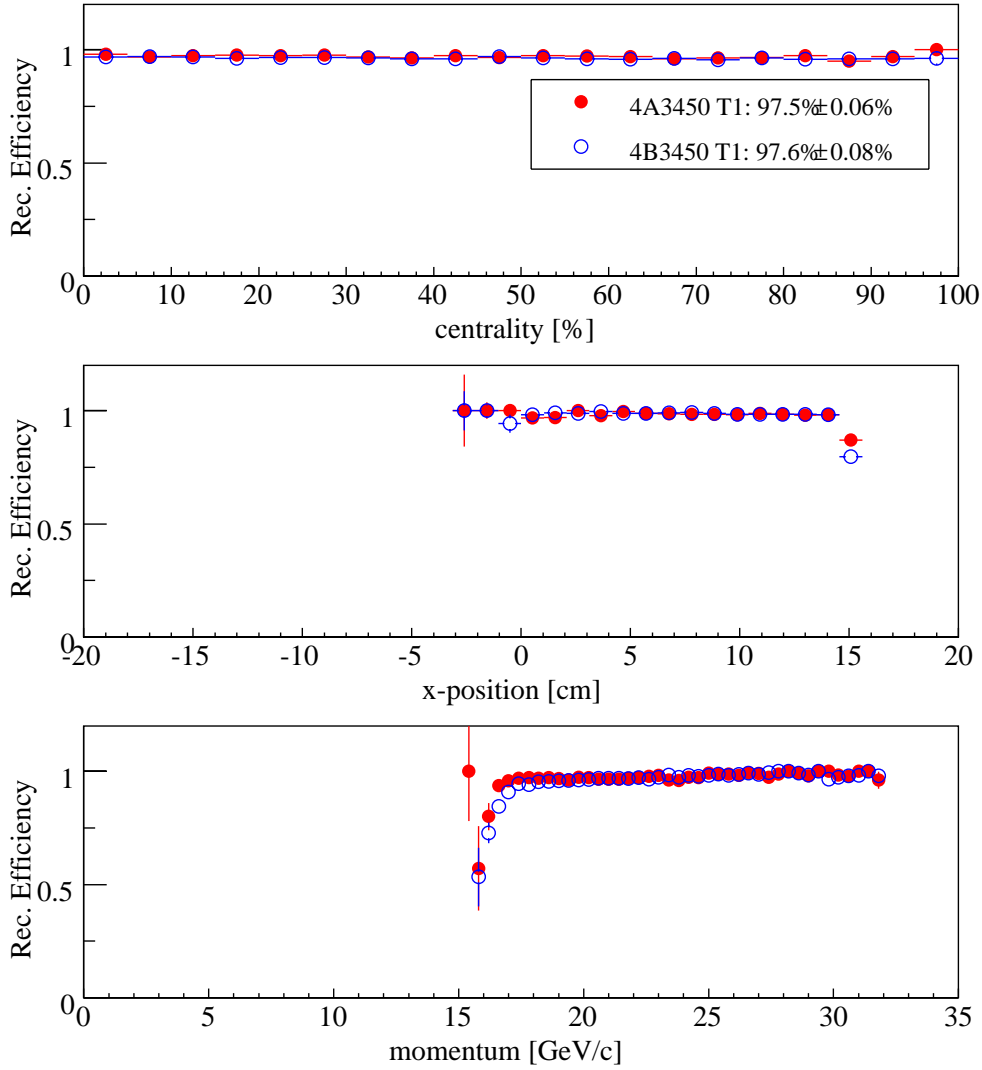


Figure 4.9: $T1$ efficiency as a function of centrality, horizontal hit position in the detector and track momentum in $d+Au$ collisions at $\sqrt{s_{NN}} = 200$ GeV.

The tracking efficiency in the FS is calculated by a reference track method [88]. The tracking efficiency for each detector is estimated by comparing the number of tracks fully reconstructed by all detectors except the one under investigation and the number of tracks by matching track segments in itself:

$$\epsilon_{trk}^{reference} = \frac{\text{number of tracks having a matching track segment in the detector}}{\text{number of tracks fully reconstructed by all other detectors}}. \quad (4.16)$$

Figure 4.9 shows the centrality (upper), the horizontal hit position in the detector (middle) and the track momentum (lower) dependence of the tracking efficiency of $T1$ in $d+Au$ collisions.

In the final analysis, the tracking efficiency at the FS is calculated by

$$\epsilon_{trk}^{FS} = \epsilon_{T1} \cdot \left[\epsilon_{T2} \cdot (1 - \epsilon_{T3}) \right] \cdot \epsilon_{T4} \cdot \epsilon_{T5} \quad (4.17)$$

for tracks with only T1, T2, T4 and T5 segments, or

$$\epsilon_{trk}^{FS} = \epsilon_{T1} \cdot \epsilon_{T2} \cdot \epsilon_{T3} \cdot \epsilon_{T4} \cdot \epsilon_{T5} \quad (4.18)$$

for regular FS tracks with T1, T2, T3, T4, and T5 segments.

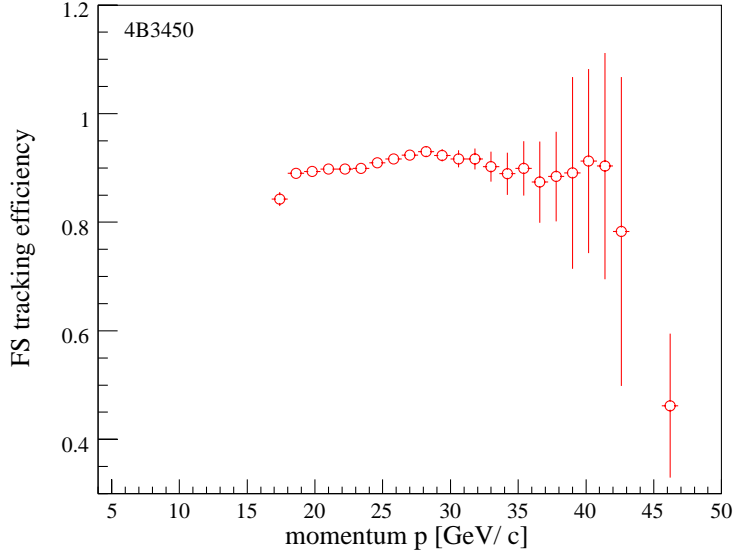


Figure 4.10: *An example of the tracking efficiency as a function of momentum for setting 4B3450 (FS).*

Figure 4.10 shows a typical momentum dependence of the FS tracking efficiency in d+Au collisions. The efficiency is around 90% and shows little dependence on the track momentum.

4.3.3 PID efficiency correction

Time of flight efficiency

The efficiency of TOFW in the MRS is determined by its geometry. 4 panels of slats are in the TOFW in the MRS, and are stacked together in a single row. Therefore tracks can pass through the wrapping of the slats, and the energy deposition in the slat becomes too low to allow the hit to be reconstructed. The efficiency is studied by reference track method [88] and can be estimated by equation 4.19,

$$\epsilon = \frac{N_{identified}}{N_{reference}} . \quad (4.19)$$

where $N_{identified}$ is the number of identified reference tracks and $N_{reference}$ is the total number of reference tracks. No slat dependence has been observed in the MRS and the efficiency of TOFW is found to be $\sim 93 \pm 2\%$ [87].

RICH efficiency

The PID efficiency by the RICH detector has been calculated as 97% for all settings and for particles above the pion threshold 3 GeV/ c producing ring images in the RICH using a GEANT simulation. But for protons (anti-protons) identified by the indirect method in the range $10 \text{ GeV}/c < p < 17 \text{ GeV}/c$ the extent of contamination by pions and kaons needs to be determined. A study on contamination in Au+Au collisions has been done [89] in the BRAHMS collaboration, and a 3% inefficiency was discovered to correct the contaminated protons. Due to the stable performance of the RICH detector throughout all physics runs in the BRAHMS experiment, these 3% are used in this analysis.

4.3.4 Physics corrections by BRAG/GEANT

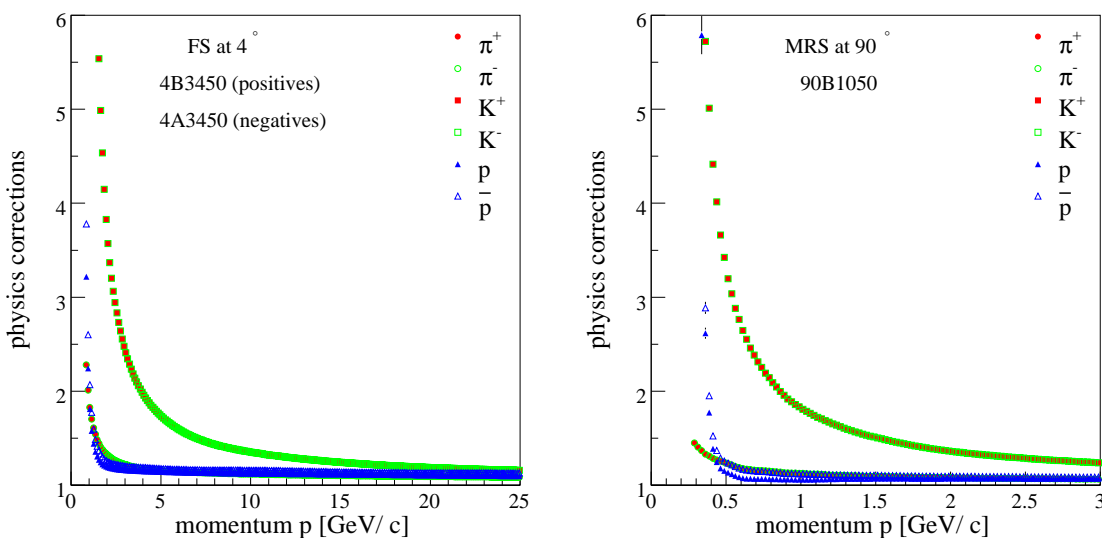


Figure 4.11: *Physics corrections by BRAG simulations, for multiple scattering, decay and absorption of particles when traversing the detectors.*

Corrections of effects due to multiple scattering, decay and absorption of produced hadrons are treated separately by a BRAG simulation. For each particle species π^+ , π^- , K^+ , K^- , p and \bar{p} , primary particles within the geometrical acceptance are simulated with a given momentum at different angles. The BRAG/GEANT simulations are carried out with the following conditions. (1) The BRAG setup is done for each angle for both MRS and FS; (2) Single particles are thrown at the nominal angle $\sim \pm 0.2^\circ$; (3) The magnetic fields are scaled according to the momentum so that the ideal tracks follow the same path for each field setting. Physics processes in the simulations, namely multiple scattering, decay and absorption, are switched on and off to calculate the corrections for each particle. The simulation output is treated as the real data, including digitization, track reconstruction and DST production. DSTs are analyzed as real data, from which the correction can be obtained by dividing the results with physics processes switched on by those with physics process switched off

for each species

$$\epsilon_{phys} = \frac{\text{number of particles while physics process on}}{\text{number of particles while physics process off}}. \quad (4.20)$$

Figure 4.11 shows an example of the corrections as a function of momentum in both MRS and FS.

4.4 Normalization and spectra construction

4.4.1 Corrections and normalization

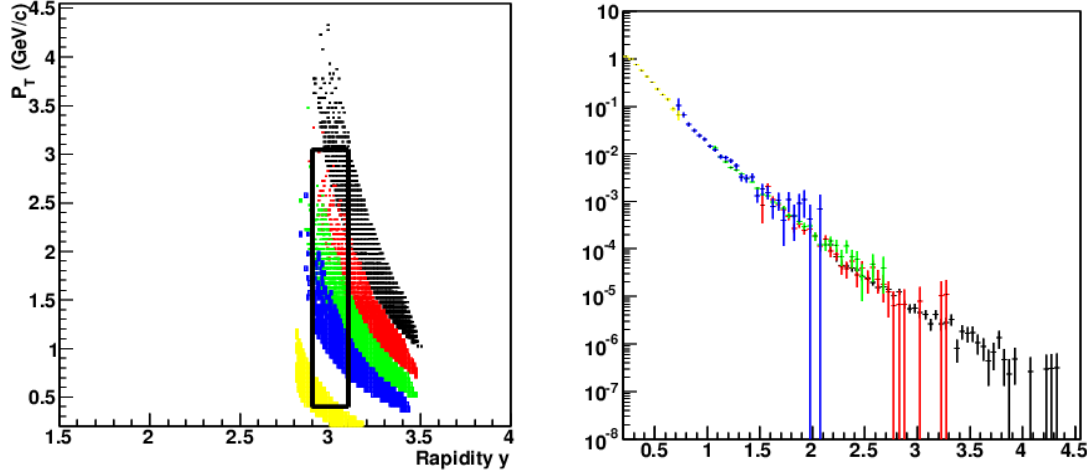


Figure 4.12: *An example of the combination of several settings in the rapidity interval $2.90 < y < 3.10$ for pions, and the construction of the final p_T spectra. Bands in the left panel stand for the acceptance of different settings, 4B427, 4B1219, 4B1723, 4B2442 and 4B3450 respectively from the bottom to the top. The spectra constructed from different settings are shown in the right panel. Errors are statistical only.*

The counts of identified hadrons in each y - p_T bin have been corrected as explained above, and a normalization factor of $2\pi N_{evt}$ has been applied. Spectra for each particle species i in a certain rapidity range are thus given by

$$\frac{d^2 N^i(p_T, y)}{2\pi N_{evt} p_T dp_T dy} = \frac{N_{data}^i(p_T, y)}{2\pi N_{evt} p_T \Delta p_T \Delta y} \times \text{Corr}_{total}(p_T, y), \quad (4.21)$$

where N_{evt} is the total number of events in the sample, $N_{data}^i(p_T, y)$ is the number of particles i measured in a Δy - Δp_T bin. In the analysis for this thesis, $\Delta p_T = 50$ MeV/c and $\Delta y = 0.2$ rapidity units ($[y - \Delta y/2, y + \Delta y/2]$) are normally used and when necessary and a coarser rapidity binning is used in addition. Corr_{total} includes all the corrections and is defined as

$$\text{Corr}_{total}(p_T, y) = \frac{\epsilon_{trig} \epsilon_{phys}}{\epsilon_{acc}(p_T, y) \epsilon_{trk} \epsilon_{pid}}, \quad (4.22)$$

where ϵ_{trig} is the trigger efficiency, ϵ_{phys} the BRAG correction for multiple scattering, decay and absorption, $\epsilon_{acc}(p_T, y)$ the geometrical acceptance correction, ϵ_{trk} and ϵ_{pid} the tracking and PID efficiency respectively. Figure 4.12 shows an example of the momentum space coverage for different FS settings.

Trigger counter efficiency

The minimum-bias trigger is estimated to select $91 \pm 3\%$ of the d+Au inelastic cross section and $71 \pm 5\%$ of the total inelastic proton-proton cross section of 41 mb [33]. To avoid the bias caused by the limited trigger counter acceptance, the p+p yields have been corrected. Our trigger selects non-single-diffractive events and we estimate using the PYTHIA generator that the correction is $13 \pm 5\%$. Please refer to the BRAHMS analysis note [90] for detailed information about how this correction factor was estimated. In this analysis an efficiency of $\epsilon_{trig} = 87.5\%$ was assumed and the particle spectra in p+p collisions have been rescaled accordingly.

4.4.2 Settings combination and final spectra

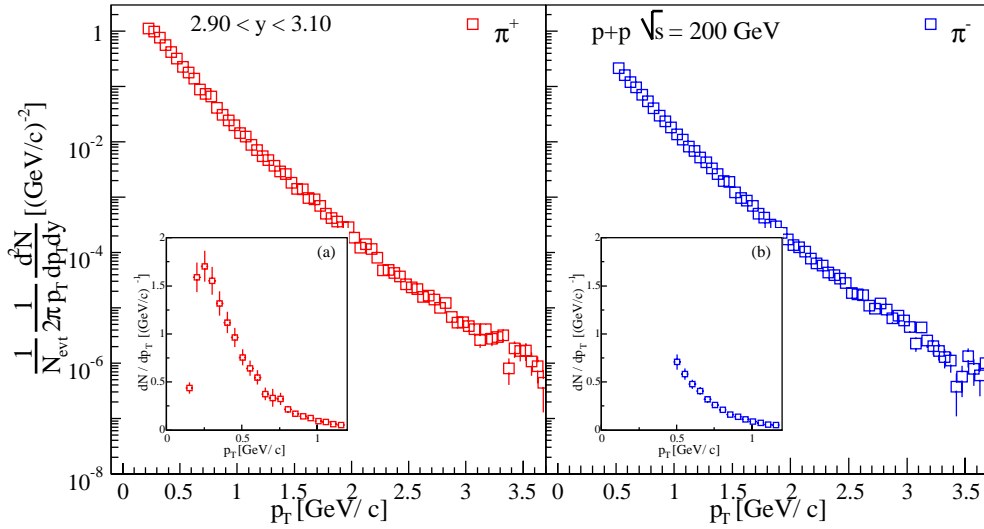


Figure 4.13: An example of the final p_T spectra for π^\pm in rapidity interval $2.90 < y < 3.10$, fully corrected by all corrections discussed above in p+p collisions. Subfigures (a) and (b) are the dN/dp_T spectra for positive and negative pions, which demonstrate the coverage in transverse momentum.

Different settings with the same MRS/FS angle but different magnetic fields are combined to produce the final spectra in order to cover a larger p_T range at each rapidity. The weighted average of results from different settings is the final spectra. The weight for setting s in a certain Δy - Δp_T bin is defined as

$$\omega_s = \frac{1}{\text{Corr}_{total}^s(p_T, y)}, \quad (4.23)$$

which ensures that settings with larger corrections have lower weights. Therefore, the final spectra for identified species i can be constructed by

$$\frac{d^2N^i(p_T, y)}{2\pi N_{evt}p_T dp_T dy} = \frac{\sum_s \frac{d^2N^{i,s}(p_T, y)}{2\pi N_{evt}p_T dp_T dy} \times \omega_s}{\sum_s \omega_s}.$$

Figure 4.13 shows the spectra of π^+ (left panel) and π^- (right panel) at forward rapidity $y = 3$ in p+p collisions. Subfigures (a) and (b) are the dN/dp_T spectra for positive and negative pions, which demonstrate the fraction of the covered cross section.

4.4.3 Errors from setting combinations

As discussed above, the spectrum at a certain rapidity is constructed by combining measurements from different settings. The variation in the result from different individual settings provides an estimation of the systematic error coming from the normalization and all the corrections discussed in the last section.

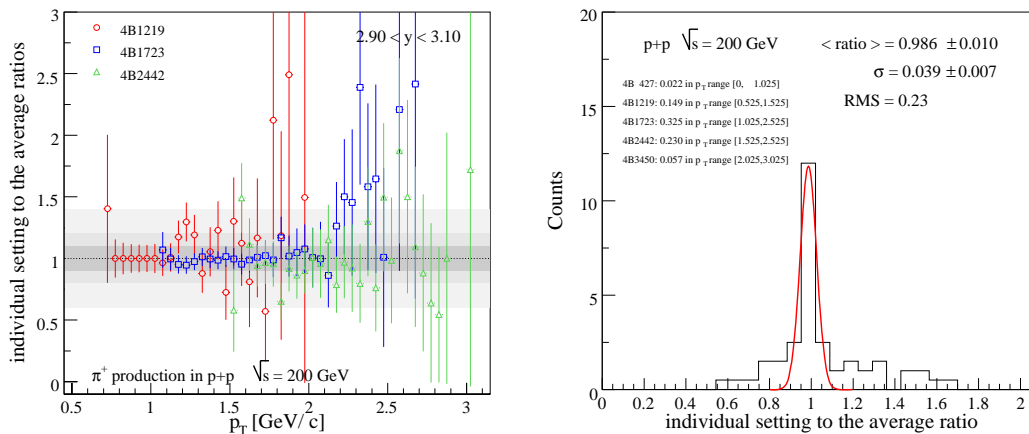


Figure 4.14: *Ratio (left figure) between spectra from different settings and the average spectrum for positive pions at $2.90 < y < 3.10$ in p+p collisions. Distribution of ratios (right figure) centers at 1, fit by a Gaussian function (curve).*

The left panel in figure 4.14 shows the ratio between the individual settings to the average of all settings, the right one shows the projection of the ratios for different settings within the overlapping p_T -range. The bands around ratio = 1 illustrate the spread of the ratios. The systematical errors for all other identified particles in d+Au and p+p collisions at $\sqrt{s_{NN}} = 200$ GeV are studied in the same way. The projection represents the systematic variation of the spectra; the distribution is centered at 1 but has non-Gaussian tails. A systematic error of approximately 20% (π^+ at forward rapidity) is deduced from the RMS.

4.5 GEANT simulation study

A GEANT simulation was made to understand the efficiency of the reconstruction process and to estimate the systematic error of the spectra associated with it. Pions

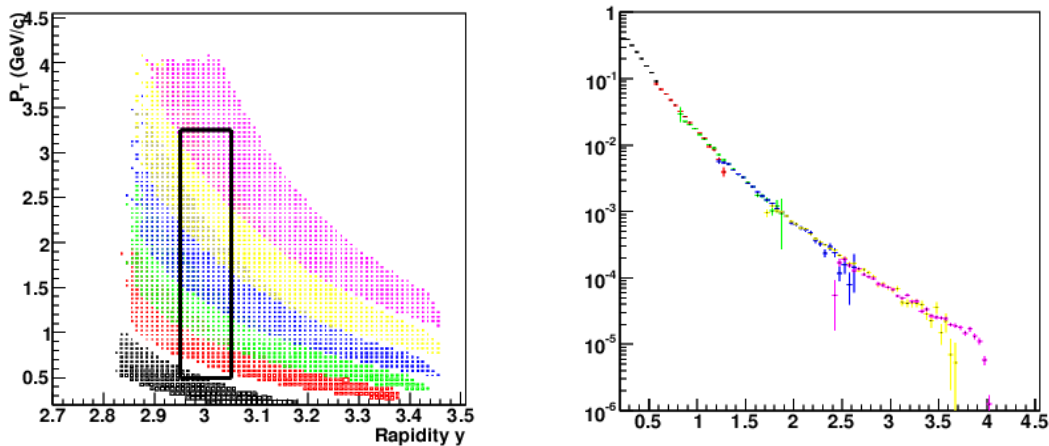


Figure 4.15: *GEANT* simulation study at $2.95 < y < 3.05$ in $p+p$ collisions at $\sqrt{s} = 200$ GeV. The left panel shows the combined acceptance from different settings, the right one shows the combined spectrum.

are generated by a Monte Carlo simulation with *GEANT*, with a fixed rapidity density dN/dy at both mid-rapidity ($y = 0$) and forward rapidity ($y = 3$). All physics processes are switched on in the simulation. In the following, the simulation of the pion production at the forward rapidity $2.95 < y < 3.05$ will be used as an example.

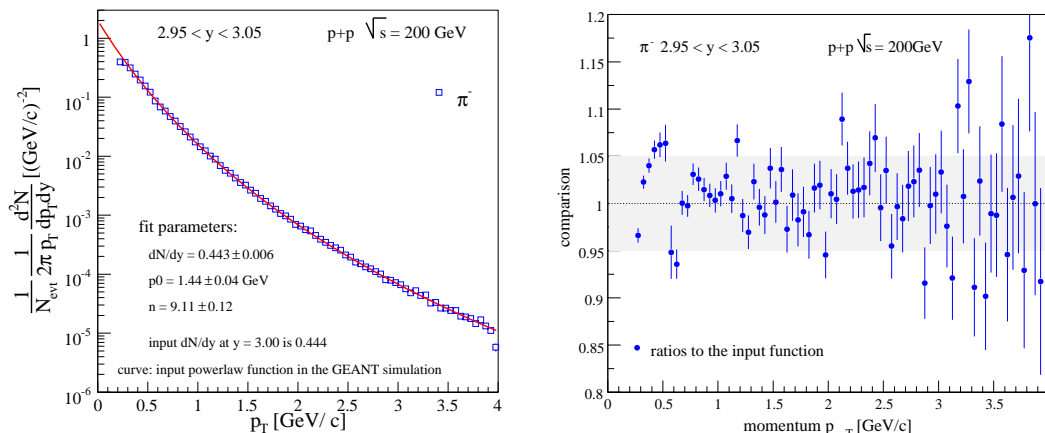


Figure 4.16: *GEANT* simulation study at $2.95 < y < 3.05$ in $p+p$ collisions at $\sqrt{s} = 200$ GeV. The left plot shows the spectrum after corrections (points), and the input function (curve). The right one shows the ratio of the fully corrected spectrum to the input function.

Negative pions are generated with the FS placed at 4° and with magnet settings for D1 (A polarity) at 6 different magnetic fields of 3450, 2442, 1723, 1219, 861 and 430 Gauss. Figure 4.15 shows good matching between settings. Figure 4.16 shows the comparison between the input function in the *GEANT* simulation and the analysis results from the simulated data. The consistency is within 5-10%, which is marked as a band at ratio = 1 in the right plot in figure 4.16. This consistency shows that the corrections implemented in the analysis are correct within 5-10%. A similar study was

done for the corrections at the mid-rapidity and demonstrates a similar reconstruction quality.

4.6 p_T extrapolation

Since the spectrometer acceptance does not cover all p_T , various fit functions are used to extrapolate the spectra to low and high p_T and to extract physics variables like particle yields dN/dy and average transverse momenta $\langle p_T \rangle$. The extrapolation introduces systematic errors originating from the choice of a specific fit function and the p_T range used in the fit.

Two equivalent forms of the invariant cross section as a function of p_T and m_T

$$f(p_T) = \frac{1}{N_{evt}} \frac{d^2N}{2\pi p_T dy dp_T},$$

$$f(m_T) = \frac{1}{N_{evt}} \frac{d^2N}{2\pi m_T dy dm_T},$$

are used to extract the yields dN/dy of identified particle production in nuclear collisions. The method is to use the fit function to extrapolate the spectra under consideration to the regions outside the acceptance and to extract the yields for the full p_T (m_T) range.

The functions which have been used for this purpose are a power law function in p_T (equation 4.24), an exponential function in p_T (m_T) (equation 4.25-4.26) and a Boltzmann function in m_T (equation 4.27):

$$f(p_T) = \frac{(n-1)(n-2)}{2\pi p_0^2} \frac{dN}{dy} \left(1 + \frac{p_T}{p_0}\right)^{-n}, \quad (4.24)$$

$$f(m_T) = \frac{1}{2\pi T(T+m)} \frac{dN}{dy} e^{-(m_T-m)/T}, \quad (4.25)$$

$$f(p_T) = \frac{1}{2\pi T^2} \frac{dN}{dy} e^{-p_T/T}, \quad (4.26)$$

$$f(m_T) = \frac{m_T}{2\pi(2T^2 + 2mT + m^2)} \frac{dN}{dy} e^{-(m_T-m)/T}. \quad (4.27)$$

See Appendix D for details of the deduction of these equations.

4.6.1 Particle yields

Yields are extracted by extrapolation, using the functions listed above. Different functions are used to fit the final spectra. In figure 4.17, the upper panels in subfigure (a) and (b) show an example of the extrapolation using a power law function and an exponential function in p_T for pion spectra at rapidity $-0.10 < y < 0.10$ in p+p collisions at $\sqrt{s} = 200$ GeV. The ratio of the spectra to the corresponding fit function are shown in the lower panels.

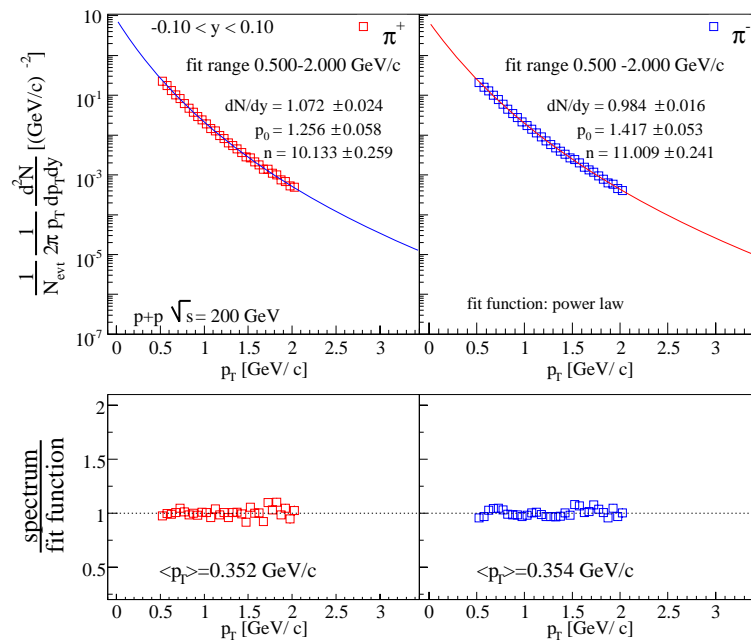
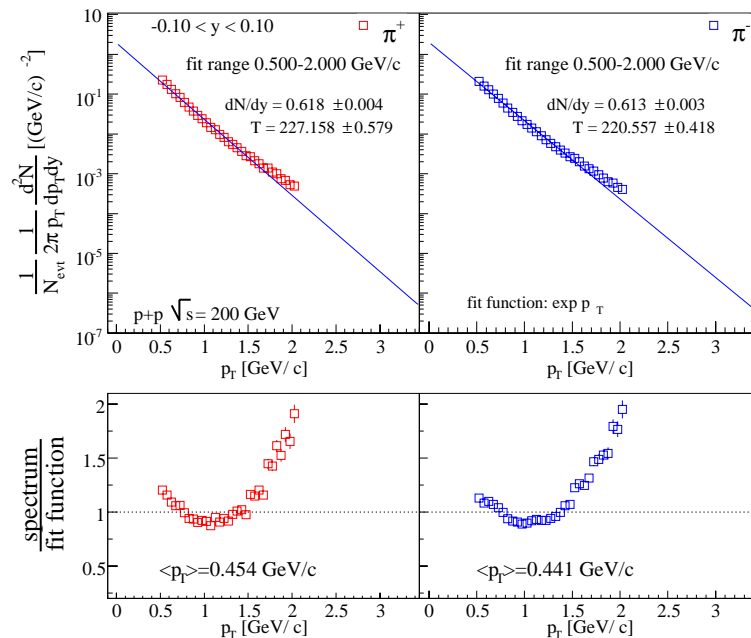
(a) *Fit function: power law in p_T* (b) *Fit function: exponential function in p_T*

Figure 4.17: Pion spectra extrapolations at $-0.10 < y < 0.10$. In subfigures (a) and (b), the upper panels show the spectra, and the lower panels show the spectra to the ratio of the spectra to the corresponding fit functions.

In figure 4.18 the upper panels in subfigures (a)-(d) show an example of the extrapolation using a power law function, an exponential function in p_T , an exponential function in m_T and a Boltzmann function for charged kaon spectra. The corresponding fit parameters are shown. The spectra to the corresponding fit functions ratio are shown in the lower panels in each subfigure.

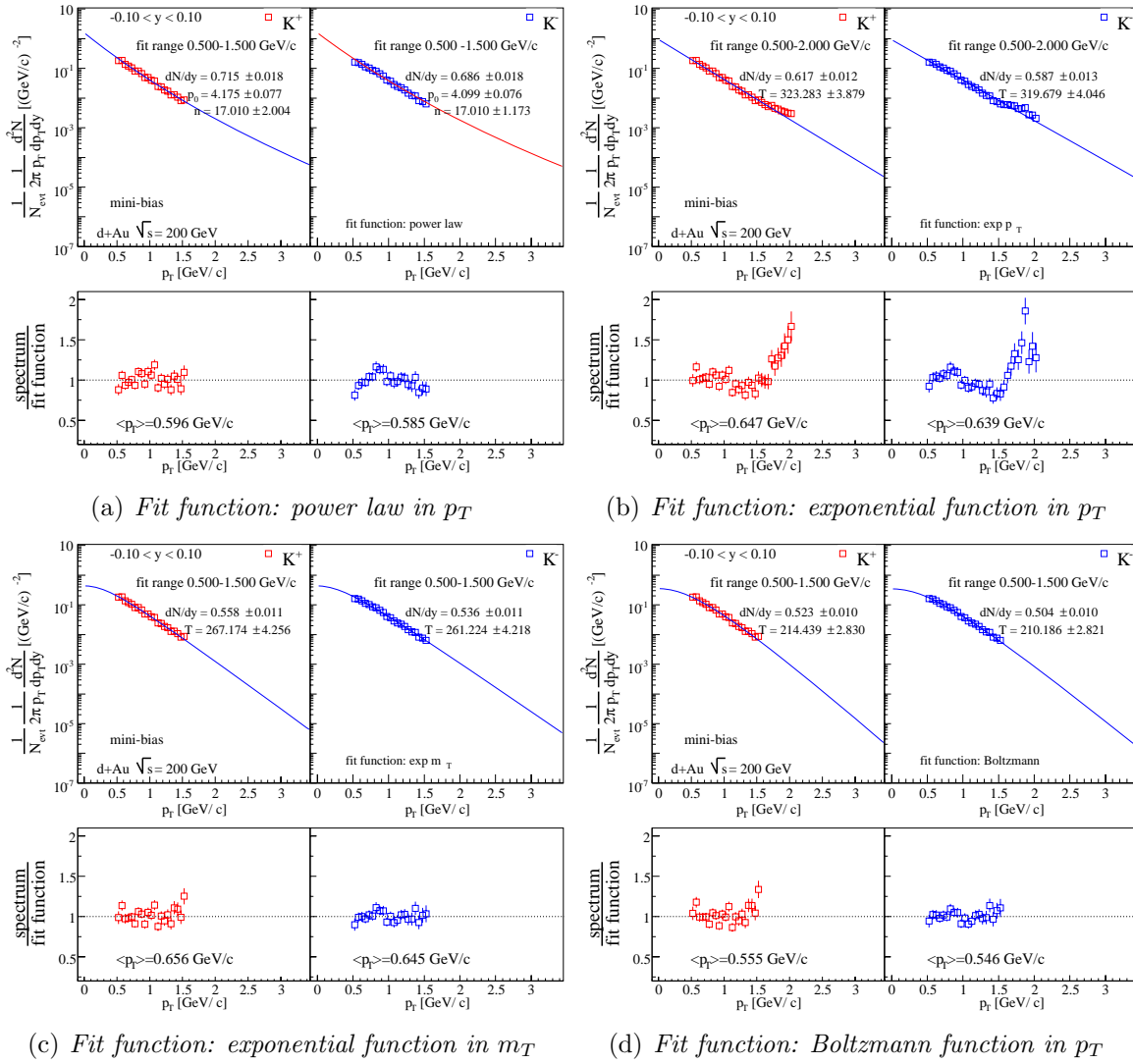
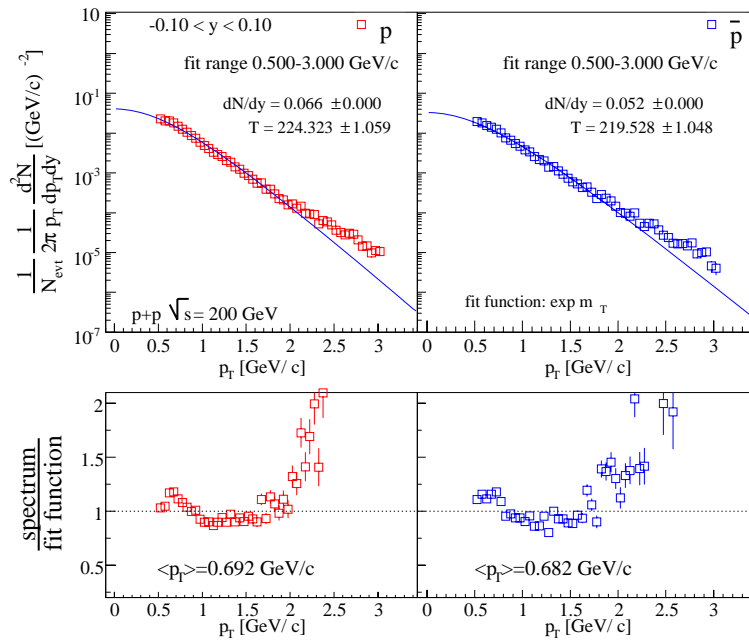


Figure 4.18: *Kaon spectra extrapolations at $-0.10 < y < 0.10$. In subfigures (a)-(d), the upper panels show the spectra, and the lower panels show the spectra to the ratio of the spectra to the corresponding fit functions.*

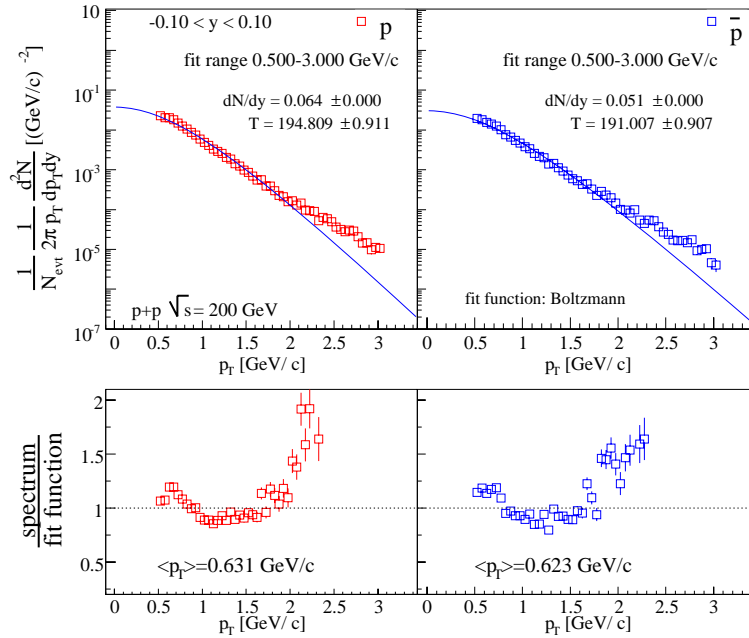
In figure 4.19, upper panels in subfigures (a) and (b) show an example of the extrapolation using an exponential function in m_T and a Boltzmann function for charged proton spectra. The corresponding fit parameters are shown. The spectra to the corresponding fit function ratios are shown in the lower panels in each subfigure.

A similar study was made on the particle production at forward rapidity $y = 3$ in minimum bias d+Au collisions at $\sqrt{s_{NN}} = 200$ GeV. Fits to spectra at other rapidities in p+p and d+Au collisions are included in Appendix E.

From the fit study at both mid-rapidity and forward rapidity in p+p collisions and d+Au collisions, a power law function in p_T for pions, an exponential function in m_T for kaons and a Boltzmann function in p_T for protons are finally chosen to estimate the integrated yields. Results from the other functions are used to estimate the systematic errors.



(a) Fit function: exponential function in m_T



(b) Fit function: Boltzmann function in p_T

Figure 4.19: Proton spectra extrapolations at $-0.10 < y < 0.10$. In subfigures (a) and (b), the upper panels show the spectra, and the lower panels show the spectra to the ratio of the spectra to the corresponding fit functions.

4.6.2 Mean transverse momentum $\langle p_T \rangle$

Calculations of the averaged transverse momentum $\langle p_T \rangle$ are done by equation 4.28,

$$\langle p_T \rangle = \frac{\int_0^\infty p_T \frac{d^2 N}{dp_T dy} dp_T}{\int_0^\infty \frac{d^2 N}{dp_T dy} dp_T}, \quad (4.28)$$

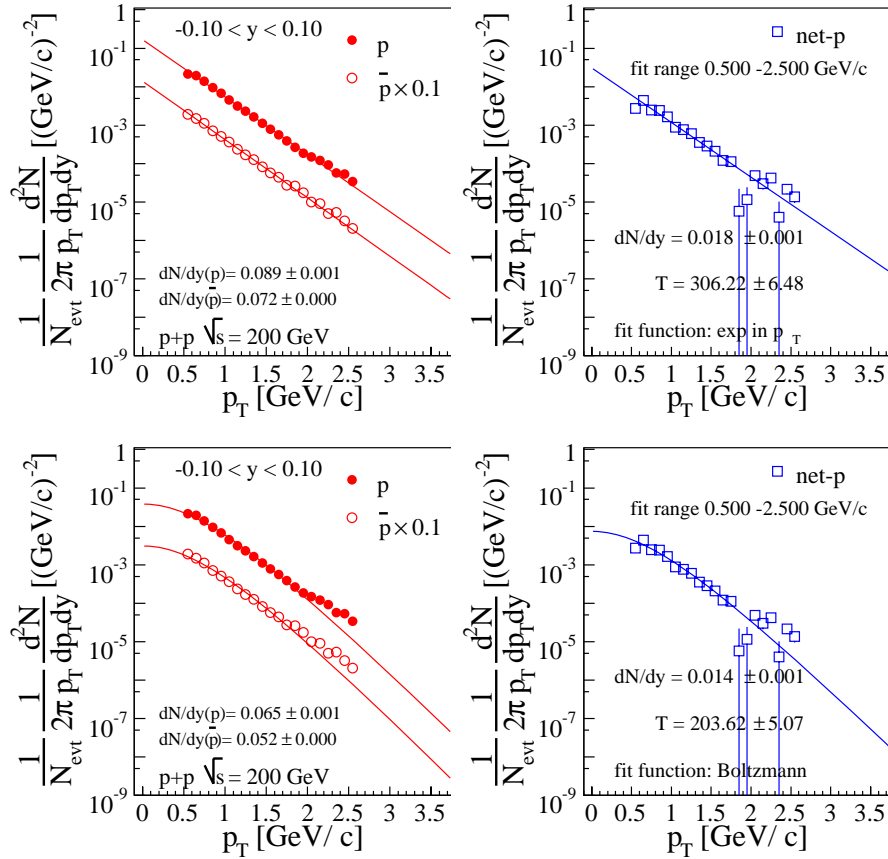
$$\langle p_T \rangle = \frac{\int_0^\infty 2\pi p_T^2 f(p_T)}{dN/dy}, \quad (4.29)$$

where $f(p_T)$ is the fully corrected and normalized spectrum

$$f(p) = \frac{1}{2\pi p_T} \frac{d^2N}{dp_T dy}. \quad (4.30)$$

In the calculation equation 4.29 is used for the $\langle p_T \rangle$ estimation. A power law function, an exponential function in m_T and a Boltzmann function are used for pions, kaons and protons respectively. The results will be presented in Chapter 5.

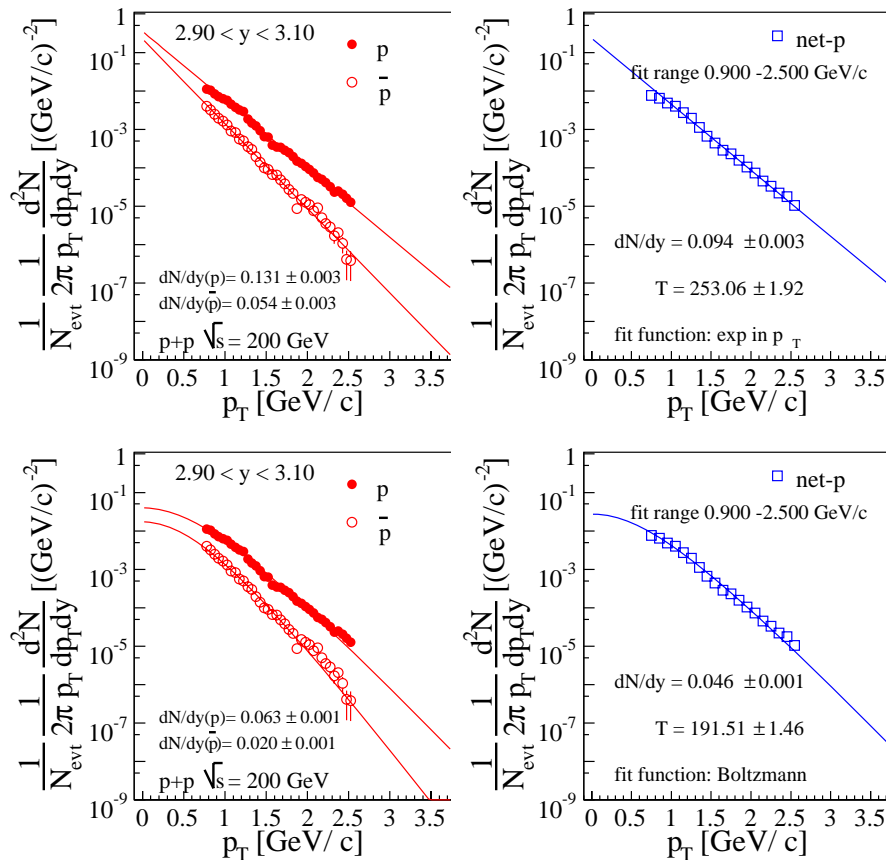
4.6.3 Yields for net-proton



(b) Fit function: Boltzmann function in p_T

Figure 4.20: An example of the p_T spectra of the net-protons in $p+p$ collisions at mid-rapidity $-0.10 < y < 0.10$, fitted by an exponential function in p_T in subfigure (a) and a Boltzmann function in subfigure (b).

Yields of net-protons can be calculated by subtracting the anti-proton yield from that of the protons, which are obtained by the method discussed above. However, the subtraction of the yields of protons and anti-protons obtained from a fit may increase the systematic error of the estimation of net-proton yields by propagating the errors



(b) Fit function: Boltzmann function in p_T

Figure 4.21: An example of the p_T spectra of the net-protons in $p+p$ collisions at forward rapidity $2.90 < y < 3.10$, fitted by an exponential function in p_T in subfigure (a) and a Boltzmann function in subfigure (b).

coming from each fitting procedure. In this analysis, the net-proton yields at a certain rapidity bin are estimated by fitting the net-proton spectra, which are defined as the spectra of the differences between the normalized and corrected proton and anti-proton counts in each p_T bin. The yields are extracted by a combination of direct counts inside the acceptance and the extrapolation by the fit functions in the region outside the acceptance.

In figure 4.20, the left panels in subfigure (a) and (b) show the spectra of protons, anti-protons at $-0.10 < y < 0.10$ and the right panels show the net-proton spectrum, fitted by (a) an exponential function in p_T and (b) a Boltzmann function within the acceptance $0.9 \text{ GeV}/c < p_T < 2.5 \text{ GeV}/c$. In figure 4.21, the left panels in subfigure (a) and (b) show the spectra of protons and anti-protons at $2.90 < y < 3.10$ and the right panels show the net-proton spectrum, fitted by (a) an exponential function in p_T and (b) a Boltzmann function within the acceptance $0.9 \text{ GeV}/c < p_T < 2.5 \text{ GeV}/c$.

4.6.4 Systematic errors

There is a systematic dependence of the integrated yields dN/dy on the choice of the fit range and fit function, which has to be included in the overall systematic error besides

the systematic errors coming from combining spectra which have been discussed in the previous section.

p_T range	0.7-1.5	0.7-2.0	0.7-2.5	0.7-3.0	0.7-3.5
exp in p_T	0.104±0.003	0.116±0.002	0.115±0.002	0.115 ±0.002	0.114±0.002
exp in m_T	0.070±0.001	0.070±0.001	0.066±0.001	0.0065±0.001	0.065±0.001
Boltzmann	0.068±0.001	0.067±0.001	0.063±0.001	0.061±0.001	0.061±0.001

Table 4.8: *Fit function and fit range dependence of proton yield dN/dy at $2.90 < y < 3.10$ in $p+p$ collisions.*

p_T range	0.7-1.5	0.7-2.0	0.7-2.5	0.7-3.0	0.7-3.5
exp in p_T	0.048±0.003	0.051±0.002	0.050±0.002	0.050 ±0.002	0.050±0.002
exp in m_T	0.025±0.001	0.024±0.001	0.023±0.001	0.022±0.001	0.022±0.001
Boltzmann	0.024±0.001	0.023±0.001	0.021±0.001	0.021±0.001	0.021±0.001

Table 4.9: *Fit function and fit range dependence of anti-proton yield dN/dy at $2.90 < y < 3.10$ in $p+p$ collisions.*

The dependence of the integrated yields on the choice of fit function and fit p_T range has been studied. In tables 4.8-4.9, the integrated yield for proton and anti-proton in the full p_T space are used as an example to show the dependence of the yield dN/dy on the fit function and fit range.

For the proton and anti-proton spectra, a power law function can be excluded because its inability to fit the spectra. The exponential functions (in p_T and m_T) give larger yields than the Boltzmann function (difference up to a factor of two) while the difference between different fit ranges for the same fit function is not so large, about 5%-15%.

Chapter 5

Spectra and yields

Particle spectra are built using the method which has been discussed in Chapter 4. Spectra of identified particles are investigated in d+Au and p+p collisions at $\sqrt{s_{NN}} = 200$ GeV at both mid-rapidity and forward rapidity, namely the spectra of positive pions, kaons and protons and their corresponding negative counterparts. Particle ratios, such as negative to positive like-particle ratios, K/π and p/π unlike-particle ratios are studied, as well as the centrality dependence of those ratios in the d+Au system. Mean transverse momentum $\langle p_T \rangle$ and rapidity densities dN/dy are extracted from the spectra.

5.1 p_T spectra

The spectra of identified particles in both d+Au and p+p collisions at $\sqrt{s_{NN}} = 200$ GeV are organized in the following way. For d+Au data, spectra at 3 different rapidities ($y = 0, 1$ and 3) are displayed for 3 different centrality classes (0-30%, 30-60% and 60-80%), as well as for minimum bias data. For p+p collisions, the spectra at 5 different rapidities, from mid-rapidity $y = 0$ to the most forward rapidity $y = 3.5$ are presented.

Figures 5.1 and 5.2 show the spectra of the identified positive and negative particles at different rapidities in minimum bias d+Au collisions at $\sqrt{s_{NN}} = 200$ GeV. Figures 5.3-5.6 show the spectra at different rapidities for different centralities in d+Au collisions. Figures 5.7 and 5.8 show the spectra of the identified positive and negative particles at different rapidities. Due to the limited number of good runs/settings at $y = 1$, only pion spectra could be extracted with sufficient statistics. In p+p collisions at $\sqrt{s} = 200$ GeV, figure 5.9 shows the identified particle spectra at mid-rapidity $y = 0$ and $y = 1$. Figure 5.10 presents the identified particle spectra at forward rapidities, $y = 3, 3.3$ and 3.5 . Errors in figures are statistical only. The systematic errors are estimated to be 20% as mentioned in the previous chapter.

5.2 Particle ratios

As mentioned in Chapter 1, particle ratios are the most direct tool to study the chemistry of the collision systems. The results for like-particle ratios (negative/positive),

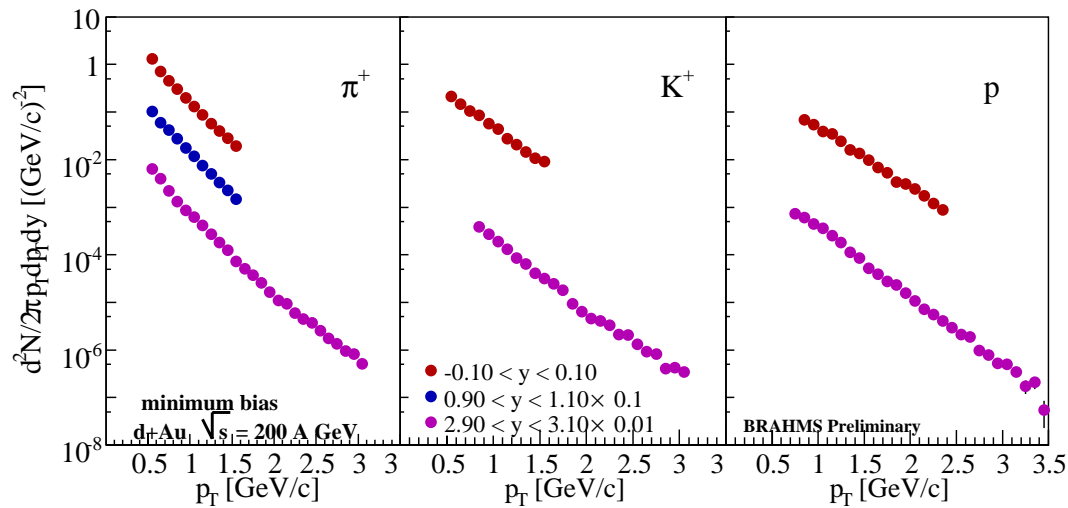


Figure 5.1: Spectra for positive hadrons in minimum bias $d+Au$ collisions at $\sqrt{s_{NN}} = 200$ GeV, scaled by factors which are given in the figure.

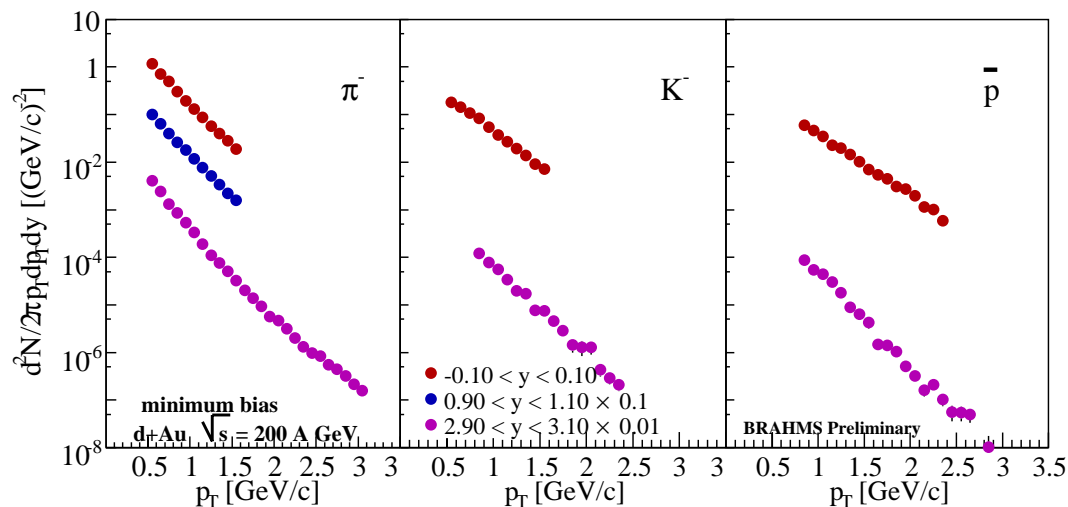


Figure 5.2: Spectra for negative hadrons in $d+Au$ collisions at $\sqrt{s_{NN}} = 200$ GeV, scaled by factors which are given in the figure.

and unlike-particle ratios (K/π and p/π) versus transverse momentum (p_T) in both $d+Au$ and $p+p$ collisions at $\sqrt{s_{NN}} = 200$ GeV are presented in the following subsections.

5.2.1 Like-particle ratios

Figures 5.11-5.12 show the like-particle ratios at three rapidities in $d+Au$ collisions. For pions, the ratio does not change much when going from mid-rapidity to forward rapidity, while for kaons and protons the ratios decrease. The ratios are independent of the centrality (figure 5.12).

Figure 5.13 shows the like-particle ratios at both mid-rapidities (upper panel) and forward rapidities (lower one) in $p+p$ collisions at $\sqrt{s} = 200$ GeV. At mid-rapidity, the

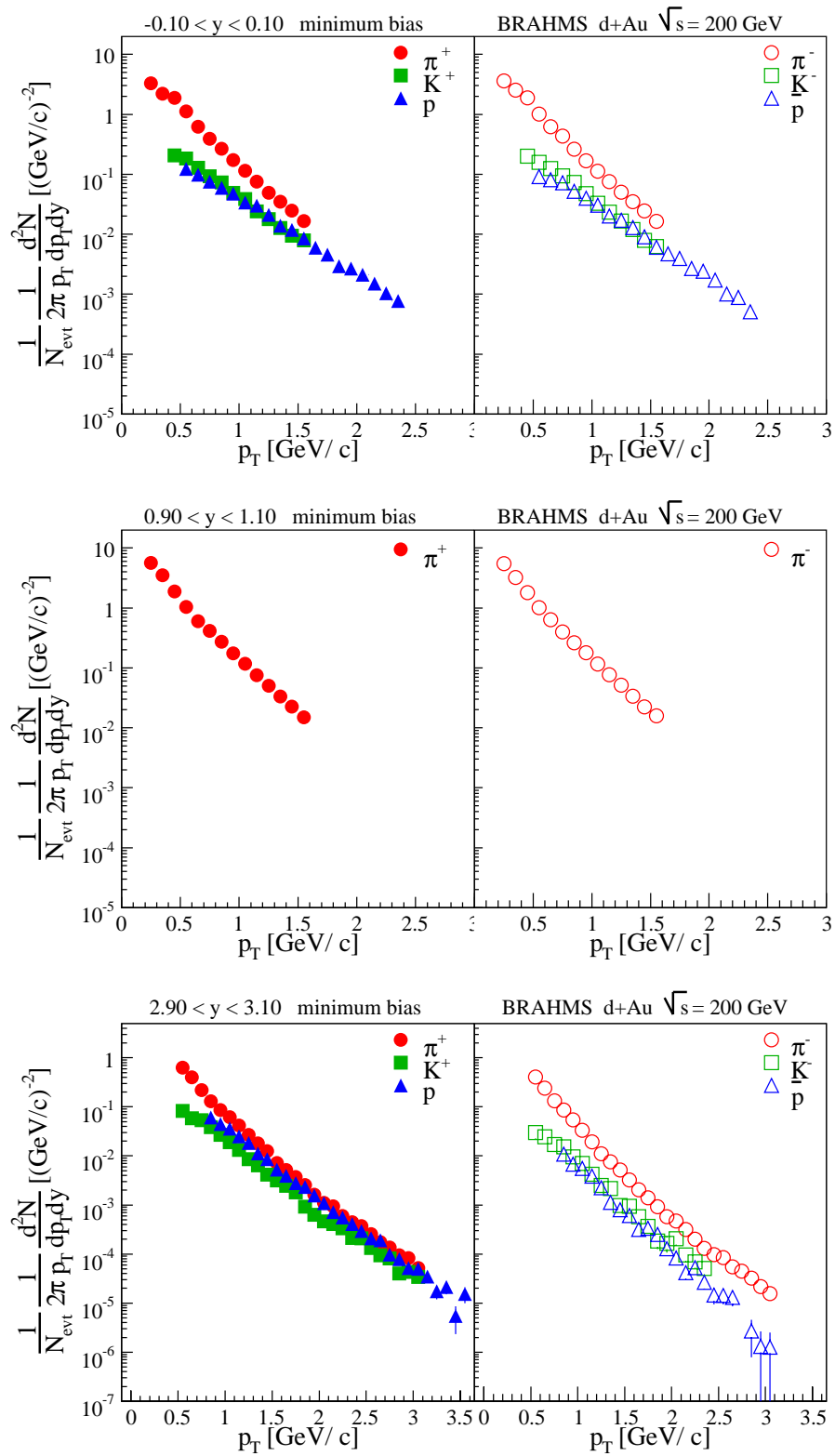


Figure 5.3: Spectra of π^\pm , K^\pm and p (\bar{p}) at rapidity $y = 0, 1$ and 3 in minimum bias $d+Au$ collisions at $\sqrt{s_{NN}} = 200$ GeV.

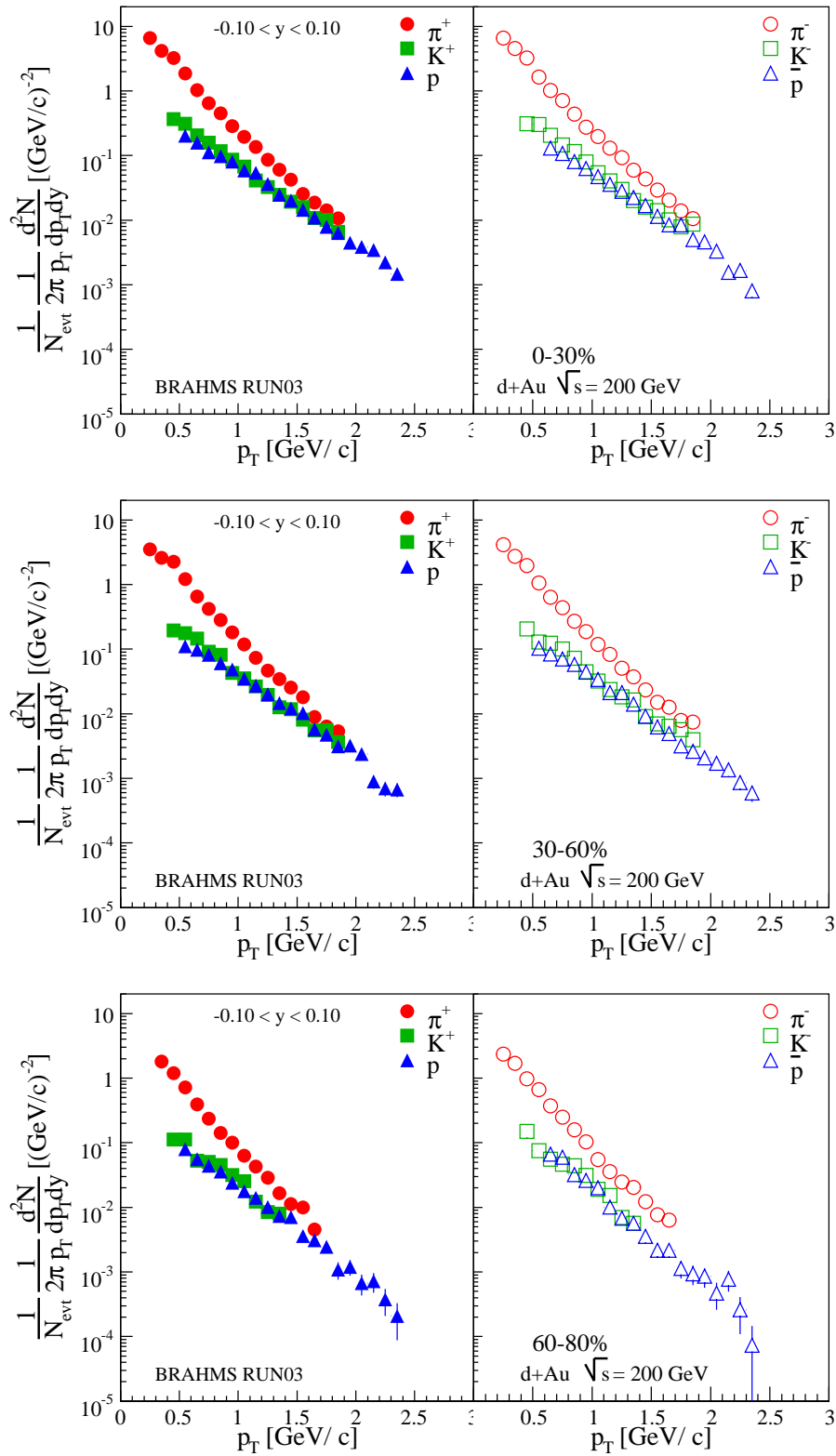


Figure 5.4: Spectra of π^\pm , K^\pm and $p(\bar{p})$ at rapidity $y = 0$ in $d+Au$ collisions for centralities 0-30%, 30-60%, 60-80%.

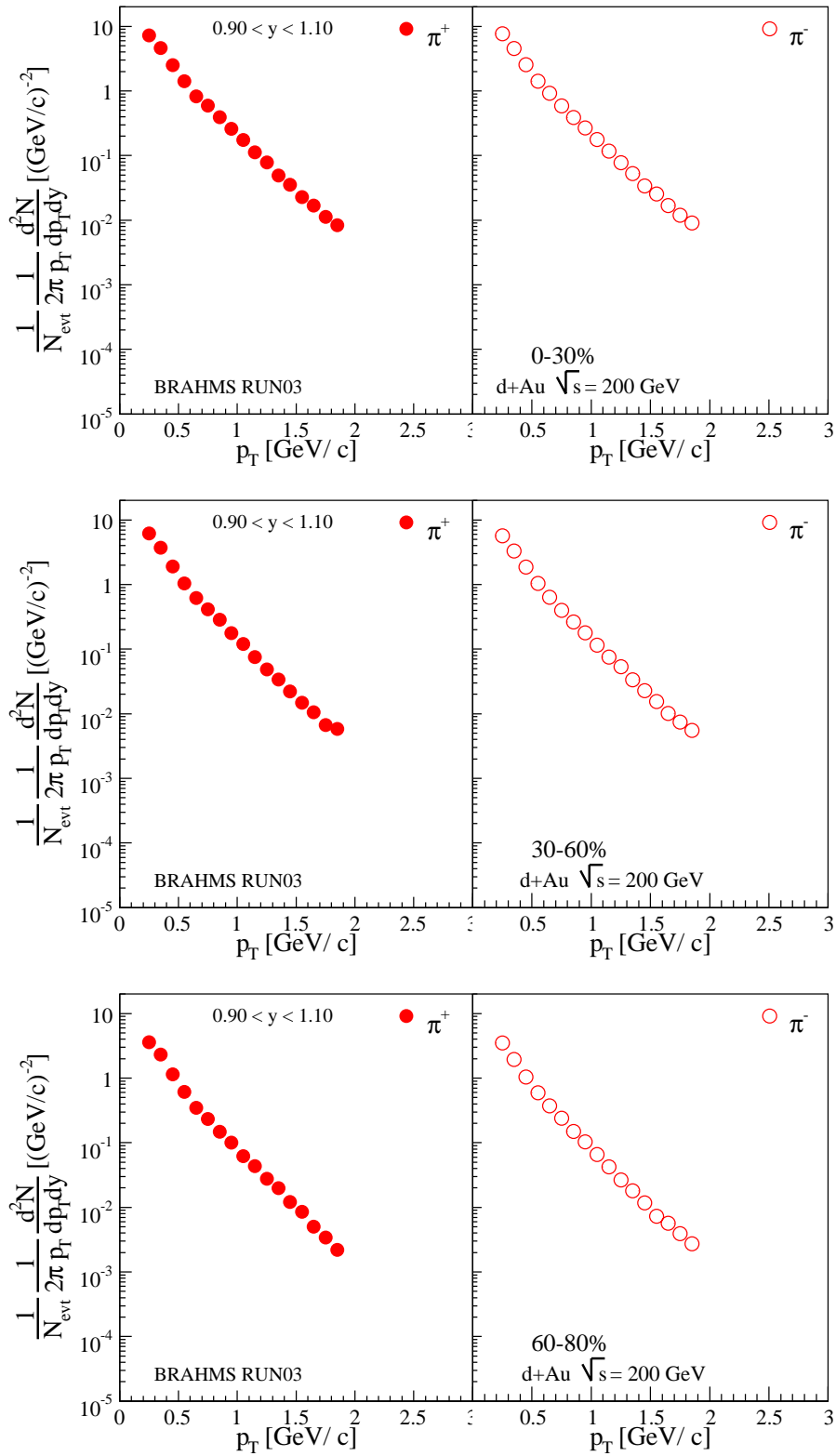


Figure 5.5: Spectra of π^\pm at rapidity $y = 1$ in $d+Au$ collisions for centralities 0-30%, 30-60%, 60-80%.

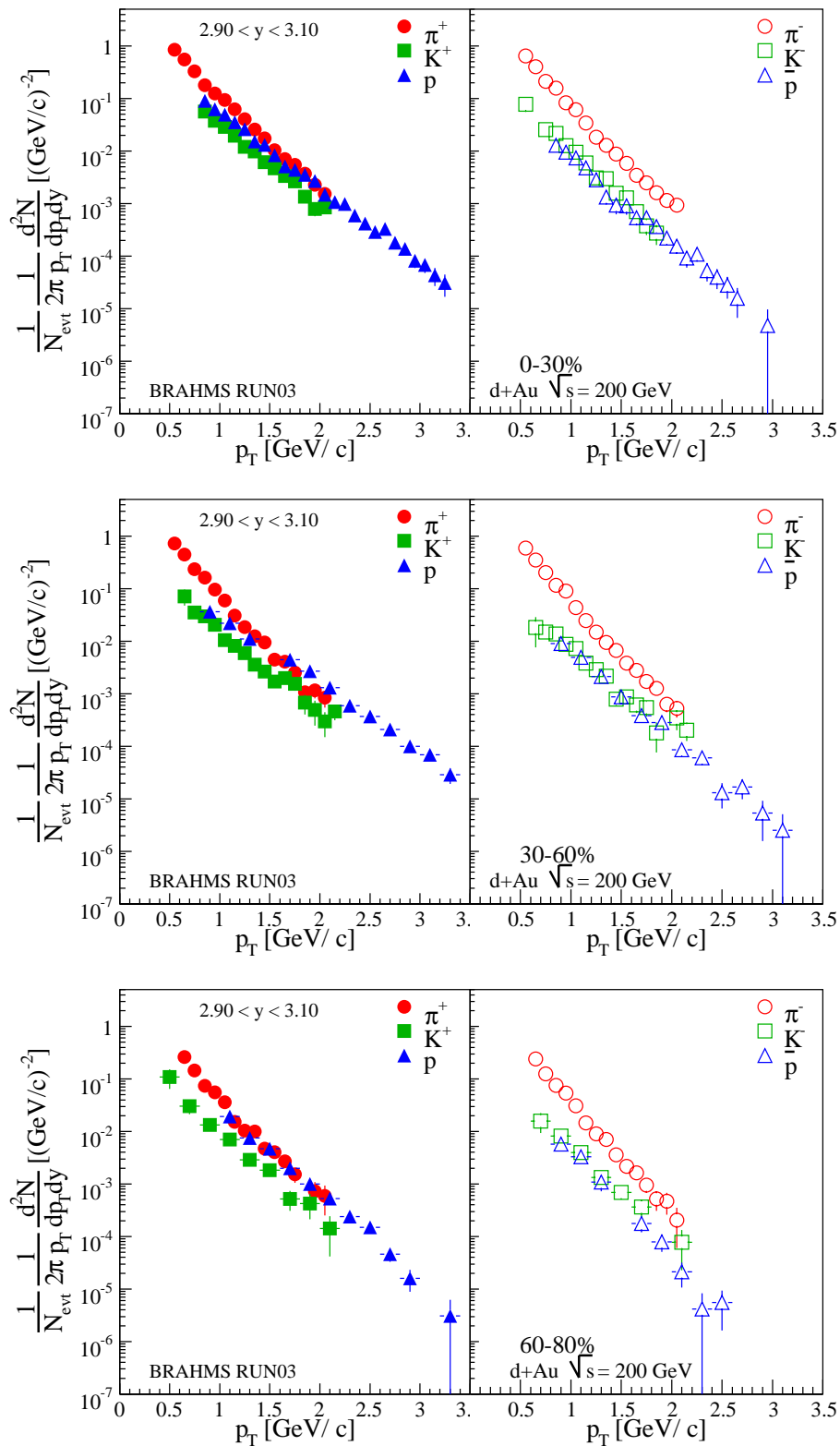


Figure 5.6: Spectra of π^\pm , K^\pm and $p(\bar{p})$ at rapidity $y = 3$ in d+Au collisions for centralities 0-30%, 30-60%, 60-80%.

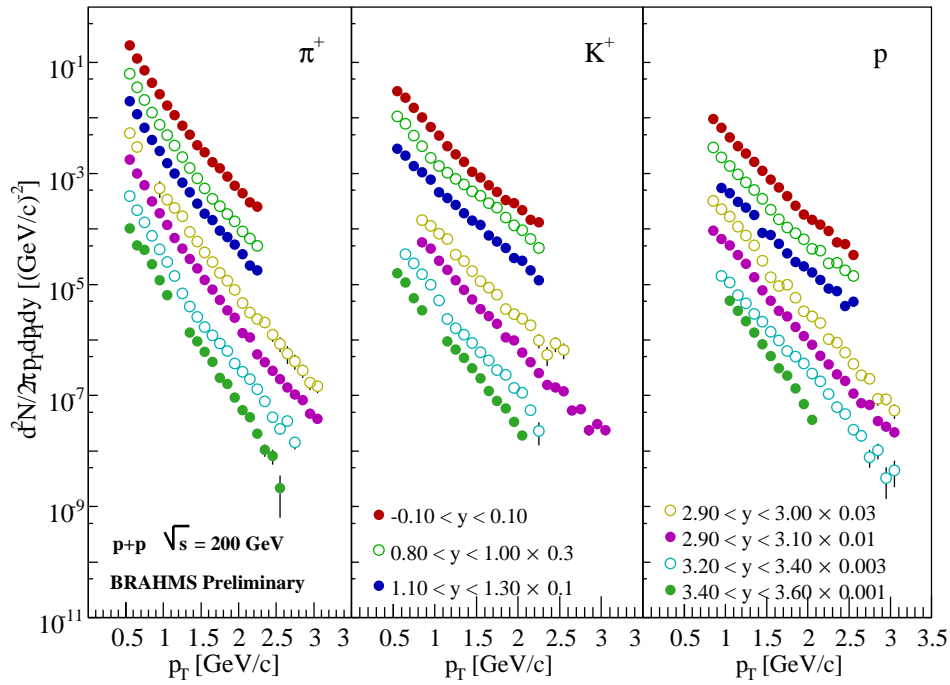


Figure 5.7: Spectra for positive hadrons in $p+p$ collisions at $\sqrt{s} = 200$ GeV, scaled by factors which are given in the figure.

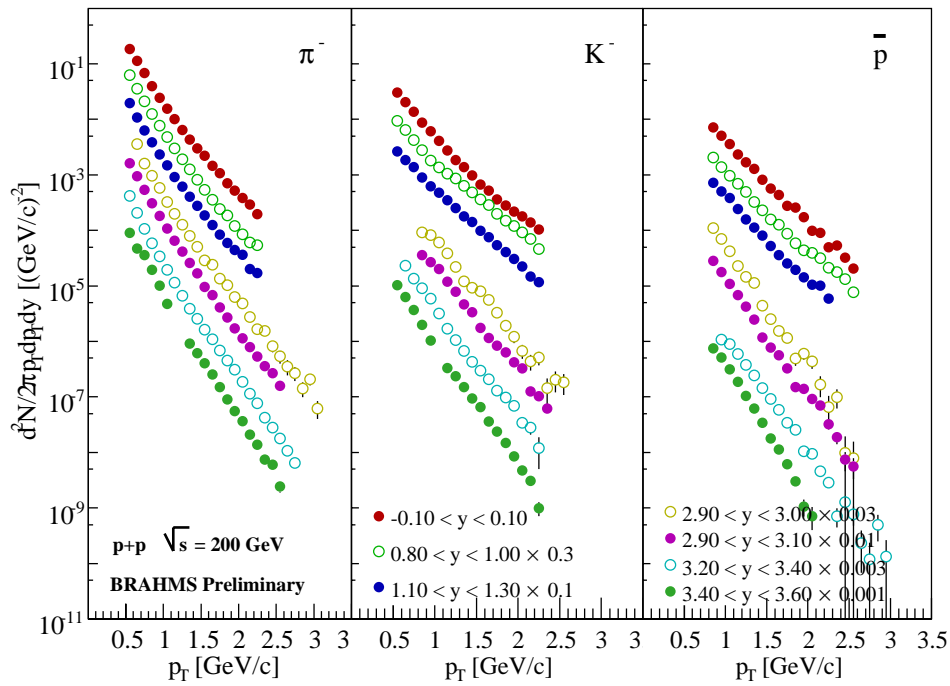


Figure 5.8: Spectra for negative hadrons in $p+p$ collisions at $\sqrt{s} = 200$ GeV, scaled by factors which are given in the figure.

ratios are rather constant with p_T . Going to forward rapidities, the K^-/K^+ and \bar{p}/p ratios decrease dramatically, and they also have a transverse momentum dependence.

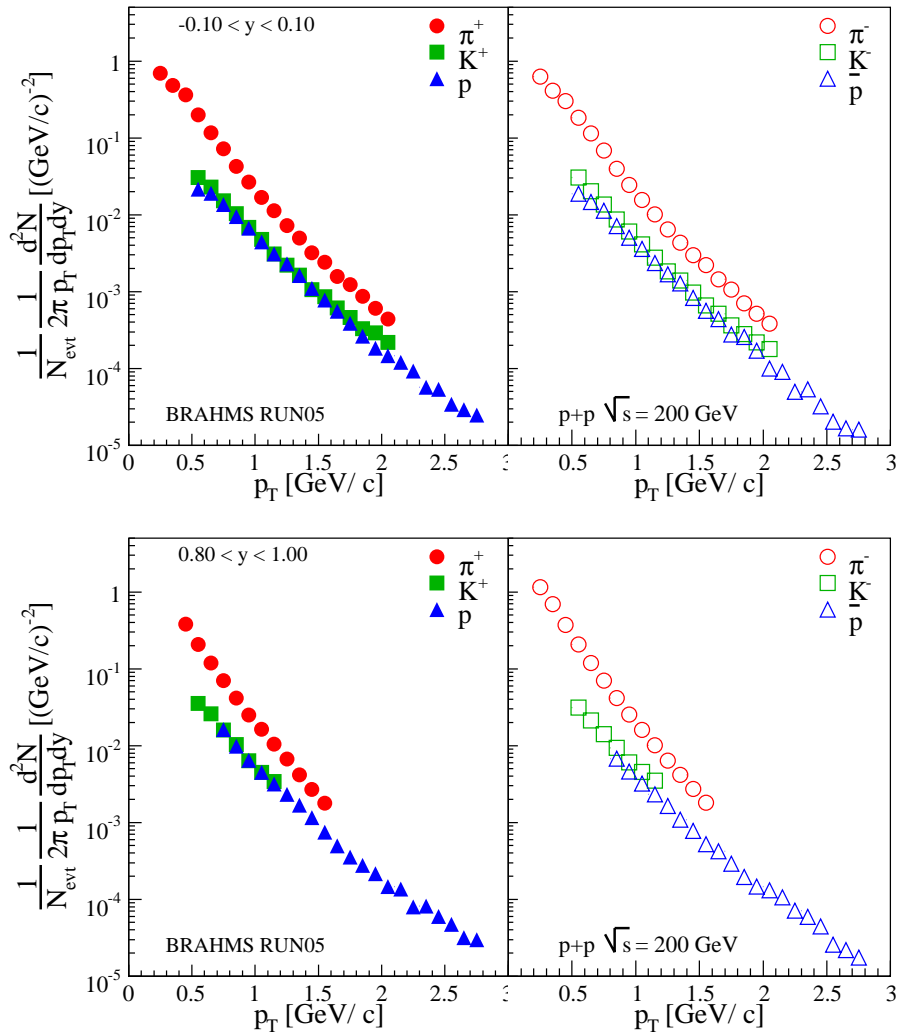


Figure 5.9: Spectra of π^\pm , K^\pm and $p(\bar{p})$ at mid-rapidity $y = 0$ and 1 in $p+p$ collisions

The \bar{p}/p ratios at forward rapidities are as low as 10%.

5.2.2 Unlike-particle ratios

Unlike-particle ratios K/π and p/π versus transverse momentum p_T are presented in this subsection for both d+Au and p+p collisions at $\sqrt{s_{NN}} = 200$ GeV.

K/π ratios

Figure 5.14 shows K/π ratios at rapidity $y = 0$ and $y = 3$ in minimum bias d+Au collisions compared to those in p+p collisions at the same rapidities. There is little difference between the results in p+p collisions and the d+Au collisions. Figure 5.15 shows K/π ratios at rapidity $y = 0$ and $y = 3$ in d+Au collisions within different centralities, (0-30%, 30-60% and 60-80%). There is no centrality dependence of K/π ratios in d+Au collisions.

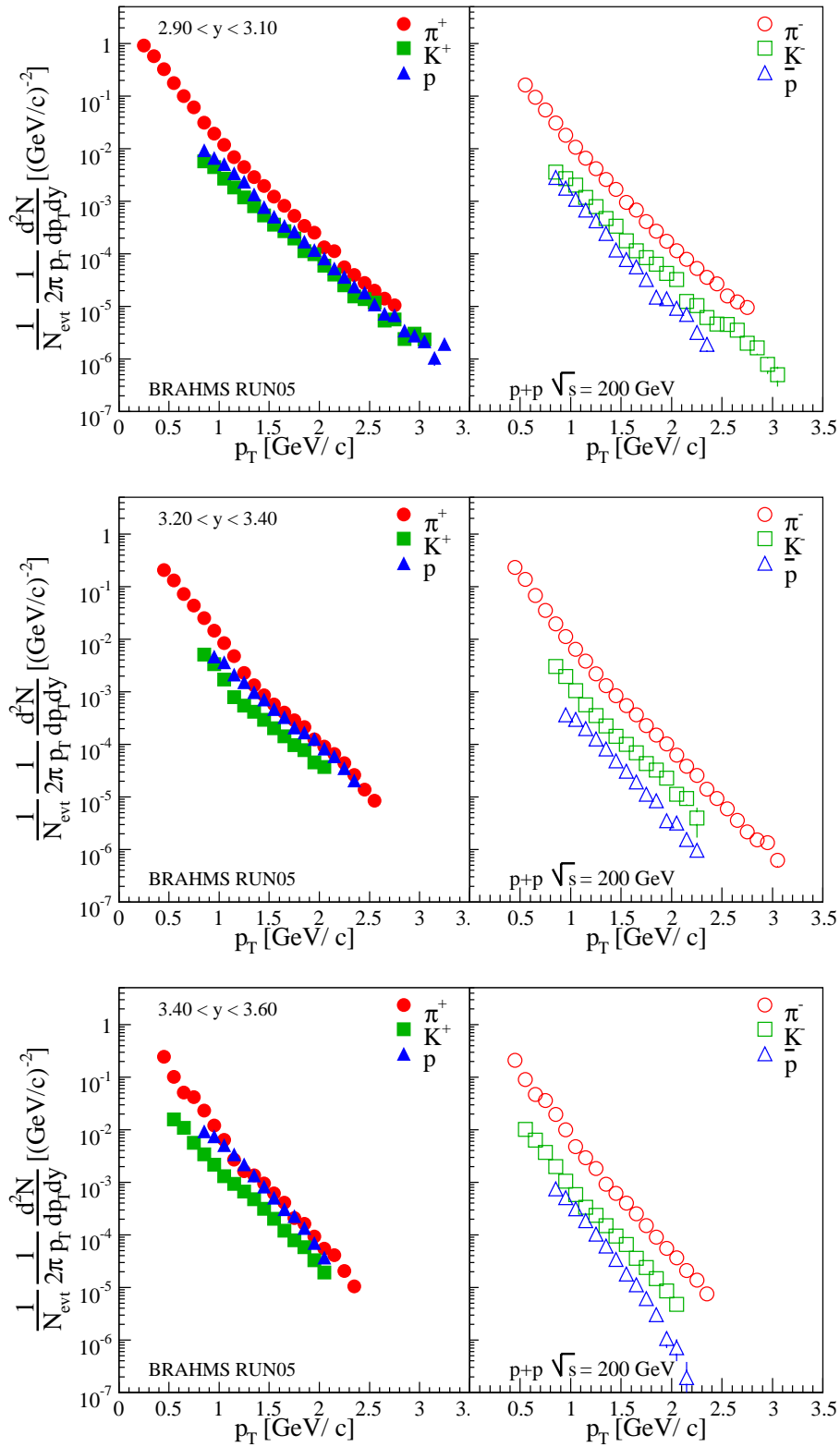


Figure 5.10: Spectra of π^\pm , K^\pm and $p(\bar{p})$ at forward rapidity $y = 3, 3.3$ and 3.5 in $p+p$ collisions at $\sqrt{s} = 200$ GeV.

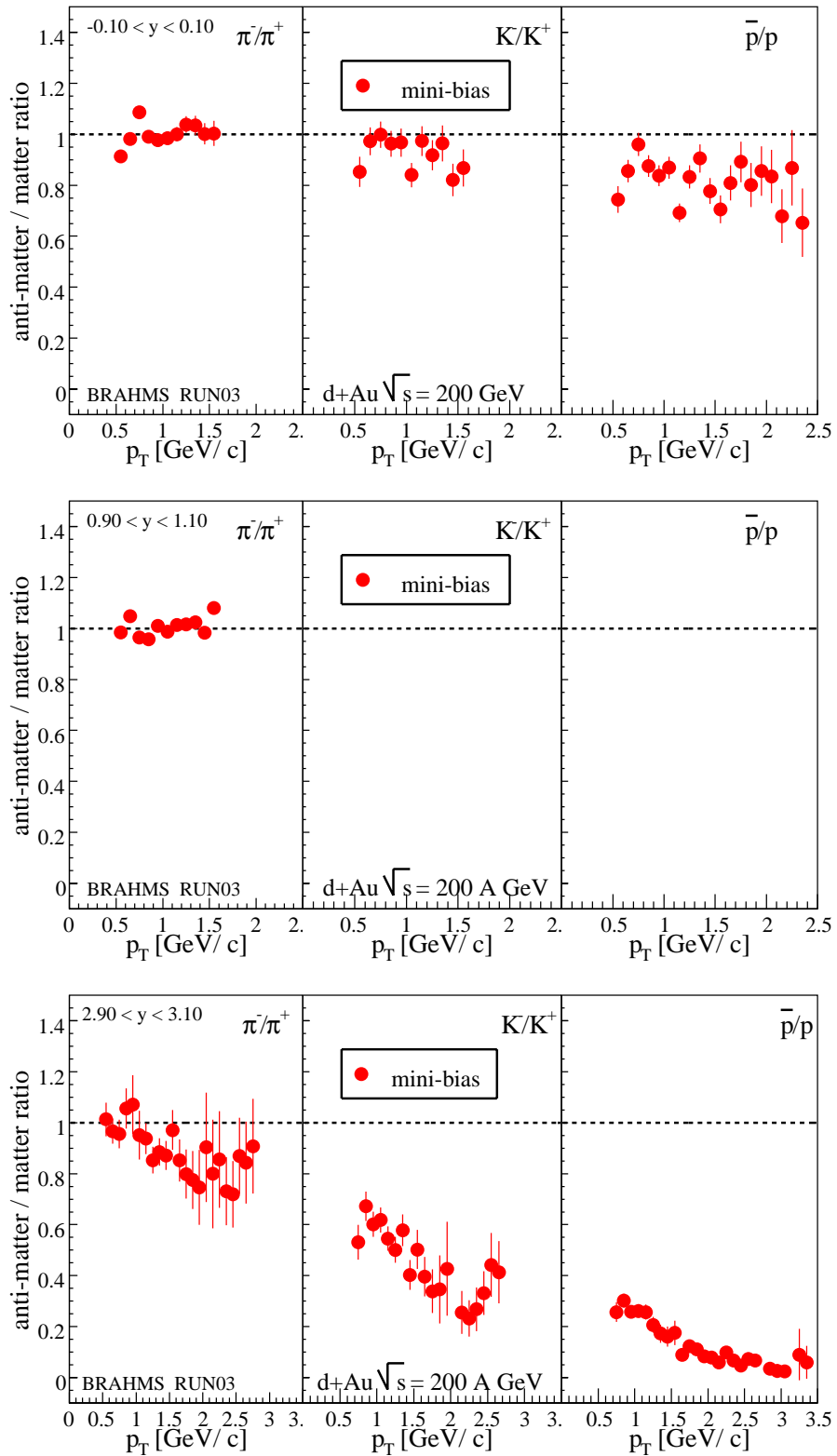


Figure 5.11: Like-particle ratios (π^-/π^+ , K^-/K^+ , and \bar{p}/p) at rapidities $y = 0, 1$ and 3 in minimum bias $d+Au$ collisions

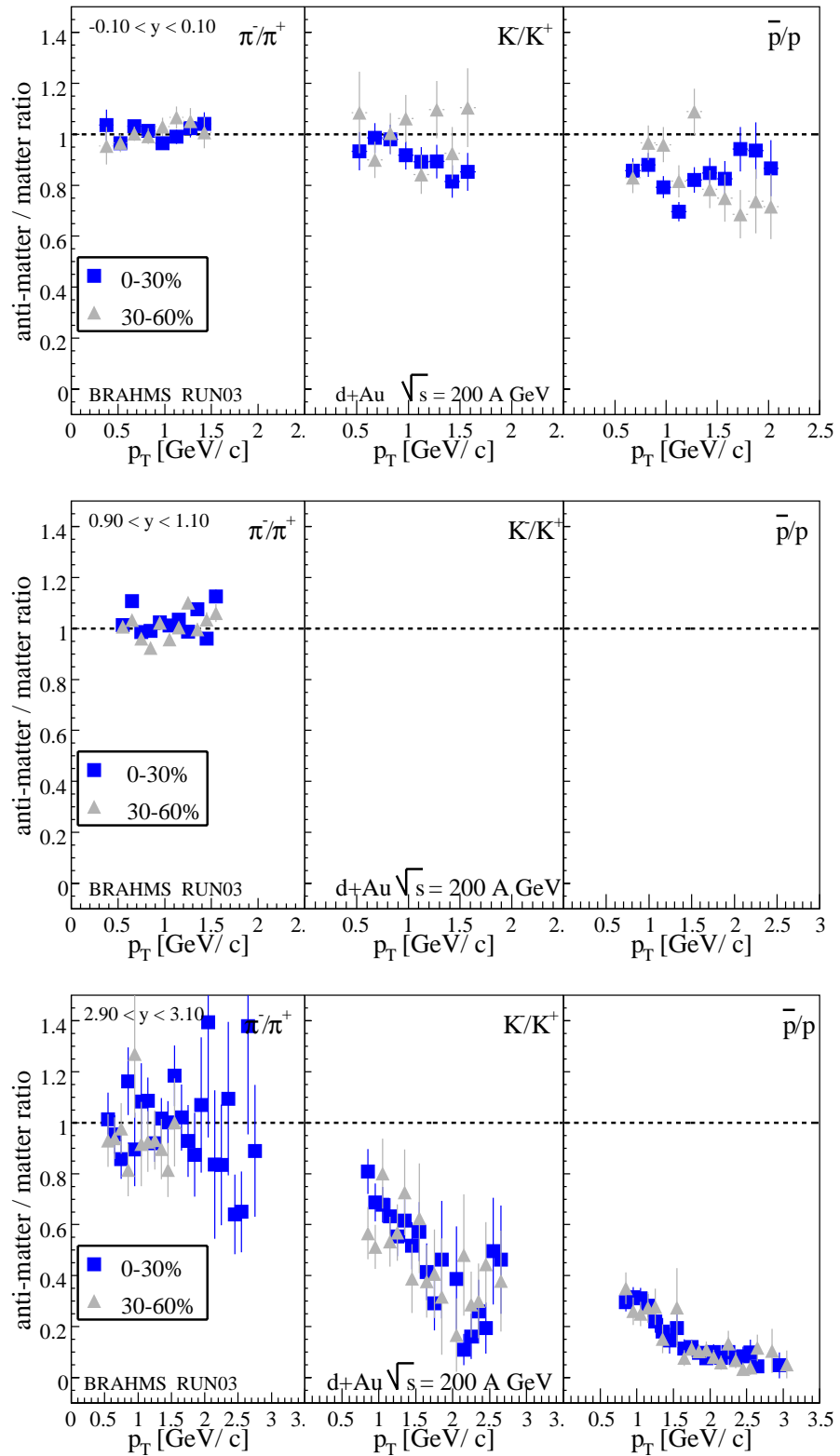


Figure 5.12: Like-particle ratios (π^-/π^+ , K^-/K^+ , and \bar{p}/p) at rapidities $y = 0, 1$ and 3 in $d+Au$ collisions in centrality classes 0-30% and 30-60%.

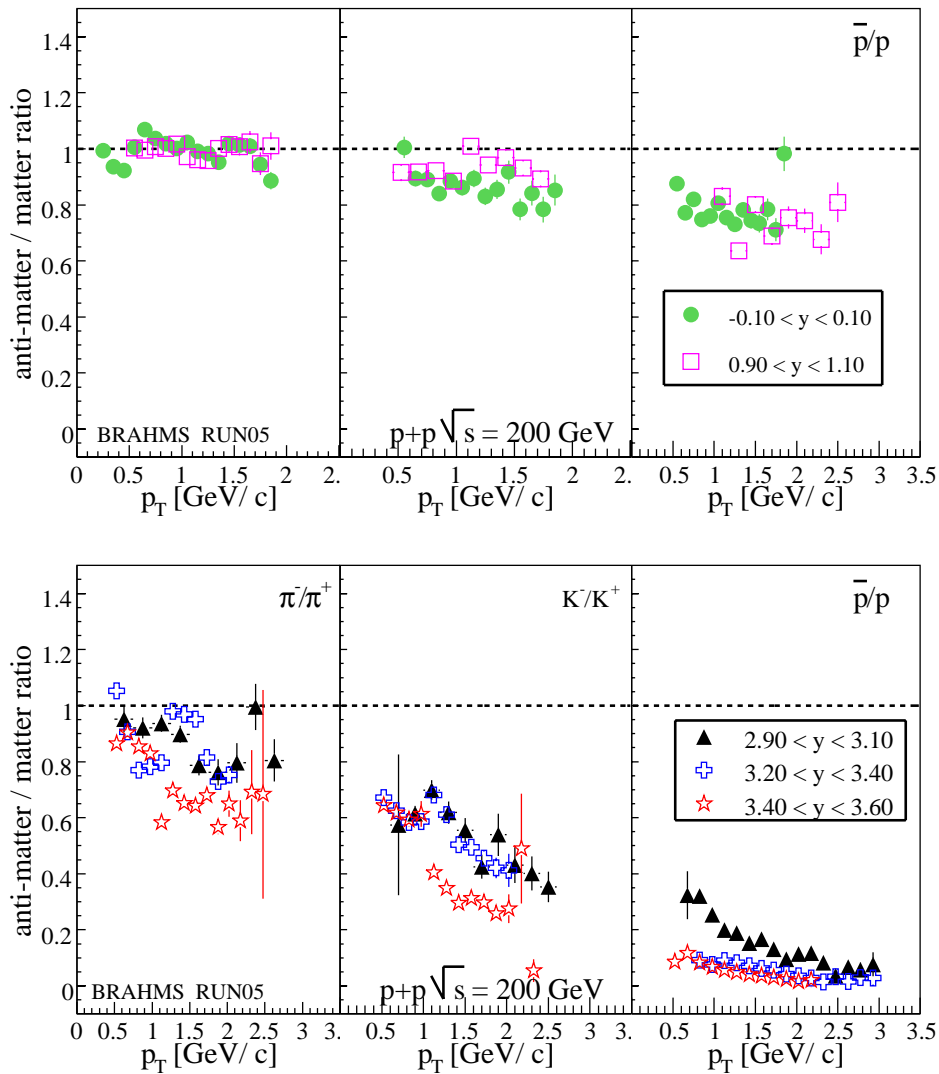


Figure 5.13: Like-particle ratios at/near mid-rapidity (upper panel) and forward rapidities (lower panel) in $p+p$ collisions.

Figure 5.16 shows K/π ratios at rapidity $y = 0, 1, 3, 3.3, 3.5$ in $p+p$ collisions at $\sqrt{s} = 200$ GeV. All ratios at all rapidities increase slightly with p_T for both systems.

p/π ratios

Figure 5.17 shows p/π ratios at rapidity $y = 0, 1.0,$ and 3 in minimum bias $d+Au$ collisions, compared to those in $p+p$ collisions at the same rapidities. There is no difference between the antiproton-to-pion ratios in $p+p$ collisions and the $d+Au$ collisions while the proton-to-pion ratios seem to be different for the two systems. Note that the protons start to dominate at high p_T at forward rapidities. Figure 5.18 shows p/π ratios at rapidity $y = 0, 1.0, 3$ in $d+Au$ collisions for different centralities (0-30%, 30-60% and 60-80%). There is no centrality dependence of p/π ratios in $d+Au$ collisions.

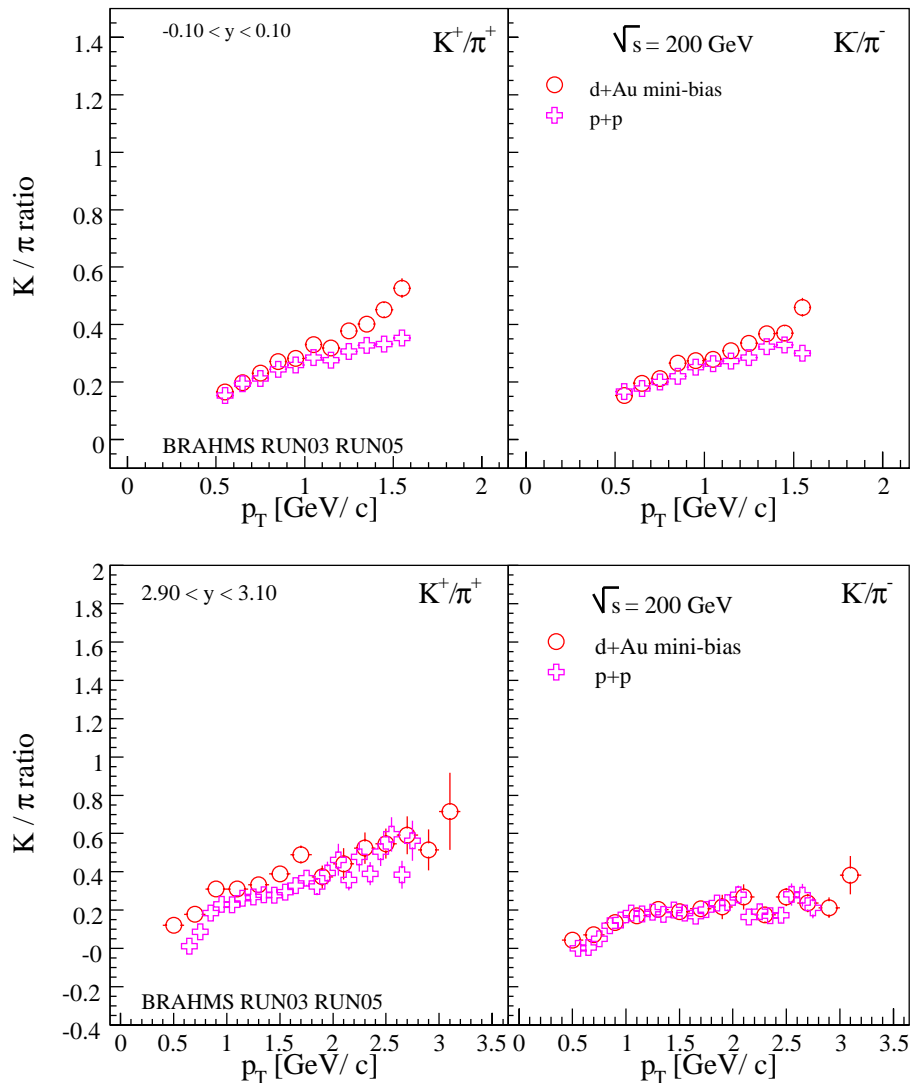


Figure 5.14: K/π ratios at rapidity $y = 0$ and $y = 3$ in $d+Au$ collisions compared to those in $p+p$ collisions at the same rapidities.

Figure 5.19 shows p/π ratios at/near mid-rapidity ($y = 0, 1$) and at forward rapidities ($y = 3, 3.3$ and 3.5) in $p+p$ collisions at $\sqrt{s} = 200$ GeV. At mid-rapidity, both the positive and negative p/π ratios are similar (upper panel). At forward rapidities the positive and negative p/π ratios behave very differently; the negative ratio is much smaller than that of the positive and constant with p_T .

5.3 Rapidity densities

Rapidity densities dN/dy are obtained by integrating the particle spectra over the full p_T range. Due to the lack of data at very low and high p_T , spectra are fitted by certain functions. The fit function is then used to extrapolate to regions outside the acceptance. For the fit, a power law function in p_T (equation 4.24), an exponential

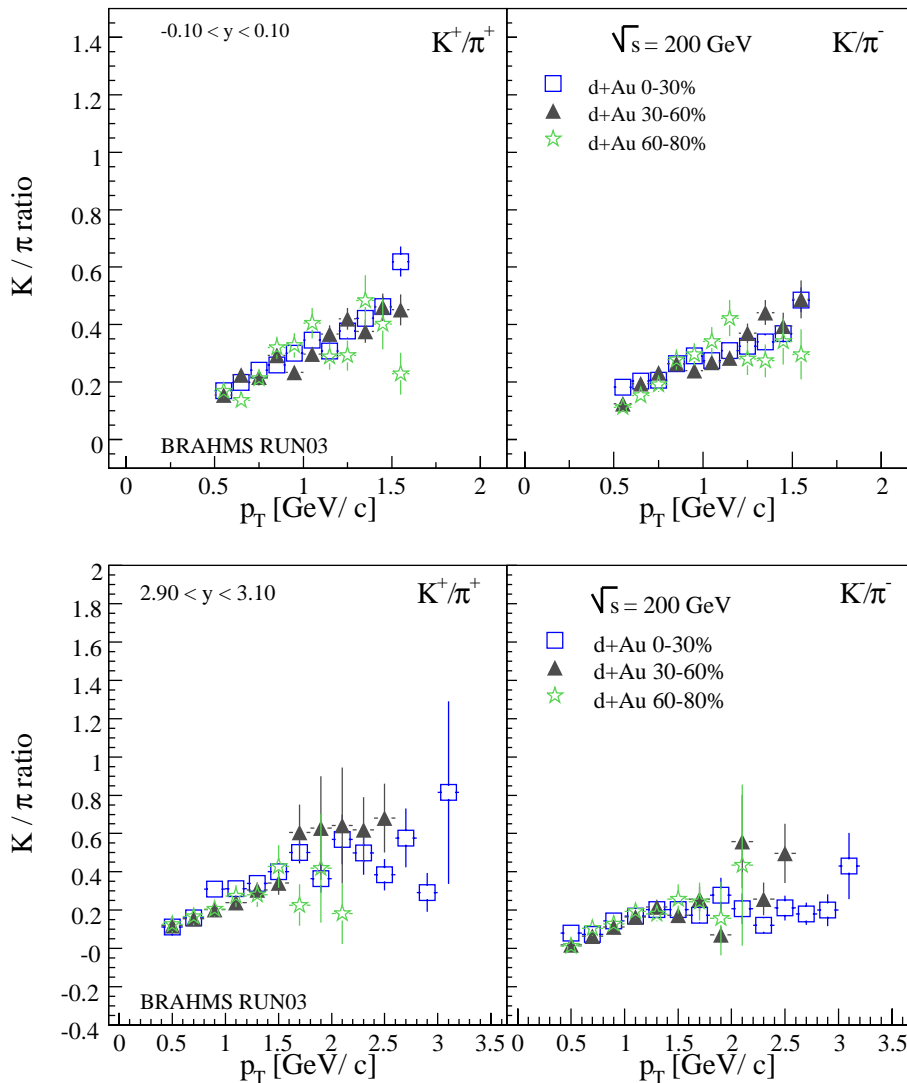


Figure 5.15: K/π ratios at rapidity $y = 0$ and $y = 3$ in $d+Au$ collisions within different centralities (0-30%, 30-60% and 60-80%).

function in m_T (equation 4.26) and a Boltzmann function (equation 4.27) are used to extract the yield of pion, kaon and protons correspondingly (see details in Chapter 4).

The results are shown in figures 5.20 and 5.21, in which (a)-(c) show the results for pions, kaons and protons respectively from p+p collisions and from d+Au collisions.¹

All particle yields, except the protons in p+p collisions at very forward rapidity, are highest at mid-rapidity and decrease when going to larger rapidities. All p_T -integrated like-particle ratios decrease with increasing rapidity in p+p reactions, while π^-/π^+ ratio stays at 1 in d+Au collisions.

¹Systematic errors due to different fit functions used in the extrapolation are shown in figures 5.20 and 5.21 as error bars for kaons and protons, but not for pions because only the power law function gives a reasonable interpretation of the spectra.

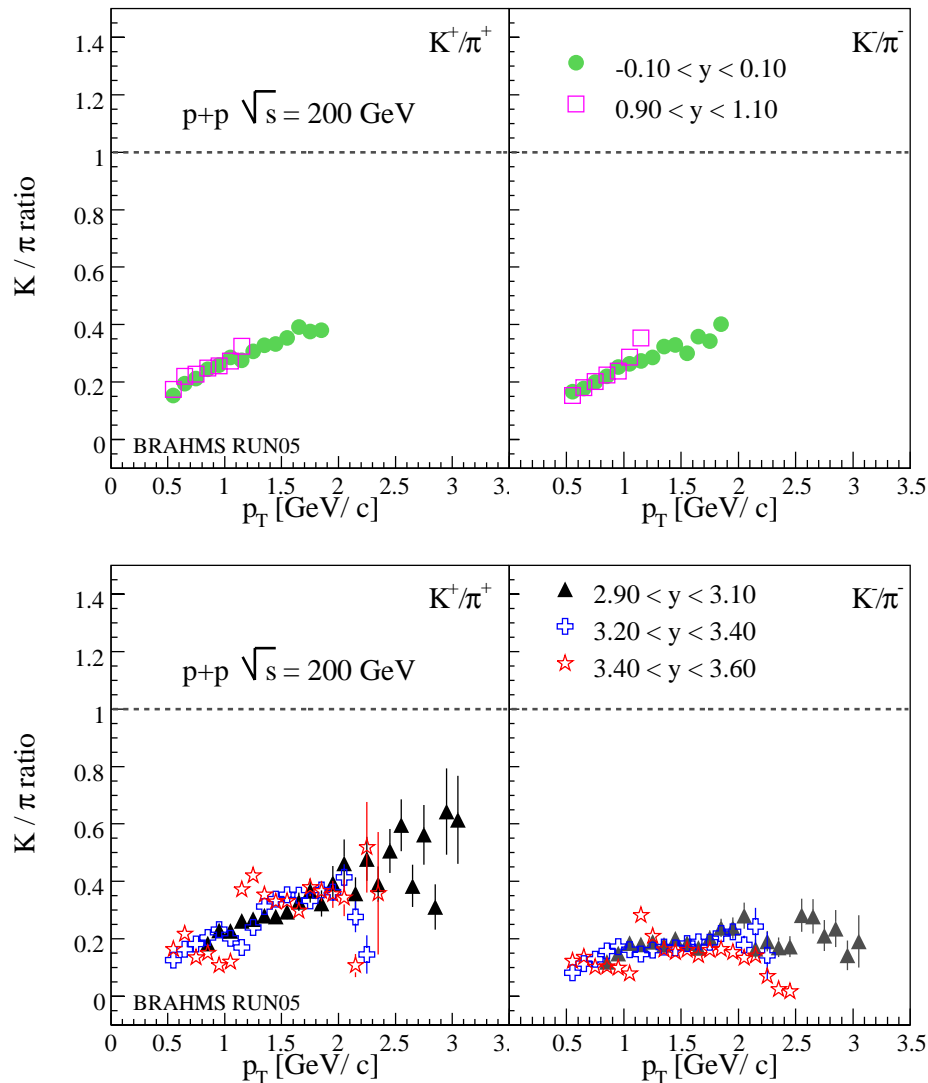


Figure 5.16: K/π ratios at mid-rapidity (upper panel) and forward rapidity (bottom panel) in $p+p$ collisions.

5.4 Mean transverse momentum $\langle p_T \rangle$

Figure 5.22 shows the rapidity dependence of the $\langle p_T \rangle$ in d+Au collisions at $\sqrt{s_{NN}} = 200$ GeV. Subfigure (a) shows the $\langle p_T \rangle$ for charged hadrons in minimum bias collisions, (b) and (c) show that for positive and negative hadrons within different centrality classes respectively. Asymmetric errors show the systematic errors coming from the different extrapolations using different fit functions. There is no significant centrality or rapidity dependence. Figure 5.23 shows the rapidity dependence of the $\langle p_T \rangle$ in $p+p$ collisions at $\sqrt{s} = 200$ GeV. Asymmetric errors shows the systematic errors coming from the different extrapolations using different fit functions. There is no strong rapidity dependence. In general, the $\langle p_T \rangle$ is larger for heavier hadrons in both system, and $\langle p_T \rangle$ in d+Au collisions is slightly larger than in $p+p$ collisions.

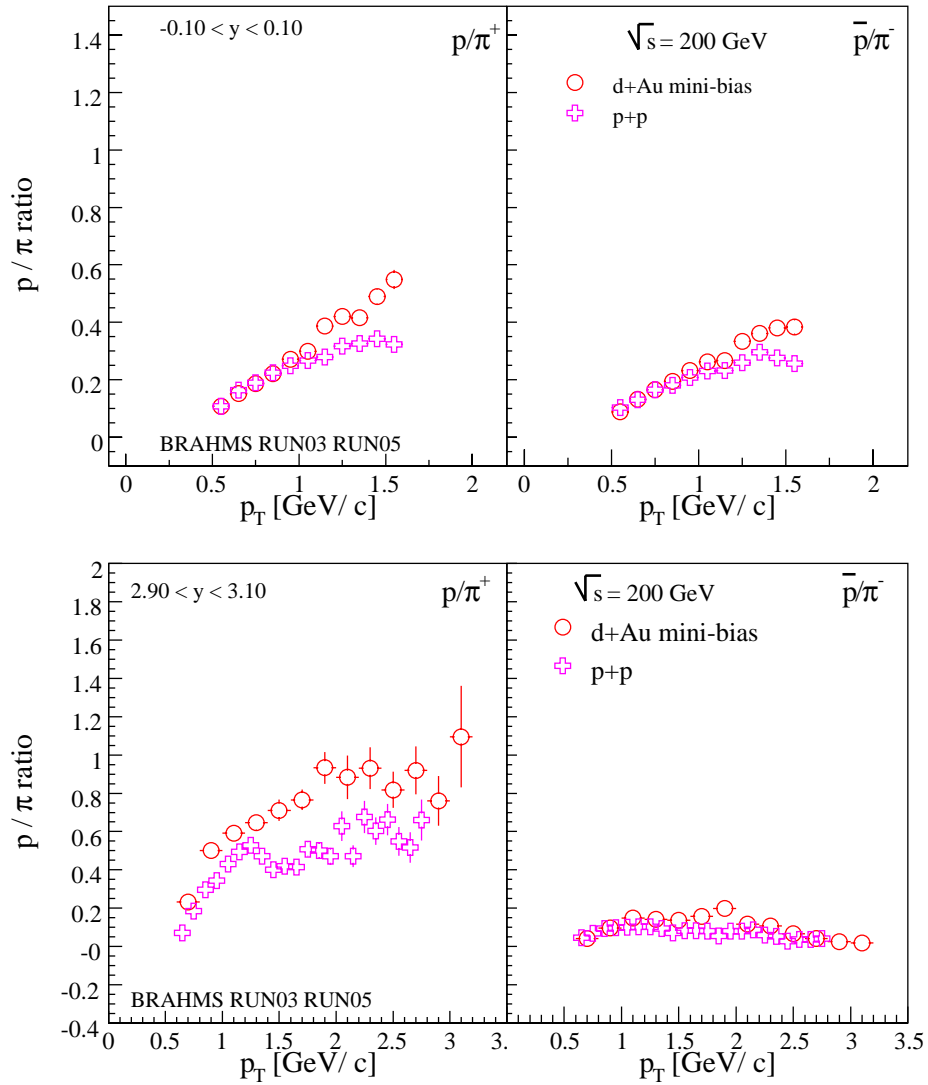


Figure 5.17: p/π ratios at rapidity $y = 0$ and $y = 3$ in minimum bias $d+Au$ collisions compared to those in $p+p$ collisions at the same rapidities.

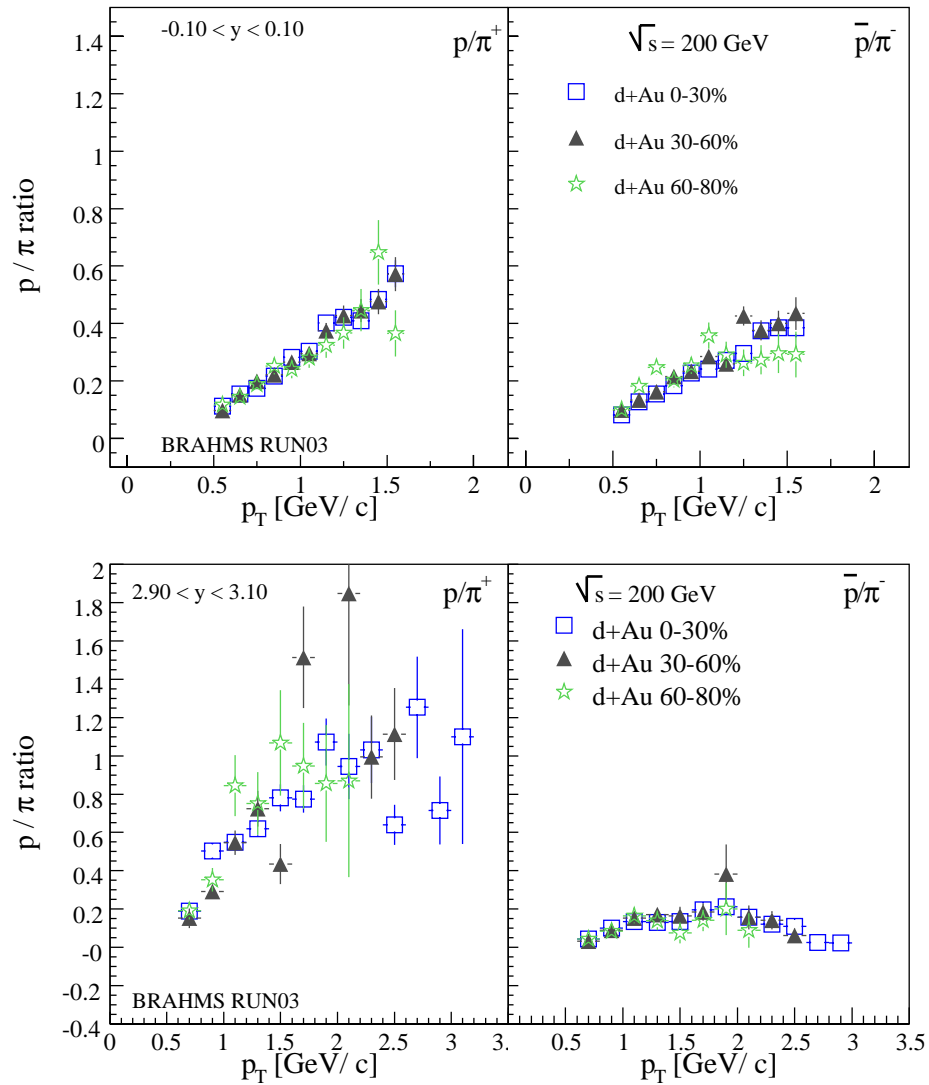


Figure 5.18: p/π ratios at rapidity $y = 0$ and $y = 3$ in $d+Au$ collisions within different centralities.

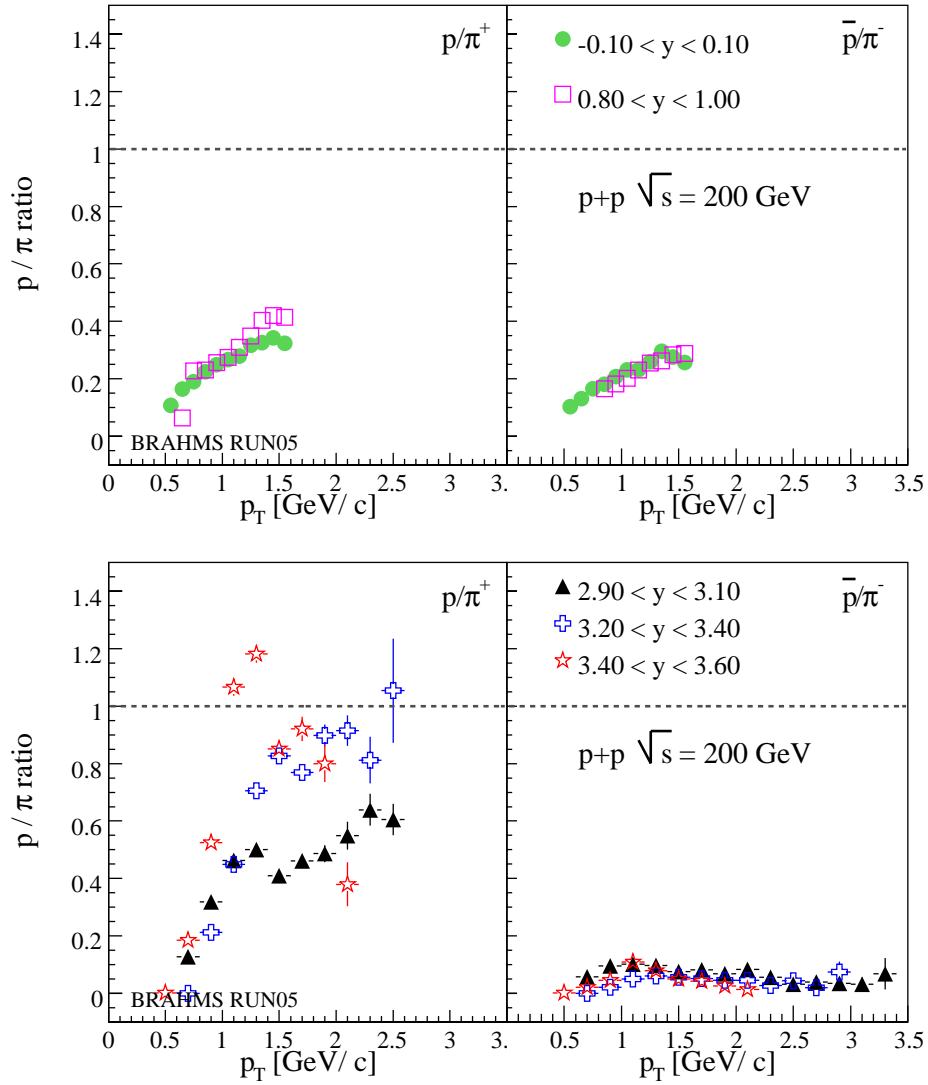
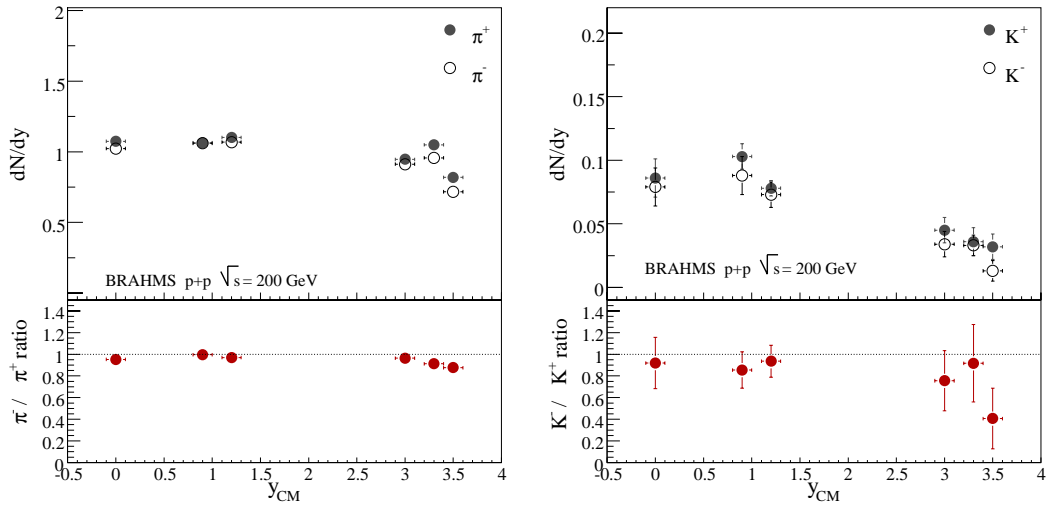
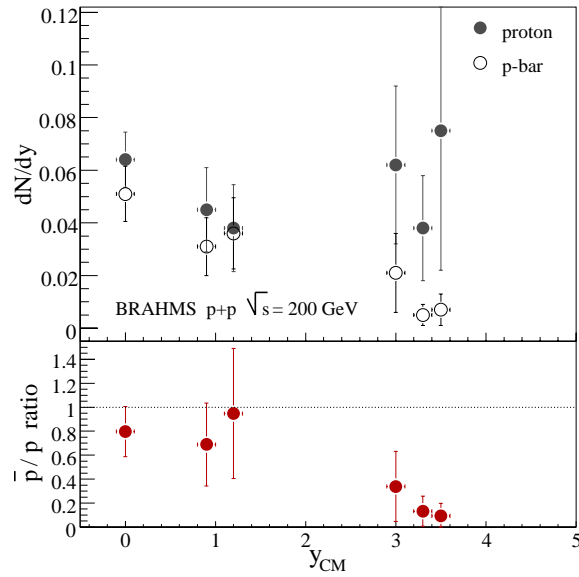


Figure 5.19: p/π ratios at/near mid-rapidity (upper panel) and forward rapidities (bottom panel) in $p+p$ collisions.

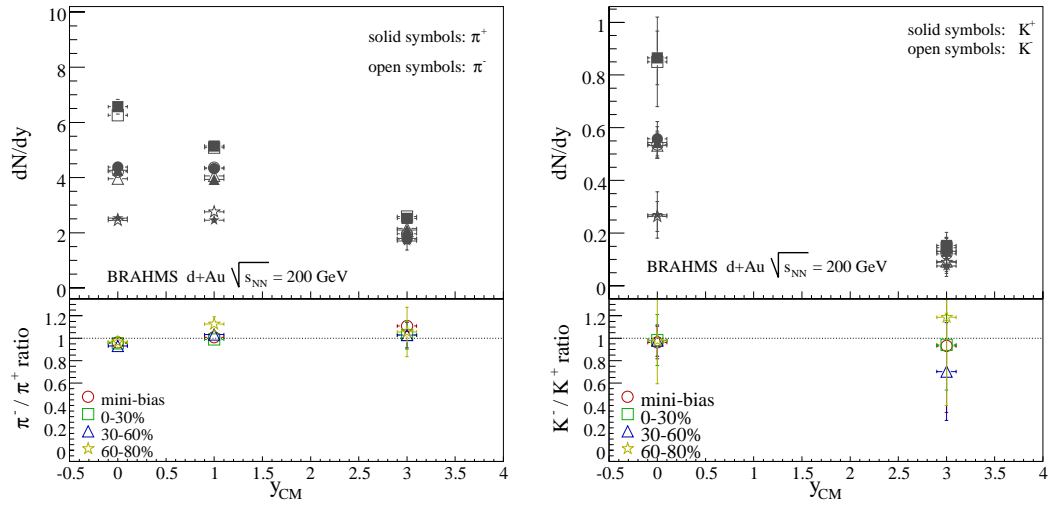


(a) Pion yields and π^-/π^+ ratio (p_T integrated) versus rapidity in $p+p$ collisions (b) Kaon yield and K^-/K^+ ratio (p_T integrated) versus rapidity in $p+p$ collisions

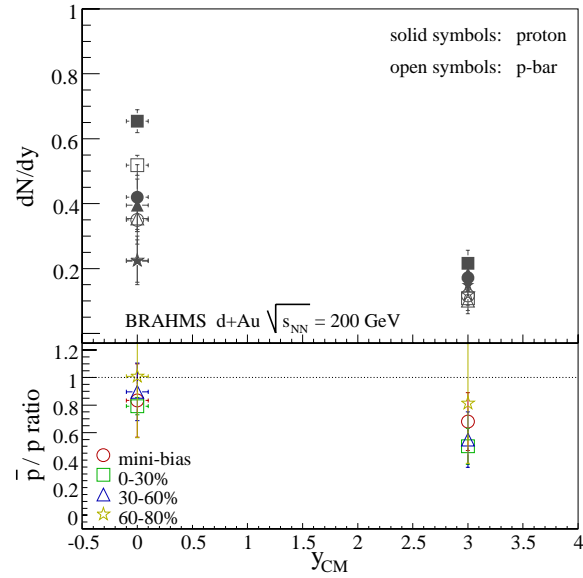


(c) Proton yields and \bar{p}/p ratio (p_T integrated) versus rapidity in $p+p$ collisions

Figure 5.20: Rapidity densities and p_T integrated particle ratios versus rapidity in $p+p$ collisions at $\sqrt{s} = 200$ GeV.



(a) Pion yields and π^-/π^+ ratio (p_T integrated) versus rapidity in d+Au collisions (b) Kaon yields and K^-/K^+ ratio (p_T integrated) versus rapidity in d+Au collisions



(c) Proton yields and \bar{p}/p ratio (p_T integrated) versus rapidity in d+Au collisions

Figure 5.21: Rapidity densities and p_T integrated particle ratios versus rapidity in d+Au collisions at $\sqrt{s_{NN}} = 200$ GeV.

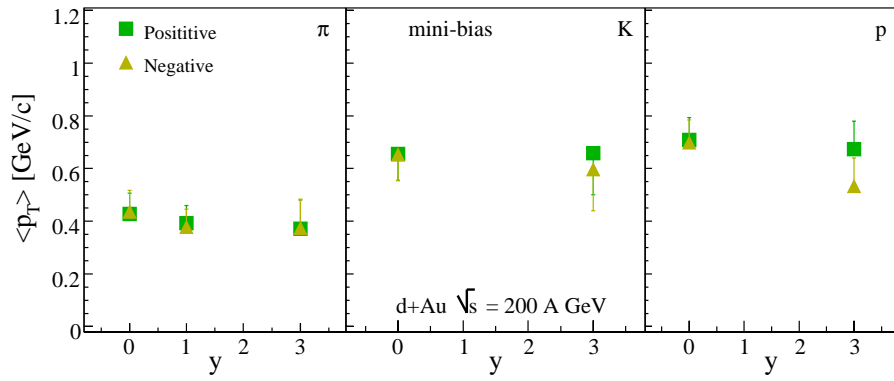
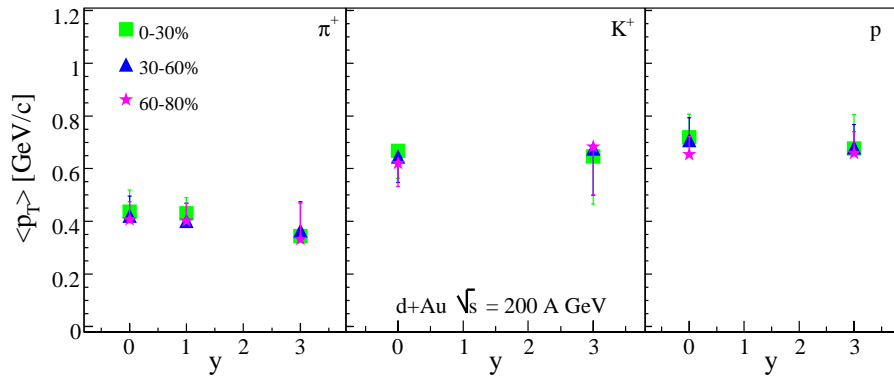
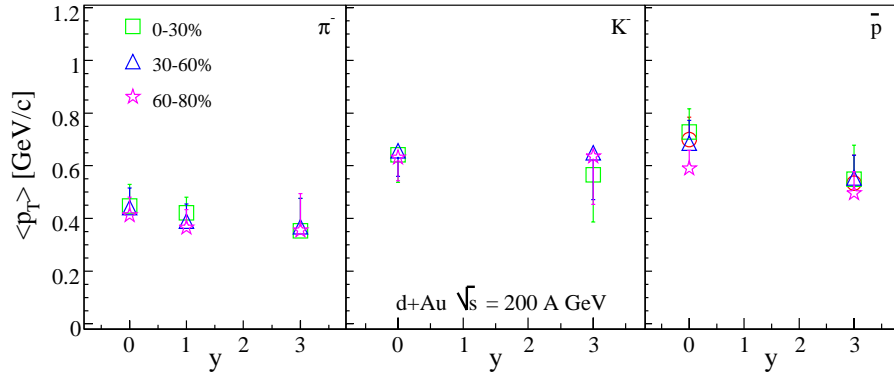
(a) $\langle p_T \rangle$ for charged hadrons in minimum bias d+Au collisions(b) Centrality dependence of $\langle p_T \rangle$ for positive hadrons in d+Au collisions(c) Centrality dependence of $\langle p_T \rangle$ for negative hadrons in d+Au collisions

Figure 5.22: $\langle p_T \rangle$ in d+Au collisions vs rapidity. Systematic errors are shown as asymmetric error bars, which come from the different extrapolations using different fit functions.

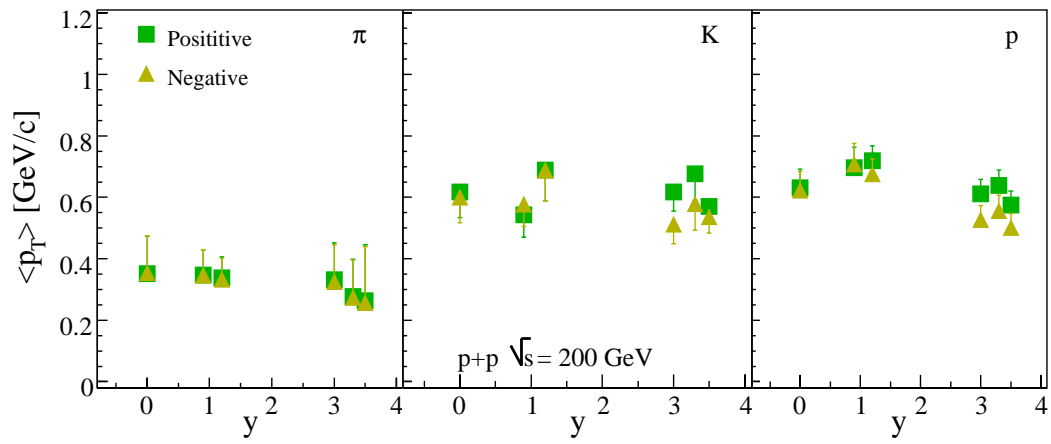


Figure 5.23: $\langle p_T \rangle$ for charged hadrons in $p+p$ collisions at $\sqrt{s} = 200$ GeV.

Chapter 6

Nuclear Modification Factors

In this chapter, nuclear modification factors in d+Au collisions at $\sqrt{s_{NN}} = 200$ GeV are presented. As introduced in Chapter 1, nuclear modification factors for identified particles in d+Au collisions may reveal the properties of the cold nuclear matter and may shed light on initial state effects such as parton saturation, nuclear shadowing and the Cronin effect. By studying the effects in d+Au collisions one can distinguish between effects due to the initial conditions in central Au+Au collisions and final state effects like jet quenching in the deconfined matter created in these reactions.

In this thesis the centrality and rapidity dependence of the nuclear modification factors are presented, using the reference spectra from p+p collisions measured by BRAHMS in RUN V, which have been presented in Chapter 5. The nuclear modification factor is defined as

$$R_{\text{dAu}} = \frac{1}{\langle N_{\text{coll}}^{\text{centrality}} \rangle} \cdot \frac{d^2 N^{\text{dAu}}/dp_T dy}{d^2 N^{\text{NN}}/dp_T dy}. \quad (6.1)$$

R_{dAu} is calculated by equation 6.1, in which the average number of collisions for different centrality classes $\langle N_{\text{coll}}^{\text{MB}} \rangle = 7.2 \pm 0.3$, $\langle N_{\text{coll}}^{0-30\%} \rangle = 12.6 \pm 0.3$, $\langle N_{\text{coll}}^{30-60\%} \rangle = 7.2 \pm 0.5$ and $\langle N_{\text{coll}}^{60-80\%} \rangle = 3.3 \pm 0.4$ are used. Note that the numbers of collisions in minimum bias and in semi-peripheral collisions are identical. These numbers are calculated by a Monte Carlo simulation [78] based on theoretical models of nuclear collisions, from which the event centrality is determined. The Glauber Model [57] is used for all RHIC experiments. Systematic uncertainties are introduced by the simulation, which are the main contribution to the systematic error of the nuclear modification factors. Most of the systematic errors related to the construction of the spectra from different settings and to efficiency corrections cancel each other because both data sets are recorded by identical detectors and identical spectrometer settings. Figure 6.1 shows the rapidity dependence of R_{dAu} for charged pions, kaons and protons in minimum bias d+Au collisions. Isospin effects due to the isospin-asymmetric p+p reference are reduced by adding particles and antiparticles. At mid-rapidity R_{dAu} is above 1 for p_T greater than approximately 1 GeV/c and the enhancement increases with p_T at least for p (\bar{p}) (subfigure (a)). At forward rapidity (subfigure (c)) the pion curve stays below 1 (pions) or approach 1 at higher p_T . Figure 6.2 shows the centrality dependence of R_{dAu} for charged pions, kaons and protons in d+Au collisions at various rapidities. The dark bands around $R_{\text{dAu}}=1$ on the left plot of each figure indicate the systematic

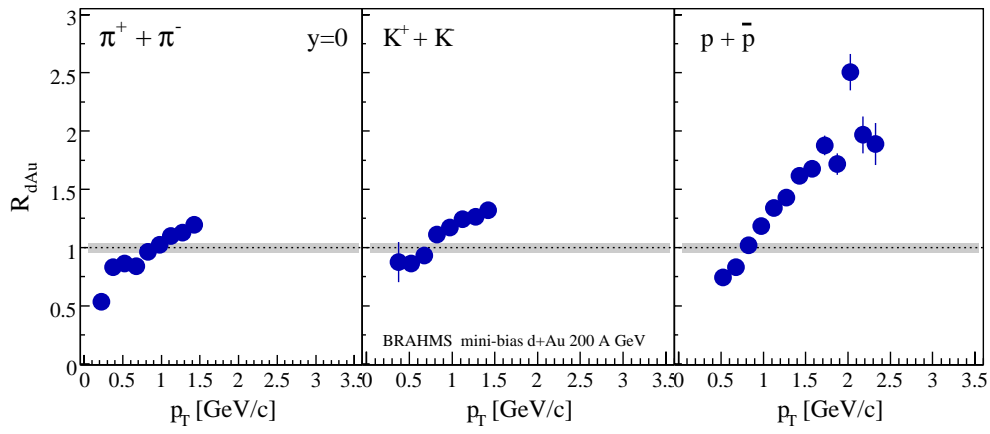
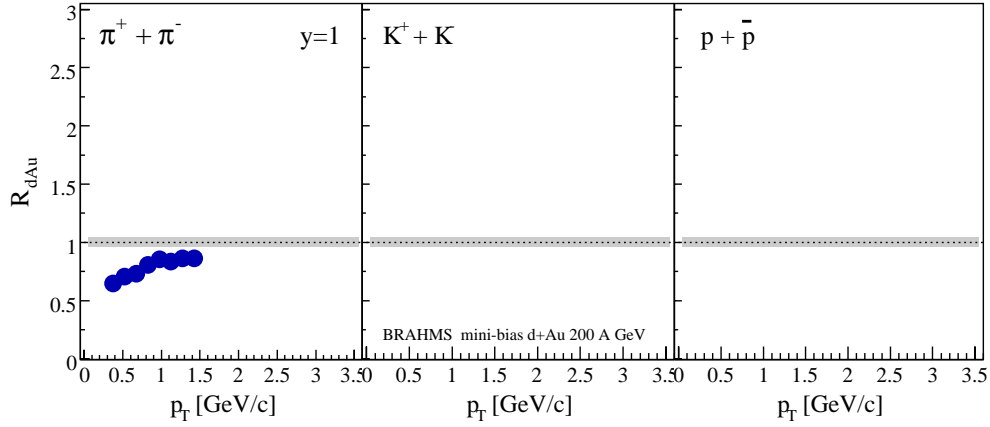
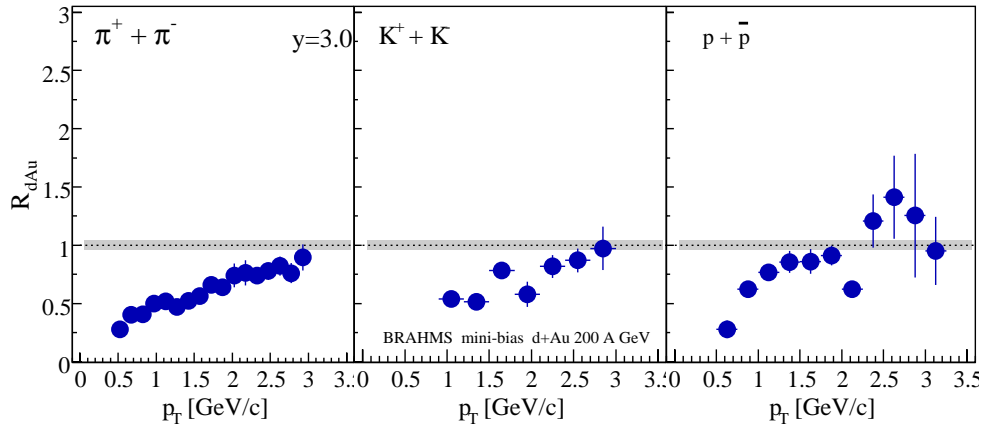
(a) $y = 0$ (b) $y = 1$ (c) $y = 3$

Figure 6.1: Rapidity dependence of R_{dAu} for charged pions, kaons and protons in minimum bias $d+Au$ collisions. Grey bands around $R_{dAu} = 1$ indicate the systematic uncertainties in $\langle N_{coll}^{MB} \rangle$.

uncertainties in $\langle N_{coll} \rangle$ for each centrality class, namely the right band stands for 60-80% peripheral collisions, the middle one for 30-60% semi-central collisions and the left one for 0-30% central collisions. In peripheral collisions, R_{dAu} approaches 1 or is

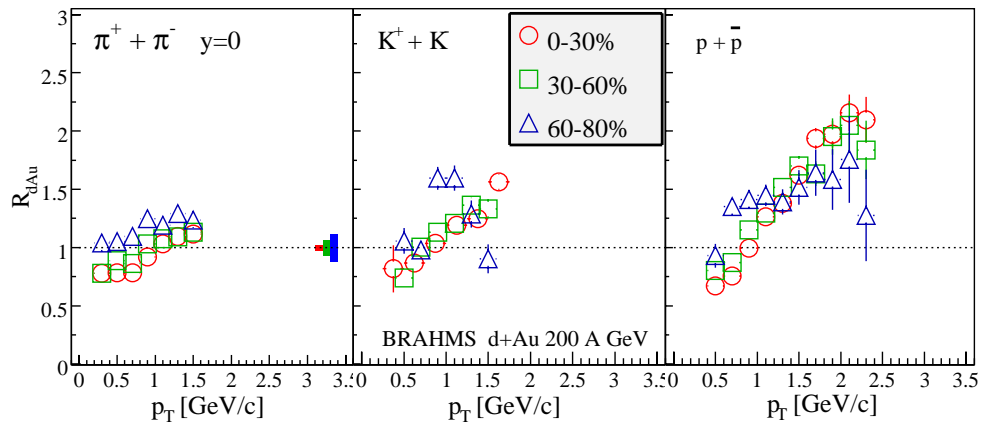
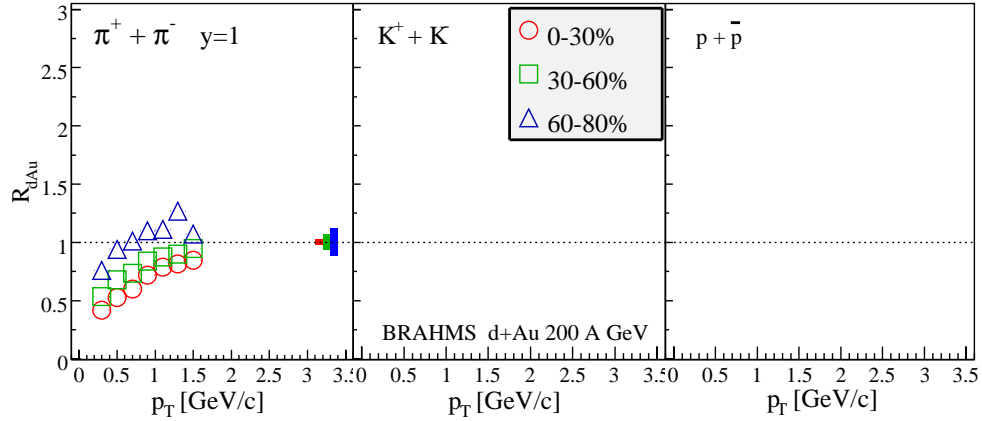
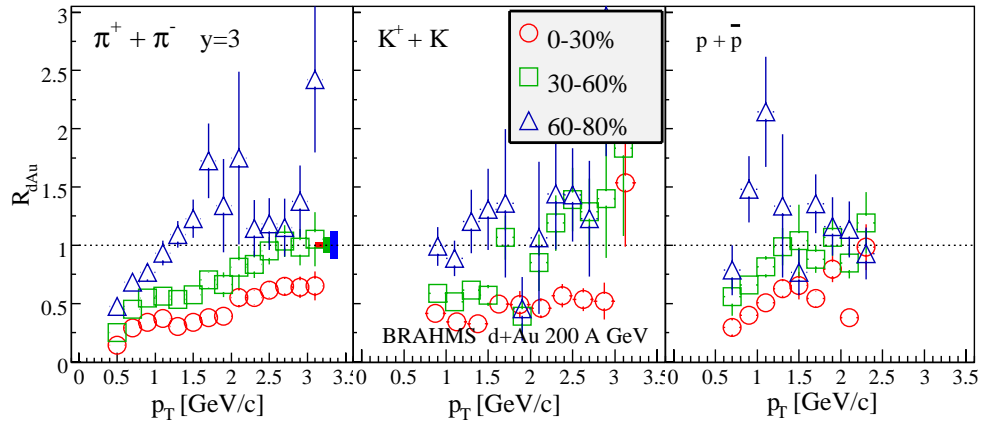
(a) $y = 0$ (b) $y = 1$ (c) $y = 3$

Figure 6.2: Centrality dependence of R_{dAu} for charged pions, kaons and protons in $d+Au$ collisions at rapidity $y=0$, $y=1$ and $y=3$. Systematic uncertainties are shown as dark bands around 1.0 on the left plots in each panel.

above 1 at all rapidities. In central collisions a strong suppression is observed for pions and kaons at forward rapidity (c).

In figure 6.3 subfigure (a) shows that at mid-rapidity $y = 0$, the differences in

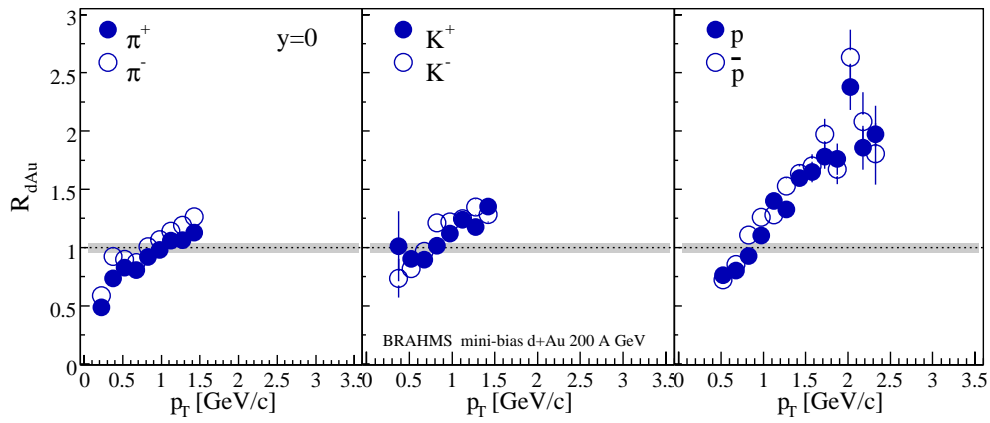
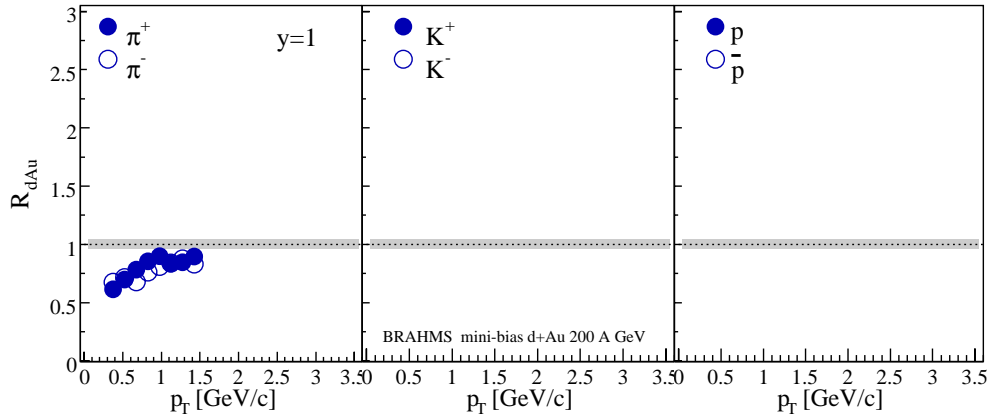
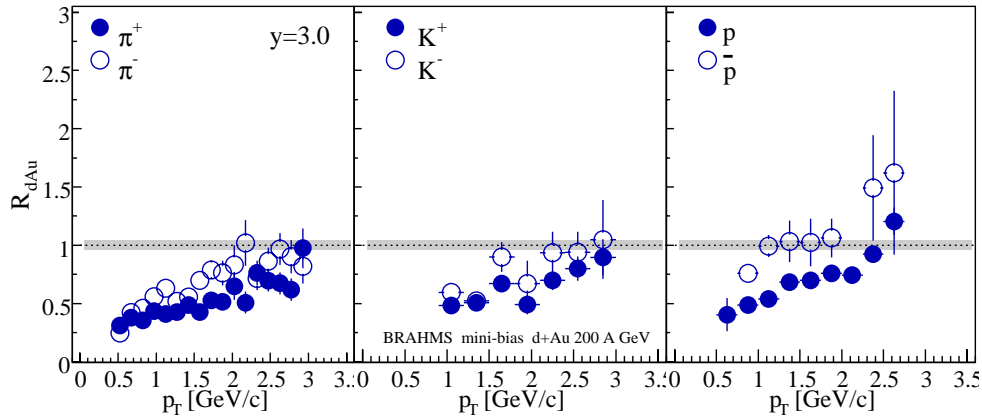
(a) $y = 0$ (b) $y = 1$ (c) $y = 3$

Figure 6.3: R_{dAu} for positive and negative pions and kaons and for protons (anti-protons) in minimum bias d+Au collisions at rapidity $y = 0, 1$ and 3 . Systematic uncertainties are shown as bands around 1.0 in each panel.

R_{dAu} between the positive and negative hadrons are negligible. But at the forward rapidity $y = 3$ (subfigure (c)), the negative hadrons show larger nuclear modification factors than those of the positive ones. These differences may be due to isospin effects.

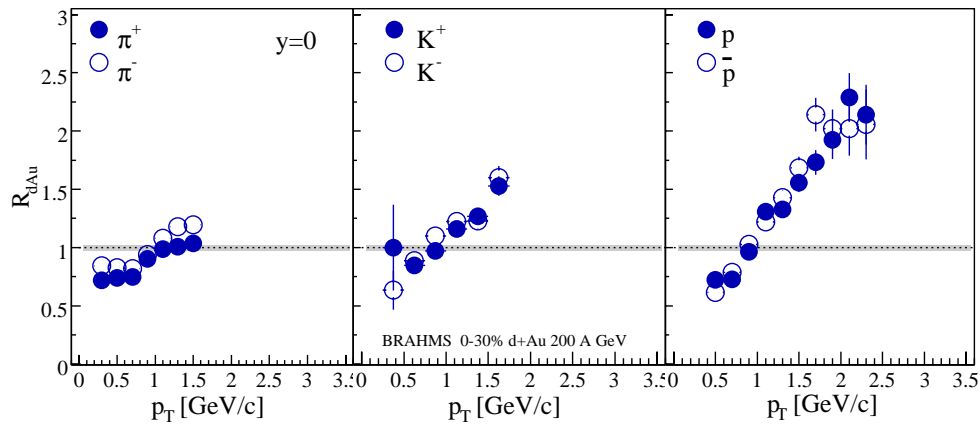
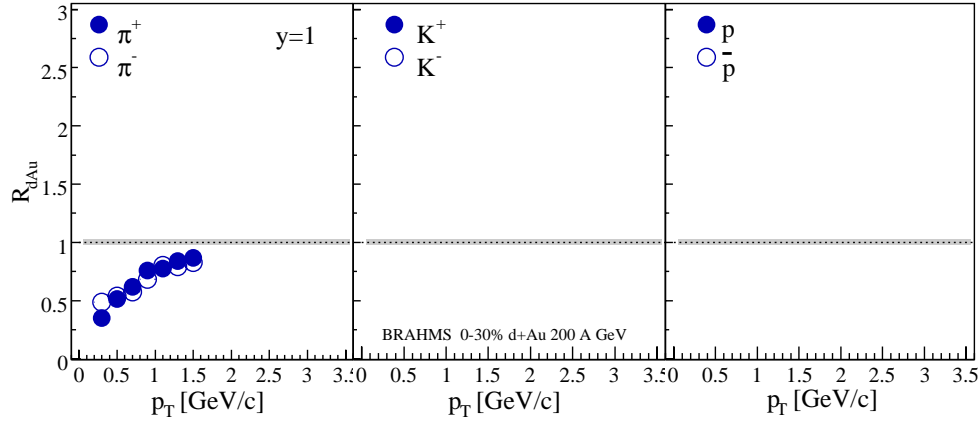
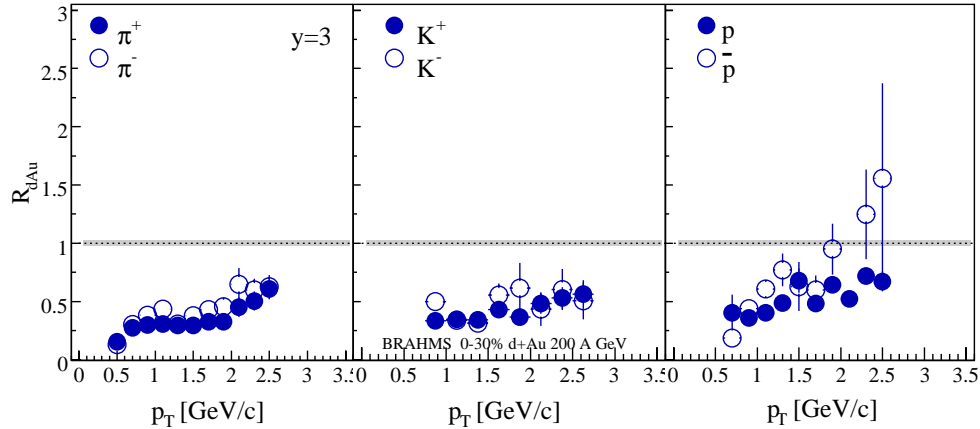
(a) $y = 0$ (b) $y = 1$ (c) $y = 3$

Figure 6.4: R_{dAu} for positive and negative pions and kaons and for protons (anti-protons) in the most central (0-30%) d+Au collisions at rapidity $y = 0, 1$ and 3 . Systematic uncertainties are shown as bands around 1.0 in each panel.

Figure 6.4 shows the comparison for the most central (0-30%) d+Au collisions. Similar results are observed here.

Instead of using R_{dAu} one can construct a similar measure R_{CP} . Here the spectra

for central and semi-central collisions are normalized to the spectrum measured in peripheral reactions

$$R_{\text{CP}}^{\text{central}} = \frac{\langle N_{\text{coll}}^{\text{peripheral}} \rangle}{\langle N_{\text{coll}}^{\text{central}} \rangle} \cdot \frac{d^2 N^{\text{central}} / dp_T dy}{d^2 N^{\text{peripheral}} / dp_T dy} . \quad (6.2)$$

The evolution of R_{CP} with rapidities for charged hadrons of different species is shown in figure 6.5. Charged hadrons of the same species are added up to obtain better statistics. In figure 6.5 at mid-rapidity R_{CP} (subfigure (a)) shows no difference between different centrality selections. Hadrons with larger mass give a larger enhancement at this rapidity. It is worthwhile to mention that the systematic errors coming from the larger uncertainty of the $\langle N_{\text{coll}} \rangle$ in the peripheral (60-80%) d+Au collisions result in larger errors in R_{CP} . At forward rapidity $y = 3$ (subfigure (c)) all the ratios are suppressed. As can be seen from the figure the suppression is stronger for the central-to-peripheral ratio than for semi-central-to-peripheral ratios for all particle species.

Figure 6.6 summaries the centrality dependence of R_{dAu} for charged pions, kaons and protons in d+Au collisions at mid-rapidity and forward rapidity. There is a difference of R_{dAu} in central and peripheral collisions. R_{dAu} for protons reach 2 at $p_T \approx 2$ GeV/ c at mid-rapidity in central and about 1.5 in peripheral collisions. At forward rapidity $y = 3$, R_{dAu} for identified charged particles is suppressed up to $p_T < 2.5$ GeV/ c for central collisions.

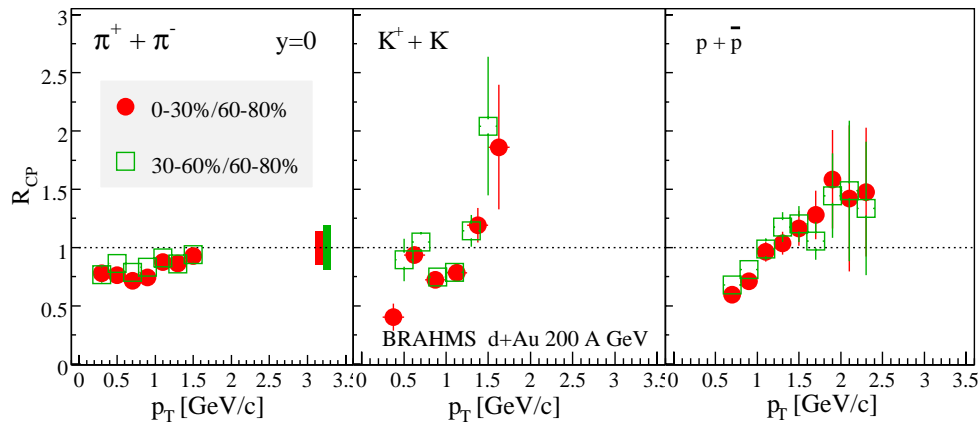
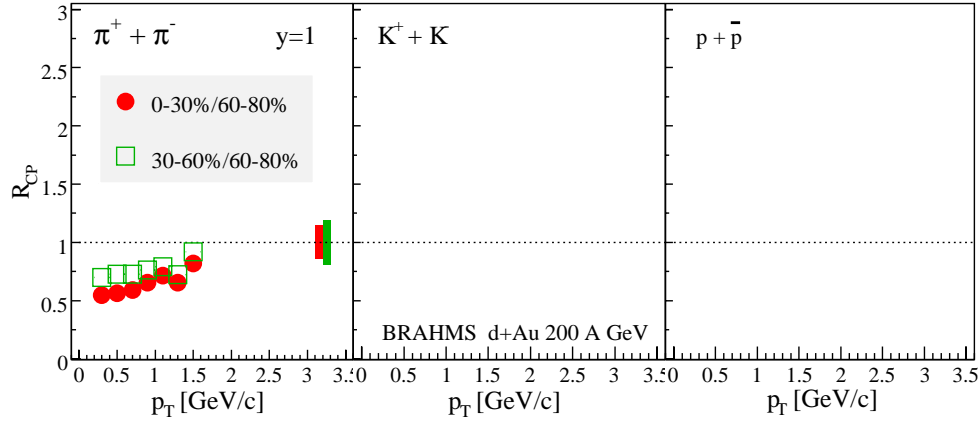
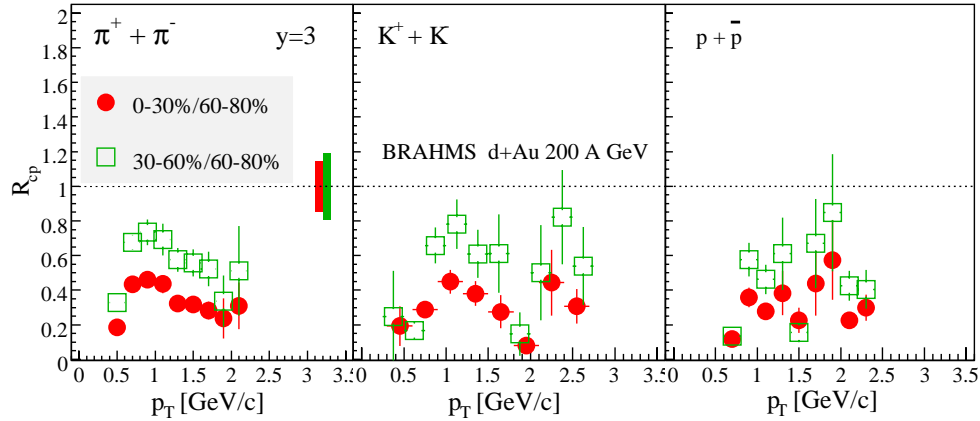
(a) $y = 0$ (b) $y = 1$ (c) $y = 3$

Figure 6.5: R_{CP} as a function of p_T for charged hadrons of different specie at mid-rapidity $y = 0, 1$ and 3 . The errors shown here are only statistical, and the bands around 1.0 are the systematic errors caused by the uncertainties of $\langle N_{coll} \rangle$. The band at the most right-hand side is for the uncertainty of R_{CP} for $30\text{-}60\%/60\text{-}80\%$, the one at the left-hand side is for $0\text{-}30\%/60\text{-}80\%$.

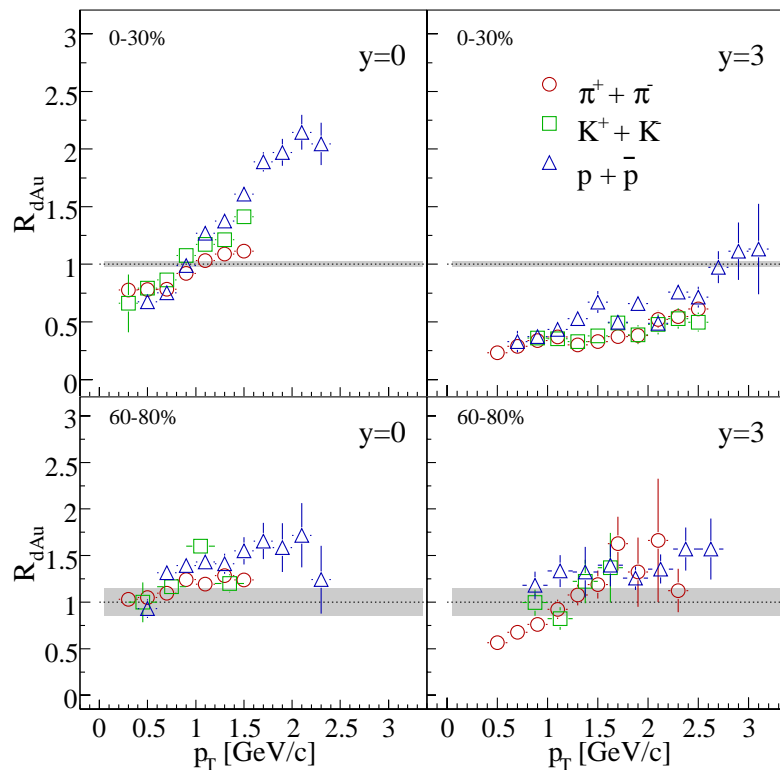


Figure 6.6: Nuclear modification factor R_{dAu} for identified charged hadrons at rapidity $y = 0$ and $y = 3$. The top panel shows 0-30% centrality bin, and the bottom one shows 60-80% centrality bin. Grey bands around $R_{dAu} = 1$ are the systematic uncertainties propagated from $\langle N_{coll} \rangle$.

Chapter 7

Stopping

Net-proton rapidity distributions in both d+Au and p+p systems are studied in order to understand stopping. The rapidity dependence of the net-proton yield in d+Au and p+p collisions may shed light on the baryon number transport in nuclear collisions. The net-proton transverse momentum spectra are constructed by subtracting the anti-proton spectra from the proton spectra p_T -bin-by- p_T -bin, using the method which has been explained earlier in Chapter 4. In this chapter, the net-proton production in d+Au and p+p collisions at $\sqrt{s_{NN}} = 200$ GeV are presented.

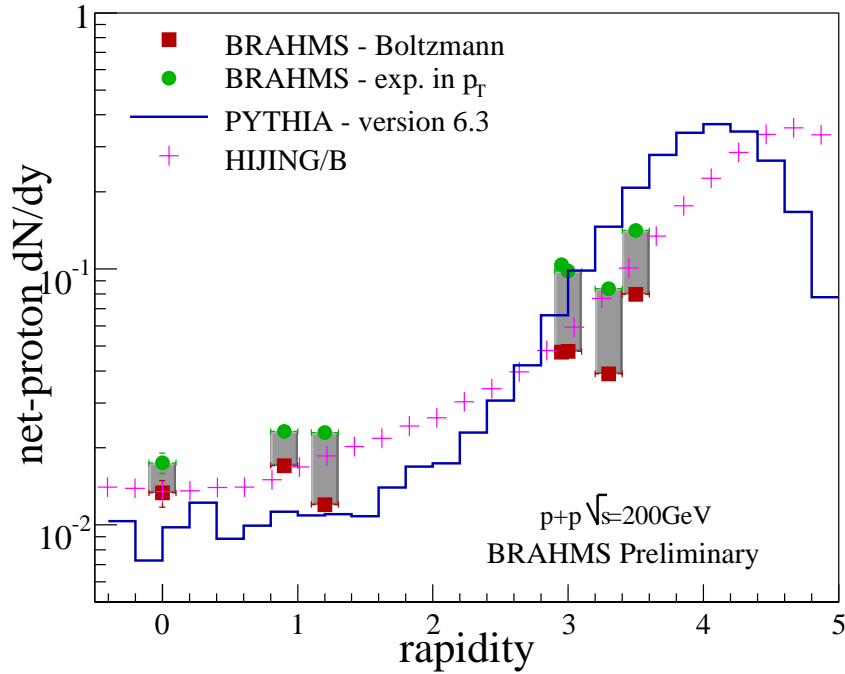


Figure 7.1: Net-proton rapidity density in p+p collisions at $\sqrt{s} = 200$ GeV. The squares are the net-proton yields obtained by using a Boltzmann function, and the dots are those obtained using an exponential function in p_T . The gray boxes between the two sets of extrapolations indicate the range of solutions which cannot be distinguished by our data.

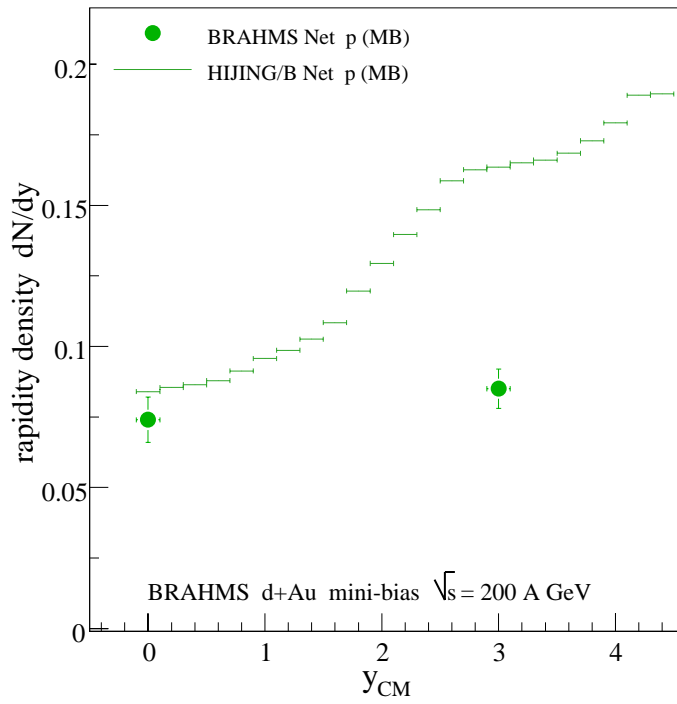


Figure 7.2: Net-proton rapidity density in minimum bias $d+Au$ collisions, compared to results by HIJING/B estimation

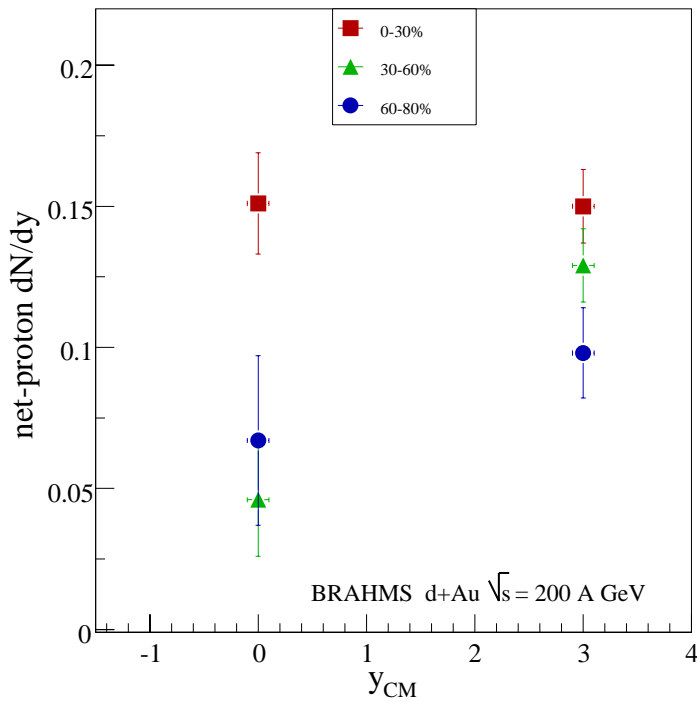


Figure 7.3: Centrality dependence of net-proton rapidity density in $d+Au$ collisions at $\sqrt{s_{NN}} = 200$ GeV.

Figure 7.1 shows the net-proton rapidity distribution in p+p collisions at $\sqrt{s} = 200$ GeV and a comparison to PYTHIA [23] and the HIJING model with baryon junction [91], including single diffractive processes. The squares are the results of a Boltzmann extrapolation, while the dots represent those from an exponential function in p_T . The region around mid-rapidity (between 0 and 1) is almost baryon-free, while a large net-proton density is observed at forward rapidity (around 3). Even though we have an uncertainty of about 50% due to the extrapolation procedure HIJING/B's estimate is closer to our data, while PYTHIA's is systematically lower at mid-rapidity and higher at forward.

Figure 7.2 and 7.3 show the net-proton rapidity density in d+Au collisions at $\sqrt{s_{NN}} = 200$ GeV of different centrality selections. Statistical errors and systematic errors ($\approx 20\%$) from the spectra construction and extrapolation are included in the error bars shown in the figure. Figure 7.2 shows a comparison with a HIJING/B estimation (histogram) in minimum bias d+Au collisions. Figure 7.3 shows the net-proton rapidity density for various centrality bins.

The experimental results at mid-rapidity are consistent with the model estimation within the errors, but HIJING/B overestimates the yield at the forward rapidity. At both rapidities, $y = 0$ and $y = 3$, the net-proton rapidity density increases with centrality.

Chapter 8

Comparisons and Discussion

In this chapter, comparisons are made between the results on spectra of identified particles in this thesis and the published data from other RHIC experiments.

The PHENIX and STAR Collaborations at RHIC have published the spectra for identified particles in the d+Au and p+p collisions at mid-rapidity. The consistency between these measurements and the one by BRAHMS is crucial for the understanding of our experiments. In the following the results presented in this work are compared to those from PHENIX and STAR, even though very different detectors were implemented, and very different techniques were used in the analysis.

8.1 Minimum bias d+Au collisions at $\sqrt{s_{NN}} = 200$ GeV

At mid-rapidity $y = 0$ our results for charged hadrons for the minimum bias d+Au data are compared with the identified particle spectra, published by both STAR [92] and PHENIX [51] Collaborations. In figure 8.1, the upper panel shows the comparison for pions, the middle one shows that for kaons, and the bottom one shows that for protons. Note that PHENIX has corrected the spectra for protons (anti-protons) for feed down from weak decays. There is agreement amongst the data sets.

8.2 p+p collisions at $\sqrt{s} = 200$ GeV

The results for p+p collisions at mid-rapidity $y = 0$ are also compared with the identified particle spectra, published by both the STAR [92] and PHENIX [51] experiments. In figure 8.2, the upper panel shows the comparison for pions, the middle one shows that for kaons, and the bottom one shows the one for protons. Errors are only statistical.

Note that the spectra for protons (anti-protons) from PHENIX have been corrected for feed down from weak decay, which explains the difference between the BRAHMS results (open diamond symbols) and those from PHENIX (round points). PHENIX π and K spectra agree with BRAHMS data within the errors, while STAR data is above the BRAHMS spectra, and for kaons the slope is also different.

At the forward rapidity $y = 3$ the published BRAHMS results [28] of particle spectra in p+p collisions are compared to the results presented in this thesis. The published

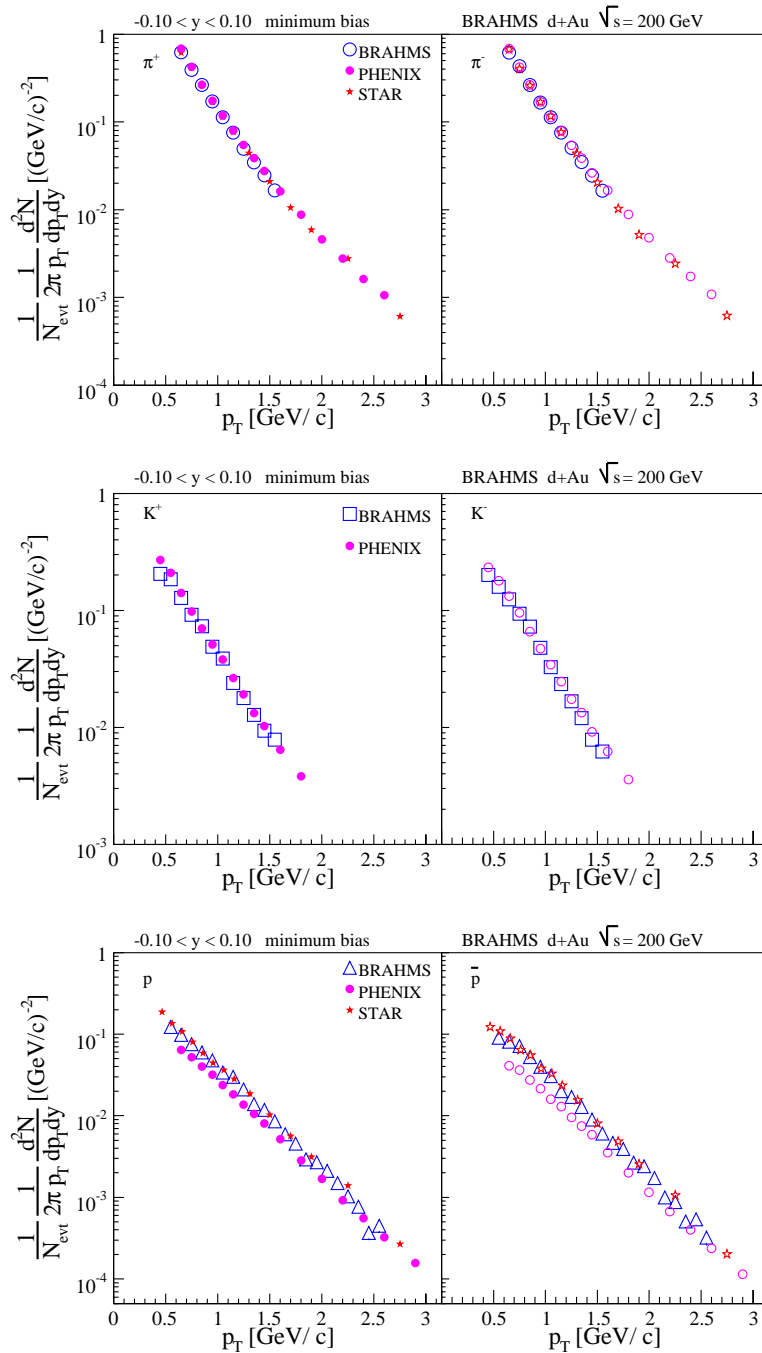


Figure 8.1: Spectra for charged hadrons at rapidity $y = 0$ in minimum bias $d+Au$ collisions compared to results from other RHIC experiments at mid-rapidity. The errors are only statistical.

data represent the analysis status of 2006 and is based on this work and an analysis done at BNL. Figure 8.3 shows the comparison for charged pions (upper panels), kaons (middle ones) and protons (bottom ones); consistency of the two analyses within the errors is seen. The most recent comparison between NLO pQCD calculations with the measurement by BRAHMS experiment for p+p collisions at $\sqrt{s} = 200$ GeV [28] are

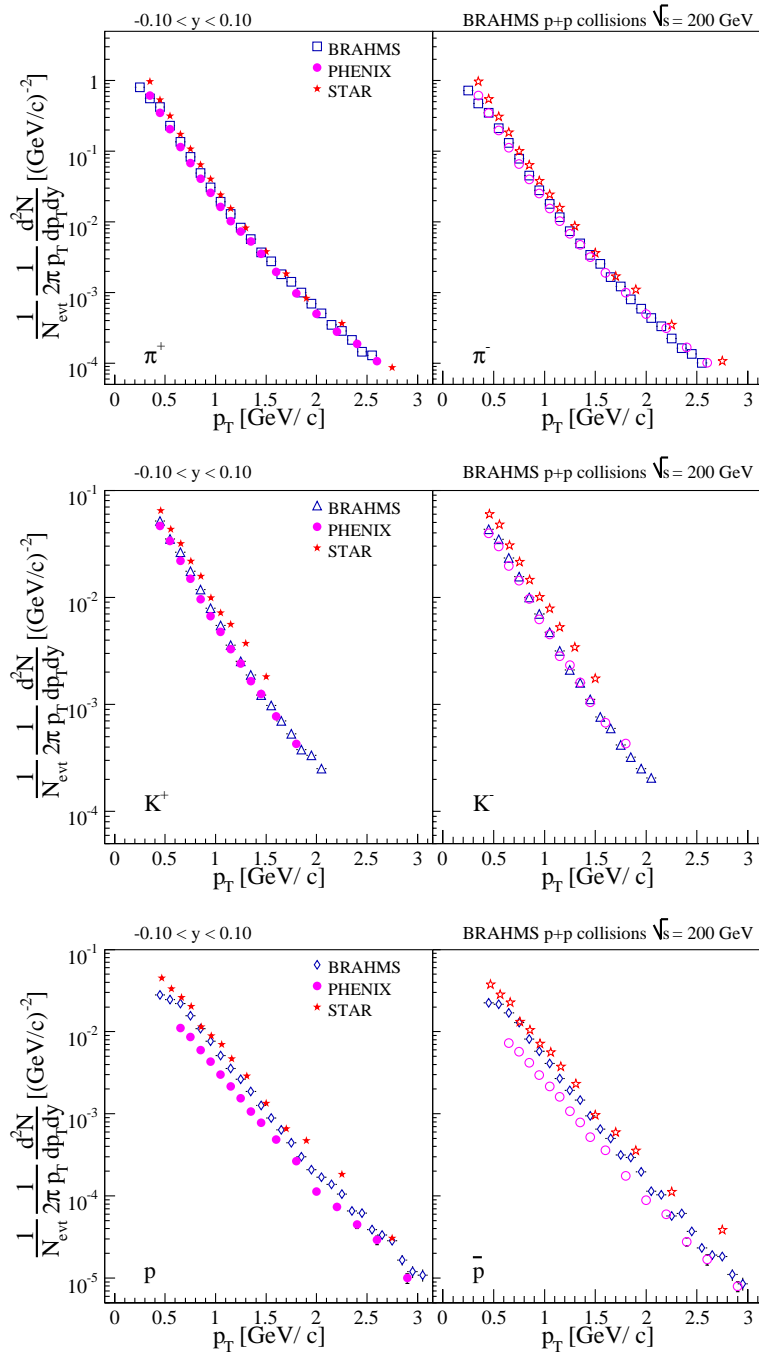


Figure 8.2: Spectra of charged hadrons at rapidity $y = 0$ in $p+p$ collisions, compared to the results from other RHIC experiments at mid-rapidity. Errors are statistical only.

shown in figure 8.4. In the top row of figure 8.4, the modified KKP (mKKP) set of fragmentation functions (solid line) produce the best agreement with the π^- and K^+ data. The p and \bar{p} are compared with the calculation using the AKK set divided by 2 (dashed line). In the bottom row, relative differences between data and calculations is shown. A good agreement between experiment and pQCD calculation had been reached for π and K production, while the $p(\bar{p})$ spectra are not properly described.

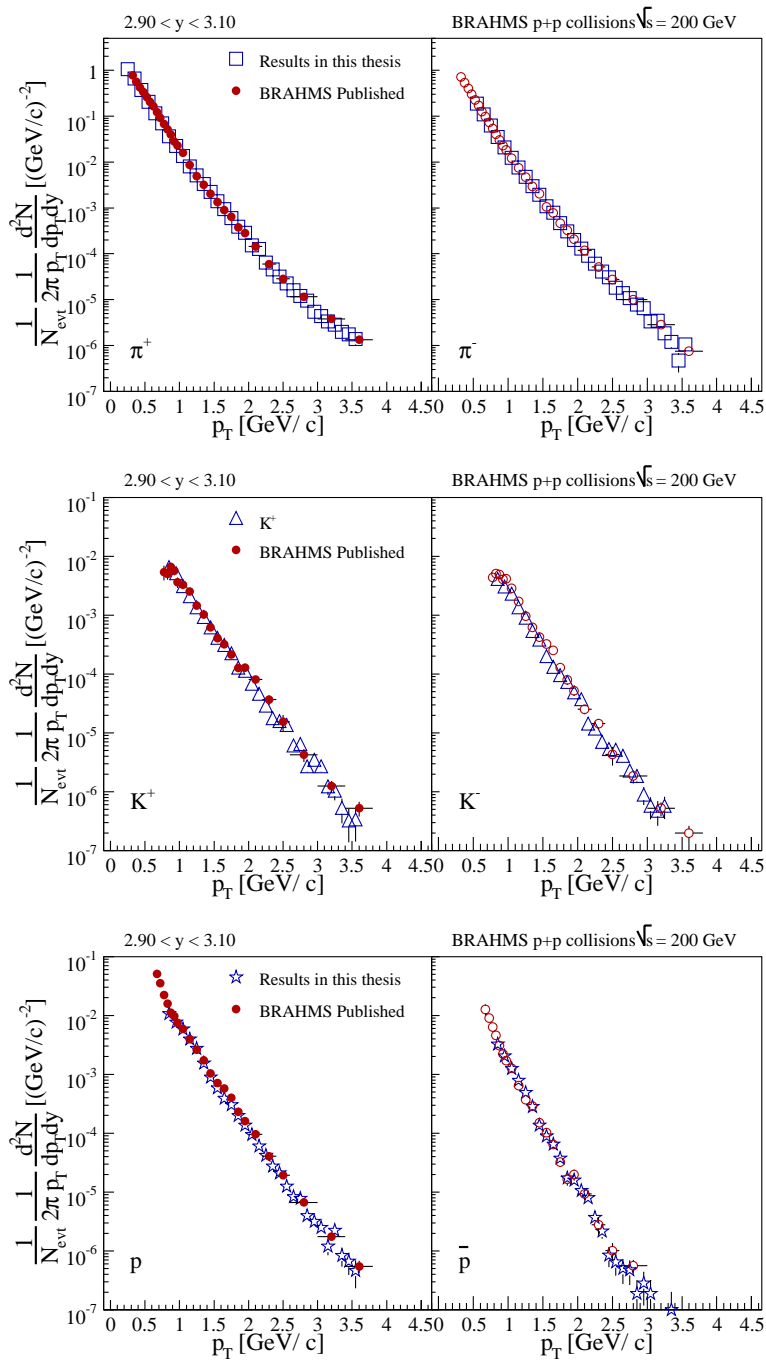


Figure 8.3: Spectra of charged hadrons at rapidity $y = 3$ in $p+p$ collisions compared to recently published BRAHMS results [28] at $y = 2.95$.

8.3 Nuclear modification factors at mid-rapidity

Figure 8.5 shows R_{dAu} for charged pions, kaons and protons (including \bar{p}) at mid-rapidity measured by the BRAHMS experiment, compared to PHENIX and STAR results. Note that the average number of binary collisions $\langle N_{coll} \rangle$ used to rescale the spectra are 7.5 ± 0.1 , 8.5 ± 0.4 and 7.5 ± 0.4 for BRAHMS, PHENIX and STAR respectively. Results from both PHENIX and STAR experiments show smaller R_{dAu} .

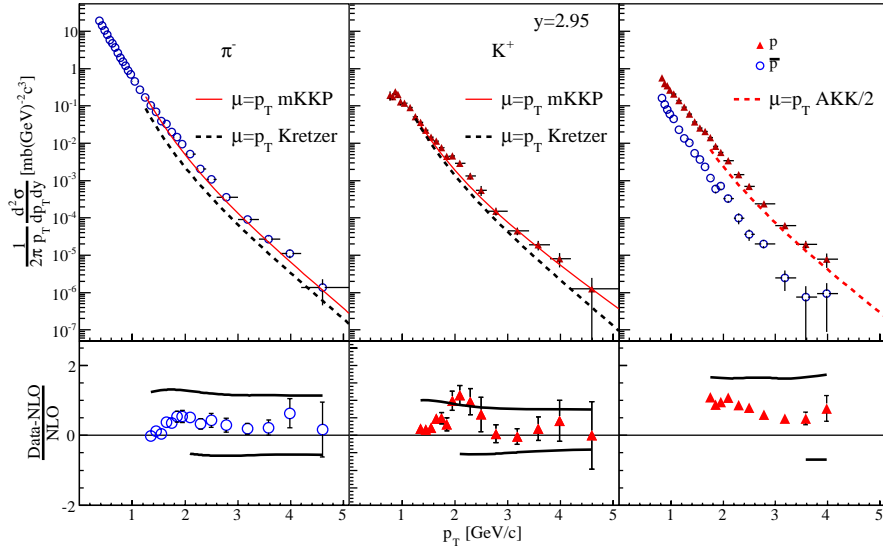


Figure 8.4: Comparison of invariant cross sections for π^- , K^+ , \bar{p} and p at $y = 2.95$ in $p+p$ collisions at $\sqrt{s} = 200$ GeV and NLO pQCD calculations with factorization and renormalization scales set equal to p_T [28].

It is worth noting that when using the same $\langle N_{\text{coll}} \rangle$ to rescale the spectra in d+Au collisions, the PHENIX results agree with our nuclear modification factors results within 15%.

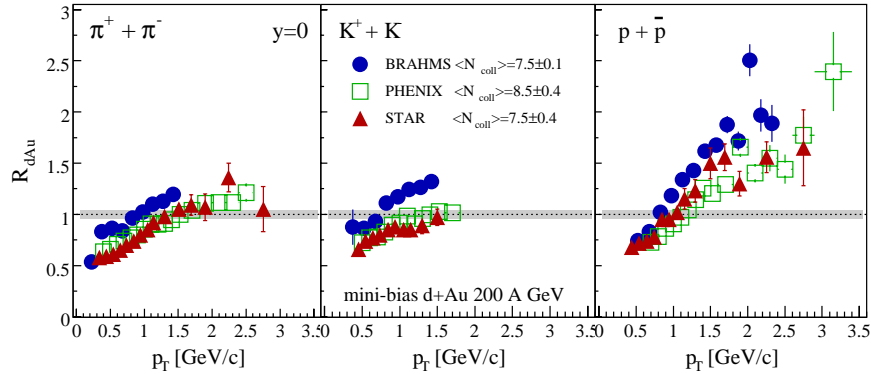


Figure 8.5: Comparison of R_{dAu} for charged pions (left), kaons (middle) and protons (including \bar{p}) (right) BRAHMS experiment to PHENIX [51] and STAR [93] results at mid-rapidity in minimum bias collisions. Note that the average number of binary collisions $\langle N_{\text{coll}} \rangle$ used to rescale the spectra are 7.5 ± 0.4 , 8.5 ± 0.4 and 7.5 ± 0.4 for BRAHMS, PHENIX and STAR respectively.

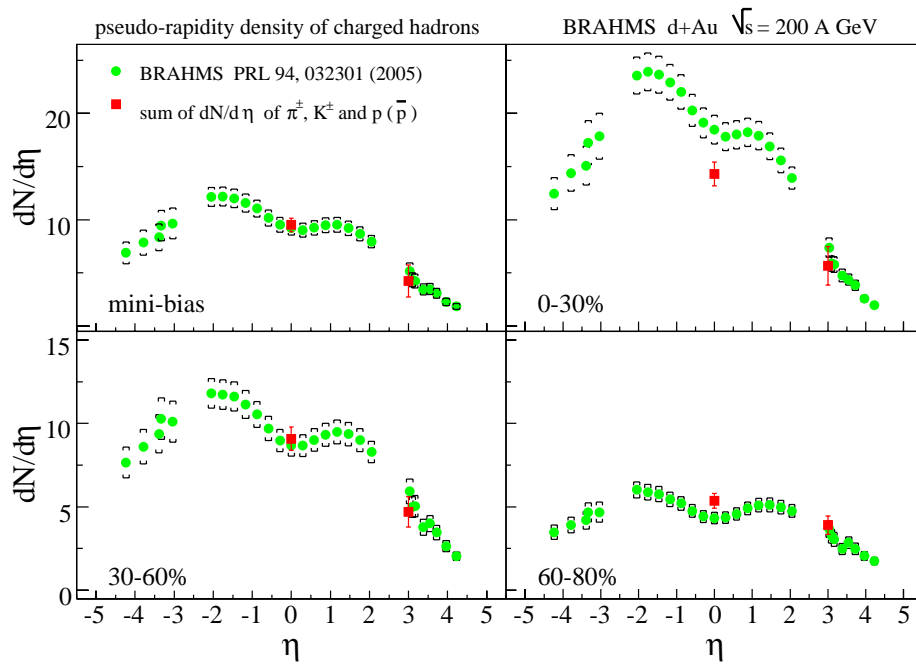


Figure 8.6: Comparison of BRAHMS measurements of the identified hadrons to the charged hadron pseudo-rapidity density distribution in $d+Au$ collisions [1] at $\sqrt{s_{NN}} = 200$ GeV. Systematic errors are included in the error bars.

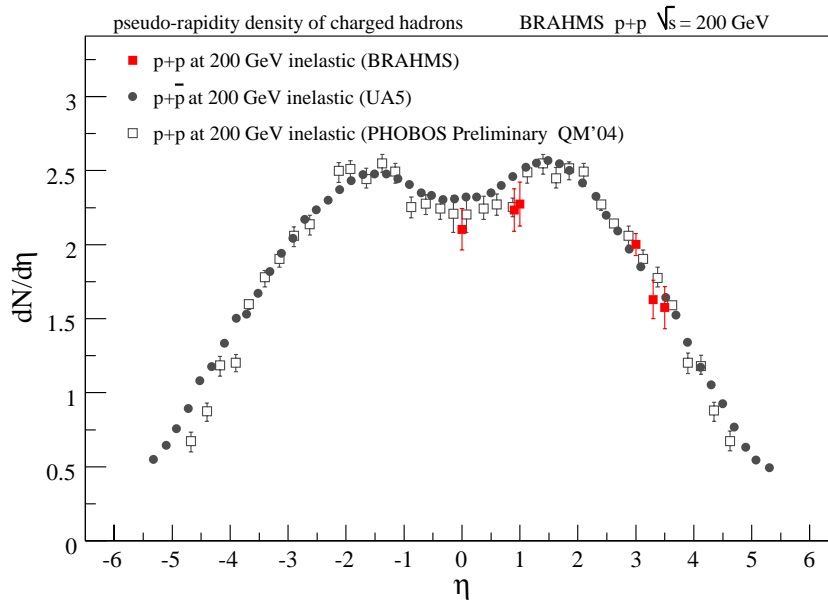


Figure 8.7: Comparison of $dN/d\eta$ of the identified hadrons to PHOBOS [94] and UA5 [95] measurements of charged hadron pseudo-rapidity distribution in $p+p$ and $p+\bar{p}$ inelastic collisions at $\sqrt{s} = 200$ GeV. Systematic errors on PHOBOS data are not shown.

8.4 Pseudo-rapidity density

The integrated yields dN/dy of all charged hadrons obtained in this thesis are converted into $dN/d\eta$ by multiplying a Jacobian factor in order to enable a comparison

with existing data or results from other experiments. Figure 8.6 shows a comparison between the $dN/d\eta$ of all identified charged hadrons obtained in this thesis, and the published BRAHMS charged hadron pseudo-rapidity distribution [1]. There is an excellent agreement for minimum bias and semi-central collisions, while the yields differ by 1-2 σ for central and peripheral collisions. Figure 8.7 shows a comparison between $dN/d\eta$ of all identified charged hadrons and the preliminary results from PHOBOS [94] and the published UA5 [95] measurements in p+p and p+ \bar{p} inelastic collisions at $\sqrt{s} = 200$ GeV. The agreement is within the errors.

8.5 Net-proton dN/dy

The net-proton rapidity density in d+Au and p+p at $\sqrt{s_{NN}} = 200$ GeV are compared with our published rapidity density in central Au+Au collisions (0-5%) [11] in figures 8.8 and 8.9. In figures 8.8 the net-proton rapidity density in central (0-30%) d+Au collisions is scaled by the ratio of the number of participants from the projectile side in Au+Au collisions to that in central d+Au collisions. After being rescaled the data points from d+Au and Au+Au overlap at the forward rapidity, while relative more net-protons are found at mid-rapidity in d+Au collisions.

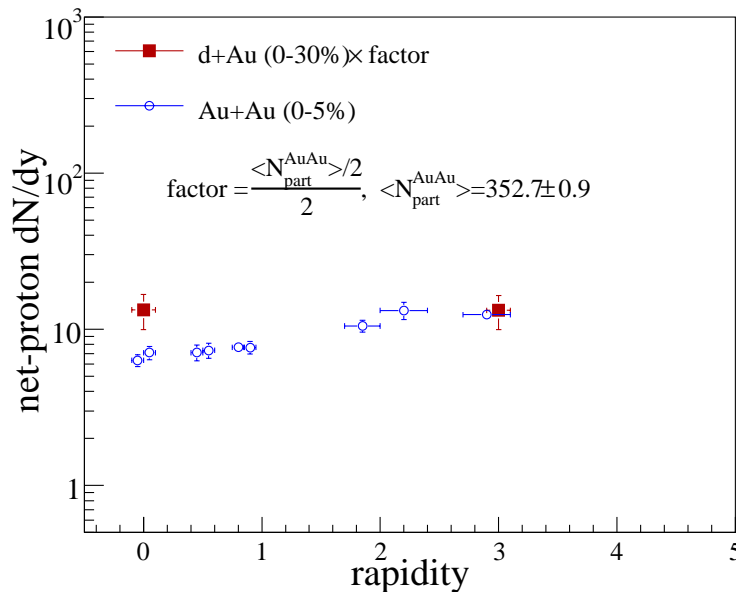


Figure 8.8: Net-proton rapidity density in central Au+Au collisions (0-5%) at $\sqrt{s_{NN}} = 200$ GeV is compared with that in central (0-30%) d+Au collisions scaled by the ratio of number of participants from the projectile in central Au+Au collisions to that number in d+Au.

In figure 8.9 the net-proton rapidity density in minimum bias p+p collisions are scaled by the average number of participant protons in central Au+Au collisions. The scaling seems to work at $y = 3$ but many more net-protons have been transported

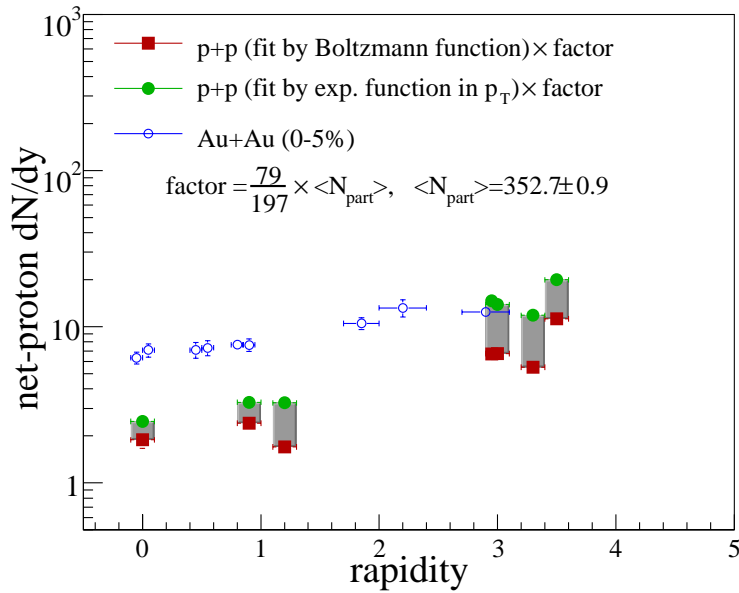


Figure 8.9: *The net-proton rapidity density central Au+Au collisions (0-5%) at $\sqrt{s_{NN}} = 200$ GeV is compared with the net-proton rapidity density in minimum bias p+p collisions scaled by the average number of participant protons in central Au+Au collisions.*

to mid-rapidity in central Au+Au collisions, indicating a higher degree of stopping in nucleus nucleus collisions.

For a comparison between our result for net-protons, net-protons at mid-rapidity [67] and net- Λ at both forward and backward rapidities measured by the STAR experiment [96] are shown in figure 8.10.

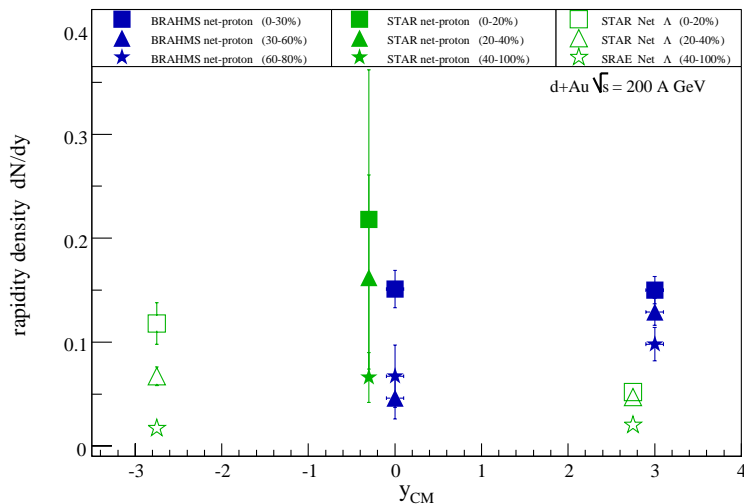


Figure 8.10: *Net-proton rapidity density in d+Au collisions at $\sqrt{s_{NN}} = 200$ GeV, compared to measurements of net-protons [67] and net- Λ [96] (open symbols) measured by STAR experiment.*

STAR's centrality selection is slightly different from the one used here (more central). However, the agreement between the different net-proton data at mid-rapidity is good. At forward rapidity the BRAHMS net-proton yields might be consistent with the STAR net- Λ yields, taking into account that the net-protons include the net- Λ to a large extent via the decay products and assuming a p/Λ ratio larger than 1. However, all data sets show the same centrality dependence; central collisions have the highest yields at all rapidities.

Chapter 9

Summary and Conclusion

Data from d+Au and p+p collisions at $\sqrt{s_{NN}} = 200$ GeV recorded during RUN03 and RUN05 by the BRAHMS experiment at RHIC have been analyzed. Minimum bias triggers and three different centrality classes (0-30%, 30-60% and 60-80%) for d+Au collisions have been employed.

Spectra for identified charged hadrons (π^\pm, K^\pm and $\bar{p}(p)$) in both d+Au and p+p collisions at $\sqrt{s_{NN}} = 200$ GeV are constructed by combining different spectrometer settings, thus covering a wide y - p_T range from mid-rapidity $y = 0$ to forward $y = 3.5$. Because of the limited number of good runs/settings in d+Au collisions at rapidity $y = 1$ due to the inefficiency of the detectors for particle identification, only the spectra of charged pions have sufficient statistics. Spectra are compared with existing published data where available (mainly at mid-rapidity) and proved to be consistent within the errors. The invariant cross sections of pions and kaons produced in p+p collisions can be described by NLO pQCD calculations at all rapidities, whereas the model fails to reproduce the proton (antiproton) spectra especially at forward rapidity.

The particle ratios, such as negative/positive, K/π and p/π ratios have been studied as a function of the transverse momentum p_T at different rapidities. In d+Au collision, like-particle-ratios show no centrality dependence. At forward rapidities the positive p/π ratio is much larger than the negative one even at high p_T .

Integrated yields dN/dy and average momentum $\langle p_T \rangle$ of each species have been extracted by extrapolating particle spectra to those regions of low p_T and high p_T which are outside the acceptance of the BRAHMS detectors. Systematic errors are carefully estimated by using various fit functions. dN/dy of identified hadrons in d+Au collisions are converted into a pseudo-rapidity distribution in order to compare with our published pseudo-rapidity density $dN/d\eta$ for charged hadrons in various centrality bins. There is an excellent agreement for minimum bias and semi-central collisions. The deduced $dN/d\eta$ for charged hadrons in p+p collisions agree with measurements by PHOBOS and UA5 p+ \bar{p} data.

Net-proton rapidity distributions in both systems are extracted by subtracting the anti-proton spectra from the proton spectra p_T -bin-by- p_T -bin, using the same extrapolation method. In p+p collisions, we found that the region around mid-rapidity (y between 0 and 1) is almost baryon-free and a large net-proton density is observed at forward rapidity. The data disfavours the PHYTIA model and favors HIJING/B. In d+Au collisions, HIJING/B agrees with our data at mid-rapidity, while it overesti-

mates that yield at forward rapidity. A comparison of the net-proton rapidity density p+p collisions, scaled by the number of participant protons, to central Au+Au collisions indicates a higher degree of stopping in the nucleus-nucleus system. In conclusion, the baryon transport in nuclear collisions is not understood.

Nuclear modification factors R_{dAu} are constructed for d+Au collisions, using the reference from p+p collisions presented in the thesis. The rapidity and centrality dependence of R_{dAu} of pions is consistent with the measurements of charged hadrons by BRAHMS. The strong suppression of pions in central collisions at forward rapidity may indicate the role of the initial state effect e.g. gluon saturation at small- x . The difference between R_{dAu} for positive and negative hadrons at forward rapidity may be due to isospin effects.

The results for d+Au and p+p collisions presented in this thesis are needed as a control system for Au+Au collisions and the p+p data is needed for the verification of model calculations e.g. pQCD. Due to the limitation of the acceptance of the BRAHMS detector and particle identification ability, the results presented in this thesis suffer from insufficient statistics and large systematical errors. More reference data with good statistics of p+p and p(d)+A collisions at ultra-relativistic energies at RHIC and at LHC are needed, especially at high rapidity which would allow to study gluon saturation effects at really small- x and thereby improve the understanding of the initial conditions in nuclear collisions.

Appendix A

BRAHMS Collaboration

I. Arsene¹¹, I. G. Bearden⁶, D. Beavis¹, S. Bekele¹⁰, C. Besliu⁹, B. Budick⁵,
H. Bøggild⁶, C. Chasman¹, C. H. Christensen⁶, P. Christiansen⁶, R. Clarke⁹,
R. Debbe¹, J. J. Gaardhøje⁶, K. Hagel⁷, H. Ito¹, A. Jipa⁹, J. I. Jørdre⁸, F. Jundt²,
E. B. Johnson¹⁰, C. E. Jørgensen⁶, R. Karabowicz³, E. J. Kim¹⁰, T. M. Larsen⁶,
J. H. Lee¹, Y. K. Lee⁴, S. Lindal¹¹, G. Løvholden¹¹, Z. Majka³, M. Murray¹⁰,
J. Natowitz⁷, B. S. Nielsen⁶, D. Ouerdane⁶, R. Planeta³, F. Rami², C. Ristea⁶,
O. Ristea⁹, D. Röhrich⁸, B. H. Samset¹¹, D. Sandberg⁶, S. J. Sanders¹⁰,
R. A. Sheetz¹, P. Staszal³, T. S. Tveter¹¹, F. Videbæk¹, R. Wada⁷, H. Yang⁸,
Z. Yin⁸, I. S. Zgura⁹

¹Brookhaven National Laboratory, Upton, New York 11973, USA,

²IReS and Université Louis Pasteur, Strasbourg, France,

³Jagiellonian University, Krakow, Poland,

⁴Johns Hopkins University, Baltimore 21218, USA,

⁵New York University, New York 10003, USA,

⁶Niels Bohr Institute, University of Copenhagen, Copenhagen 2100, Denmark,

⁷Texas A&M University, College Station, Texas 17843, USA,

⁸University of Bergen, Department of Physics, Bergen 5007, Norway,

⁹University of Bucharest, Bucharest, Romania,

¹⁰University of Kansas, Lawrence, Kansas 66069, USA,

¹¹University of Oslo, Department of Physics, Oslo, Norway.

(48 physicists from 11 institutions)

Appendix B

Kinematics

Momentum vector

The momentum vector of a particle p is defined by a contravariant vector with four components p^μ :

$$p^\mu = (p^0, p^1, p^2, p^3) = (E, \vec{p}) = (E, \vec{p}_T, \vec{p}_z) = (E, \vec{p}_x, \vec{p}_y, \vec{p}_z) , \quad (\text{B.1})$$

where \vec{p}_T is the transverse momentum, and its value is defined as

$$p_T = \sqrt{p_x^2 + p_y^2} = \sqrt{p^2 - p_z^2} . \quad (\text{B.2})$$

p_z is the longitudinal momentum. In the spherical coordinates system (\vec{p} , θ and ϕ),

$$\begin{aligned} p_T &= p \cdot \sin \theta , \\ p_z &= p \cdot \cos \theta . \end{aligned}$$

The transverse mass of a particle is defined as

$$m_T = \sqrt{p_T^2 + m^2} . \quad (\text{B.3})$$

Rapidity and pseudo-rapidity variables

The rapidity variable y for describing the kinematic condition of a particle, is defined in terms of its energy-momentum components,

$$y = \frac{1}{2} \ln \left(\frac{E + p_z}{E - p_z} \right) , \quad (\text{B.4})$$

which is an additive constant in the Lorentz frame of reference. From equation B.4, one can obtain the following relations:

$$\begin{aligned} E &= \sqrt{p_T^2 + m^2} \cosh y = m_T \cosh y , \\ p_z &= \sqrt{p_T^2 + m^2} \sinh y = m_T \sinh y . \end{aligned} \quad (\text{B.5})$$

It is convenient to calculate the pseudo-rapidity η when the energy and momentum of the particle are not available, while the longitudinal angle θ between particle momentum \vec{p} and the beam axis is available. The pseudo-rapidity variable of a particle is defined as

$$\eta = -\ln \left[\tan\left(\frac{\theta}{2}\right) \right], \quad (\text{B.6})$$

which can be written as

$$\eta = \frac{1}{2} \ln \left(\frac{p + p_z}{p - p_z} \right). \quad (\text{B.7})$$

From equations B.6 and B.7 one can obtain similar relation between energy-momentum and η :

$$\begin{aligned} p &= p_T \cosh \eta, \\ p_z &= p_T \sinh \eta. \end{aligned} \quad (\text{B.8})$$

From equations B.5 and equations B.8, one can find the relation between rapidity and pseudo-rapidity, with a Jacobian factor from the variable transformation,

$$\frac{dN}{d\eta dP_T} = \sqrt{1 - \frac{m^2}{m_T^2 \cosh^2 y}} \frac{dN}{dy dp_T}, \quad (\text{B.9})$$

where m_T is the transverse mass determined by equation B.3, and $\sqrt{1 - \frac{m^2}{m_T^2 \cosh^2 y}}$ is the Jacobian factor. The integral of $dN/dy dp_T$ ($dN/d\eta dp_T$) with respect to p_T gives the integrated rapidity (pseudo-rapidity) density dN/dy ($dN/d\eta$).

Appendix C

Some Characteristics of RHIC

At RHIC, the nuclei are fully accelerated to $E/A = 100$ GeV,

- velocity of a nucleon

$$\beta_N = \frac{\sqrt{(E/A)^2 - m_N^2}}{E/A} = 0.999956 ; \quad (\text{C.1})$$

- rapidity of beam:

$$y_b^{200 \text{ GeV}} = \frac{1}{2} \ln \left(\frac{E + p_z}{E - p_z} \right) = \frac{1}{2} \ln \left(\frac{1 + \sqrt{1 - (A \cdot m_N/E)^2}}{1 - \sqrt{1 - (A \cdot m_N/E)^2}} \right) = 5.36 ; \quad (\text{C.2})$$

- design luminosity of the machine, for Au+Au collisions:

$$\mathcal{L} = \frac{f \cdot n_1 \cdot n_2}{4\pi \cdot \sigma_x \cdot \sigma_y} = 2 \cdot 10^{26} / \text{cm}^2 \text{s} , \quad (\text{C.3})$$

in which f is the frequency of the collider, n_1 and n_2 are the number of particles in each beam bunch, and σ_x and σ_y are the width of Gaussian characterizations of the bunches profiles in the horizontal and vertical directions in the plane of the RHIC ring.

- collision rate for A+B collisions:

$$R_{\text{coll}} = \mathcal{L} \cdot \sigma_{\text{AB}} , \quad (\text{C.4})$$

which is ≈ 1400 Hz for Au+Au collisions, where $\sigma_{\text{AuAu}} \sim 6.8b$.

Appendix D

Fit functions

In an experiment the normalized particle spectrum is measured as:

$$f(p_T) = \frac{d^2N}{2\pi p_T dp_T dy} = f(m_T) = \frac{d^2N}{2\pi m_T dm_T dy} . \quad (\text{D.1})$$

from which one can estimate the rapidity density dN/dy by integrating the spectrum in terms of p_T or m_T .

A series of fit functions, such as a power law function in p_T , an exponential function in p_T or m_T , and a Boltzmann function in m_T are used in this analysis, and are meant to describe the p_T or m_T spectra over the measured momenta range. They are

$$\begin{aligned} \text{Power law in } p_T & : A \cdot \left(1 + \frac{p_T}{p_0}\right)^{-n} , \\ \text{Exponential in } p_T & : B \cdot e^{-p_T/T} , \\ \text{Exponential in } m_T & : C \cdot e^{-m_T/T} , \\ \text{Boltzmann in } m_T & : D \cdot m_T \cdot e^{-[(m_T-m)/T]} , \end{aligned}$$

in which the coefficients A , B , C and D are normalization factors to be determined. These functions are used to extrapolate particle spectra to low and high p_T , which are outside the BRAHMS acceptance, to estimate the rapidity density dN/dy , or so-called integrated particle yields.

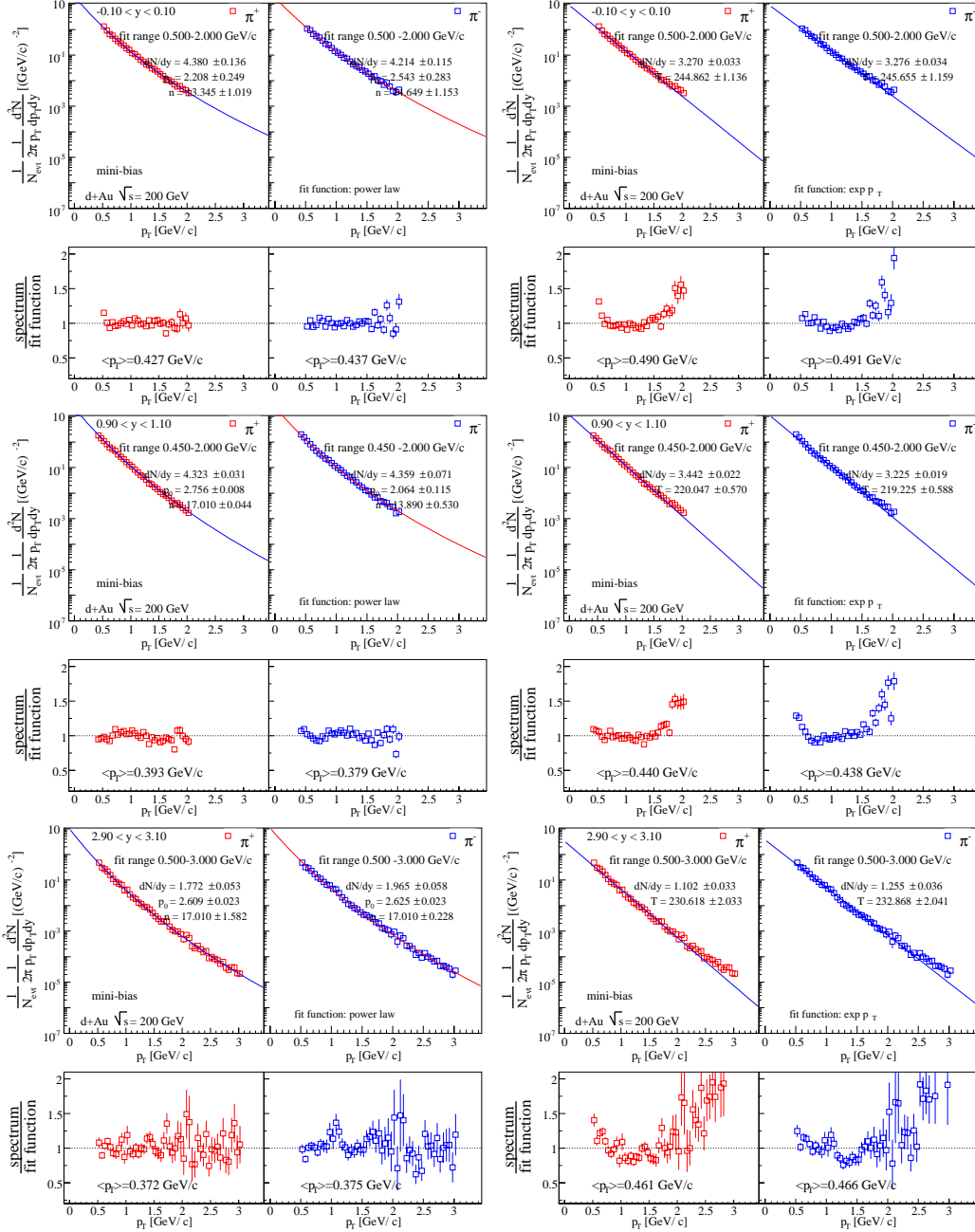
$$\frac{dN}{dy} = \int_0^\infty 2\pi p_T f(p_T) dp_T = \int_0^\infty 2\pi m_T f(m_T) dm_T . \quad (\text{D.2})$$

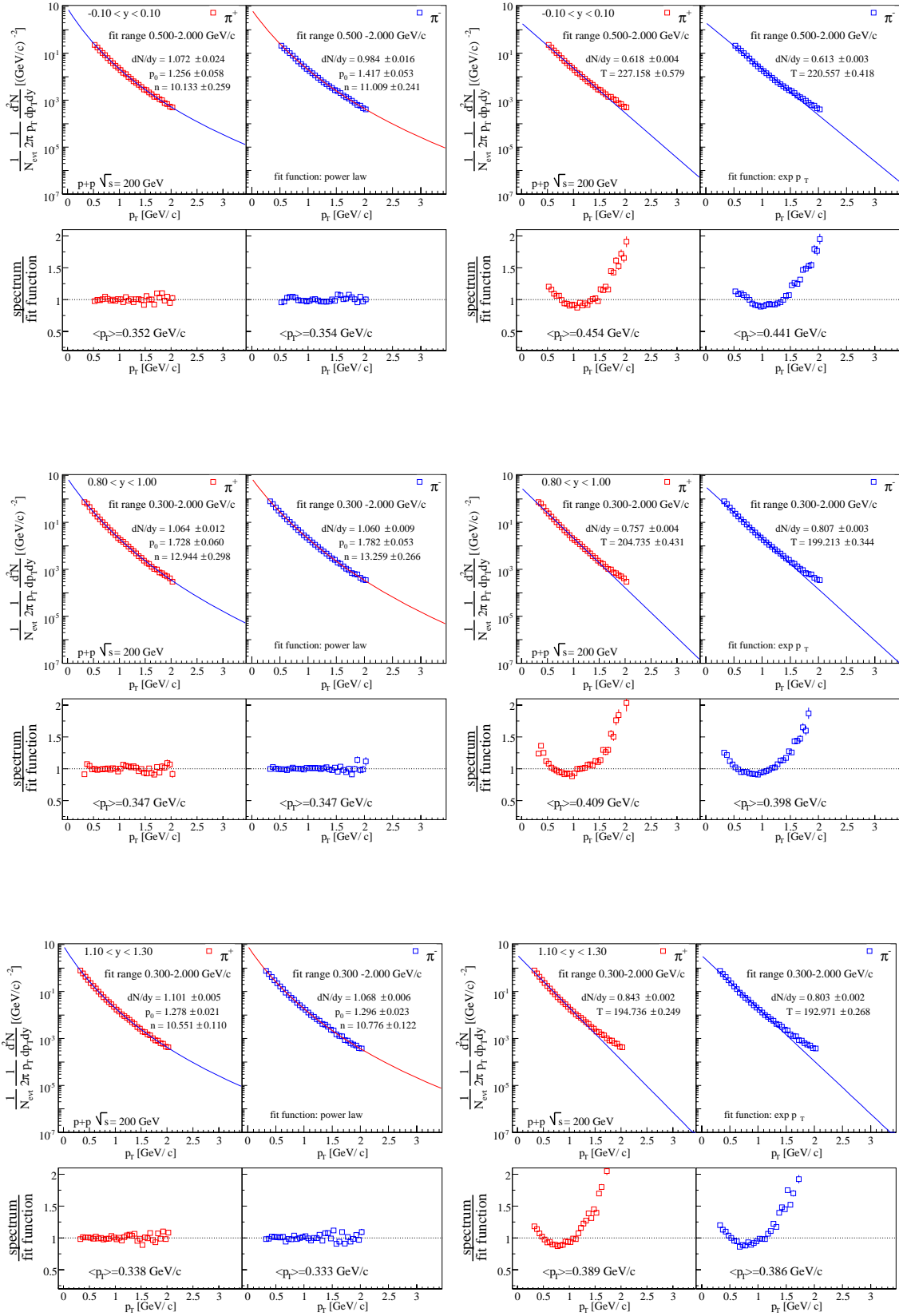
By inserting the fit functions listed above into equation D.2, one can determine the constants A , B , C and D , and yield

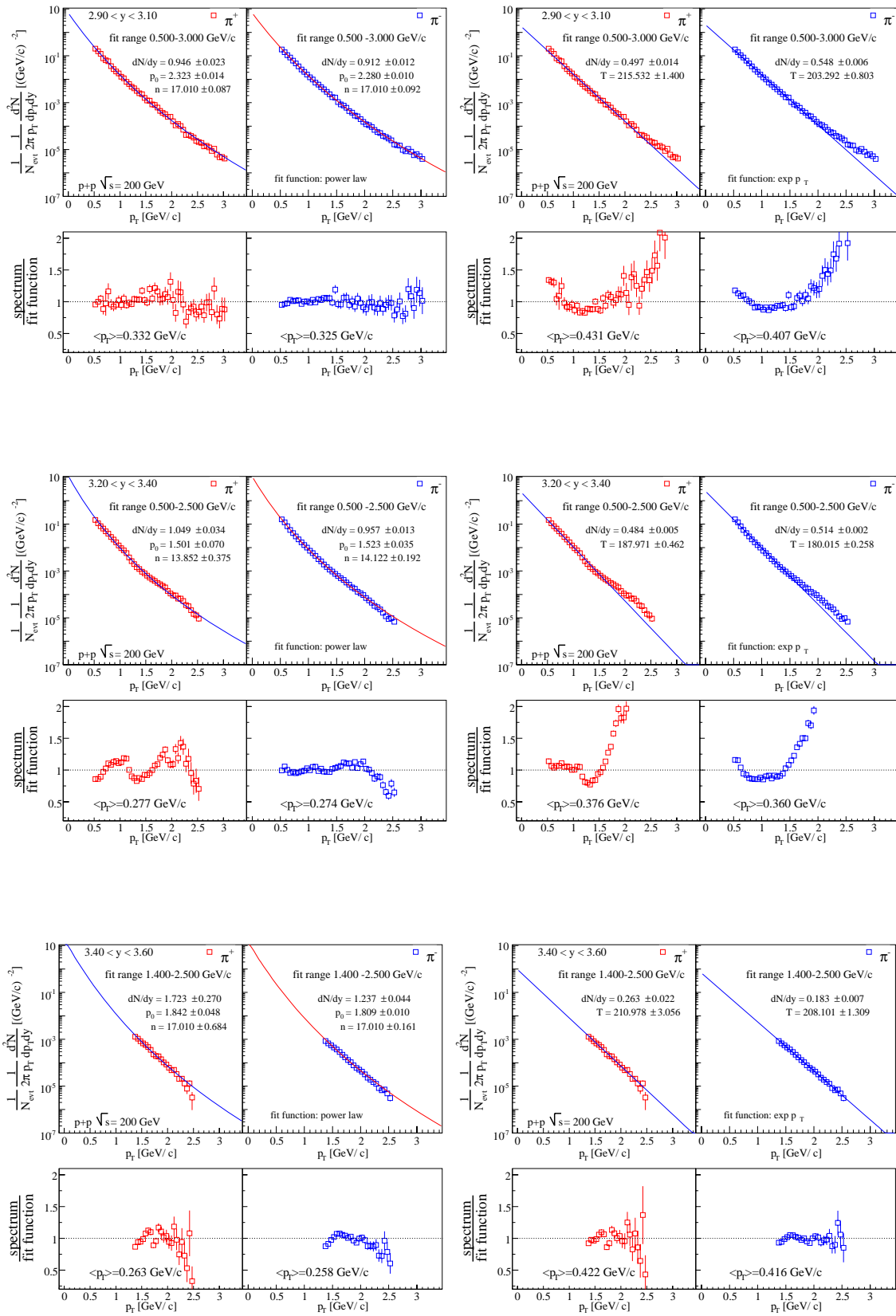
$$\begin{aligned} \text{Power law in } p_T & : f(p_T) = \frac{(n-1)(n-2)}{2\pi p_0^2} \frac{dN}{dy} \left(1 + \frac{p_T}{p_0}\right)^{-n} ; \\ \text{Exponential in } p_T & : f(p_T) = \frac{1}{2\pi T^2} \frac{dN}{dy} e^{-p_T/T} ; \\ \text{Exponential in } m_T & : f(m_T) = \frac{1}{2\pi T(T+m)} \frac{dN}{dy} e^{-(m_T-m)/T} ; \\ \text{Boltzmann in } m_T & : f(m_T) = \frac{m_T}{2\pi(2T^2 + 2mT + m^2)} \frac{dN}{dy} e^{-(m_T-m)/T} . \end{aligned}$$

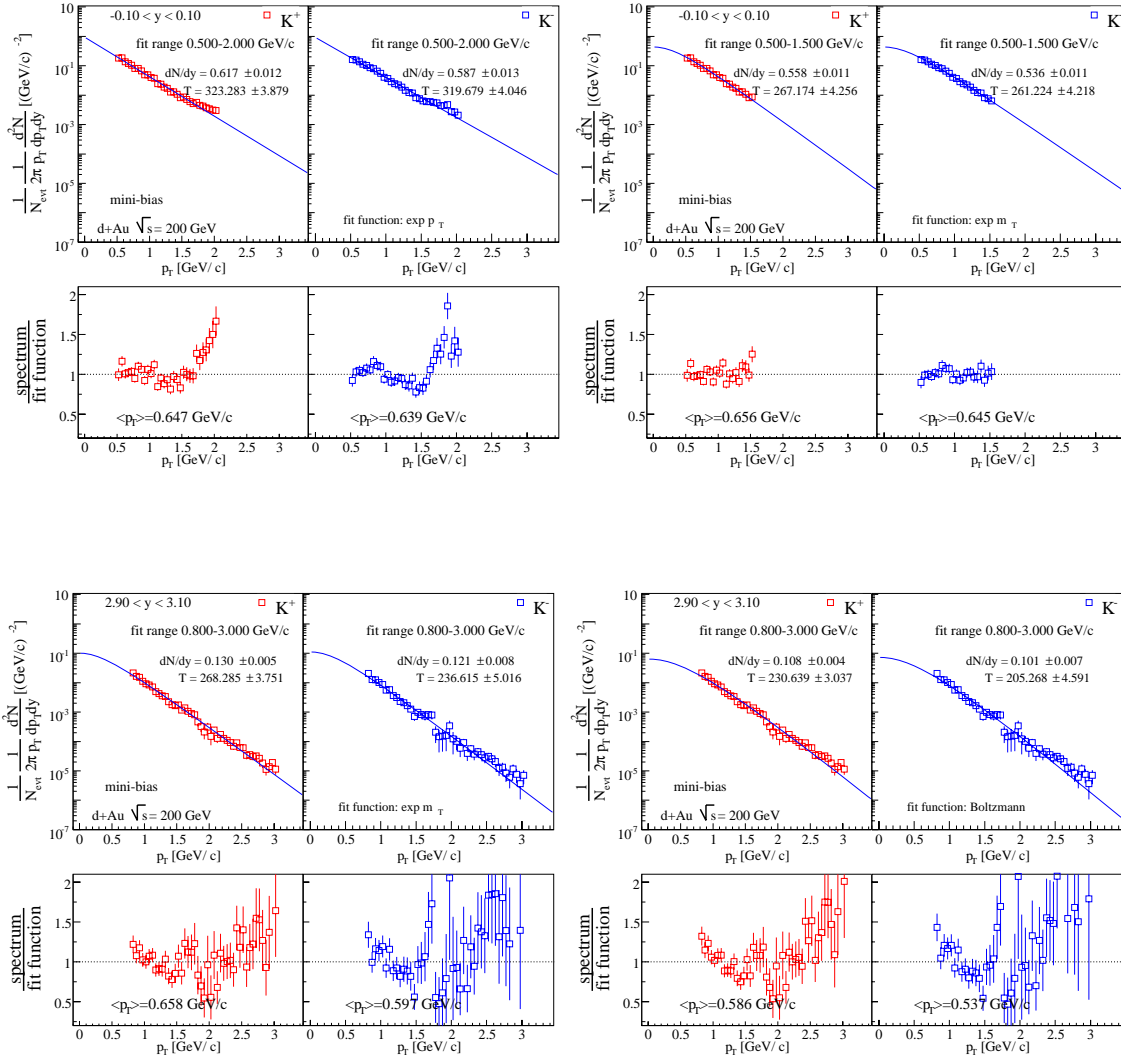
Appendix E

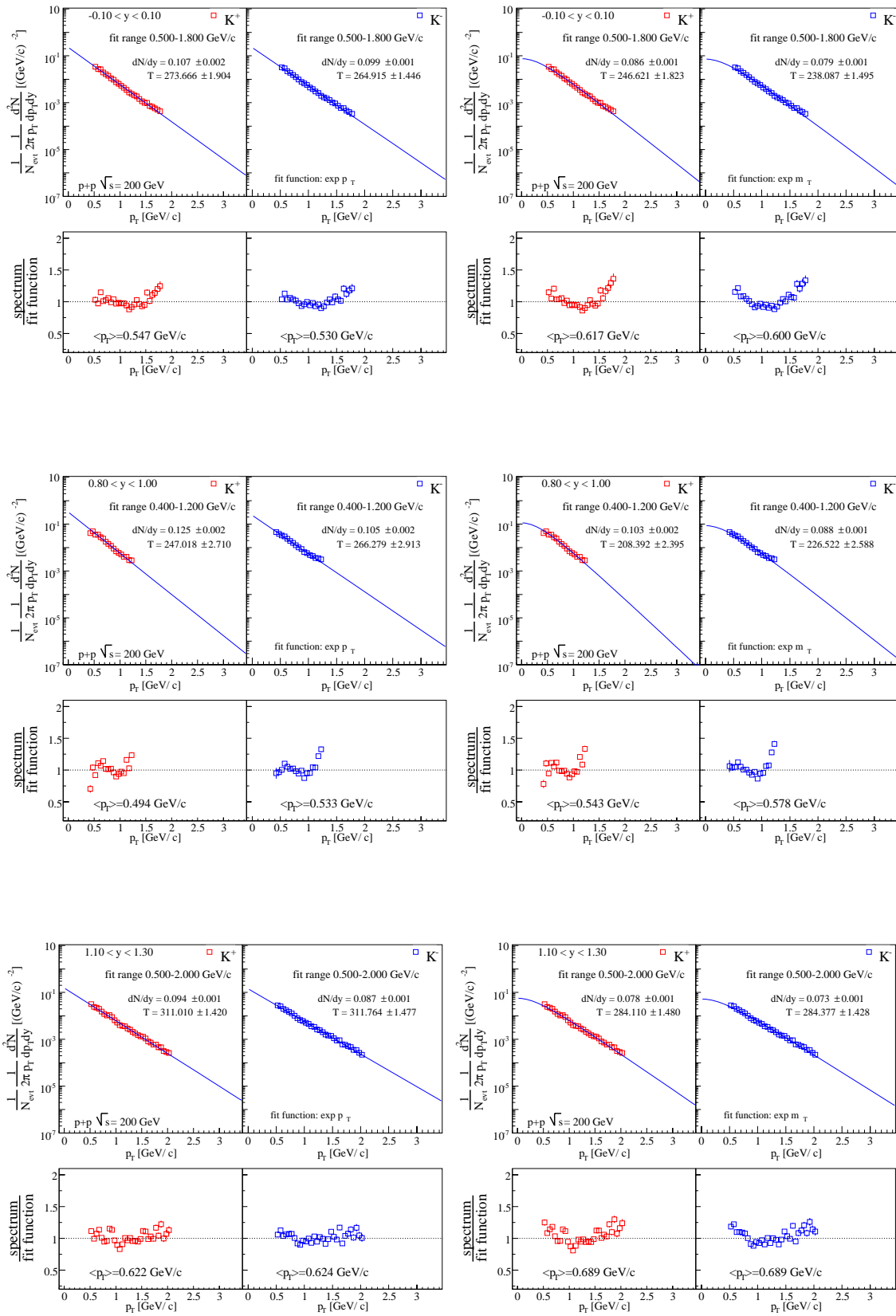
Spectra and fit study

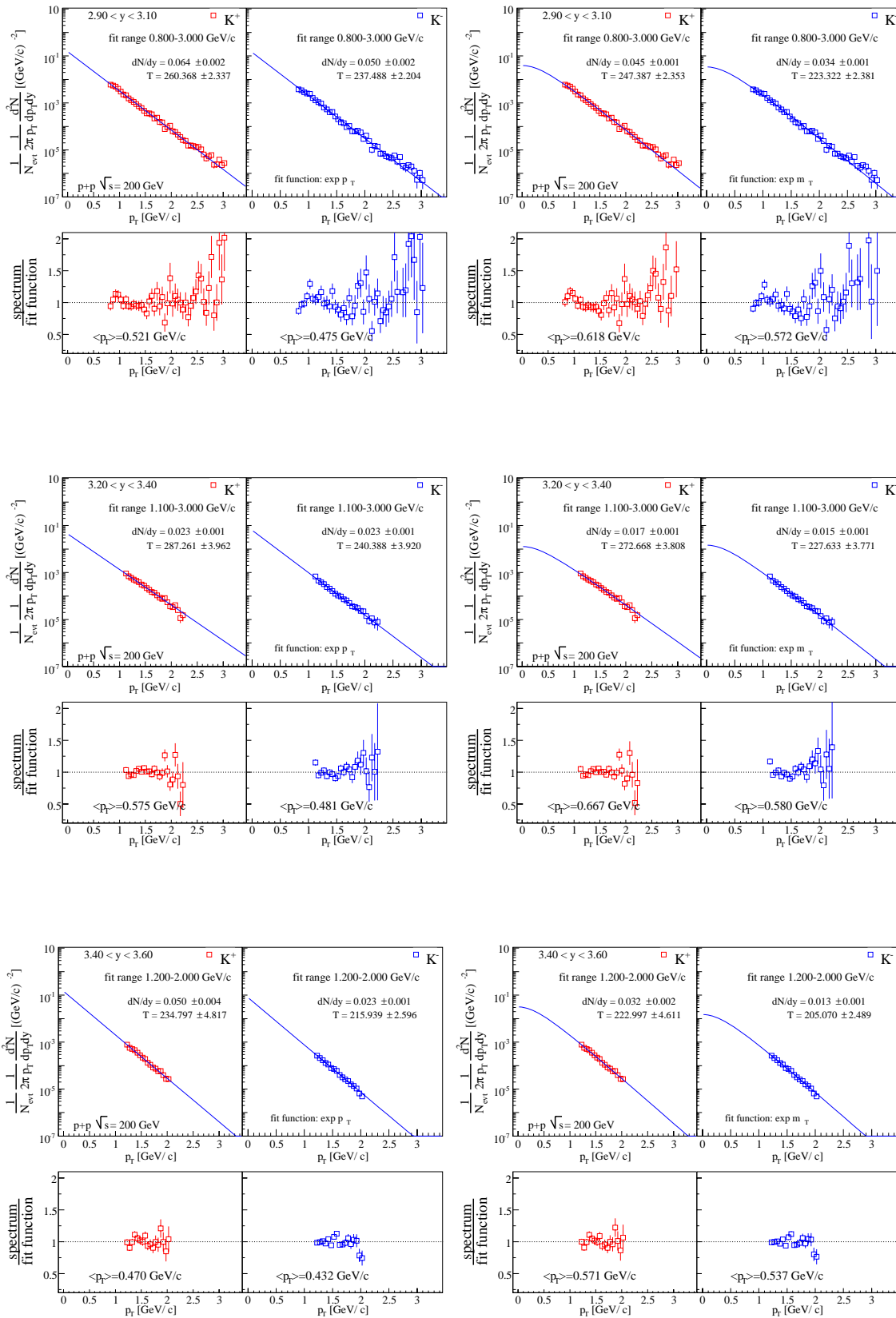


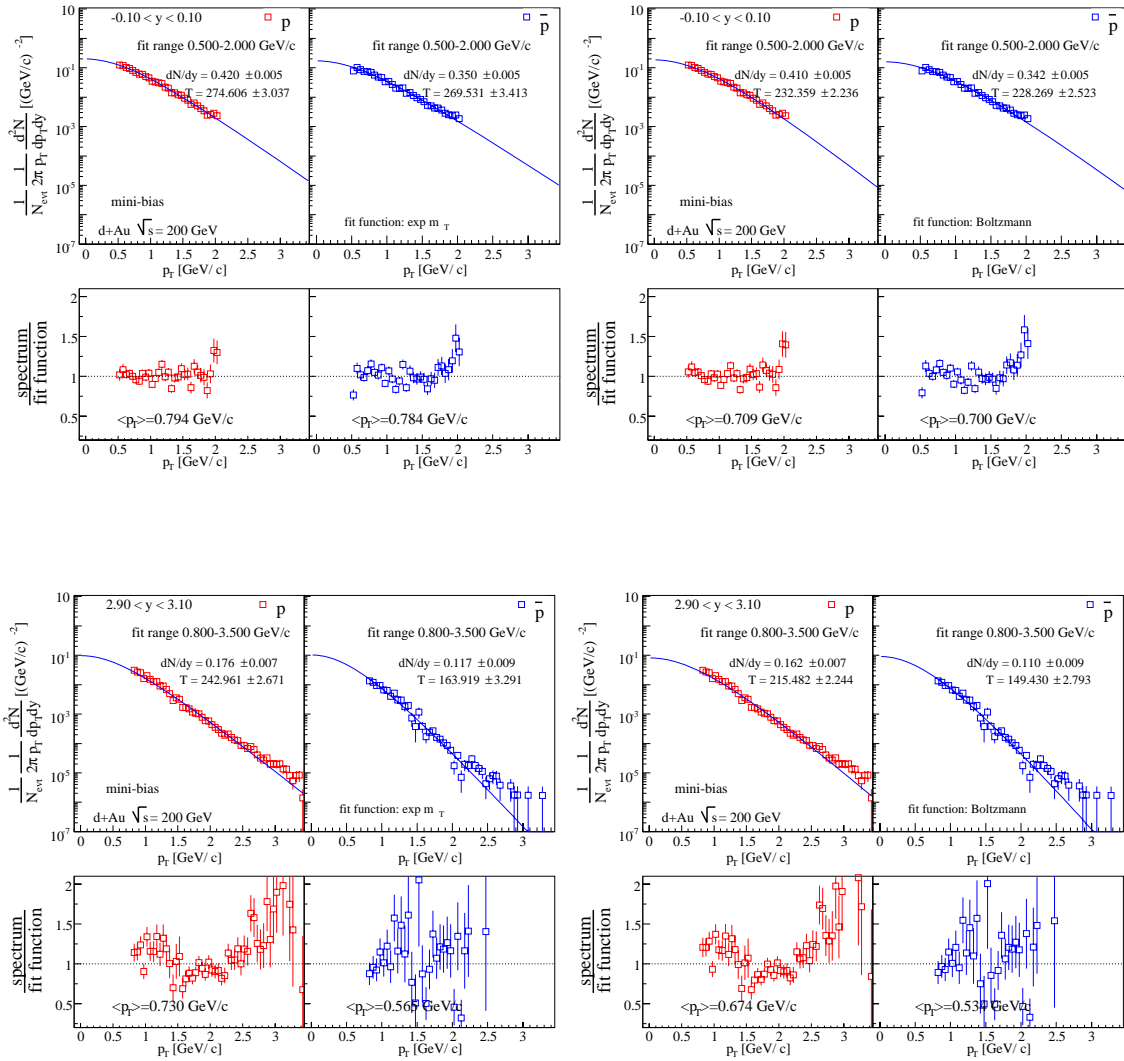


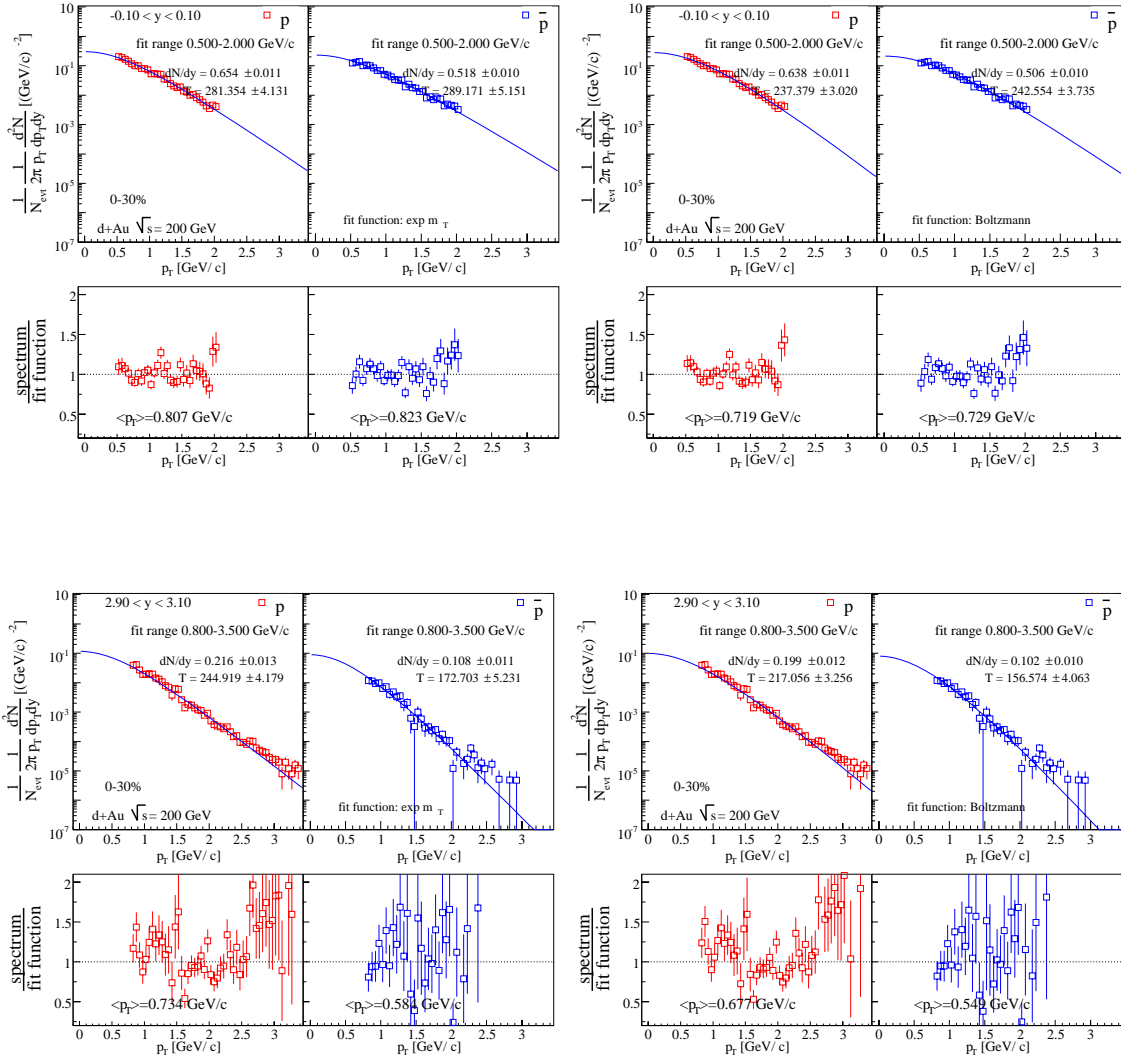


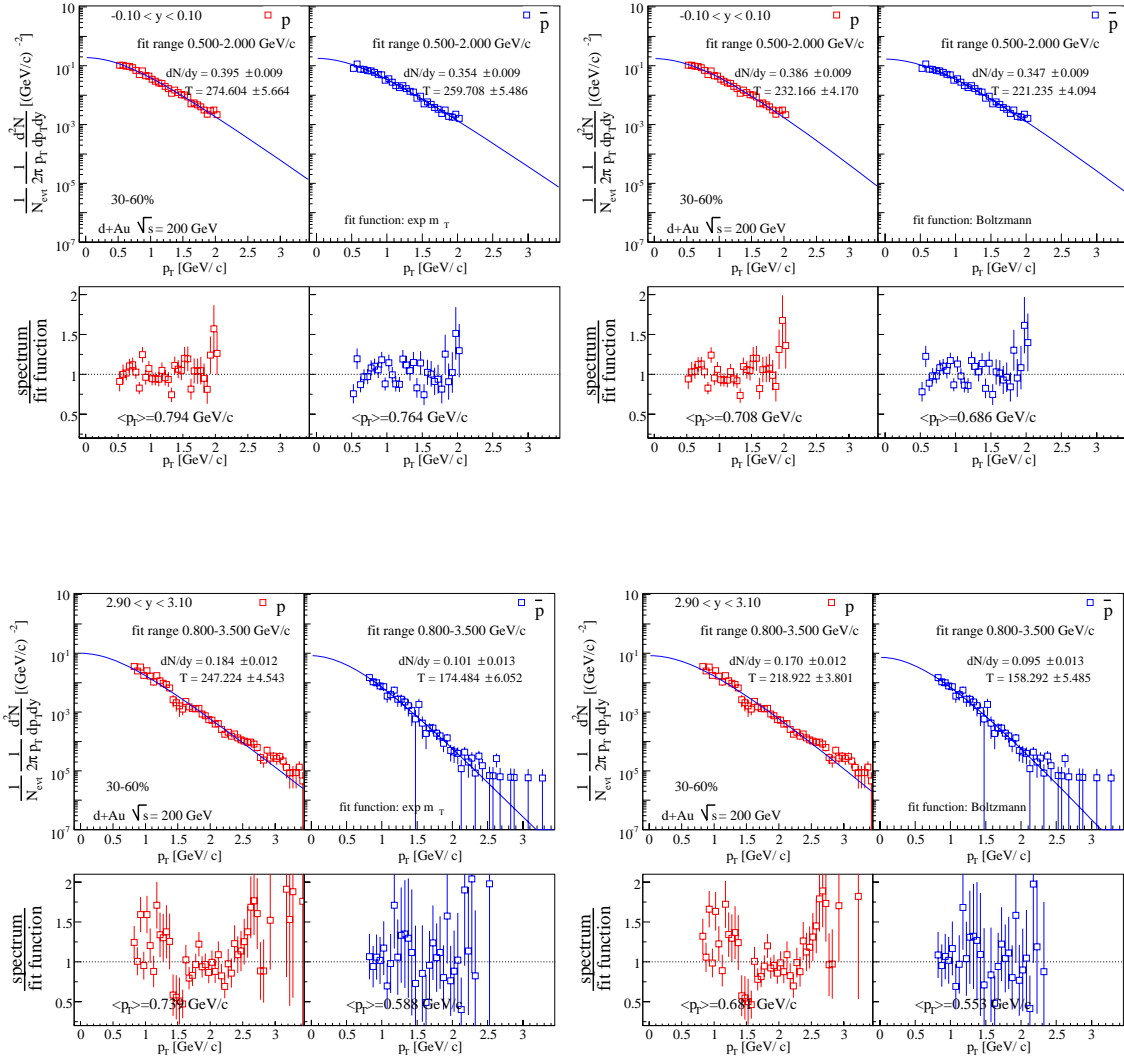


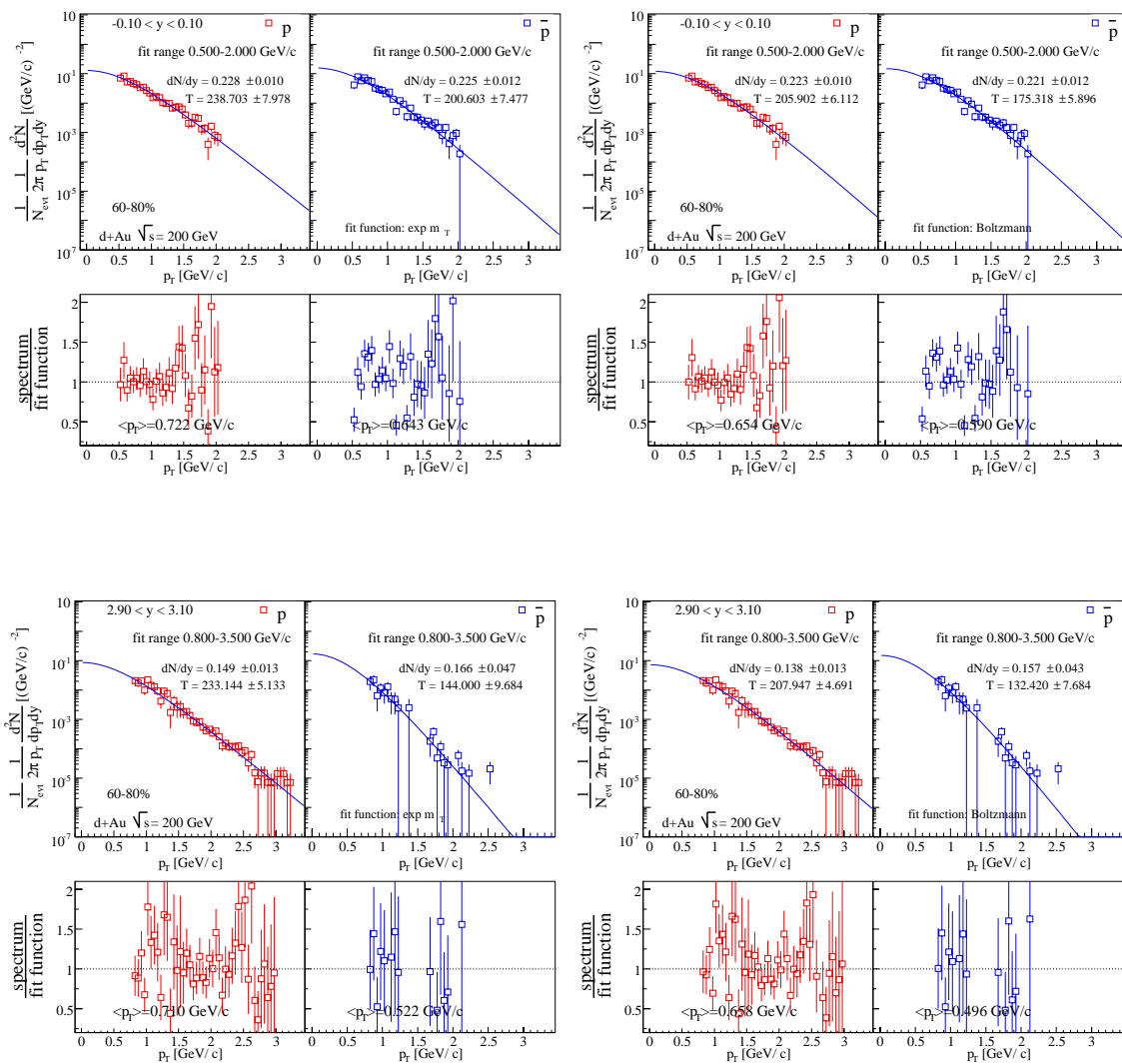


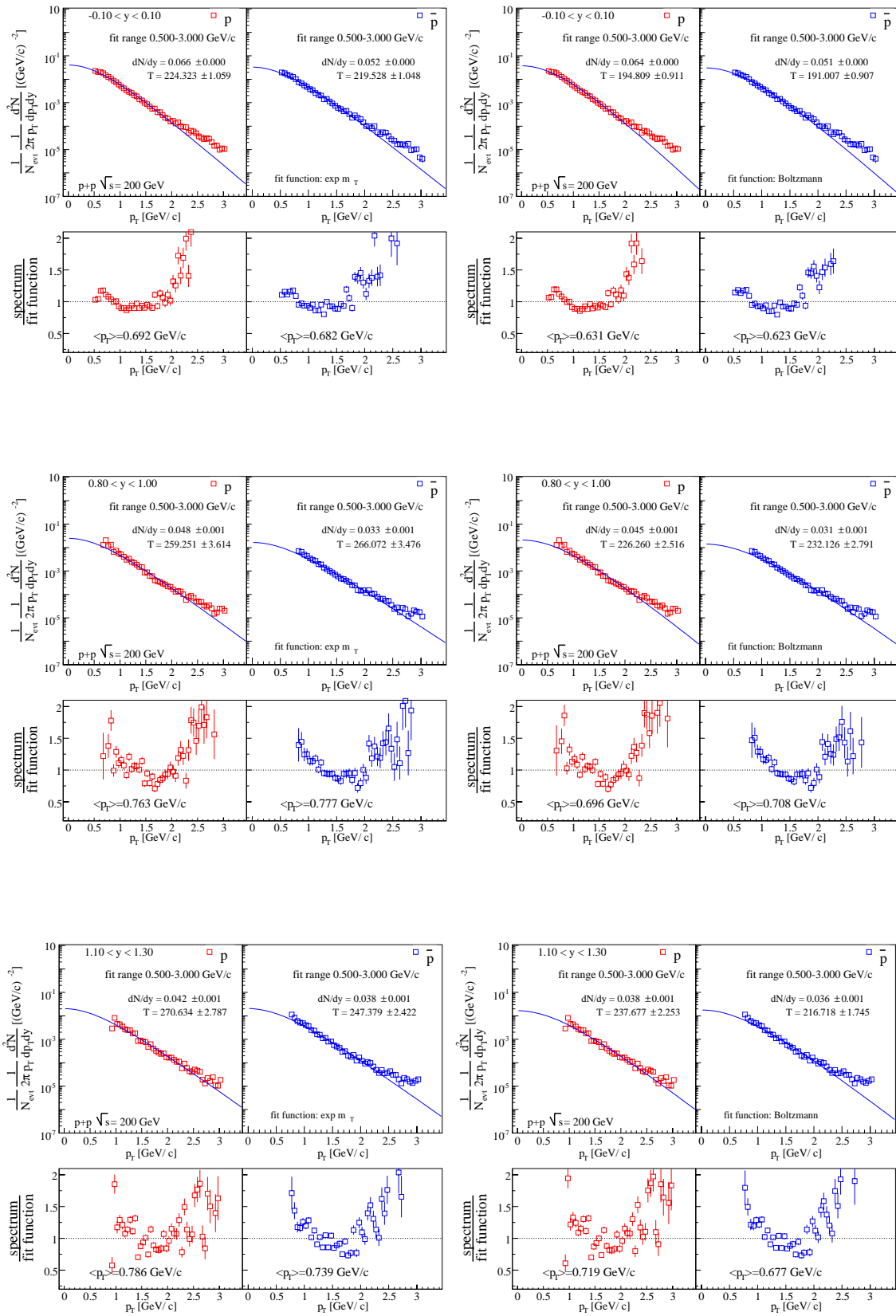


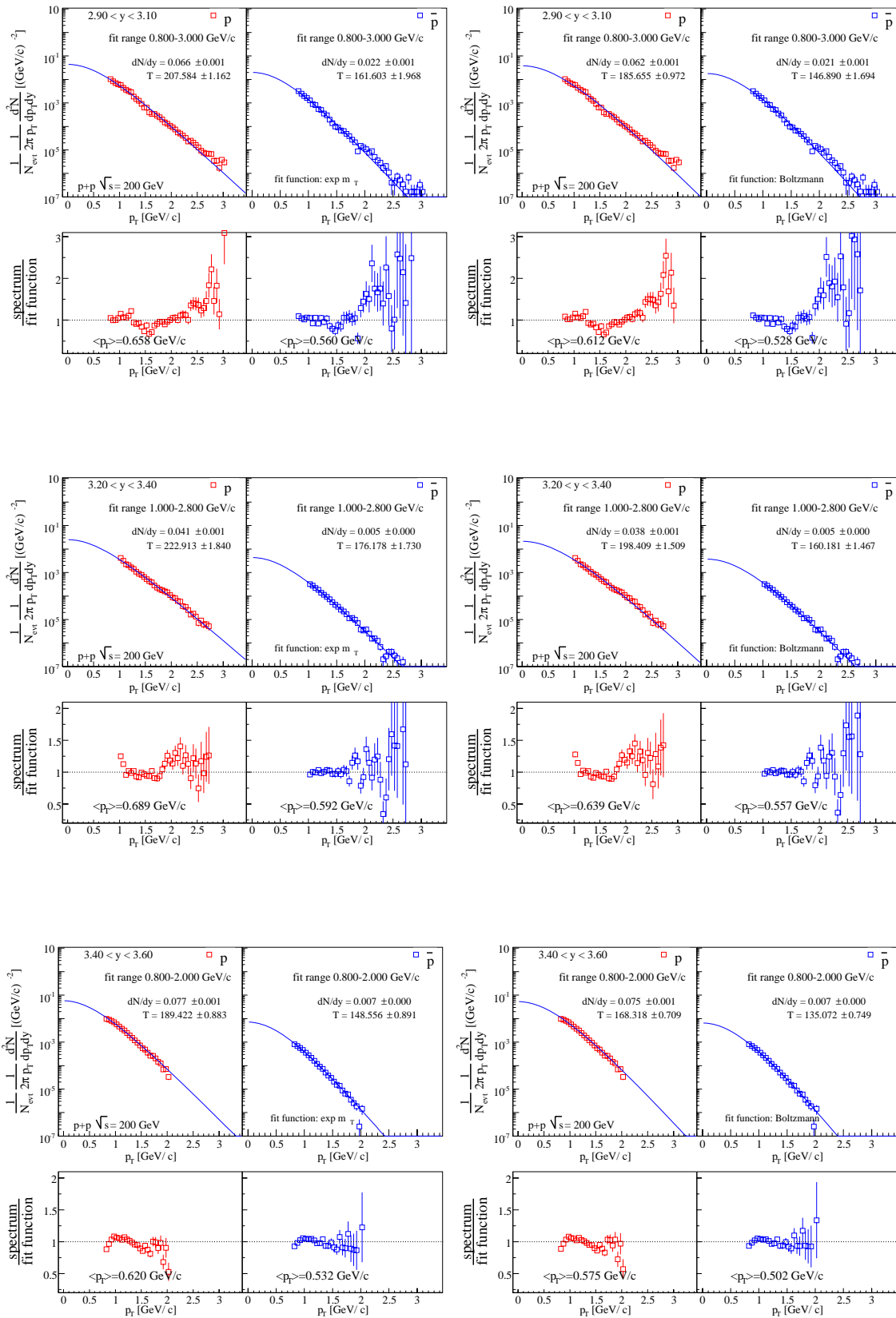












Appendix F

Publications

As main contributor

- H. Yang [BRAHMS Collaboration], *Rapidity dependence of identified hadron production in d+Au collisions at $\sqrt{s_{NN}} = 200$ GeV*, Rom. Rep. Phys. **58**, 5 (2006).
- H. Yang [BRAHMS Collaboration], *Hadron production at forward rapidity in nuclear collisions at RHIC*, Czech. J. Phys. **56**, A27 (2006).
- H. Yang [BRAHMS Collaboration], *Strangeness production in p+p and d+Au collisions at RHIC*, J. Phys. G **32** (2006) S491.
- H. Yang [BRAHMS Collaboration], *Identified particle production in d+Au and p+p collisions at RHIC*, J. Phys. G **34**, S619 (2007)
- I. Arsene *et al.* [BRAHMS Collaboration], *Production of mesons and baryons at high rapidity and high p_T in proton-proton collisions at $\sqrt{s} = 200$ GeV*, Phys. Rev. Lett. **98**, 252001 (2007)
- E-J. Kim and H. Yang [BRAHMS Collaboration], *Nuclear modification factors in d+Au and Au+Au collisions at $\sqrt{s_{NN}}=200$ GeV*, Proceedings for the International Nuclear Physics Conference (INPC 2007) in Tokyo, Japan.

As collaborator

- D. Röhrich *et al.* [BRAHMS Collaboration], *Properties of matter at forward rapidities at RHIC*, Nucl. Phys. A **749**, 295 (2005).
- I. Arsene *et al.* [BRAHMS Collaboration], *Rapidity dependence of high p_T suppression at $\sqrt{s_{NN}}=62.4$ GeV*, submitted to Phys. Lett. B, [arXiv:nucl-ex/0602018].
- I. Arsene *et al.* [BRAHMS Collaboration], *Nuclear modification factor for charged pions and protons at forward rapidity in central Au + Au collisions at 200 GeV*, Phys. Lett. B **650**, 219 (2007)

- P. Staszal for the BRAHMS Collaboration, *Recent results from the BRAHMS experiment*, Nucl. Phys. A **774**, 77 (2006).
- R. Karabowicz for the BRAHMS Collaboration, *Nuclear modification factor for identified hadrons at forward rapidity in Au+Au collisions at 200 GeV*, Nucl. Phys. A **774**, 477 (2006).
- E.-J. Kim for the BRAHMS Collaboration, *System and rapidity dependence of baryon to meson ratios at RHIC*, Nucl. Phys. A **774**, 493 (2006).
- H. Ito for the BRAHMS Collaboration, *Rapidity dependence of pion elliptic flow*, Nucl. Phys. A **774**, 519 (2006).
- T. M. Larsen for the BRAHMS Collaboration, *High p_T suppression vs system size and energy*, Nucl. Phys. A **774**, 541 (2006).
- I. G. Bearden for the BRAHMS Collaboration, *Recent high lights from BRAHMS*, J. Phys. G **34**, S207 (2007)
- T. M. Larsen for the BRAHMS Collaboration, *Nuclear modification factors at forward rapidity in Au-Au and Cu-Cu collisions at $\sqrt{s_{NN}} = 62.4$ GeV*, J. Phys. G **34**, S603 (2007)
- J. H. Lee for the BRAHMS Collaboration, *Particle suppression at high- x_F in Au+Au collisions at RHIC*, J. Phys. G **34**, S611 (2007)
- C. Nygaard for the BRAHMS Collaboration, *Rapidity dependence of coalescence in Au-Au collisions at $\sqrt{s_{NN}} = 200$ GeV*, J. Phys. G **34**, S1065 (2007)
- S. Sanders for the BRAHMS Collaboration, *Rapidity and pt dependence of identified-particle elliptic flow at RHIC* J. Phys. G **34**, S1083 (2007)

Bibliography

- [1] BRAHMS Collaboration, I. Arsene *et al.*, Phys. Rev. Lett. **94**, 032301 (2005), nucl-ex/0401025.
- [2] J. D. Bjorken, Phys. Rev. **D27**, 140 (1983).
- [3] L. D. Landau, Izv. Akad. Nauk SSSR Ser. Fiz. **17**, 51 (1953).
- [4] L. D. McLerran, Lect. Notes Phys. **583**, 291 (2002), hep-ph/0104285.
- [5] W. Busza and A. S. Goldhaber, Phys. Lett. **B139**, 235 (1984).
- [6] C. Y. Wong, Phys. Rev. **D30**, 972 (1984).
- [7] NA49, H. G. Fischer, Nucl. Phys. **A715**, 118 (2003), hep-ex/0209043.
- [8] W. Busza and R. Ledoux, Ann. Rev. Nucl. Part. Sci. **38**, 119 (1988).
- [9] C. Y. Wong, *Introduction to High-Energy Heavy Ion Collisions* (Singapore: World Scientific, 1995).
- [10] BRAHMS Collaboration, I. Arsene *et al.*, Nucl. Phys. **A757**, 1 (2005), nucl-ex/0410020.
- [11] BRAHMS, I. G. Bearden *et al.*, Phys. Rev. Lett. **93**, 102301 (2004), nucl-ex/0312023.
- [12] STAR Collaboration, J. Adams *et al.*, Nucl. Phys. **A757**, 102 (2005), nucl-ex/0501009.
- [13] BRAHMS Collaboration, I. Arsene *et al.*, Phys. Rev. Lett. **91**, 072305 (2003), nucl-ex/0307003.
- [14] PHENIX Collaboration, K. Adcox *et al.*, Nucl. Phys. **A757**, 184 (2005), nucl-ex/0410003.
- [15] PHOBOS Collaboration, B. B. Back *et al.*, Nucl. Phys. **A757**, 28 (2005), nucl-ex/0410022.
- [16] PHENIX, S. Afanasiev *et al.*, Phys. Rev. Lett. **99**, 052301 (2007), nucl-ex/0703024.
- [17] STAR, J. Adams *et al.*, Phys. Rev. Lett. **95**, 122301 (2005), nucl-ex/0504022.

- [18] J. W. Cronin *et al.*, Phys. Rev. **D11**, 3105 (1975).
- [19] M. E. Peskin and D. V. Schroeder, *An Introduction to Quantum Field Theory* (USA: Addison-Wesley, 1995).
- [20] H. Fritzsche, M. Gell-Mann, and H. Leutwyler, Phys. Lett. **B47**, 365 (1973).
- [21] F. Karsch, Nucl. Phys. **A698**, 199 (2002), hep-ph/0103314.
- [22] E. V. Shuryak, Phys. Rept. **61**, 71 (1980).
- [23] T. Sjostrand, Comput. Phys. Commun. **82**, 74 (1994).
- [24] J. C. Collins, D. E. Soper, and G. Sterman, Adv. Ser. Direct. High Energy Phys. **5**, 1 (1988), hep-ph/0409313.
- [25] R. Vogt, Heavy Ion Phys. **17**, 75 (2003), hep-ph/0207359.
- [26] PHENIX, S. S. Adler *et al.*, Phys. Rev. Lett. **91**, 241803 (2003), hep-ex/0304038.
- [27] BRAHMS Collaboration, F. Videbaek, Proceedings at the Winter Workshop on Nuclear Dynamics, Bigsky, Montana (2007), <http://www4.rcf.bnl.gov/brahms/WWW/pubs/2007/wwnd07Videbaek.pdf>.
- [28] BRAHMS Collaboration, I. Arsene *et al.*, Phys. Rev. Lett. **98**, 252001 (2007), hep-ex/0701041.
- [29] M. Arneodo, Phys. Rept. **240**, 301 (1994).
- [30] D. F. Geesaman, K. Saito, and A. W. Thomas, Ann. Rev. Nucl. Part. Sci. **45**, 337 (1995).
- [31] K. J. Eskola, V. J. Kolhinen, and R. Vogt, Nucl. Phys. **A696**, 729 (2001), hep-ph/0104124.
- [32] R. Vogt, Phys. Rev. **C70**, 064902 (2004).
- [33] BRAHMS Collaboration, I. Arsene *et al.*, Phys. Rev. Lett. **93**, 242303 (2004), nucl-ex/0403005.
- [34] N. Armesto, J. Phys. **G32**, R367 (2006), hep-ph/0604108.
- [35] D. Antreasyan *et al.*, Phys. Rev. **D19**, 764 (1979).
- [36] Y. L. Dokshitzer, Sov. Phys. JETP **46**, 641 (1977).
- [37] V. N. Gribov and L. N. Lipatov, Sov. J. Nucl. Phys. **15**, 438 (1972).
- [38] G. Altarelli and G. Parisi, Nucl. Phys. **B126**, 298 (1977).
- [39] E. A. Kuraev, L. N. Lipatov, and V. S. Fadin, Sov. Phys. JETP **45**, 199 (1977).
- [40] I. I. Balitsky and L. N. Lipatov, Sov. J. Nucl. Phys. **28**, 822 (1978).

- [41] L. V. Gribov, E. M. Levin, and M. G. Ryskin, Phys. Rept. **100**, 1 (1983).
- [42] A. H. Mueller and J.-W. Qiu, Nucl. Phys. **B268**, 427 (1986).
- [43] A. Dumitru, (2002), nucl-th/0203035.
- [44] J.-P. Blaizot and F. Gelis, Nucl. Phys. **A750**, 148 (2005), hep-ph/0405305.
- [45] D. Kharzeev, Y. V. Kovchegov, and K. Tuchin, Phys. Lett. **B599**, 23 (2004), hep-ph/0405045.
- [46] L. D. McLerran and R. Venugopalan, Phys. Rev. **D50**, 2225 (1994), hep-ph/9402335.
- [47] L. D. McLerran and R. Venugopalan, Phys. Rev. **D49**, 3352 (1994), hep-ph/9311205.
- [48] L. D. McLerran and R. Venugopalan, Phys. Rev. **D49**, 2233 (1994), hep-ph/9309289.
- [49] T. Hirano and Y. Nara, J. Phys. **G30**, S1139 (2004), nucl-th/0403029.
- [50] P. B. Straub *et al.*, Phys. Rev. Lett. **68**, 452 (1992).
- [51] PHENIX Collaboration, S. S. Adler *et al.*, Phys. Rev. **C74**, 024904 (2006), nucl-ex/0603010.
- [52] A. Accardi and M. Gyulassy, J. Phys. **G30**, S969 (2004), nucl-th/0402101.
- [53] A. Accardi and M. Gyulassy, Phys. Lett. **B586**, 244 (2004), nucl-th/0308029.
- [54] A. Krzywicki, J. Engels, B. Petersson, and U. Sukhatme, Phys. Lett. **B85**, 407 (1979).
- [55] M. Lev and B. Petersson, Z. Phys. **C21**, 155 (1983).
- [56] M. Gyulassy and X.-N. Wang, Comput. Phys. Commun. **83**, 307 (1994), nucl-th/9502021.
- [57] P. Shukla, (2001), nucl-th/0112039.
- [58] Z.-W. Lin and C. M. Ko, Phys. Rev. **C68**, 054904 (2003), nucl-th/0301025.
- [59] B. Zhang, C. M. Ko, B.-A. Li, and Z.-W. Lin, Phys. Rev. **C61**, 067901 (2000), nucl-th/9907017.
- [60] Z.-W. Lin, S. Pal, C. M. Ko, B.-A. Li, and B. Zhang, Phys. Rev. **C64**, 011902 (2001), nucl-th/0011059.
- [61] Z.-W. Lin, S. Pal, C. M. Ko, B.-A. Li, and B. Zhang, Nucl. Phys. **A698**, 375 (2002), nucl-th/0105044.

- [62] B. Zhang, *Comput. Phys. Commun.* **109**, 193 (1998), nucl-th/9709009.
- [63] B. Andersson, G. Gustafson, G. Ingelman, and T. Sjostrand, *Phys. Rept.* **97**, 31 (1983).
- [64] B.-A. Li and C. M. Ko, *Phys. Rev.* **C52**, 2037 (1995), nucl-th/9505016.
- [65] R. C. Hwa and C. B. Yang, *Phys. Rev. Lett.* **93**, 082302 (2004), nucl-th/0403001.
- [66] R. C. Hwa and C. B. Yang, *Phys. Rev.* **C70**, 037901 (2004), nucl-th/0404066.
- [67] L.-J. Ruan, Pion, kaon, proton and antiproton spectra in d+Au and p+p collisions at $\sqrt{s_{NN}} = 200$ GeV at the Relativistic Heavy Ion Collider, PhD thesis, University of Science and Technology of China, 2005, nucl-ex/0503018.
- [68] O. E. J. Claus, High p_T Charged Hadron Production at RHIC, PhD thesis, Niels Bohr Institute, Copenhagen University, 2004.
- [69] T. W. Ludlam and N. P. Samios, *Z. Phys.* **C38**, 353 (1988).
- [70] H. Hahn *et al.*, *Nucl. Instrum. Meth.* **A499**, 245 (2003).
- [71] STAR Collaboration, K. H. Ackermann *et al.*, *Nucl. Instrum. Meth.* **A499**, 624 (2003).
- [72] PHENIX Collaboration, K. Adcox *et al.*, *Nucl. Instrum. Meth.* **A499**, 469 (2003).
- [73] PHOBOS Collaboration, B. B. Back *et al.*, *Nucl. Instrum. Meth.* **A499**, 603 (2003).
- [74] BRAHMS Collaboration, M. Adamczyk *et al.*, *Nucl. Instrum. Meth.* **A499**, 437 (2003).
- [75] O. E. J. Claus, Charged Particle Production in Au+Au Collisions at $\sqrt{s_{NN}} = 130$ GeV, PhD thesis, Niels Bohr Institute, Copenhagen University, 2001.
- [76] Y. Blyakhman, Beam beam counters and charged particle multiplicity in the BRAHMS experiment at RHIC, PhD thesis, New York University, 2001, UMI-30-09288.
- [77] S. Bultmann *et al.*, *Nucl. Instrum. Meth.* **A535**, 415 (2004).
- [78] <http://kunuc10.phsx.ku.edu/sanders/cent2npart.html>, F. Videbaek, (2002).
- [79] H. Ito, Charged-Particle Production in Au+Au Collisions at $\sqrt{s_{NN}} = 130$ GeV and $\sqrt{s_{NN}} = 200$ GeV, PhD thesis, University of Kansas, 2002.
- [80] BRAHMS Collaboration: <http://brahms-web.brahms.bnl.gov>.
- [81] J. I. Jørdre, Performance of the Time Projection Chambers of the BRAHMS Experiment at RHIC, Master's thesis, University of Bergen, 2000.

- [82] T. Larsen, Efficiency Calculations for the Time Projection Chambers in the BRAHMS Experiment at the RHIC Accelerator, Master's thesis, University of Oslo, 2003.
- [83] BRAHMS Analysis Note 27, 29, 34, 38, P. Staszel, (2001).
- [84] R. Karabowicz, Particle Track Identification in the Drift Chambers of the BRAHMS Experiment, Master's thesis, Jagiellonian University, 2002.
- [85] BRAHMS Collaboration, Conceptual Design Report of *The BRAHMS experiment at RHIC*, K. Ashktorab, (1995).
- [86] D. Ouerdane, Charged Particle Production in Au+Au Collisions at $\sqrt{s_{NN}} = 200$ GeV, PhD thesis, Niels Bohr Institute, Copenhagen University, 2003.
- [87] P. H. L. Christiansen, Stopping in central $\sqrt{s_{NN}} = 200$ GeV Au+Au collisions at RHIC, PhD thesis, Niels Bohr Institute, Copenhagen University, 2003.
- [88] <http://zefir.if.uj.edu.pl/staszel/brahms/fseffic/indexnew.html>, P. Staszel, (2001).
- [89] <http://www4.rcf.bnl.gov/brahms/WWW/private/meetings/Dec2002/richeff.pdf>, F. Videbaek, (2002).
- [90] BRAHMS Analysis Note on *Corrections to pp cross sections due to trigger counter acceptance*, F. Videbaek, (2006).
- [91] S. E. Vance, M. Gyulassy, and X. N. Wang, Phys. Lett. **B443**, 45 (1998), nucl-th/9806008.
- [92] STAR Collaboration, J. Adams *et al.*, Phys. Lett. **B637**, 161 (2006), nucl-ex/0601033.
- [93] STAR Collaboration, J. Adams *et al.*, Phys. Lett. **B616**, 8 (2005), nucl-ex/0309012.
- [94] PHOBOS Collaboration, R. Nouicer *et al.*, J. Phys. **G30**, S1133 (2004), nucl-ex/0403033.
- [95] UA5 Collaboration, G. J. Alner *et al.*, Z. Phys. **C33**, 1 (1986).
- [96] STAR Collaboration, B. I. Abelev *et al.*, Submitted to Phys. Rev. C (2007), arXiv:0706.0472 [nucl-ex].